The Role of Pulsing and Humidity in Plasma-based Nitrogen Fixation:

a Combined Experimental and modeling study

Elise Vervloessem

Supervisors

Prof. dr. Annemie Bogaerts | Prof. dr. ir. Nathalie De Geyter

Thesis submitted for the degree of

Doctor of Science: Chemistry

Doctor of Engineering Physics

Faculty of Science
Departement Chemistry

Faculty of Engineering and
Architecture

De rol van pulsen en vochtigheid in plasmagebaseerde stikstoffixatie: een gecombineerde experimentele en computationele studie

Elise Vervloessem

Promotoren

Prof. dr. Annemie Bogaerts | Prof. dr. ir. Nathalie De Geyter

Proefschrift voorgelegd tot het behalen van de graad van
Doctor in de Wetenschappen: chemie
Doctor in de ingenieurswetenschappen: toegepaste natuurkunde

Aan de Universiteit Antwerpen en de Universiteit Gent te verdedigen
door Elise Vervloessem

Antwerpen & Gent 2023

Universiteit Antwerpen

Faculteit Wetenschappen
Departement Chemie

GHENT UNIVERSITY

Faculteit
Ingenieurswetenschappen
en Architectuur

Members of the Jury

Members of the individual PhD commission

Prof. dr. Erik Neyts (Chair)
Plasma Lab for Applications in Sustainability and Medicine (PLASMANT) – Antwerp, University of Antwerp

Prof. dr. Annemie Bogaerts (promotor)
Plasma Lab for Applications in Sustainability and Medicine (PLASMANT) – Antwerp, University of Antwerp

Prof. dr. ir. Nathalie De Geyter (promotor)
Research Unit Plasma Technology (RUPT), Ghent University

External jury members

Prof. dr. Pegie Cool
Laboratory of Adsorption and Catalysis (LADCA), University of Antwerp

Prof. dr. Ir. Christophe Leys
Research Unit Plasma Technology (RUPT), Ghent University

Prof. dr. Siegfried Vlaeminck
Duurzame Energie- en Lucht- en Watertechnologie (DuEL), University of Antwerp

Prof. dr. Ir. Filip De Turck
Internet Technology and Data Science Lab (IDLab), Ghent University

Prof. dr. Rony Snyders
Chimie des Interactions Plasma-Surface, University of Mons Materia Nova Research Center

Summary

Nitrogen (N) is an indispensable building block for all living organisms as well as for pharmaceutical and chemical industry. In a nutshell, N is needed for plants to grow and beings to live and nitrogen fixation (NF) is the process that makes N available for plants as food by converting N_2 into a reactive form, such as ammonia (NH_3) or nitrogen oxides (NO_x), upon reacting with O_2 and H_2. The ever-growing population, however, requires more fixed N than the Earth can provide. For this reason we have been supplementing the soil with additional N, first by natural sources (e.g. by recycling organic waste from plants, humans and animals and by planting N_2 fixing legumes) and later also through synthetic fertilizer to make up for the high demand.

Since the invention of synthetic fertilizers, food production increased drastically and enabled mass population expansion. 50 % of the world's population today depends on the industrial Haber-Bosch process for NH_3 production from N_2 and H_2 (in the form of CH_4). Nevertheless, due to its significant carbon footprint it does not fit into the sustainable world we are trying to achieve. The Haber-Bosch process has been extensively optimized during its 100-year existence and there is currently no viable alternative or complementary process to meet our continuously growing needs. Therefore, it is of pivotal importance to research alternative ways for nitrogen fixation to ensure continuous but sustainable improvement of synthetic fertilizer production. Although these alternative ways might not fully substitute the Haber-Bosch process, they can present an appealing auxiliary technology of nitrogen fixation, especially in remote areas with abundant renewable electricity.

One of these technologies under research is plasma technology. Plasma is a partially ionized gas containing a wide range of species which enable non-conventional chemistry. A commercial plasma-based nitrogen fixation process would imply a green and energy-efficient fertilizer and base chemicals production that is: (1) carbon neutral, and (2) compatible with renewable energy sources.

The thesis first gives a general introduction (to frame the scope and provide the necessary background) and a description of the methodology (**Chapters I and II**).

The **aim of this thesis** is to elucidate (wet) plasma-based nitrogen fixation with a focus on (1) the role of pulsing in achieving low energy consumption, (2) the role of H_2O as a hydrogen source in nitrogen fixation and (3) elucidation of nitrogen fixation pathways in humid air and humid N_2 plasma in a combined experimental and computational study.

Furthermore, this thesis aims to take into account the knowledge-gaps and challenges identified in the discussion of the state of the art. Specifically, (1) we put our focus on branching out to another way of introducing water into the plasma system, i.e. H_2O vapor, (2) we de-couple the problem for pathway elucidation by starting with characterization of the chosen plasma, next a simpler gas mixture and building up from there, (3) we include modelling, though not under wet conditions and (4) we focus on also analyzing species and performance outside liquid H_2O.

In **Chapter III**, the plasma source, a pulsed non-equilibrium plasma, called the *Soft Jet*, is characterized to provide us with the necessary knowledge for the following Chapters. The Soft Jet consumes a small amount of power (0.1 W) compared to other sources. The gas temperature during the pulse is elevated far above room temperature (1750 K), however, the time – and space averaged temperature is close to room temperature due to the low duty cycle of the plasma pulses.

Subsequently, we study the NO_x production of the Soft Jet operating in dry air in **Chapter IV** and elucidate the reason for its very low energy consumption by using a quasi-1D chemical kinetics model and experiments. The model shows that the non-thermal Zeldovich mechanism is the main NO producing reaction in this plasma, in line with other NO_x producing air plasmas. The model reveals that the strong temperature drop in between pulses affects the NO_x production and decomposition reactions (back – and forward reactions of the Zeldovich mechanism) positively, enabling efficient use of the power put into the plasma.

In **Chapter V**, H_2O is added to the experiment in two ways: (1) by adding H_2O vapor to the feed gas, meaning we are working in humid air and humid N_2 and (2) by placing the plasma above a liquid-filled container. We show that the selectivity of plasma-based NF in humid air and humid N_2 can be controlled by changing the humidity in the feed gas. Most interestingly, a.o. experiments with isotopically labelled H_2O show that the H_2O vapor, and not liquid H_2O, is the main source of H for NH_3 synthesis. This suggests NH_3 is mainly formed in the gas phase opposed to the liquid phase, contrary to what is suggested predominantly in literature. This can be taken into account in future wet

plasma-based NF designs by focussing on increasing the water vapor content in the plasma.

In the last study (**Chapter VI**), the pathways toward nitrogen-fixated species in the gas phase are studied in more detail. Using optical emission spectroscopy, Fourier-transform infra-red spectroscopy and in-line removal of HNO_2, we identify a significant loss pathway for HNO_2 and NH_3, where these molecules are synthesized simultaneously, i.e. downstream from the plasma, HNO_x reacts with NH_3 to form NH_4NO_x which decomposes into N_2 and H_2O or precipitates. To prevent ineffective nitrogen fixation, this pathway should be considered in future works aimed at optimizing nitrogen fixation. Additionally, this Chapter and Chapter V show that NH_3 production can be achieved in both N_2 and air plasmas using H_2O as a H source.

The **Conclusions and Outlook (Chapter VII)** recaps the research questions that were (partially) answered by this thesis and places them into the context of the state of the art. In conclusion, this thesis adds further to the current state of the art of plasma-based NF both in the presence of H_2O and in dry systems.

The thesis closes with a point of view on future research in the field of wet plasma-based nitrogen fixation. In short, (1) it would be important to validate our results further in other plasma setups and to attempt to apply the knowledge presented in this thesis for performance enhancement, (2) when the underlying chemistry of wet plasma-based NF has been more established and the advantages and disadvantages have been mapped, we can look for synergies with other NF fields, for example plasma-electrochemistry, and (3) wet plasma-based NF is in an earlier research stage compared to dry plasma-based NF,

nonetheless is it important to also focus on the technological aspects of this application.

At the beginning of each Chapter you will find the aim and/or summary of the Chapter in Layman's terms.

Samenvatting

Stikstof (N) is een onmisbare bouwsteen voor alle levende organismen (plant, dier en mens), alsook voor de farmaceutische en chemische industrie. Stikstoffixatie is het proces dat N beschikbaar maakt als voedsel voor planten door N_2 om te zetten in een reactievere vorm van N zoals ammoniak (NH_3) of stikstofoxides (NO_x) door reactie met O_2 en H_2.

De groeiende populatie vraagt meer gefixeerd N dan de aarde kan voorzien. Bijgevolg vullen we de bodem aan met N om te voldoen aan de hoge vraag, eerst via natuurlijke bron (bijv. door recyclage van organisch plant-, dier-, en menselijk afval en door het planten van N_2 fixerende peulvruchten) en later door het gebruik van synthetische meststoffen.

Sinds de uitvinding van synthetische meststoffen is de voedselproductie drastisch toegenomen met een enorme bevolkingsexplosie als gevolg. 50% van de wereldpopulatie hangt af van één industrieel proces genaamd Haber-Bosch, dat aan zogenaamde synthetische stikstoffixatie doet door H_2 (in de vorm van CH_4) en N_2 om te zetten in NH_3. Door zijn grote ecologische voetafdruk past het huidige industriële proces echter niet in de duurzame wereld waarnaar we streven. Haber-Bosch is in zijn 100 jarig bestaan continu verbeterd en op dit moment hebben we geen haalbaar alternatief dat dezelfde ondersteuning biedt.

Synthetische meststoffen zijn van vitaal belang, maar zijn tegelijkertijd ook milieubelastend. Daarom is het uiterst belangrijk om alternatieve manieren om stikstof te fixeren te onderzoeken zodat we een continue maar duurzame verbetering in deze industrie kunnen verzekeren.

Ondanks dat deze alternatieve technologieën misschien Haber-Bosch niet volledig zullen vervangen in de voorzienbare toekomst, kunnen ze een interessante bijkomende syntheseweg bieden, zeker in verafgelegen gebieden waar hernieuwbare energie overvloedig aanwezig is. Een van de alternatieven die momenteel veel interesse krijgt, is plasmatechnologie. Plasma is een deels geïoniseerd gas bestaande uit een brede waaier aan deeltjessoorten die atypische chemie mogelijk maken. Een gecommercialiseerd plasmaproces voor het fixeren van stikstof zou een groene en energie-efficiënte productie van meststoffen en basischemicaliën betekenen die (i) koolstofneutraal, en (ii) compatibel is met hernieuwbare energiebronnen.

De thesis begint met een algemene introductie om het werk te kaderen en de nodige achtergrondinfo te verschaffen (**Hoofdstuk I**). Verder geeft **Hoofdstuk II** een beschrijving van de methoden gebruikt in de volgende hoofdstukken.

Het **doel van deze thesis** is om plasma-gebaseerde stikstoffixatie verder te ontrafelen, met een focus op (1) de rol van gepulst plasma in het bereiken van een lage energieconsumptie, (2) de functie van water als een waterstofbron in stikstoffixatie en (3) het doorgronden van de onderliggende stikstoffixatiechemie in vochtige lucht- en stikstofplasma's in een gecombineerde experimentele en modeleerstudie.
Daarnaast, streeft deze thesis om de kenniskloof en uitdagingen, besproken in de huidige stand van de techniek mee in rekening te brengen. Specifiek betekent dit dat (1) we focussen op vertakken naar een andere manier om water te introduceren in het plasma-systeem,

i.e. waterdamp, (2) we het complex probleem inzake de onderliggende chemische paden ontkoppelen door te starten met een karakterisatie van het plasma, vervolgens gebruik te maken van een eenvoudiger gasmengsel, en uit deze kennis verder op te bouwen, (3) we modelleerwerk opnemen, doch niet in een vochtig maar droog gasmengsel en (4) we focussen op deeltjesanalyse en de prestatie buiten vloeibaar water.

In **Hoofdstuk III** wordt de plasmabron, een gepulst niet-evenwichtsplasma, genaamd de *Soft Jet*, gekarakteriseerd om ons de nodige informatie te geven voor de volgende studies. De Soft Jet consumeert weinig vermogen (0.1 W) in vergelijking met andere plasmabronnen. Tijdens de puls bevindt de gastemperatuur (1750 K) zich ver boven kamertemperatuur. Dankzij de lage arbeidscyclus van de plasmapulsen is de gemiddelde gastemperatuur – in tijd en ruimte – echter dicht bij kamertemperatuur.

Daaropvolgend bestuderen we in **Hoofdstuk IV** de NO_x-productie van de Soft Jet in droge lucht. Hierin doorgronden we de redenen voor de lage energieconsumptie door gebruik te maken van een quasi-1D chemisch kinetiek model in combinatie met experimenten. Het model toont aan dat het niet-thermisch Zeldovich mechanisme de voornaamste NO-produceerende reactie is. Daarnaast toont het model aan dat de sterke daling in temperatuur tussen de pulsen de NO_x productie- en afbraakreacties (vooruit- en teruggaande reacties van het Zeldovich mechanisme) positief beïnvloedt en zo efficiënt gebruik van het aangelegd vermogen mogelijk maakt.

In **Hoofdstuk V** wordt H_2O toegevoegd aan het experiment op twee manieren: (1) door H_2O damp toe te voegen aan het inlaatgas, wat

betekent dat we met vochtige lucht en vochtige stikstof werken en (2) door het plasma boven een vloeistofhoudend reservoir te plaatsen. Meest opvallend zijn de experimenten die o.a. via isotopen-gekenmerkt H_2O aantonen dat hoofdzakelijk H_2O damp en niet vloeibaar H_2O de waterstofbron is voor NH_3 synthese. Dit suggereert dat NH_3 voornamelijk gevormd wordt in de gasfase veeleer dan in de vloeistoffase, in tegenstelling tot wat vaak beschreven wordt in de literatuur.

In het laatste hoofdstuk (**Hoofdstuk VI**) onderzoeken we meer gedetailleerd de onderliggende chemie voor de vorming van stikstofgefixeerde deeltjes in de gasfase. Door gebruik te maken van optische emissiespectroscopie, Fourier-transformatie infrarood spectroscopie en geïntegreerde verwijdering van HNO_2, identificeren we een significant verliesmechanisme van HNO_2 en NH_3, dat belangrijk is wanneer deze twee moleculen samen worden gevormd. Om ineffectieve stikstoffixatie te voorkomen is het belangrijk om dit mechanisme mee in rekening te nemen in toekomstig onderzoek naar alternatieve methoden om stikstof te fixeren.

De **Conclusies en Vooruitzichten (Hoofdstuk VII)** vatten de onderzoeksvragen die (deels) beantwoord werden bondig samen en bespreken deze in de context van de huidige stand van de techniek. We concluderen dat deze thesis een verdere toevoeging is aan de stand van de techniek o.a. in het veld van plasma-gebaseerde stikstoffixatie, zowel in het bijzijn water als in droge systemen.
Tot slot wordt de thesis afgesloten met een perspectief op toekomstig onderzoek in het veld van (waterbevattende) plasma-gebaseerde stikstoffixatie dat er beknopt als volgt uitziet: (1) het is belangrijk om

onze resultaten verder te valideren in andere plasma opstellingen en om inspanningen te leveren om de kennis voorgesteld in deze thesis toe te passen voor prestatieverbetering, (2) wanneer er meer duidelijkheid is over de onderliggende chemie en de voor- en nadelen in kaart zijn gebracht kunnen we op zoek gaan naar synergiën met andere stikstoffixatie velden, bijvoorbeeld plasma-elektrochemie en (3) ondanks dat plasma-gebaseerde stikstoffixatie met water zich in een vroeger onderzoek stadium bevindt in vergelijking met zijn droge variant, is het belangrijk om in parallel te focussen op de technologische aspecten van de applicatie.

Aan het begin van ieder Hoofdstuk vind je het doel en/of een samenvatting van het Hoofdstuk geschreven in lekentaal.

Failure is only the opportunity to begin again.
Only this time, more wisely.

I poured your tea just because I wanted to,
and for no other reason.
- Iroh

Acknowledgements

Firstly, I would like to thank my promotors, Annemie and Nathalie, for their support and the opportunity to be a part of PLASMANT and RUPT. I would like to recognize Annemie especially. Thank you. Saying Annemie's conscientiousness and dedication is legendary is not an understatement.

I would like to extend my sincere thanks to the members of my jury. I appreciate your time and genuine interest in my work.

I had two **impressive** mentors and colleagues that literally made my PhD happen, but I only have one page. Anton, thank you for your passion, patience and ~~composure~~ level-headedness. Yury, thank you for your honesty, boldness and commitment. (XXX) You both challenged me and it was amazing to have had the experience of working with you both.

I was very lucky to be part of PLASMANT and RUPT, thank you for the on and off topic discussions and banter. Thank you for the chatter in the halls and unexpected visits in B.2.31, for us… or the library of stuff we have carefully selected (hoarded).. Thank you, Tim P., Karel, Karen and Priyanka, for fixing ~~too many of~~ my problems. Thank you XXX

Eline, Claudia and Senne, thank you for sharing the last four years with me. It was invaluable having both colleagues you could discuss anything research-related with, as well as friends to laugh with in between. This was unique experience to have shared, wasn't it. ~~Hope to share many more.~~ Callie, you slotted in so perfectly and I am not just saying that because you doubled our tea selection. Thank you. Then, our minions: Björn your determination to solve a problem that is not yours is remarkable… ~~Your ability to find problems is equally as remarkable.~~ Luckily, there is Joachim at your side to bring us all some even-temperedness. Thank you both.

And how could I not mention the grandpa's, Yannick, Vincent, Stijn, Jonas, Kristof and Inne. You were our first plasma-mentors and showed us how things worked around here in building B.

This endeavour would not have been possible without the support of family and loved-ones.

Commented [AB7]: 😊

Commented [NDG8]: I added a tab to make it consistent.

Formatted: Font: Bold

Commented [YG9]: Add more details, the reader might not be familiar with this specific technique.

Commented [AB10]: Not clear what you mean. Maybe they are switched in the text? Please check.

Commented [ev11]: I am not sure, maybe a figure would be better?

Commented [AB12R11]: Yes, I agree. That would give more useful information to the reader.

Commented [ev13]: Still need to fill in: maybe (in random order), Chuanlong, Pepijn, Tim E., Roel, Parisa, Colin, Ivan, Rani, Hamid, Shangkun, Robin, Stijn, Fatime, Kevin, Elli, Rouba, Maryam, Sara, Patrick, but many more I am sure

Commented [AB14R13]: Ok ☺

Commented [AN15]: Only the case under specific circumstances.

Commented [YG16]: This needs an introductory sentence.

Bedankt, mama en papa, om me te motiveren om te doen wat mij persoonlijk drijft en me altijd de boodschap te geven dat ik genoeg ben. Yoanne, spijtig genoeg ben ik geen hersenchirurg geworden, dus geen Ferrari voor jou. Dodged that bullet. Ilias, ik ben blij dat ik letterlijk een stukje van jou in mijn thesis heb kunnen steken. ~~Allezwel~~, erop eigenlijk.

Bedankt, Ilse en Filip, voor de ondersteuning, in het bijzonder tijdens de pandemie, maar uiteraard ook daarbuiten.

Bedankt, Maarten, om me de moed te geven die eerste mail te sturen, om me liefde te geven en liefde te doen voelen, om me – in alle betekenissen van het woord – de tijd te geven zodat ik dit doctoraat kon afmaken zonder compleet zot te worden en zoveel meer.

Thanks, buddies, you made sure I stayed sane throughout this journey. I am so lucky to have found you. I could have been born in another city and we would have never met… ~~sounds like a fragile little thing our friendship, no?~~ 😉 Thanks for the video calls, games and dancing around in kitchens.

There once was a chemist. I do not remember how long he researched for, nor what he had researched, just that he once did. When he knew the end of his life was nearing, the chemist wrote down a list of names, reaching from the coffee table to the end of his garden. He had a large garden. "These are the people I owe thanks to.", he said, handing the list to his family. Nevertheless, during his funeral, the speaker only reached the kitchen sink. Maybe the names in the garden were written in small print. Maybe he had forgotten his glasses. "At least, ~~I put them out in the sun for a while~~they had the better view.", the chemist reasoned as he rolled up his list and left.~~.~~

Commented [AB17]: Very good!

Commented [AN18]: This section needs revision. It is not well-structured at the moment.

Formatted: Font: Italic

Formatted: Font: Italic

CONTENTS

I. INTRODUCTION

This Chapter discusses the context and background necessary to support the work presented in Chapters II-VI and is based on the following published works:

Vervloessem, E., Gromov, M., De Geyter, N., Bogaerts, A., Gorbanev, Y., & Nikiforov, A. (2023). NH_3 and HNO_x formation and loss in nitrogen fixation from air with water vapor by non-equilibrium plasma. *ACS Sust. Chem. Eng.*, 11, 4289-4298. DOI:10.1021/acssuschemeng.3c00208

Vervloessem, E., Gorbanev, Y., Nikiforov, A., De Geyter, N., & Bogaerts, A. (2022). Sustainable NO_x production from air in pulsed plasma: elucidating the chemistry behind the low energy consumption. *Green Chem.*, *24*, 916–929. DOI:10.1039/d1gc02762j

Vervloessem, E., Aghaei, M., Jardali, F., Hafezkhiabani, N., & Bogaerts, A. (2020). Plasma-based N_2 fixation into NO_x: Insights from modeling toward optimum yields and energy costs in a gliding arc plasmatron. *ACS Sust. Chem. Eng.*, *8*(26), 9711–9720. DOI:10.1021/acssuschemeng.0c01815

Gorbanev, Y., Vervloessem, E., Nikiforov, A., & Bogaerts, A. (2020). Nitrogen fixation with water vapor by non-equilibrium plasma: toward sustainable ammonia production. *ACS Sust. Chem. Eng.*, *8*, 2996–3004. DOI:10.1021/acssuschemeng.9b07849

This Chapter gives the context necessary to understand why we are doing this research, both broadly (why do we need alternative ways to make fertilizer?) and more specifically (what (fundamental) questions remain open in the field of plasma-based nitrogen fixation?).
Next to this, it also gives background information on the chemistry and physics that will be used in the following Chapters.

1. Nitrogen fixation as a global problem

1.1 What is nitrogen fixation?

Nitrogen (N) is an indispensable building block for all living organisms as well as for pharmaceutical and chemical industry. It is needed for DNA, RNA [a], i.e. the molecules that store and transfer genetic information, and it is a constituent of proteins that function as messengers, catalysts, receptors… In short, they form the structural basis for cell-based life[1]. Global N is predominantly present in the form of chemically-inert atmospheric N_2, which makes up 78% of the air. In order to make it accessible for living organisms, N_2 has to be transformed to a reactive form, such as ammonia (NH_3) or nitrogen oxides (NO_x), upon reacting with H_2 or O_2 gas, in a process called nitrogen fixation (NF)[2]. This can be achieved through naturally occurring, highly energy-consuming processes (abiotic) and through specialized micro-organisms (biotic)[3–5].

In a nutshell, N is needed for plants to grow and beings to live and NF is the process that makes N available for plants as food.

1.2 Why do we need synthetic NF?

The ever-growing population, requires more fixed N than the Earth can provide. For this reason we have been supplementing the soil with additional N, first by natural sources (e.g. by recycling organic waste from plants, humans and animals and by planting N_2 fixing legumes[6]) and later also through synthetic fertilizer[2] to make up for the high demand. Since the invention of synthetic fertilizers, food production increased drastically and enabled mass population expansion[7]. Figure

[a] DNA, deoxyribonucleic acid and RNA, ribonucleic acid.

1 shows the world population from 1900 to 2015 in red and below it – in green – the population that would be supported without the use of synthetic N fertilizer[7–11]. About 232 million tons of fixed N would be needed per year by 2050, as projected by Bodirsky et al.[12]. Biological NF is estimated on 100-175 million tonnes per year in comparison[13], though one must keep in mind this is unevenly distributed across the globe.

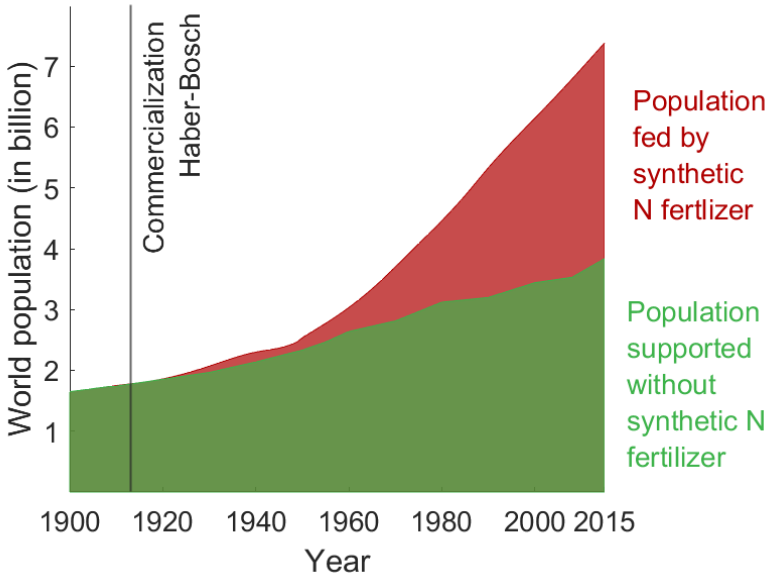

Figure 1 World population supported with (red) and without (green) synthetic nitrogen fertilizer as a function of time since 1900. 1913, the year Haber-Bosch was commercialized, is annotated. Based on data from Erisman et al.[10], Smil et al.[7], Stewart et al.[11], Gapminder population data (before 1950)[8] and UN database (population after 1950)[9].

1.3 How do we synthetically fix our nitrogen today?

The most important industrial process in the field of NF is the Haber-Bosh (HB) process: a thermo-catalytic conversion of N_2 and H_2 into ammonia (NH_3) (R I.1)[14].

$$3H_2 + N_2 \rightarrow 2NH_3 \qquad \Delta H_r^0 = -92\ kJ$$ R I.1

The year HB was commercialized (1913) is annotated on Figure 1, emphasizing the link between HB and population expansion. Approximately 80% of the globally produced NH_3 is used for plant growth[2]. Moreover, NH_3 is a commodity chemical used as an important building block for the production of pharmaceutical compounds, and it is also used in cleaning solutions, textile industry, as a greener fuel, as a deNOx agent in automotive industry, etc.[3, 4] The price for mineral and organic fertilizer is approximately 0.7 euro/kg N and 2 euro/kg N, respectively, depending on the region. In 2022 the price has doubled compared to 2020, a peak that has been decreasing again in 2023. Due to its great economic importance, the HB process has been extensively optimized during its 100-year existence, and there is currently no viable alternative or complementary process bringing the same support[15].

1.4 Why is there a drive to develop an improved way to synthetically fix nitrogen?

While supporting 50% of the world's population[10] (Figure 1), the HB process depends on fossil fuels (natural gas) for energy and, for the majority of HB chemical plants, as a source of H_2[16,17]. This industrial NF process requires 1.8% of the total energy production worldwide[16], 3 – 5% of the globally produced natural gas, and it emits more than 417 million tons of CO_2 per year. According to statistics from 2021, this was more than 1/3 of the yearly CO_2 emissions from the chemical industry combined[3,18,19]. Second in line were high-value chemicals (i.e. ethylene, propylene, benzene, toluene and mixed xylenes; 258 million

tons; 2021) followed by EtOH(l) (250 million tons; 2021)[20]. Modern HB plants use a part of their CO_2 emission (150 Mt/year) to produce a solution of urea and ammonium nitrate (UAN) used as fertilizer, however, this cannot offset the carbon emission[21].

Moreover, because of the harsh conditions (high temperature and pressure) required for its operation, HB is only economically feasible on large scales[22], resulting in massive centralized production and subsequent costly distribution of the produced NH_3. Despite the rise of renewable energy, current HB plants cannot accommodate the intermittency of fluctuating sources, such as wind and solar[23]. Currently, the main supplier of CH_4 in Europe is no longer available due the recent geopolitical events, making CH_4-based HB less feasible in Europe.

Also noteworthy is that NH_3 and hence HB is the starting point for all mineral fertilizers. For example, HNO_3, one of the main constituents of nitrogen-based and some K-based fertilizers and one of the world's 15 largest commodity chemicals[24], is commercially produced via the Ostwald process, which converts NH_3 into HNO_3 in two steps via NO_x[25], which is then combined with NH_3 to create NH_4NO_3, and afterwards used in fertilizer (see Figure 2 and Reaction R I.2-R I.5).

$4NH_3 + 5O_2 \rightarrow 4NO + 6H_2O$	$\Delta H_r^0 = -902\ kJ$	R I.2
$2NO + O_2 \rightarrow 2NO_2$	$\Delta H_r^0 = -114\ kJ$	R I.3
$3NO_2 + H_2O \rightarrow 2HNO_3(aq) + NO$	$\Delta H_r^0 = -117\ kJ$	R I.4
$NH_3 + HNO_3(aq) \rightarrow NH_4NO_3$		R I.5

The production of HNO_3 is therefore directly limited by NH_3 production through the HB process. This means 50% of the world’s population alimentation depends on one single chemical process.

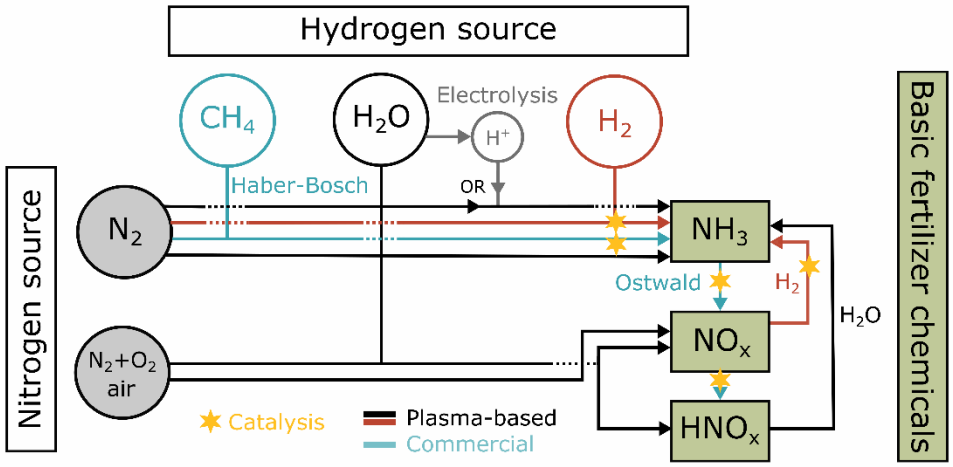

Figure 2 Various pathways for NF with a focus on the different possible hydrogen sources. Each full line represents a possible pathway towards basic fertilizer chemicals. The current industrial process is shown in blue. (Catalyst-free) plasma-based processed are indicated with black and red lines, red to bring attention to the fact H_2 (blue, green or grey) gas is used. Commercial processes that (usually) use catalysis are indicated with a yellow star.

Other primary drivers for the development of an alternative commercial NF process are: (i) the need for more modular processes making fertilizer production (with currently NH_3 as its main base chemical) possible in regions with limited or no access to commercial sources, and (ii) a need to combat the rising cost and associated emission, safety and security concerns of fertilizer transport from a centralised large scale plant[26]. A small-scale fertilizer production unit making use of the local wind- and other alternative and renewable sources can serve these needs.

Next to its indispensable use in fertilization, NH_3 shows potential as a flexible long-term energy carrier and zero-carbon fuel, with an energy density of about 22 MJ/kg, which is less than but comparable with fossil

fuels[27]. Hence, rethinking NH_3 production is of even more vital importance as it can play a role in our journey to carbon-neutrality[28].

Thus, while a synthetic NF process is necessary, the current industrial process does not fit into the concept of sustainable production. However, HB currently is the most energy-efficient process for NH_3 synthesis. There are no easy reductions in energy consumption left; bettering the way nitrogen is fixed requires drastic changes in the technology and innovation.

1.5 Not more but better NF

We are in need of more sustainable NF methods to support human alimentation, but we still need a reliable supply of fertilizers nonetheless. At the same time agriculture is the largest contributor to nitrogen pollution[12]. Synthetic NF could therefore be seen in direct opposition to the current (again) active public and political debate on the nitrogen crisis, i.e. the predicament concerned with a surplus of fixed nitrogen with a detrimental effect on our environment[29]. What is the role of an NF process developer or fundamental researcher in the nitrogen crisis debate?

As humans we have had a significant (often negative) influence on the full Earth's nitrogen cycle[1]. Cycling reactive N has more than doubled in the last century[30], however, more than 50% of the applied fertilizer is lost to the atmosphere and water streams[23] and only 16% of the applied N ends up in our food[31], which shows synthetic N is not used efficiently. Reactive N is lost in the chain, mainly through excretion by livestock (2/3 of their ingested N) and gaseous emissions from the stables or fields (20%). 55% is reused through the use of manure as fertilizer[32], though up until now destroying N waste has been cheaper than reusing

the streams, this will most likely not be cost efficient anymore in the near future.

Since the 1990s NO_x emissions have been subject to pollution control[30,33] and nitrogen critical loads [b] have been prominent in governmental ecological protection policies since the 1980s in farming, industry, urbanization, transport, etc.[34]. We know better what is needed and what the sustainable limits are; or at least, doing better now has become more eminent to our future well-being.

In this framework, it is indeed necessary to tackle all issues regarding the N cycle with great attention. We need to adapt the way we use and apply the fertilizer to minimize our impact on the environment and therefore allow for us to thrive, ànd we need to ensure enough reactive nitrogen is present in the soil to sustain the current population. Both matters are pressing.

With such an interconnected problem, it is not straightforward to identify the effort that will make the biggest impact. It is our job to keep the context of the problem in mind. For example, Huang et al. showed that when fertilizer could meet the demand close to the field only when the crop needs it, nutrient loss and NH_3 pollution would be reduced[35]. An example of this is split application[c] which, when used alone, reduced the NH_3 emissions by 25%[35]. Also, the current commercial process would not operate well at a small scale, nor would it (remotely) on site. The production capacity of a HB plant typically ranges from 2000 – 3000 t NH_3 per day[36], 1 – 100 t NH_3 per day can be regarded as small

[b] The nitrogen critical load is an official level of exposure to nitrogen containing species, below which significant harmful effects in terms of acidification and/or eutrophication of the environment do not occur to present knowledge[34].

[c] Applying fertilizer to the field on multiple timepoints throughout the season opposed to applying all fertilizer at once.

scale, though it is difficult to put a range on this[37]. Consequently, if we were to implement this to reduce soil pollution, a small-scale process, ideally compatible with renewable energy sources would be needed, which can simultaneously tick the box for a more sustainable production process.

Lastly, diversification of fertilizer production is a key point in providing sustainable fertilizers. At the moment, the majority of fixed N comes from one source, namely HB, regardless of local restrictions and advantages. Curated solutions for specific regions should be considered, keeping availability of resources (H_2, H_2O, CH_4), scale and energy supply possibilities in mind.

The whole system of processes needs continuous improvement, however, one should not only focus on the problem that is deemed most promising, highly urgent or of the most critical importance. Fundamental research looks further than that.

1.6 Alternative methods for nitrogen fixation, and specifically plasma-based NF

Considerable efforts are devoted to provide alternative and greener approaches at an industrial scale[15,25,38–42]. These include reimagining HB or developing alternative or complementary processes for NF, such as enzyme-based, plasma-based [15,41,43,44], and (electro-)catalytic methods with both heterogeneous and homogeneous catalysts[15,45]. Among the different techniques mentioned, plasma-based NF is particularly appealing because of its flexibility and synergy with sustainable energy sources[15,37,44,46,47].

Figure 2 summarizes the different possible NF plasma-based processes possible (red and black) starting from different H and N

sources, next to the current industrial processes (in blue). It should be emphasized that, though the focus is often on NH_3 production, $(H)NO_x$ synthesis is also a valid way to fix N. It can be converted into other N containing products such as NH_3 and is a commercially valuable product in a.o. the fertilizer industry, as explained before. The main goal is making N available in a more reactive form, be it $(H)NO_x$ or NH_3. Currently, the industrial way to make N available is by N reduction, i.e. NH_3 formation.

Another realm, though outside of the scope of this thesis, is the combination of plasma with catalysis (not included in Figure 2, though similar paths can be followed). 90% of all commercial industrial chemical processes include catalysis[48]. Due to the large role catalysis plays in industrial processes, great effort has been put into plasma catalysis research[49].

Current improvements in the HB process are mainly concerned with the methane reforming for H_2 extraction, which accounts for over 80% of the total energy required for NH_3 production[50]. The challenges and potential of improved HB-based fertilizer production, i.e. blue and green ammonia, are well described in literature[51,52]. In brief, green and blue ammonia are produced using HB but with a reduced or zero carbon footprint, respectively, through the electrification of the heating process, carbon capture and storage (CCS), the use of electrolysis-based hydrogen, etc.[53]. There is a long way to go: in 2020, of the 185 million tons of NH_3 produced only a small fraction of a percent (10 000 tons) was electrolysis-based.

2. Plasma-based NF

Plasma is an ionized gas with collective properties. It consists of charged species (ions and electrons) and neutral species (photons, excited and ground state atoms, radicals and molecules). Plasma-based processes are interesting to be considered as an alternative for synthetic NF[54].

2.1 Advantages of a plasma-based conversion process

A plasma reactor is powered by electricity, and can be easily turned on/off, so it can be integrated with fluctuating renewable electricity sources[15,18] by providing peak shaving and grid stabilization[44]. Moreover, it has no economy of scale, hence it can produce fertilizers in small scale plasma-based reactors right where they are needed, reducing or even eliminating transport costs, together with increasing availability of fertilizers in remote[d] areas[38]. Furthermore, it offers a cheap process, as it operates at ambient pressure and temperature, i.e. at milder conditions than the HB process. The fact that plasma-based NF can use abundant feedstock like air, nitrogen, and water is appealing as well[23,44].

Interestingly, the theoretical minimum energy cost of plasma-based NF into NO is 0.2 MJ/mol N, i.e., 2.5 times lower than the HB process[55] (see later). This is attributed to the fact that in plasma, the applied electric energy is predominantly transferred to the electrons, which activate the gas molecules by electron impact excitation, ionization and

[d] There is no set criterion to determine whether a process is remote or local. One way to look at it would be by comparing the fraction of the total cost related to transport. In a local process, the transport cost does not make up a significant portion of the production process, while in a remote case it does make up a significant fraction. Depending on the region, the “cut-off point” might be different.

dissociation reactions, and consequently, the gas does not have to be heated as a whole for the conversion process, thereby limiting the energy cost[43,54,56].

The economic feasibility of plasma-based processes is discussed in Chapter IV, while the state of the art is discussed in section 5, of this Chapter.

3. The fundamentals of plasma

99% of the visible universe is made up of plasma. We can see plasmas in the form of stars, including - of course - our own Sun, nebulas, auroras and lightning[54]. Most of the plasmas on earth, however, are artificial; Electrical arcs were the first studied in the early 1800s.

Currently a range of plasma types are researched and applied in daily life, with most notable applications in the field of lasers, thin film deposition, abatement of volatile organic compounds (VOCs), lighting, in the treatment of surfaces such as hardening and etching (most notable computer chips), in medicine (sterilization, deactivation of micro-organisms, tissue engineering…) and gas conversion, the focus of this thesis[54].

3.1 Properties of a plasma

A plasma is a complex state of matter with a number of collective properties and non-equilibrium processes. Below, a few are highlighted to support the discussions further in the thesis.

3.1.1 Library of species

As explained before, a plasma starts with neutral molecules, positive ions and electrons but quickly evolves to a chemical cocktail of molecules, atoms, ions, photons, electrons and a range of excited

species. It is very typical for a plasma to have a set of reactions associated with it in the thousands, due to this wide range of species.

3.1.2 Conductivity and quasi-neutrality

Due to the charged species (electrons and ions) present, a plasma is electrically conductive. However, plasma is electrically neutral, meaning that among the molecules, atoms (both in the ground and excited state), electrons, ions and photons, the positively and negatively charged species are balanced.

3.1.3 Temperature

Temperature essentially gives information on the kinetic energy of a group of species. Because of the specific nature of a plasma, however, one temperature most often does not describe the whole plasma. For example, the electron temperature can become much higher compared to the temperature of other species because of their light mass. Indeed, electrons take up energy much more easily and transfer that energy to the heavy particles through collisions[57], since $\frac{m_H}{m_e} = 1840$, where m_H is the mass of an H atom and m_e is the mass of an electron. Therefore, we typically characterize the plasma based on the temperatures related to the different kind of species present. Most commonly, the electron temperature (T_e), the gas temperature (T_g) or rotational temperature, which is most of the time representative of the temperature associated with the heavy species (atoms, molecules, ions), and the vibrational temperature (T_v), associated with the vibrationally excited species, are indicative for the application and behaviour of the plasma.

In a thermal plasma, all species have the same temperature ($T_e \approx T_g \approx T_v$), meaning the plasma is in thermal equilibrium. In a non-thermal or non-equilibrium plasma the species are not in equilibrium with each

other, conventionally meaning the $T_g \leq T_v << T_e \leq 10^5$ K. In a quasi-thermal, also called warm plasma, the temperature is in between thermal and non-thermal plasma, with only a significantly elevated T_e ($T_e >> T_g \approx T_v$). Lastly, in a cold plasma the T_g stays at (or near) room temperature[54]. In this thesis, a non-equilibrium plasma is used.

3.1.4 Luminosity

A part of the heavy particles can be excited due to the high energy present in a plasma. Afterwards they can fall back to a lower state, or their ground state, by photon emission, which is one of the processes responsible for the light emission of a plasma. This property will be used in Chapter VI.

3.1.5 Timescales

The chemical and physical cocktail in a plasma results in a wide range of timescales associated with the numerous (transport) processes that take place. Figure 3 shows the most important plasma processes and their timescale, ranging over 12 orders of magnitude[57].

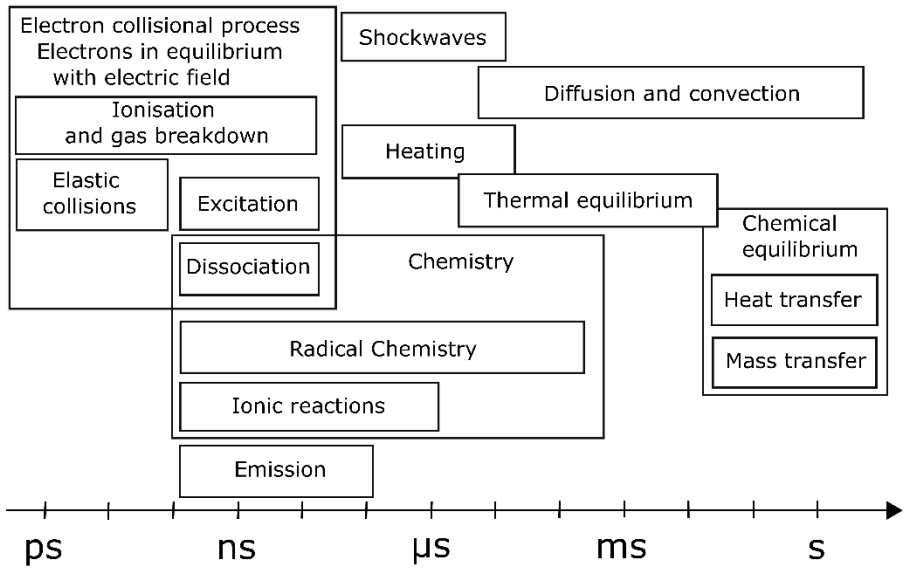

Figure 3 Timescales of relevant collisional and transport processes in atmospheric-pressure plasmas. Adapted from Bruggeman et al.[57].

4. The fundamentals of plasma chemistry

Plasma offers three main characteristics that make it attractive for gas conversion chemistry. (1) They contain a high concentration of energetic and chemically active species like electrons, ions, atoms, excited states, radicals and photons. (2) At least some of these components have an energy density that can be significantly higher than the energy densities encountered in conventional chemistry. (3) Related to this, plasmas can be far from thermodynamical equilibrium, enabling high concentrations of chemically active species while keeping the bulk temperature low in comparison[54].

4.1 Enabling chemistry through energy transfer

Energy transfer processes in plasmas enable non-conventional chemistry. The ones relevant to this thesis are briefly discussed hereafter.

4.2 Electrons and electron impact reactions

Electrons are the first to receive energy from the electric field in a plasma, due to their small mass, and they distribute it among the other plasma components. The amount of energy going into each possible energy transfer process, i.e. electronic excitation, vibrational excitation, dissociation and ionization, depends on the gas composition and the reduced electric field, which is the ratio of electric field over gas number density. This parameter is very important in plasmas and it determines the electron energy distribution function (EEDF), i.e. how many electrons of a certain energy there are. Consequently, by influencing the electron parameters (density, temperature, EEDF) one can often control the plasma chemistry.

4.3 Electronic excitation

Electrons can transfer their energy to another species, resulting in an electronically excited species (R I.6)

$$e + A(g, E_i) \rightarrow e + A(E_j) \qquad \text{R I.6}$$

where A is a molecule or atom in the ground (g) or electronically excited state (E_x). Electronically excited species show different kinetics compared to ground state species.

4.4 Vibrational excitation and transfer of vibrational energy

Electrons can also vibrationally excite molecules (e-V,R I.7) and those excited molecules can exchange vibrational energy in vibrational-vibrational (VV, R I.8) and vibrational-translational exchange reactions (VT, R I.9), through which vibrational energy is transferred to heat.

$$e + A(g, v_i) \rightarrow e + A(v_j)$$ R I.7

$$A(v_i) + A(v_j) \rightarrow A(v_i - 1) + A(v_j + 1)$$ R I.8

$$A(v_i) + M \rightarrow A(v_i - 1) + M$$ R I.9

4.5 Ladder climbing

Ladder climbing is a phenomenon where the vibrational energy of a molecule is step-wise increased through VV and e-V exchanges. In this way, the energy needed for each step is lower compared to direct electron impact vibrational excitation to the same level, allowing for a higher population of high vibrationally excited molecules.

4.6 Vibrational distribution functions

The above processes, be it between molecules of the same kind (e.g. N_2-N_2), different kind (e.g. O_2-N_2) or with atoms (e.g. N_2-N), determine the distribution of (vibrational) energy within one type of molecule, visualised by the vibrational distribution function (VDF), which sets out the normalized density of a vibrationally excited molecule as a function of the molecule's vibrational energy or vibrational level.

illustrates a set of simplified VDFs. Under thermal equilibrium, the translationally, rotationally and vibrationally excited species follow a Boltzmann distribution (I.1) [58]

$$\frac{n_i}{N} = \frac{g_i \exp\left(-\frac{E_i}{k_b T_g}\right)}{\sum_i g_i \exp\left(-\frac{E_i}{k_b T_g}\right)} \qquad \text{I.1}$$

where N is the total number of molecules, E_i is the energy of the i^{th} state, g_i is its statistical weight describing the degeneracy of the i^{th} state, k_b is the Boltzmann constant and T_g is the gas temperature[58]. Typically, the normalized density is shown in logarithmic scale, seeing as from the ground state upward the population of each level lowers drastically.

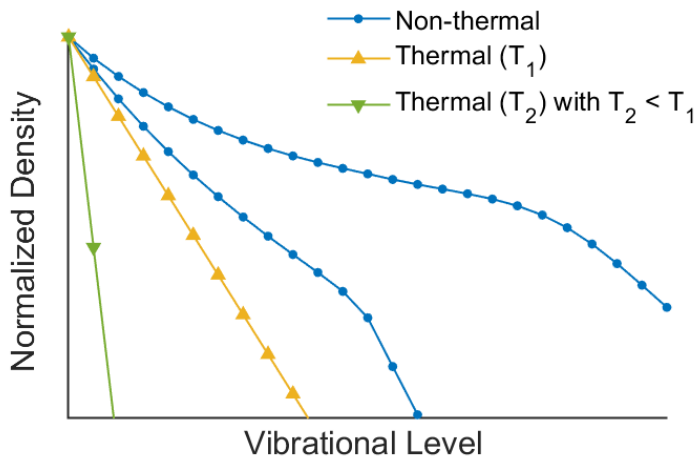

Figure 4 Illustrative VDF, showing the normalized density as function of the vibrational level of a molecule for two non-thermal cases (blue, dot), a thermal case at T1 (yellow; upside triangle) and a thermal case at T2 (green, downside triangle), with T2 < T1.

Two examples of thermal VDFs are shown in green (T_1) and yellow (T_2), where $T_2 < T_1$. Two examples of non-thermal VDFs are shown in blue, typically they are elevated above the thermal distribution for a particular gas temperature associated with that VDF and do not have a Boltzmann (straight) distribution, though they can show a quasi-Boltzmann distribution as well[59]. Simply said, when a system shows a

non-thermal VDF for a certain species, there are more (higher) vibrationally excited molecules present than would be expected in the equilibrium situation. (Note: an under-population of these vibrationally excited species would also be considered non-equilibrium.) The process of stepwise increasing the vibrational energy in a molecule, i.e. ladder climbing, creates a *plateau* in the VDF.

The surplus of vibrationally excited species can effectively lower the energy barrier for reactions, as illustrated in Figure 5 for N_2. N_2 is vibrationally excited from the ground state via electron impact vibrational excitation and/or ladder climbing processes such as VV exchange. The increase in potential energy lowers the activation barrier of the reaction coordinate, effectively facilitating N_2 splitting into 2N. The vibrational efficiency (α) determines how efficient the vibrational energy is used in lowering the energy barrier, with α = 1 being 100% efficiency.

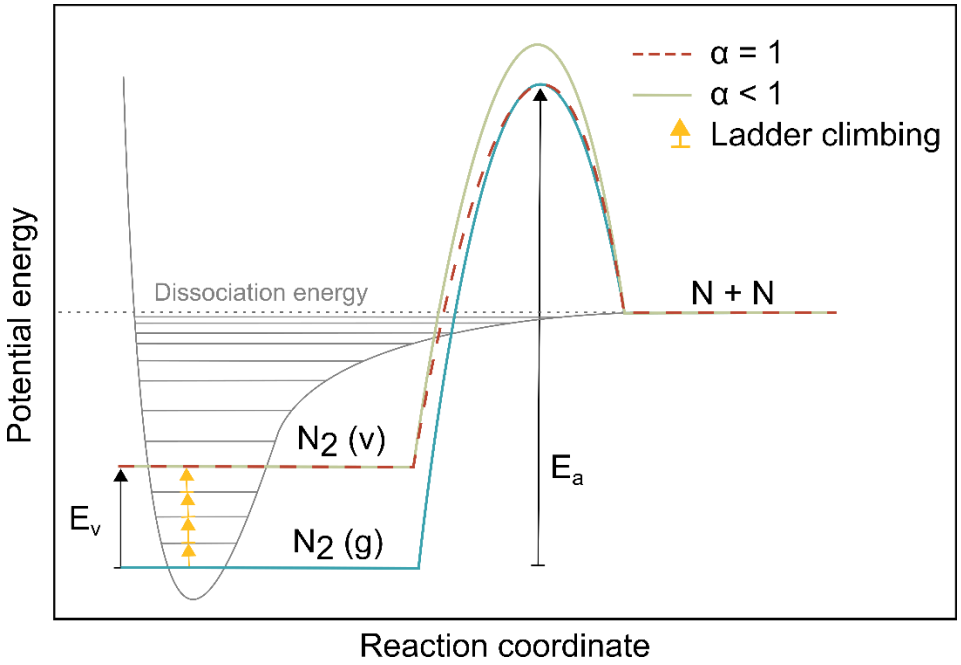

Figure 5 Ladder climbing and schematic reaction coordinate for N_2 splitting for different vibrational levels of N_2. α stands for the vibrational efficiency, with α=1 meaning full efficient use of the vibrational energy. Based on a similar figure by Mehta et al.[60].

5. A literature overview of plasma-based nitrogen fixation

As stated by many authors[23,25,44,61], plasma, if correctly applied, can be active, selective and efficient in applications associated with NF. This section gives an overview of the state of the art relevant to frame the work presented in Chapters IV-VI. Plasma-based catalytic NF is not discussed in detail.

5.1 Structure of the overview

There are two main ways to fix nitrogen: by oxidation into most commonly NO_x and HNO_x and by reduction into NH_3. Figure 2 shows the different types of plasma-based N_2 fixation pathways into NO_x and NH_3 by means of different $N_2/O_2/H_2O/H_2$ gas combinations: (1) NO_x can be formed in plasma from an N_2/O_2 feed gas in different ratios[59,62], of which the most accessible is air, but it can also be formed in other N_2/O_2, N_2/H_2O and $N_2/O_2/H_2O$ combinations, like humid air. Note that NO_x can be used directly in the production of HNO_3[37] (see above) or can be reduced post-plasma for the production of NH_3[46]. (2) NH_3 is mostly produced in plasma from N_2/H_2 using plasma-catalytic systems[47], but can also be formed via plasma treated liquid H_2O in different forms and/or humid (i.e., water vapour-containing) air, humid N_2 or $N_2/O_2/H_2O/H_2$ in other ratios[59].

The following discussion on the state of the art is structured as follows. The different plasma-based NF systems are divided into dry and wet systems, meaning without and with the presence of water, be it in liquid or gaseous form. In these sections, the performance and underlying chemistry of oxidation and reduction are discussed. In the case of dry systems, this division is very clean, while under wet systems there is

more interconnection as wet systems inherently show both oxidation and reduction simultaneously.

5.2 Dry systems (N_2/O_2;N_2/H_2)

5.2.1 Nitrogen oxidation

Performance

The Birkeland-Eyde process was the first commercialized plasma-based NF installation in 1903[42] and was soon after fully replaced by the thermal-catalytic Haber-Bosch process. More than a century later, a wide range of plasma types have been studied for plasma-based NO_x production, driven by the need for an alternative to the current industrial process and other applications[63], including thermal plasmas[42,64], spark discharges[65,66], radio-frequency (RF) discharges[67], laser-produced discharges[68], corona discharges[65,69], glow discharges[70,71], (packed bed) dielectric barrier discharges (DBD)[70,72], microwave discharges (MW)[73–77], different types of arc discharges[38,41,62,70,78–80] (including pulsed arc and gliding arc) and plasma jets in contact with water[69,81].

An overview of the reported energy consumption (EC) and product concentrations is given in Table 1. The NO_x concentration is generally in the range of 1 to 14 %, which is in the range of 0.1 – 68 g/h, while the EC spans over a very large range within 5 orders of magnitude (0.28 – 1673 MJ/(mol N)). Important to note, the best performance values in terms of yield and EC apply to low-pressure plasma reactors, but they did not account for the energy required to maintain low pressure and cooling of the reactor; moreover, these values (1980s)[76] have not been reproduced since then (entries 25 and 26 in Table 1). Currently, the best performing atmospheric-pressure plasmas are the

recently reported atmospheric MW plasma by Kelly et al. (2 MJ/(mol N), entry 20)[77] and two modified gliding arc reactors, using an effusion nozzle (2.1 MJ/(mol N), entry 18)[82] and elevated pressure (1.8 MJ/(mol N) entry 19)[83]. Without additional parts a rotating gliding arc performs worse than the presented MW, however, a MW reactor often needs a low-pressure starting sequence with active cooling, which is not included in the reported EC. A take-away is that the most promising results have been achieved in warm plasmas (e.g. MW and arc) opposed to cold plasma types (e.g. DBD and corona).

In general, to the best of our knowledge, the theoretical minimum EC for plasma-based NO_x production (0.2 MJ/(mol N)) had not yet been reached before the work presented in Chapter IV was submitted. Around the same time, Britun et al. confirmed that this low EC can indeed be achieved through their work in another pulsed plasma (entry 26).

The wide range when it comes to EC and production rate reflects (1) improvement through time, as we for example can see clearly in the evolution of the rotating gliding arc (entries 18 – 20) and (2) the (maybe inherent) difference in performance of distinguishable plasma types. One should also keep in mind maximising performance should not be considered in isolation. As an example, DBDs generally perform sub-par compared to many other configurations in Table 1, however, they are still considered as they are very compatible with catalysts, a different but potentially promising route.

The largest challenge in developing a plasma setup is the reverse correlation between EC and yield. Low EC often comes at a low yield and vice versa.

Table 1 Overview of the different reported NO_x concentrations and associated EC in various types of plasma reactors in literature. More elaborate discussions on the state of the art of plasma-based NO_x production can be found in the papers of Bogaerts & Neyts[44], Jardali et al.[62], Rouwenhorst et al.[37] and Winter et al.[23].

Plasma type	Concentration (%) (products)	Production rate (g/h)	EC (MJ/(mol N))	Ref.	Entry
Electric arc (Birkeland-Eyde)	2 (NO)	10740	2.4 – 3.1	42,64	1
Electric arc with water injection	4.7 (NO)	-	3.5	84	2
Spark discharge	- (NO and NO_2)	-	20.27 and 40	65	3
Transient spark discharge	0.04 (NO) 0.01 (NO_2)	0.09	8.6	66	4
Pin-to-plane ns-pulsed spark discharge	- (NO_x)	0.001[e]	5.0 – 7.7	70	5
Pulsed arc discharge	0.02 (NO) 0.08 (NO_2)	0.18	10.6	85	6
RF crossed discharge	0.02 (NO) 0.6 (NO_2)	0.08	24 – 108	67	7
Laser-produced discharge	- (NO and NO_2)	-	8.9	68	8
(Positive/negative) DC[f] corona discharge	- (NO and NO_2)	-	1057/1673	65	9

[e] Based on average molecular weight of NO and NO_2, as the selectivity is not reported.
[f] Direct current (DC)

Plasma type	Concentration (%) (products)	Production rate (g/h)	EC (MJ/(mol N))	Ref.	Entry
Pin-to-pin DC glow discharge	0.7 (NO_x)	1.9	2.8	[71]	10
Batch DBD	0.1 (NO) 0.2 (NO_2) 0.3 (N_2O)	0.01	56 – 140	[70]	11
Packed DBD (γ-Al_2O_3)	0.4 (NO) 0.6 (NO_2)	0.5	18	[72]	12
Propeller arc	0.3 (NO) 0.09 (NO_2)	1.2	4.2	[70]	13
Pulsed milli-scale gliding arc	0.8 (NO) 0.25 (NO_2)	0.1	2.8 – 4.8	[38,41]	14
Pulsed gliding arc	0.5 (NO) 0.7 (NO_2)	<0.1	4.8	[38]	15
Gliding arc plasmatron	1.35 (NO) 0.15 (NO_2)	18	3.6	[59]	16
Rotating gliding arc	5.4 (NO_x)	7.0	2.5	[62]	17
Rotating gliding arc (effusion nozzle)	5.9 (NO_x)	7.4	2.1	[82]	18
Rotating gliding arc (elevated pressure, 3 bar)	4.8 (NO_x)	68.9	1.8	[83]	19
Atmospheric-pressure MW plasma	3.8 (NO_x)	85.9	2.0	[77]	20
MW plasma	0.3 (NO)	1.7	3.8	[73]	21

	0.02 (NO_2)				
MW plasma with catalyst ($MoCO_3$)*	6 (NO)	30.4	0.84	86	22
Pulsed MW discharge*	6 (NO)	-	0.6	75	23
MW plasma with magnetic field*	14 (NO)	-	0.28	76	24
Pulsed plasma jet (Soft Jet)	0.02 (NO_x)	<0.1	0.42	87, this work	25
Pulsed DC spark	± 0.01 (NO)	0.3	0.4	88	26

*obtained at reduced pressure (0.01 – 0.07 atm)

Minimum theoretical energy consumption for plasma-based NO production. To make one NO molecule through $N_2 + O \rightarrow NO + N$ we need 1 eV or 0.096 MJ/mol, if all energy is directed towards this reaction[55]. There are three main loss channels that can lower the efficiency of this reaction (η)[54]:

$$\eta = \eta_{ex} \cdot \eta_{rel} \cdot \eta_{chem} \qquad \text{I.2}$$

η_{ex} is determined by the energy losses related to the excitation of low productive degrees of freedom. Indeed, the most efficient way to perform this reaction is through vibrational excitation, while other excitations lower this factor. η_{rel} is related to energy losses outside of the active discharge zone, i.e. VT-relaxation. Lastly, η_{chem} is mainly related to losses through exothermic reactions[55].

In literature, 0.2 MJ/mol is generally used as the minimum theoretical energy consumption for plasma-based NO production[15,44]. This number assumes that η_{ex} and η_{rel} are close to 1, meaning the reaction is dominated by vibrational excitation. It is assumed that the limiting factor is due to losses in exothermic reactions and vibrational energy losses like VV and VT exchanges, i.e. η_{chem}, which is estimated to be 50%[54]. It is evident from this explanation that this number is dependent on the assumptions made regarding efficiency losses, i.e. the 50% loss due to $\eta_{chem}$is an estimation, which could be chosen slightly higher or lower.

Underlying chemistry

A number of literature reports discuss the underlying chemical mechanisms, either purely experimental[69] or supported by modelling[41,59,62,80]. It is generally known that the most energy-efficient pathway to NO_x is via the non-thermal Zeldovich mechanism promoted by vibrational excitation[37,41,44,59,62,69]. This is represented by reactions

R I.10 and R I.11; where g and v stand for the ground state and the vibrationally excited states of the molecule, respectively. The mechanism (R I.10 and R I.11) inherently includes the thermal Zeldovich mechanism, i.e. the Zeldovich reactions from the ground state only.

$$O_2(v,g) + N \rightarrow NO + O \qquad \text{R I.10}$$

$$N_2(v,g) + O \rightarrow NO + N \qquad \text{R I.11}$$

Vibrationally excited molecules decrease the activation energy barrier, facilitating the reaction[44], as explained in this Chapter before (section 4.6). The Zeldovich mechanism can thus be exploited by overpopulation of the vibrational levels (non-thermal VDF, see section 4.6). A so-called “vibrational-translational (VT) non-equilibrium” can be induced through pulsing[58,70] and low values of the reduced electric field[41]. Exploiting the non-thermal Zeldovich mechanism to achieve the theoretical minimum EC in practice is one of the holy grails in plasma-based NO_x production research. Furthermore, besides the direct formation of NO_x, minimising its destruction via back reactions and maximising the fraction of gas treated by the plasma are two other common challenges in this research field[37,59,62].

5.2.2 Nitrogen reduction

Performance

The commercial NH_3 production process is a catalytic one, which is also possible in the field of plasma-catalytic NH_3 synthesis. Looking at dry plasma-based N reduction literature, catalytic systems are most common. Also, in the last 25 years, most plasma-based NH_3 synthesis has been performed in DBD[60], with RF and MW second[89]. Plasma-catalytic NF typically proceeds in N_2/H_2 plasmas, though there are examples that use CH_4/N_2[90], operating in a range from low (5-700 Pa)

to atmospheric pressure. The energy consumption in DBDs ranges from 18 – 180 MJ/mol, with outliers at 786 and 4950 MJ/mol[90–99]. The lowest EC's are reported by Aihara et al. (18 MJ/mol)[98], Bai et al. (33 MJ/mol)[91] and Peng et al. (36 MJ/mol)[97]. The NH_3 outlet concentrations range from 0.008 to 2.3% [90–101], with production rates ranging from 0.003 to 0.4 g/h [90–99], among these the best performing are Aihara et al. (0.12 g/h)[98] and Bai et al. (0.4 and 0.18 g/h)[90,91], which is an order of magnitude to two orders of magnitude lower at best compared to the NO_x production rate discussed in section 5.2.1. Another potential synthesis was proposed by Hollevoet et al., who combined plasma nitrogen oxidation with catalytic reduction to ammonia (PNOCRA)[46,102] via lean NO_x trap technology, achieving a favourable yield (>1%; or 17 g/h) and EC (4.6 MJ/mol NH_3)[46].

Underlying chemistry

The majority of setups described in literature for plasma-based NH_3 production in dry conditions involve a catalyst, meaning the underlying chemistry involves surfaces and associated processes like Eley-Rideal and Langmuir-Hinshelwood mechanisms[47,103]. The influence of the catalyst and the plasma are coupled with each other, which makes it challenging to study both effects separately but also together. To keep the discussion within the scope of the thesis, i.e. to support the discussions in Chapters IV-VI, the underlying chemistry will be discussed in a more general way focussing on important species and intermediates that – in a first assumption – are similar in both catalytic and non-catalytic dry NH_3 synthesis.

In N_2/H_2 feed mixtures, the best performance is mostly found in N_2 rich mixtures, meaning non-stoichiometric ratio's, which has been attributed to a higher fraction of energy that must be deposited into N_2 because

of its strong triple bond[95,96,98,104–106].

It is widely assumed that the synthesis from H_2 and N_2 starts form the dissociation, ionization and excitation of the feed gasses[91,107,108] (R I.4-R I.5), X, v_x and E_x are ground, vibrational and electronic states, respectively). The dissociation is followed by the formation of NH radicals, which is considered an important intermediate (R I.6). NH is seen as the precursor of NH_3 and its concentration has a strong effect on the NH_3 production rate[107,109,110]. Next, NH_3 is produced through stepwise addition of H and H_2 (R I.7-R I.19), meaning NH_2 is not a necessary intermediate (R I.9)[96,99,107,111].

N_2 activation

$$N_2(X, v_x, E_x) + e \rightarrow 2N + e \qquad \text{R I.12}$$

$$H_2(X, v_x, E_x) + e \rightarrow 2H + e \qquad \text{R I.13}$$

Precursor formation

$$N + H \rightarrow NH \qquad \text{R I.14}$$

$$NH + H \rightarrow NH_2 \qquad \text{R I.15}$$

Stepwise addition and NH_3 formation

$$NH + H_2 \rightarrow NH_2 + H \qquad \text{R I.16}$$

$$NH + H_2 \rightarrow NH_3 \qquad \text{R I.17}$$

$$NH_2 + H \rightarrow NH_3 \qquad \text{R I.18}$$

$$NH_2 + H_2 \rightarrow NH_3 + H \qquad \text{R I.19}$$

There is no general agreement on the importance of each N_2 activation channel facilitating NH_3 synthesis. Direct dissociation[112], ionization[91,94,113], electronic excitation[98,112,114] and vibrational excitation[115–120] have all been put forward as important in different plasmas[60]. The larger the contribution of N_2(v) can be made, the more energy efficient the NH_3 synthesis would be. Based on modelling, Hong et al.[115] and van ‘t Veer et al.[112] identified that reactions between

radicals and vibrationally and electronically excited molecules played a more significant role in the formation of NH and NH_3 than ion-ion interactions[115]. Electron impact dissociation of N_2 has been proposed as the first step[96,112]. In case of a catalytic surface, also dissociative adsorption of N_2 has been proposed[47] as well as $N_2(v)$ dissociation followed by adsorption[118–120]. There is also no consensus on the rate determining step. As summarized by Zhou et al.[89], hypotheses include the formation of NH_x on the catalyst surface[92], recombination of N and H and dissociative adsorption of N[93,106,117].

Plasma-catalytic processes show promise, and the interest is well-founded if one looks at the successful history of catalytic processes. A synergistic combination of cold plasma and catalysis in theory affords higher reaction productivity in a way that is not achievable with conventional thermal catalysis[18, 19], at least partly due to the excitation of the strong bonds in N_2 by plasma[20, 21], and/or the facile generation of H atoms[22, 23]. Regardless of whether a plasma-based process, might or might not involve a catalyst, it is more straightforward to elucidate the underlying chemistry in a non-catalytic system, due to the complex nature of plasma-catalysis[110].

5.3 Wet systems (N_2/H_2O(g/l);N_2/O_2/H_2O(g/l))

Water can be introduced in a plasma system in a range of different ways: liquid (films), vapor and droplets are discussed in this overview. When H_2O is introduced in the system as a liquid, there is a build-up of NF products in the liquid. This can be NH_3 in the form of NH_4^+, and/or oxidation products of N like nitrite (NO_2^-) and nitrate (NO_3^-). Therefore, the plasma-based synthesis of reactive oxygen species (ROS) and reactive nitrogen species (RNS) in water is often referred to as plasma-activated water (PAW) or plasma-treated water (PTW)[121–123]. Though

the publications on wet N oxidation and reduction are relatively sparse, compared to dry systems, interest has been increasing in the last 10 years[89,124].

Plasma-liquid setups are often investigated in the field of plasma medicine for the production of reactive oxygen and nitrogen species (RONS)[125] and water treatment. Though their focus, in a sense, often is NF as well, they will not be discussed here, as their framework is different: (i) they often inherently need liquid water close to the plasma source, (ii) energy cost is often not the limiting factor (hence noble gasses are often used) and (iii) (tunability of) short-lived species play a more significant role opposed to stable NF species.

Due to evaporation taking place in virtually all setups, water vapor is always present, though in different quantities. Therefore, when a setup with H_2O vapor is discussed in this overview, it refers to H_2O vapor added to the inlet gas mixture, unless stated otherwise.

5.3.1 Nitrogen oxidation

Performance

For wet N oxidation, we look at N_2/H_2O and $N_2/O_2/H_2O$ mixtures, with the most readily available air/H_2O. Next to NO_x formation (R I.25), water also enables deep oxidation of N into HNO_2 and HNO_3 (R I.26-R I.27), which can dissolve in the liquid as NO_2^- and NO_3^-[126,127] (R I.29-R I.32). A common by-product is H_2O_2[128] (R I.28; see further under *Underlying Chemistry*).

Error! Reference source not found. gives an overview of plasma setups involving water, including the gas mixture, water state, reduction and oxidation products and their production rates and energy consumption expressed for the total NF and for NH_3/NH_4^+ production, if the reported date allowed its calculation. Ions and neutral molecules

are used to distinguish between species measured in the liquid phase (e.g. NH_4^+) or the gas phase (e.g. NH_3), respectively. Every entry reports production of N oxidized species; they typically underperform in production rate and energy consumption compared to their dry gas phase counterparts ($N_2/O_2/H_2O(l)$ vs. N_2/O_2), discussed in section 5.2.1. The production rate ranges from <0.01 to 669 mg/h, which is two to three orders of magnitude lower compared to the state of the art of dry N oxidation (Table 1; 10 – 68900 mg/h). The pulsed transient spark by Janda et al.[122] (120 mg/h, 7.2 MJ/mol; entry 11), the spray type jet in combination with UV irradiation by Peng et al.[105] (177 mg/h; entry 6) and the falling water film DBD by Liu et al.[127] (669 mg/h, 43 MJ/mol; entry 8) show the best performance. While the EC of gas phase oxidation spans over one order of magnitude, the range for wet oxidation spans more than three orders of magnitude, with the best performing setup - in terms of EC - in the same order of magnitude as their dry counterpart (7.2 MJ/mol (wet) vs 1.8 MJ/mol (dry)) at much lower production rates (0.13 g/h (wet) vs. 69 g/h (dry)). There are three points to make on this comparison and performance evaluation.

(1) The wet and dry oxidation of N are not directly comparable to one another: dry oxidation produces NO_x, while wet oxidation can synthesize HNO_3/NO_3^- in one step, meaning it would replace the full commercial Ostwald process, while dry oxidation needs one more step for deep oxidation into HNO_3. However, this does not equalize the performance of wet and dry oxidation, as initial splitting and oxidation of N is the limiting step, meaning the main conclusion still stands. A good example to illustrate this point is the hybrid NO_x/O_3 plasma system studied by Dinh et al.[129]. An NO_x producing plasma followed by an ozone producing DBD was studied, enabling full conversion of NO_x

into HNO_3(l) at a production rate of 8.46 g/h and 8 MJ/mol N, including both the energy cost for the NO_x and the DBD plasma. Essentially, this is a dry N oxidation system adapted for deep oxidation, hence it is a suitable reference point. Firstly, when comparing the production rate and energy cost of Dinh et al.'s system to the trends in Table 1 discussed before, it shows the performance of wet N oxidation is still sub-par, the exception is for entry 10 in Table 2, by Janda et al.[122] (7.2 MJ/mol), though it comes at a low production rate. Secondly, the arc system used for NO_x production described in this work has a low production rate (3.25 g/h) and high energy consumption (5.3 MJ/mol N) compared to the best performing NO_x-producing plasmas (Table 1), meaning we can expect easy changes will dramatically improve the performance. The current state of the art thus suggests that for plasma-based N oxidation, dry systems perform better.

(2) However, most wet systems described in literature are focussed on N reduction, using H_2O as a H source, opposed to oxidation, which means the oxidation performance is logically inferior compared to dry plasma-based oxidation, as optimizing performance is not the aim of the majority of the works reported. Section 5.4, goes into more detail on this point.

(3) Lastly, wet systems have not been studied as extensively yet as dry systems, which will also be discussed in more detail in Section 5.4.

Table 2 Overview of wet plasma-based N oxidation and reduction systems. Nd stands for “not defined”, meaning the data necessary to calculate the metric are not reported.

Plasma type	Gas composition	Production rate (mg/h)[a]		EC (MJ/(mol N))	Ref.	Entry
Plasma above a liquid (H_2O) surface						
DBD above H_2O surface		NH_4^+ 0.10-0.14	NO_2^- 0.28-0.83 NO_3^- 0.22-0.45	nd	130,131	1
Pulsed jet above H_2O and ethanol (EtOH)	N_2/H_2O(l)	NH_4^+ 4.90	NO_2^- 0 NO_3^- 41.02	1139 /total N 3750/NH_3	132	2
	N_2/EtOH(l)	NH_4^+ 52.23	NO_2^- 0 NO_3^- 4.42	340/total N 351/NH_3		
Dielectric beads (DB)-filled DBD above H_2O	N_2/H_2O	NH_4^+ 0.05 NH_4^+ 0.38 (DB)	NO_2^- 0.11 NO_2^- 0.10 (DB) NO_3^- 0.13 NO_3^- 0.07 (DB)	3244/total N 3729/NH_3	133	3
Plasma above a liquid (H_2O) surface + UV irradiation[b]						
DBD above liquid + UV	N_2/H_2O(l)	NH_4^+ 12 µM/h[c] NH_4^+ 29 µM/h (UV)[c]	NO_2^- 27 µM/h[c] NO_2^- nd (UV)[c] NO_3^- nd[c] NO_3^- 13 (UV)[c]	987.2/NH_3	134	4
	Air/H_2O(l)	NH_4^+ 54 µM/h[d] NH_4^+ 27 µM/h[d]	NO_2(g) 21 µM/h[d]	nd		5

DBD above H_2O surface + UV	$N_2/H_2O(l)$	NH_4^+ 0.01 NH_4^+ 0.04 (UV)	NO_2^- 0.0011 NO_2^- 0.0007(UV) NO_3^- 0.0017 NO_3^- 0.003 (UV)	nd	[135,136]	6
Spray-type yet + UV	$N_2/H_2O(l)$	NH_4^+ 1.53 NH_4^+ 2.55 (UV)	NO_2^- 44.6 NO_2^- 111.2 (UV) NO_3^- 2604[e] O_3^- 3348 (UV)[e]	nd	[105]	7
Plasma + introduction of liquid H_2O (droplets, water film, plasma-in-water, electrospray, water vapor)						
DBD + H_2O droplets	$N_2/H_2O(g/l)$	NH_4^+ 0.18	NO_2^- 0.46 NO_3^- 2.67	1350/total N 7854/NH_3	[137]	8
DBD falling water film	$Air/H_2O(l)$		NO_3^- 669.6	43/total N	[127]	9
Bubble discharge	$N_2/H_2O(l)$	NH_4^+ 0.16	NO_2^- 17.86 NO_3^- 17.94	680 /total N 48750/NH_3	[138]	10
		NH_3 4.5	NO_x 15	919/total N 1747/NH_3		
Pin-to-flowing liquid	$Air/H_2O(l)$	NH_3 0	NO 84.96 NO_2 78.59 HNO_2 50.67	12.7/total N	[139]	11
		NH_4^+ 0	NO_2^- 11.84 NO_3^- 2.02	248/total N		
Pulsed transient spark + H_2O electrospray	Air/H_2O(microdroplets)	NH_3/NH_4^+ 0	NO 106 NO_2 0.35 HNO_2 0.027	9.3/total N	[122]	12

	Air/H_2O(g)	NH_3/NH_4^+ 0	NO 99 NO_2 16.3 HNO_2 14.5	7.2/total N		
	Air	NH_3/NH_4^+ 0	NO 106 NO_2 3.4 HNO_2 0.08	7.8/total N		
Pulsed spark “Soft Jet”	N_2/H_2O(g/l)	NH_4^+ 0.26	NO_2^- 0.35 NO_3^- 0.02	15 MJ/mol total N 100 MJ/mol NH_3	This thesis, [140]	13
	Air/H_2O(g/l)	NH_4^+ 0.03	NO_x^- 0.69	21 MJ/mol total N 240 MJ/mol NH_3		
Hybrid plasma-electrocatalytic/electrochemical systems						
Plasma-electrochemical system	N_2/H_2O(l)	NH_4^+ 0.36	NO_x^- 1.3 mM/h[f]	139/total N[g]	[141]	14
Hybrid plasma-electrocatalytic system (Cu-nanowires)	Air/H_2O(l)	NH_4^+ 23.2	NO_x^- 2.5 mM/h[h]	924.48/total N 910.8/NH_3	[142]	15
Plasma-activated electrolysis	N_2/H_2O(l)	NH_3/NH_4^+ 0	NO 6.3 H_2 2.9	1350/total N	[143]	16

[a] Mind the production rate in this table is expressed in mg/h, while in other places in the text and in Table 1, it is sometimes expressed in g/h to allow for easier comparison when placed next to each other.
[b] Irradiation not included in EC calculation.
[c] Treatment time (tt) = 10 min
[d] tt = 20 min, UV data for this tt not included.
[e] 100 times higher compared to the other NO_3^- production rate reported in their work (50 mg/h), this might be a mistake, therefore it was not discussed under wet N oxidation.
[f] Data on cell volume not reported.
[g] Calculated from one reported number in the paper, no data on power or its calculation.
[h] Data needed for calculation not reported. Based on estimation.

Underlying mechanisms

In N_2/H_2O and $N_2/O_2/H_2O$ plasmas, it is generally accepted that H_2O homolytically dissociates into H and OH (R I.20)[89]. Other proposed mechanisms include R I.23 and R I.24, though this was in a ns pulsed system[144]. It has been shown that OH can play a role in N oxidation through the extended Zeldovich mechanism (R I.25)[139,145]. Gromov et al. compared a dry system with a wet system (pin-to-flowing water film) and observed a drop in NO production efficiency when moving from dry to wet. One of their explanations was that the extended Zeldovich mechanism might be less efficient than its dry counterpart[139].

Also the *regular* Zeldovich mechanism can take place, as R I.21 produces O radicals from water, that can be used in R I.25.

For so-called *deep oxidation* of N, OH can react with NO and NO_2 resulting in the formation of HNO_2 and HNO_3 (R I.26 – R I.30) and with another OH to form H_2O_2 (R I.28)[122,127,146]. HNO_x and H_2O_2 dissolve in H_2O (R I.31 – R I.32)[122].

H_2O decomposition

$e + H_2O \rightarrow OH + H + e$ R I.20

$e + OH \rightarrow H + O + e$ R I.21

$H_2O \xrightarrow{UV\ irradiation\ 120-170\ nm} OH + H$ R I.22

$O + H_2O \rightarrow OH + OH$ R I.23

$N_2^* + H_2O \rightarrow N_2(g) + H + OH$ R I.24

Extended Zeldovich mechanism

$N + OH \rightarrow NO + H$ R I.25

Deep N oxidation

$NO + OH \rightarrow HNO_2(g)$ R I.26

$NO_2 + OH \rightarrow HNO_3(g)$ R I.27

$2OH \rightarrow H_2O_2(g)$ R I.28

$NO + H_2O_2(g) \rightarrow HNO_2(g) + OH$ R I.29

$NO_2 + H_2O_2(g) \rightarrow HNO_3(g)$ R I.30

$HNO_2(g) \rightarrow HNO_2(aq) \rightarrow NO_2^- + H^+$ R I.31

$HNO_3(g) \rightarrow HNO_3(aq) \rightarrow NO_3^- + H^+$ R I.32

Gromov et al. (Table 2, entry 11) showed by using isopropanol as an OH scavenger, that OH was responsible for 30% of the produced NO_x^- [139], suggesting that R I.26, R I.27 and by extension also R I.28; R I.29 and R I.30 can play a significant role in NO_x formation.

NO_x^- can also be formed via R I.33 and R I.34, with R I.33 more favoured compared to R I.34, due to the higher solubility of NO_2 in comparison with NO[147]. However, they have much lower rates and can generally not compete with R I.26-R I.30[89]. Indeed, HNO_3 and HNO_2 are more easily dissolved in water compared to NO and NO_2[g]. HNO_2 formation in the gas phase and its significant role on NO_2^-(aq) formation was confirmed in humid air and electrospray containing air by Janda et al.[122]. Also, HNO_2 formation via R I.26 was in line with their observations[122]. Sakakura et al. suggested NO_x^- was formed by the reaction with $OH^\cdot$ and N_{atom}, alternatively, they proposed NO formation from N_{atom} and $OH^\cdot$ followed by R I.20, after which HNO_2 is taken up by the liquid and further oxidizes into NO_3^-[131]. On the same topic, Janda et al. concluded from their comparison of products in dry, humid and

[g] Based on their Henry's constants: k_H HNO_3 = 2.1 ·10^6 mol $kg^{-1}atm^{-1}$, k_H HNO_2 = 50 mol $kg^{-1}atm^{-1}$; k_H NO_2 = 0.007 mol $kg^{-1}atm^{-1}$; k_H NO = 0.0018 mol $kg^{-1}atm^{-1}$ all at 298.15 K[123,147].

electrosprayed air that, when there is no H_2O available in the gas phase either, both dissolved NO_2 is necessary in equal or greater amounts than dissolved NO, for NO_2^- formation to occur (R I.33-R I.34)[122].

$$2NO_2 + H_2O(l) \rightarrow NO_3^- + NO_2^- + 2H^+ \quad \text{R I.33}$$

$$NO + NO_2 + H_2O(l) \rightarrow 2NO_2^- + 2H^+ \quad \text{R I.34}$$

In the liquid, NO_2^- is converted into NO_3^- via H_2O_2 (R I.35) and NO_2^- (R I.36)[89].

$$NO_2^- + H_2O_2(aq) \rightarrow NO_3^- + H_2O(l) \quad \text{R I.35}$$

$$NO_2^- + NO_2^- + O_2(aq) \rightarrow 2NO_3^- \quad \text{R I.36}$$

Lastly, NO can also be further oxidized into NO_3 or N_2O_5, though it can be reasonably assumed that this pathway does not have a significant contribution, seeing as they, when measured, were not present in the studies included in this overview. The same applies to NO_2's dimer, N_2O_4.

5.3.2 Nitrogen reduction

Performance Wet N reduction, in essence, aims to use H_2O as a H source in one-step NH_3 synthesis[28-31]. H_2 is costly and energy intensive to produce, while H_2O is a raw and abundant material.

Table 2 shows the performance indicators of the setups that are discussed below. Most of the studies are performed in N_2/H_2O mixtures, though Haruyama et al.[134] and Sun et al.[142] also measure NH_3 in the liquid phase when using air/H_2O. The NH_3 production rate spans over three orders of magnitude (0.001 – 23 mg/h) and the range of EC spans over four orders of magnitude (7.2 – 48750 MJ/mol), meaning they underperform compared to dry N reduction (0.3 – 400 mg/h; 18 – 180 MJ/mol). Note, dry reduction needs H_2.

When taking into account a balance between production rate and EC,

plasma-electrocatalytic systems seem to have the best performance (entry 11 and 12; 0.36 mg/h at 139 MJ/mol in N_2; 23.2 mg/h at 910 MJ/mol in air)[141,142]. Looking at the range of different plasma types and ways to introduce water, one can see this subfield is in an earlier stage compared to dry plasma-based NF. Many of the studies are exploratory or focus on more fundamental questions (e.g. What is the role of the H_2O liquid surface? Which plasma species are important?), meaning optimizing for the best performance is not the main focus yet. The following sections discuss the main characteristics of the systems in Table 2, sorted by how H_2O is introduced.

Liquid water. *(entry 1-16)* Sakakura et al.[130,131,135,136] and Haruyama et al.[134] studied a similar DBD above a H_2O container/reservoir in a number of works and focused on the pathways towards NF species (*entry 1, 4, 6*). They concluded that the plasma-liquid interface is the main reaction locus for NH_3 formation and that the surface area is therefore important, resulting in studies using for example H_2O droplets and H_2O films. In response, Liu et al. studied a falling water film DBD and improved wet oxidation drastically, though they saw no NH_3 production, which was mainly attributed to the air used opposed to pure N_2[127,142].

Kubota et al. compared a N_2 jet above water *versus* EtOH(l). Though it was shown EtOH(l) was more performative for NH_4^+ production (entry 2), one has to keep in mind that EtOH(l) is not a raw material like H_2O(l)[132]. Nonetheless, it can give more insight on the pathways towards NF products (see below).

UV-irradiation. *(entry 4-6)* Sakakura et al.[135,136], Haruyama et al.[134] and Peng et al.[105] studied setups with a liquid surface in combination with UV irradiation of the liquid surface to increase the

availability of precursors at the plasma-liquid interface. All four systems showed an increase in NH_4^+ upon UV irradiation (2-4 fold), NO_2^- decreases in all four cases, and NO_3^- increased in the case of Peng et al.[105] and Sakakura et al.[135,136], while in the case of Haruyama et al.[134] its production decreased.

(Micro)droplets. *(entry 8 and 12)* Toth et al. studied a coaxial DBD with water droplets introduced in the plasma by an atomizer, producing NO_x^- and NH_3 (entry 8)[137]. Comparing H_2O and H_2 as a H source, they found that both H_2O vapor and droplets produced more NF species in total and the NH_3 production was comparable between H_2 and H_2O. Additionally, water vapor showed a slightly higher rate for NH_3 production compared to water droplets, possibly due to an increased availability of H_2O molecules. Though the EC is comparably high (7845 MJ/mol), the process is continuous and scalable, with room for improvement in the area of the H_2O-atomization[137]. Janda et al. studied water droplets as well, though in air, and did not observe NH_3 production[122]. On the other hand, Gromov et al, observed a reduction in efficiency when H_2O (liquid) was added, which they attributed to the energy loss due to evaporation[139]. Adding H_2O as a gas could potentially avoid this loss, but needs to be verified.

Plasma-in-liquid. *(entry* 10*)* Peng et al.[138] studied an *in situ* NF system where plasma is formed in bubbles under water, measuring both production in the liquid and the gas phase. They report one of the best production rates (4.6 mg/h), though at a very high EC (1747 and 4.8×10^4 MJ/mol).

Water vapor. *(entry 8, 12)* In $N_2/H_2/H_2O$ mixtures in a catalyst (Ru/Al_2O_3) -packed DBD, it has been shown that H_2O-vapor (0-0.21%) is a good promotor for NH_3 formation at low energy densities (<1200

J/L), increasing its energy yield with 30%[148]. In air or N_2 mixtures, studies using water vapor are limited[89,122]. Both studies show the same (entry 8)[137] or increased (entry 12)[122] performance when H_2O droplets were changed to vapor, though NH_3 production only takes place in the N_2/H_2O(g) mixture[137].

Plasma-electrochemical/-catalytic systems. *(entry 14-16)* In plasma-electrocatalytic ammonia synthesis, nitrogen is reduced by electrons driven by an applied bias at atmospheric pressure and low temperatures[26]. Plasma activation of N_2 can overcome the first limitation of electrocatalytic NH_3 production, namely the high overpotentials that are required for N_2 activation. Still, a standing limitation of this synthesis method is the limited NH_3 production selectivity compared to H reduction[26,143,149]. Interesting to note is the synthesis route proposed by Sun et al., where first NO_x was produced in air by an AC plasma spark in water, followed by an electrolyser converting NO_x into NH_3[142] (Table 2, entry 15). Another plasma-electrocatalytic system was proposed by Hawtof et al., showing a relatively low EC (139 MJ/mol). Note, H_2SO_4 was added to the liquid as a H source and to trap the formed NH_3[141].

Underlying chemistry

The reactions between N_2/H_2O and air/H_2O are complex because of the simultaneous oxidation and reduction of N_2 taking place. With the current knowledge, the plasma-based NH_3 synthesis mechanism from N_2/H_2O and N_2/H_2 systems could be similar, though research on the underlying mechanisms in this area is lacking. Toth et al. performed a test where H_2O was replaced by an equivalent amount of H_2 gas in the inlet and observed similar NH_3 production rates, which could support this hypothesis[137].

(1) N_2 is activated, with the formation of atomic N, excited N_2 (N_2(v,E)) and molecular N_2 ions (N_2^+) (R I.12 – R I.13; section 5.2.2). This is proposed as a crucial step by many authors studying wet N reduction systems[105,135,136,141]; (2) Next, H_2O, the H source, is dissociated into H and OH radicals via electron impact or UV irradiation (R I.20, R I.22) and possibly OH splits further into H and O radicals (R I.21)[125]. (3) Then, it is assumed NH is formed, either through N_2* reacting with H_2O directly[136] or H reacting with N_2* after H_2O decomposition[105]. (4) NH is then further hydrogenated, similar to the reaction scheme in N_2/H_2 mixtures explained above. NH_2 could be a much more important intermediate compared to N_2/H_2 mixtures, seeing as R I.17 is expected to have a much lower importance. Indeed, in N_2/H_2O mixtures, limited H_2 production has been observed[136,150], but in general its fraction is logically much lower than in N_2/H_2 mixtures. Next to NH_3, by-products include NO_2^-/HNO_2, NO_3^-/HNO_3, NO/NO_2 and H_2O_2 (R I.26 – R I.32) if both gas and liquid phase products are considered.

With regards to the N_2/H_2O ratio, a more systematic study is needed to elucidate this dependence. The range of H_2O fractions in most studies was low (0-3%[122,137]) and not subject of the study.

The next sections summarize suggested pathways and propositions regarding the underlying mechanisms discussed in the reported works (Table 2).

Reaction locus. Liquid[105,130,131,134], gas[137] and gas+liquid[105,134] have been proposed as the reaction locus for NH_3 formation. Peng et al. proposed HNO_x was formed in the liquid phase, while NH_3 was formed in both the gas and the liquid[105]. Hawtof et al. proposed solvated electrons and H radicals to play a crucial role in plasma-electrocatalytic NH_3 synthesis. In their setup, this was confirmed by

electron and H scavengers, hence they suggested liquid as the reaction locus[141]. Sakakura et al. proposed that the plasma-liquid interface is the most important reaction locus for their type of setup[136]. Lastly, Toth et al. also suggested that NH_3 is formed in the gas phase and that the plasma-liquid interface plays little to no role in this system, contrary to what has been suggested previously[137]. This confirms the work discussed in Chapter V. Thus, the very role of liquid H_2O in plasma-based NF remains unclear.

Plasma-liquid interface. When a plasma-liquid (P/L) interface is present, the liquid surface has been identified by different authors as a vital player in NF[130,131,134,135], which is not illogical as the liquid H_2O is the only source of H except for evaporated H_2O. Haruyama et al. observed an increase in NF species production as a result of increasing the plasma-liquid surface area[134]. Following this, designs with an increasing P/L surface have been put forward: water flowing films, aerosol droplets and plasmas with a larger surface increase the contact area and hence the synthesis rate[105,122,127]. On the other hand, Gromov et al. compared a dry (pin-to-plate) and a plasma-liquid system (pin-to-water flowing film) and observed a decrease in NF in the presence of a liquid H_2O film, which they attribute to energy loss to evaporating H_2O[139].

The extraction of H from the liquid surface is assumed to be the rate limiting step for NH_3 formation in plasma-liquid systems, by authors using similar systems (plasma above a water-filled container). Haruyama et al. confirmed this for their system using D_2O/H_2O and the kinetic isotope effect[134]. UV radiation of the surface is one way used to increase the available H at the P/L surface through R I.22, and has been shown to increase NF (up to 4 fold) compared to their UV-less

counterpart [105,134–136]. Sakakura et al. showed that N_2*/N_2^+ based NH_3 pathways are improved by UV irradiation, while N_{atom} based pathways are not influenced, likely because N_{atom} reactivity with H_2O is already high, also suggesting they follow different mechanisms[135]. Lastly, Haruyama et al. pointed out, confirmed by their experiments, that UV also increases the decomposition of NH_3 and the latter should therefore be tapped off in practical applications[134].

While the importance of a plasma-liquid interface is proposed by many works, it is not necessarily a universal pathway for plasma-based NF as those works focus on very similar systems and there are other works that present a counterbalance to this predominant narrative[137,139]. The importance of a plasma-liquid surface is therefore likely system-dependent and needs to be looked into further.

Suggested pathways and important species. A number of suggestions on how H is introduced into NH_3 have been made. Sakakura et al. suggested that NH_4^+ could be formed via reaction between N_2*/N_2^+ with H_2O and H to produce N_2H^+, which then acts as a promotor and as a H source[131]. In another study of theirs, they suggested NH_4^+ was formed through N_{atom} and/or N_2*/N_2^+ extracting H from H_2O on the liquid surface as another pathway[135] next to H_2O decomposing first[136]. Additionally, they concluded that it is important to form a reaction field in which activated N (N_{atom} and/or N_2*/N_2^+) would be able to react quickly[136]. Both Sakakura et al. and Haruyama et al. stated NH is expected to dissolve in H_2O and reduce further there[134,136], meaning they suggest NH_3 is formed in the liquid.

Kubota et al.[132] compared EtOH(l) and H_2O(l) as the liquid and found EtOH(l) increased NH_4^+ production from 4.9 to 53.2 mg/h, while reducing the oxidation pathway drastically (41.0 to 4.4 mg/h NO_x^-),

meaning in EtOH(l) the reduction of N is more facile than its oxidation. EtOH(l) has H atoms in the form of C–H and O–H available, while H_2O only has the O–H type. Because the abstraction of the labile H from C–H is easier compared to O–H of H_2O, this results in a mixture of OH + H when H_2O is used and predominantly H in case of EtOH(l). The comparison suggests that reduction involves a pathway with H in both H_2O and EtOH(l) while oxidation mainly happens through an OH pathway[132]. The increase in total NF when moving from H_2O to EtOH(l) could be attributed mainly to the facile abstraction of H in case of EtOH(l) compared to H_2O, but also other factors, for example the decrease in by-product synthesis (e.g. H_2O_2) could play a role, though this was not tested.

Another possible pathway for NH_3 formation is the reduction of NO_x/NO_x^- by H_2O, which was tested via water droplet DBD by Toth et al. by introducing HNO_3/NO_3^- droplets in the plasma. This test suggested the contribution of this pathway was small and the direct reduction of N_2 appears to be dominant[137]. In a plasma-electrocatalytic system proposed by Sun et al.[142] (entry 10), this pathway did result in significant NO_x to NH_4^+ conversion. Note that the oxidation and reduction took place in separate cells.

From these works, we can conclude that in terms of pathways/mechanisms, studies have not yet gone very deep, which is understandable considering the novelty and multi-phase aspect of the field. Most works indicate N activation, be it as N_{atom}, N_2* and/or N_2^+ as an important step, as well as H availability. Whether NH_3 is formed in the gas phase, liquid phase or both is inconclusive based on the current literature.

Tuning selectivity. In a wet plasma, a whole range of NF species can be produced, therefore, the tunability of the product selectivity is under study. At the same time, this insight can shed light on the pathways towards the different NF species. Usually, high selectivity towards NH_3 or HNO_3 is preferred. For example, Sakakura et al. used pH-controlled trap cells and were able to tune the NF composition while keeping the total NF capacity constant, under certain conditions[130].
It is interesting to map the influence of O_2 on wet NF, seeing as air is raw and abundant. Haruyama et al. observed a proportional decrease in NH_3 production when moving from pure N_2 to an air plasma above H_2O, suggesting that contamination with oxygen does not affect NH_3 production in plasma-liquid systems[134]. On the same topic, Sakakura et al. could tune the selectivity by changing the gas phase oxygen concentration while keeping the total NF constant[130]. Seeing as there was no change in total NF in a O_2-free system, this suggests the limiting step for both N oxidation and reduction does not involve O_2.
While H is important for reduction, OH is the main precursor for NO_x, HNO_3/NO_x^- and H_2O_2 formation. As confirmed by Sakakura et al. using electron spin resonance (ESR) measurements, oxygen in the gas phase increases OH production in the liquid water phase and in this way promoted a pathway to NO_x^- in H_2O[130]. Since both H and OH originate from H_2O dissociation, tuning these species is a challenge.

Another work by Sakakura et al. investigated the role of N_{atom} and N_2*, with a short and long life-time, respectively, for different plasma-H_2O surface distances, and found increasing the distance could tune the selectivity towards NH_3 production opposed to oxidation through the suppression of $HO^{\cdot}$ and H_2O_2 production at longer distances, which

decreases NO_x^- synthesis[131]. In summary, Sakakura et al. concluded that the reactions in the liquid could be controlled by modulating active species in the gas phase[131].

Peng et al. observed that when plasma is generated inside H_2O (opposed to on the surface), the selectivity of the oxidation product is shifted towards NO_3^-, while the reduction selectivity remains similar, which can be attributed to the higher concentration of O species in the case of plasma-in-water, facilitating the conversion of NO to NO_2[138]. NO is a main precursor for HNO_2/NO_2^- while NO_2 is the main precursor for HNO_3/NO_3^-. Additionally, also direct NO_2^- to NO_3^- conversion through for example H_2O_2 could be of different importance between plasma-on-water and plasma-in-water systems, however, this was not studied.

Lastly, Tsuchida et al. found that the NH_3 selectivity could be increased from 41 to 83% in their DBD above liquid H_2O, by adding dielectric beads, which increased the atomic N in the plasma[133].

This shows the selectivity is tuneable in different ways, which adds flexibility, customizability and can also help improve the general NF performance.

5.4 Summary and outlook

In summary, Table 2 shows various plasma sources that study wet plasma-based NF for oxidation and reduction. In terms of production rates and EC they underperform in comparison with dry systems or do not focus on production rates or EC, hence this information is often lacking (Table 2). This is likely because the field is relatively new, most studies are exploratory and/or focus on elucidating NF pathways. The discussion on the proposed pathways showed a lot is still unclear, and on many topics there is no consensus. The following section summarizes the main gaps in knowledge in wet plasma-based NF.

Analysis outside liquid H_2O. In terms of species production, often the focus is limited to the liquid. Only some works study both the gas and liquid phase in equal detail[138], which could be because the liquid was put forward as most important [130,131,134,135]. At the same time, it is clear the production (in the liquid) is influenced heavily by the gas phase composition[122,130,131,135–137]. Analyzing both would thus improve elucidation.

Pathway elucidation and de-coupling effects. Combined oxidation and reduction in wet plasma systems and the multi-phase nature of wet systems complicate pathway elucidation. The insight on mechanisms is lacking and there is no consensus on the role of H_2O, and the transport of plasma species into the liquid is poorly understood. Most pathways/mechanistic studies use a very similar wet plasma system with a DBD above a liquid surface[130,131,133,135,136]. Though this resulted in a good set of fundamental studies on the underlying mechanisms in this type of setup, the proposed pathways likely reflect this overrepresentation.

Seeing as wet NF systems are inherently more complicated than dry

systems because of their array of reaction loci, de-coupling the effects is therefore even more crucial. For example there is H_2O vapor present in virtually every setup, its isolated effect on the H_2O oxidation and reduction pathways, however, has been scarcely studied[122,137].

Modelling studies are more complicated when a liquid is present, usually requiring more-dimensional models[151–154]. A big challenge is the lack of fundamental reaction rate coefficients and cross-section data developed specifically for the liquid phase. The knowledge on gas to liquid transport is limited under non-equilibrium, which makes modelling transport from the gas to the liquid phase especially challenging[61,151].

Studying more diverse plasma types and ways to introduce H_2O. Compared to dry NF, the array of plasma types for wet systems is still limited. Moreover, even though the overview above illustrates that increasing the availability of H_2O is crucial to improve wet NF, there are limited studies that branch out into other ways to introduce H_2O into the system[122,137]. Bruggeman and Leys[155], and Kovacevic et al.[156] discuss a broad spectrum of plasmas in and in contact with liquid H_2O, illustrating the wide range of possibilities.

The overview shows that both plasma-based N oxidation and (perhaps more interesting) reduction can take place in wet plasma systems using raw and abundant materials, like H_2O, air and N_2, avoiding H_2 as a H source. The summary illustrates there are many areas that have not been studied yet, including dedicated studies for improving the performance, which shows the potential is considerable.

6. Other Alternative NF methods

There are a number of HB-alternatives proposed in literature. Here we very briefly discuss the three main ones. Each field has its challenges and assets and this text certainly does not cover all of them.

Next to direct NF methods, i.e. converting N_2 into NF products, there are also a number of alternative fertilizer technologies under research such as recovery methods[157] ranging from reusing ammonia emission through bioscrubbing[158] the conversion of urine into fertilizer[159].

6.1 Thermochemical reduction

Thermochemical N_2 reduction is the most closely related to HB but at low pressure (1 – 10 bar) and low temperature (<600 K). Compared with ambient temperatures this is still a high-temperature process and the requirement for H_2 is a drawback. Therefore, unconventional highly active and electron-rich catalysts and supports are under investigation to decrease the temperature further[160].

6.2 Biological NF

Biological NF research is concerned with reproducing the core nitrogenase enzyme process for application in the fertilizer industry, i.e. mimicking the behaviour of NF micro-organisms that play a role in naturally enriching the soil. It is a self-regulating process that consumes renewable and environmentally benign substances like carbohydrates at ambient conditions[15,161]. The underlying (bio)chemistry is complex and our understanding is incomplete, but the concept has a lot of potential to radically change the way we grow our crops [161,162]. Oldroyd and Dixon conclude that introducing legume symbiosis and nitrogenase for enrichment of the soil are complex engineering processes and therefore this field will be unlikely to deliver genuine

solutions in the next 20 years[163]. As a supplementary or supportive method in for example soil that does not require as much nitrogen, biological NF can provide us some support in a shorter timeframe[164].

There are a number of adjacent technologies under investigation in the field of bio-engineering that do not specifically mimic biological NF but instead use bacteria directly in the soil. In addition to fertilization, this field aims to employ the additional benefits bacteria have to offer, such as increasing resistance to biotic and abiotic stress[165].

6.3 Electrochemical and photo(electro)chemical NF

Electrochemical and photo(electro)chemical NF systems have also been explored, often in combination with a catalyst. As with plasma, they have less rigorous requirements in terms of yield, they also focus on decentralised systems[160] and can use abundant materials like N_2 and H_2O under mild conditions[166,167]. Electrolysis setups are relatively simple[89,149,168] and both electrochemical and photo(electrochemical) systems are powered by electricity, which fits with the goal of industrial process electrification[89,124,169]. However, as discussed by Xue et al., Deng et al. and Zheng et al., (photo)(electro)chemical N reduction faces great challenges, such as overcoming the dissociation barrier of N_2, weak binding strength of N_2 to heterogeneous catalysts, and the competition of other products[166,167,170]. Indeed, the NH_3 yield and production rate of this type of NF process is very limited by the competition between N_2 reduction, the H_2 evolution reaction and other species such as NH_2NH_2[23,166,170] and poor performance due to the low solubility of nitrogen in aqueous electrolytes[89,124,149,168,169,171]. The extremely low amounts of NH_3 pose significant analytical challenges[167].

The electrochemical oxidation field is still very much in its infancy and is therefore difficult to discuss[160,170].

7. Aim of this thesis

Plasma technology offers an attractive alternative or complementary technique to fix N in a way that is more in line with the current needs and sustainability standards. The improvements in performance and the leaps of gained insights in dry plasma-based NF literature in the last years to decades show the potential and, in combination with economical and interdisciplinary studies, also the technical applicability of plasma-based NF. Wet plasma-based NF, on the other hand, is currently the little brother of dry plasma-based NF, meaning there are still many more open-ended questions. The works presented in this thesis add to the state of the art in two main ways.

Firstly, this thesis aims to take into account the identified knowledge-gaps and challenges summarized at the end of the last section. Specifically, (1) we put our focus on branching out to another way of introducing water into the plasma system, i.e. H_2O vapor, (2) we de-couple the problem for pathway elucidation by starting with characterization of the chosen plasma, next a simpler gas mixture and building up from there, (3) we include modelling, though not under wet conditions (the high complexity, made it not feasible within the timing of this thesis) and (4) we focus on also analyzing species and performance outside liquid H_2O.

Secondly, in a more concrete way, this thesis adds to the elucidation of wet plasma-based NF by, contributing to two of the main open-ended research questions in this field.

1. What is the role of liquid vs gaseous H_2O in wet plasma-based NH_3 formation?

2. What are the important chemical pathways towards plasma-based nitrogen fixated species (NH_3/$(H)NO_x$) in a wet environment?

Lastly, in connection with points (2) and (3), regarding decoupling and modelling, we aim to elucidate the role of pulsing in reaching a low energy consumption for NO_x formation from dry air. We will start with this last research question, before moving to wet plasma-based NF.

Figure 6 illustrates the global approach of this thesis.

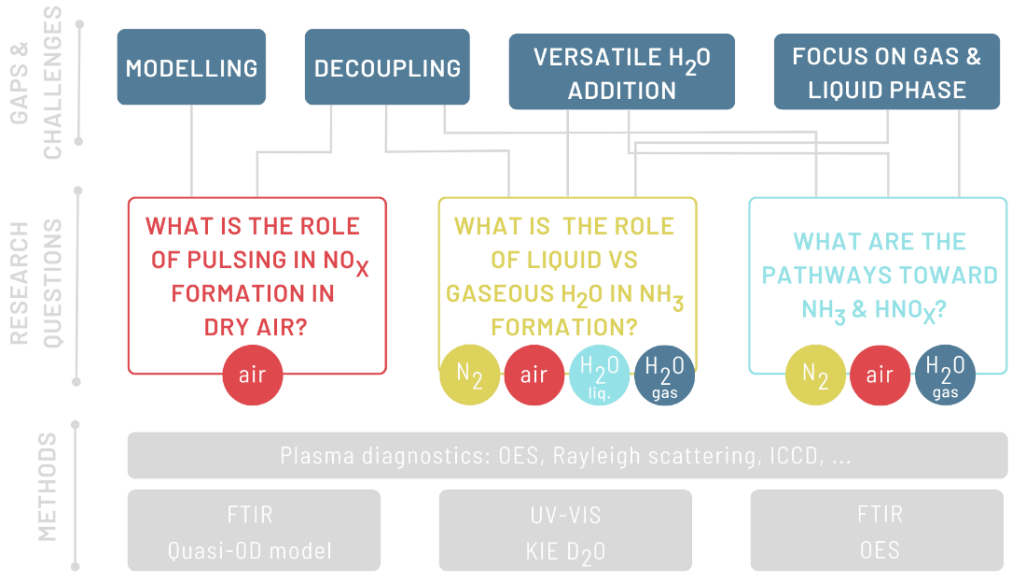

Figure 6 Global picture of the thesis including points of focus, research questions and the most important methods.

II. METHODOLOGY

This Chapter focusses on the experimental and modelling methodology, presented in Chapters III – VI, based on the following published works:

Vervloessem, E., Gromov, M., De Geyter, N., Bogaerts, A., Gorbanev, Y., & Nikiforov, A. (2023). NH_3 and HNO_x formation and loss in nitrogen fixation from air with water vapor by non-equilibrium plasma. *ACS Sust. Chem. Eng.*, 11, 4289-4298. DOI:10.1021/acssuschemeng.3c00208

Vervloessem, E., Gorbanev, Y., Nikiforov, A., De Geyter, N., & Bogaerts, A. (2022). Sustainable NO_x production from air in pulsed plasma: elucidating the chemistry behind the low energy consumption. *Green Chem.*, *24*, 916–929. DOI:10.1039/d1gc02762j

Gorbanev, Y., Vervloessem, E., Nikiforov, A., & Bogaerts, A. (2020). Nitrogen fixation with water vapor by non-equilibrium plasma: toward sustainable ammonia production. *ACS Sust. Chem. Eng.*, *8*, 2996–3004. DOI:10.1021/acssuschemeng.9b07849

Vervloessem, E., Aghaei, M., Jardali, F., Hafezkhiabani, N., & Bogaerts, A. (2020). Plasma-based N_2 fixation into NO_x: Insights from modeling toward optimum yields and energy costs in a gliding arc plasmatron. *ACS Sust. Chem. Eng.*, *8*(26), 9711–9720. DOI:10.1021/acssuschemeng.0c01815

Materials, chemicals and equipment referred to in this and the following Chapters are listed in the Materials Chapter (Chapter VIII).

Often a plasma process or a process in general is rated based on macroscopic performance indicators; for example, how much NO_x is produced and at what energy cost. However, to make improvements efficiently, it is important to first gain underlying insight into the chemistry and physics involved.

A first step is getting to know the system, in this case the plasma, we are working with through so-called characterization: if we know how hot or cold the gas is, how the plasma is formed and how the gas swirls, it is much easier to figure out how to make improvements. Additionally, the performance is evaluated. This insight can be obtained through methods such as the ones discussed in this Chapter.

1. Electrical characterization

Plasma formation and power. Electrical characterization mainly concerns the voltage and current profiles as a function of time. A key characteristic of a plasma that can be measured through this is the power going into the system, which shows how much energy is consumed during the plasma-based conversion. The multiplication of the current and voltage waveforms gives a power profile as a function of time. In case of a pulsed source, this quantifies the time-resolved characteristics of the plasma, i.e. the pulse pattern, and hence the duty cycle (ratio of the pulse width over the pulse period).

Power can be used to describe many different characteristics of the system, therefore it is important to specify and understand what kind of power is meant. The next sections explain *instantaneous power*, *average power*, *plasma power* and *total power* (also called plug power).

The *instantaneous power* is calculated by $P(t) = V(t)I(t)$ and gives the power at one time t, providing information on, for example, the peak power, important in pulsed plasmas. Here, P is the power in watts, V is the voltage in volts and I is the current in ampere. The *average power,* on the other hand, $\bar{P} = \frac{1}{T_D} \int_0^{T_D} V(t)I(t)$ considers the power going into the system over a full discharge period T_D, or more general:

$$\frac{1}{n}\sum_{i=1}^{n} V_i \times I_i \qquad \text{II.1}$$

Another important distinction is made between the plasma power and the total power (Figure 7). The *total power* is the sum of all power consumed by the wall plug, also commonly called the *plug power*, while the *plasma power* is the energy per time unit sustaining the plasma and

is thus related to the *chemical efficiency* of the discharge, i.e. the power that influences the plasma chemistry and therefore the efficiency of the chemical conversion. When talking about the total power, the term plug-to-x (e.g. plug-to-NO_x) can be used[83]. Maximizing the power fraction going into the plasma, i.e. minimizing the power losses, is a physical/electrical engineering question outside the scope of this thesis. Here, when the power is discussed, be it instantaneous power or averaged power, it will always be the power deposited into plasma (plasma power), unless specified otherwise. Figure 7 shows a schematic diagram of the total power, or wall plug power, of which commonly only a fraction is the plasma power.

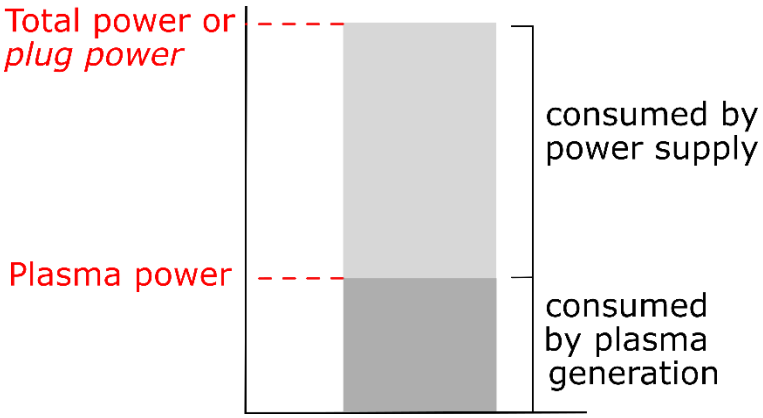

Figure 7 Representation of the total power divided up into the power consumed by the power supply and by plasma generation.

In Chapters III, the waveforms are measured using a voltage probe (Tektronix P6015A, see Chapter VIII, Materials, Table 13, entry 26) and a current probe (Pearson Current Monitor 2877, Table 13, entry 27), connected to a LeCroy WaveSurfer 64Xs oscilloscope (Materials, Table 13, entry 28).

2. Optical characterization

Information on the physics and the chemistry can be obtained through (i) passive optical diagnostic techniques and (ii) active optical diagnostic techniques. The former analyzes the spontaneous radiation emitted from the plasma, the latter sends in light of a known wavelength and analyzes the resulting emission from the plasma.

2.1. Infra-red camera

Gas temperature on a macroscopic scale. An infra-red (IR) camera can be used to measure the temperature of different (outside) areas of the setup. In the presented experiments, the camera's resolution is such that the measured temperature can be seen as time-averaged. This means we obtain a better understanding of the heating of the casing and the surrounding gas as a function of the gas flow rate, operation time and gas composition, which are useful a.o. as modelling input, though the information should be used complementary to other diagnostics. A more dedicated and advanced technique making use of IR light is Fourier transform IR spectroscopy, which is generally used for the quantitative and qualitative detection of molecules (see section 3.1.1).

In Chapter III, the IR images are taken using a TiS45 Fluke IR camera (Chapter VIII, Materials, Table 13, entry 29).

2.2. ICCD camera

Visualising the plasma as a function of time*.* An intensified charged coupled device (ICCD) is suited to visualize a discharge that is operating on a microsecond timescale since it can operate under low-light conditions, by increasing the number of electrons that are

generated within the intensifier, and down to nanosecond exposure times, with the fast shutter.

In Chapter III , a Hamamatsu C8484 ICCD camera with a 100 ns exposure time is used (Chapter VIII, Materials, Table 13, entry 30).

2.3. Rayleigh scattering

Gas temperature of the afterglow. Rayleigh scattering is an active spectroscopic method typically used for gas temperature measurements, as the Rayleigh scattering signal is proportional to the density of the heavy scattered particles[172]:

$$I \sim \sum_i \sigma^i n^i = \sum_i \sigma^i \frac{p}{T_g k_B} \qquad \text{II.2}$$

where k_B is the Boltzmann constant and σ^i is the Rayleigh scattering cross-section of heavy particles. The gas temperature can therefore be calculated as the ratio of the intensity of the scattered laser light I_{ref} corresponding to a known reference temperature T_{ref} (for example, independently measured room temperature) and the scattered intensity when it passes through the plasma I_p:

$$T_g = \frac{I_{ref}}{I_p} T_{ref} \qquad \text{II.3}$$

This means Rayleigh scattering can determine the gas temperature where there is a proper line of sight for the laser.

In Chapter III, the laser scattering experiments are performed in ambient conditions, with a pulsed Litron nano-S Nd:YAG laser (wavelength 532 nm, pulse energy 12 mJ, repetition rate 10 Hz, pulse duration 8 ns; Chapter VIII, Materials, Table 13, entry 31). The laser beam has a Gaussian shape with a diameter of 0.5 mm. The scattered light is collected, perpendicularly to the laser beam, by a Hamamatsu

C8484 ICCD camera with a 532 nm filter (Chapter VIII, Materials, Table 13, entry 30). The synchronization between the laser pulse and the ICCD camera is achieved by an SRS delay generator DG535 (Chapter VIII, Materials, Table 13, entry 32). The experimental setup is shown in Figure 8.

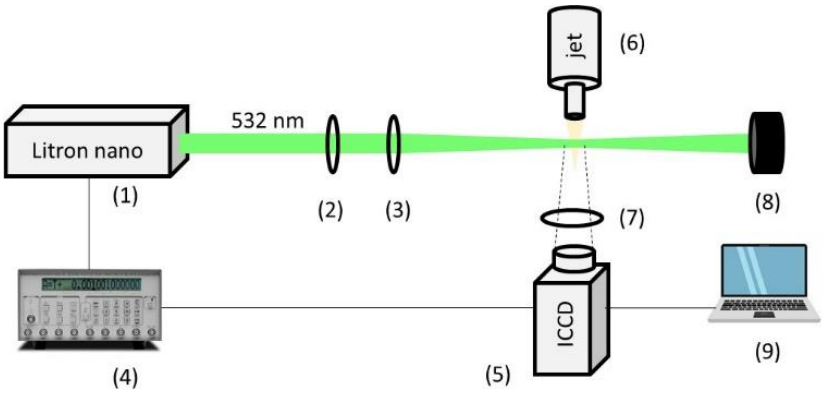

Figure 8 Rayleigh scattering spectroscopy setup including: Nd:YAG laser at 532 nm (1), polarizer (2), lens f=500 mm (3), delay generator (4), ICCD camera (5), plasma jet (6), filter 532 nm (7), beam dump (8), PC with control software (9).

2.4. OES

Optical emission spectroscopy (OES) is a frequently used non-invasive and passive diagnostic method for the characterisation of plasma[173]. Light emitted from the plasma is recorded and used to identify transitions by assessing the light's intensity as a function of the wavelength. The position of the lines and their intensity contains information on the plasma[172]. (As OES is able to qualitatively and semi-quantitatively determine species, it can also be classified under 3 Chemical diagnostics)

Line position. One of the central principles of OES is the excitation of particles (atoms, molecules and ions) and their decay. Since the energy of a transition, and therefore the emitted light of de-

excitation, is characteristic of the species, the central wavelength is an identifier for the species making the transition[173]. The central wavelength of an emission line λ_0 is proportional to the photon energy $E = E_p - E_k$, which corresponds to the energy gap of the transition from level p with energy E_p to level k with energy E_k (lower in energy):

$$\lambda_0 = \frac{hc}{E_p - E_k} \qquad \text{II.4}$$

where h is Plank's constant and c is the speed of light.[174]

Line intensity. The line intensity is quantified by the emission coefficient of the excited species and depends only on the density of the excited level $n(p)$, which depends on the plasma parameters (T_e, n_e, T_g, n_n,…)[173,174].

In Chapters III and VI, two main applications of OES were used: the *measurement of the gas temperature* and the identification and *semi-quantification of excited species* and their corresponding ground state. The setups are shown in Figure 9a and b, respectively.

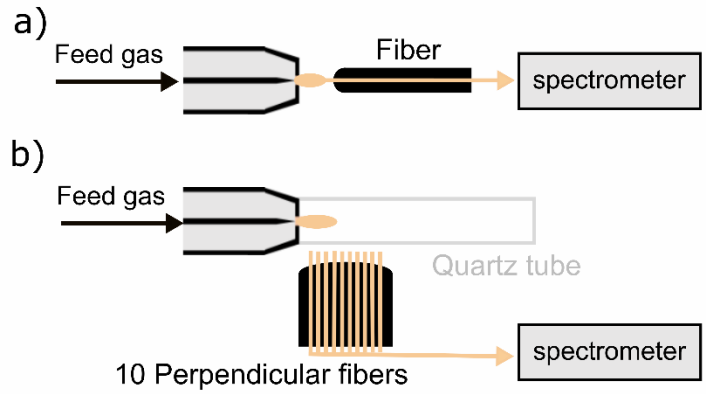

Figure 9 Basic gas analysis experimental setup as used in Chapter III and VI. (a) OES setup axial to the jet used for gas temperature and species measurements. (b) OES setup perpendicular to the afterglow

using 10 fibers for spatially resolved measurements (1-10 mm from the nozzle) used for species measurements.

2.4.1. Gas temperature

In the case of non-equilibrium atmospheric-pressure plasmas, the rotational temperature T_{rot} can be used as an indicator of the gas translational temperature due to the very high frequency of collisions, which leads to equilibrium between different rotational states of the colliding particles. Determination of T_{rot} assumes a Boltzmann distribution of rotational/vibrational states[173].

In this thesis, the OES temperature measurements were based on relative intensity measurements of spectral lines of the second positive system of nitrogen (N_2 $C^3\Pi_u \rightarrow B^3\Pi_g$ transition). The discharge emission was collected with fiber optics (diameter 600 μm) directly facing the region where a bright electrical discharge is generated. An Avantes spectrometer (AvaSpec-3048, 300-390 nm; Chapter VIII, Materials, Table 13, entry 33) is used to partially resolve rotational structure of the N_2 bands. The spectrometer is calibrated with a 250-2400 nm Hamamatsu halogen lamp and power supply (Chapter VIII, Materials, Table 13, entry 34 and 35, respectively). The rotational temperature was spatially and time averaged. MassiveOES software is used to fit the experimental and theoretical spectra, providing T_{rot} as a result of the fitting process as described in Sremački et al.[172].

2.4.2. Excited species

First, the species are identified using the recorded spectra. To identify the fingerprint (i.e. line positions) of a molecule, the book by Pearse and Gaydon[175] is used. The wavelength for transitions of atoms and ions can be found in the NIST database[176]. For a selection of specific OH, NO and N_2^+ transitions, the LIFBASE database is available[177].

To correlate intensities of excited species measured in OES to ground state densities and to compare different bands (i.e. different species) with each other, a number of corrections and approximations have to be considered as follows:

(1) Collisional quenching of excited states is taken into account.

(2) The measured intensities are corrected for the spectrometer sensitivity and fiber optics transparency at different wavelengths.

(3) The intensities are corrected to take into account the difference in excitation probabilities associated with the different transitions used. This means the emission of the excited states can be linked to the emission of the ground state.

This approach is based on the following approximations (similar to corona approximation[178]): (1) Transitions upwards for ionization and excitation occur solely through electron impact. (2) Transitions downwards only occur through spontaneous emission and radiative decay. These two points mean we do not take into account collisional recombination, collisional excitation, three-body recombination, step-wise excitation, charge exchange, and VV and VT processes[174]. (3) The difference in excitation probability is calculated assuming a Maxwell electron energy distribution; in other words, it is a simplified approach to population densities in non-equilibrium plasmas. We infer that the corrections we made suffice to support the discussion of the obtained results.

The methodology is explained below for the case of a $N_2/O_2/H_2O$ plasma containing NH, NO and N_2 as main species of interest but a similar reasoning can be used for other species.

The *NH($A^3\Pi$–$X^3\Sigma$) transition* can be detected at 336.00 nm; there are no major interferences in this region. The main pathway for production of NH($A^3\Pi$–$X^3\Sigma$) is through NH_3. It is commonly accepted that NH($A^3\Pi$–$X^3\Sigma$) is a good indication of the NH_3 density[179].

$NH_3 + e \rightarrow NH(A^3\Pi) + H_2 + e$ k(σ)[180] R II.1

The *NO($A^2\Sigma^+$–$B^2\Pi$) transition* is detected at 226.94 nm. In Chapter VI, the NO($B^2\Pi$–$X^2\Pi$) transition (around 340 nm[175]) is only observed in the afterglow. Both NO($A^2\Sigma^+$) and NO($B^2\Pi$) states are formed mainly through:

$e + NO \rightarrow e + NO(A^2\Sigma^+)$ k(σ)[181] R II.2

$e + NO \rightarrow e + NO(B^2\Pi)$ k(σ)[181] R II.3

The *N_2 ($C^3\Pi$–$B^3\Pi$; Second Positive System; 337 nm) transition*[175] is measured and used for gas temperature determination.

Correction for quenching of the species of interest by H_2O, O_2 and N_2. Quenching reduces the fraction of the state that can be observed through photon emission[182] and collisional quenching reduces the effective branching ratio of a spontaneous transition $i \rightarrow k$. Following Hartinger et al.[183], the quenching of the excited species can be expressed as shown in eq. II.5. Here *q* represents the fraction of the excited species that is present after quenching.

$$q = \frac{A}{A+Q}, where\ Q = \sum n_i v_{ri} \sigma_I \qquad \text{II.5}$$

A Einstein transition coefficient (s^{-1})

Q effective quenching rate (s^{-1})

n_i number density of the quenching partner i (cm^{-3})

v_{ri} relative velocity ($cm.s^{-1}$)

σ_I Cross-section (cm^2)

In case quenching coefficients instead of Cross-sections are given, Q is expressed as follows:

$$Q = \sum n_i \, k_{iq} \qquad \text{II.6}$$

k_{iq} quenching coefficient ($cm^3.s^{-1}$)

The Einstein transition coefficient denotes the total spontaneous emission rate of the upper level, which is equal to its reciprocal lifetime. For NO($A^2\Sigma^+$–$^2\Pi$) and NH($A^3\Pi$–$X^3\Sigma$), A is taken from LIFBASE[177] and from Zhou et al.[184], respectively. The values are reported in Table 3. Q is a sum over all possible quenchers, taking into account their density.

The relative speed of the quencher to the quenched molecule is calculated as follows:

$$v_{rel} = \sqrt{\frac{8kT}{\pi\mu}} \qquad \text{II.7}$$

with $\mu = \frac{1}{\frac{1}{m_1}+\frac{1}{m_2}} = \frac{m_1 m_2}{m_1+m_2}$ in ($g.particle^{-1}$)

Meaning $m_i = \frac{1}{M_i \cdot N_A}$

with:

$k = 1.380649 \times 10^{-16} cm^2.g.s^{-2}.K^{-1}$, for v_{rel} expressed in($cm.s^{-1}$).

This also means that:

$$k_{iq} = \sigma_i v_{rel} \qquad \text{II.8}$$

For both the quenching coefficients and Cross-sections, a wide range of values are found in literature. In Chapter VI, the Q values from three

sources are calculated and their average is used as the quenching coefficient. The three sets of constants are shown in Table 4.

With q known, the signal corrected for quenching is calculated using eq. II.9:

$$I_{measured} = I_{orginal} \cdot q \qquad \text{II.9}$$

q fraction of the signal that is visible after quenching

$I_{measured}$ measured signal

$I_{original}$ the signal without quenching

Table 3 Einstein transition coefficients of NH($A^3\Pi$–$X^3\Sigma$) and NO($A^2\Sigma^+$).

Einstein transition coefficient A (s^{-1})		
NO($A^2\Sigma^+$–$^2\Pi$)	9.8×10^5	185
NH($^3\Pi$–$^3\Sigma$)	1.39×10^6	184

Table 4 The Cross-sections and rate coefficients for NH(A3Π) and NO(A2Σ+) quenching by N2, O2 and H2O as collisional quenchers.

Quencher	**Cross-section (NH($A^3\Pi$)) (cm^2)**				**Rate coefficient (NO($A^2\Sigma^+$)) ($cm^3.s^{-1}$)**					
	Set A		Set B		Set C		Set D		Set E	
N_2	0.1×10^{-16}	182	0.0061×10^{-16}	186	0.00047×10^{-10}	187	0.00065×10^{-10}	188	0.00074×10^{-10}	187
O_2	1.5×10^{-16}	182	4.3×10^{-16}	186	1.47×10^{-10}	187	1.46×10^{-10}	188	1.59×10^{-10}	189
H_2O	9.8×10^{-16}	182	9.8×10^{-16}	186	7.71×10^{-10}	187	7.8×10^{-10}	188	7.58×10^{-10}	189

Correction for sensitivity. The difference in light collection of the spectrometer at different wavelengths is measured and used to correct the NH($A^3\Pi - X^3\Sigma$) and NO($A^2\Sigma^+ - {}^2\Pi$) band intensities. As a light source, a Hamamatsu D2 model L7293 lamp is used with a C9598 power supply (Chapter VIII, Materials, Table 13, entry 34 and 35, respectively).

Correction for excitation probability. The correction for the excitation probability can be applied under the approximation that the system behaves as assumed in the corona model explained above.
Direct electron impact excitation requires electrons with an energy above 5.48 eV and 3.68 eV, for NO($A^2\Sigma^+ - {}^2\Pi$) and NH($A^3\Pi - X^3\Sigma$),[190] respectively, i.e. the corresponding excitation probability will be different by the following factor (eq. II.10):

$$\frac{P(NO)}{P(NH)} = \frac{n_{e>5.48\ eV}}{n_{e>3.68\ eV}} \times \frac{\exp\left(\frac{EE_{NO}}{k_b \cdot T_e}\right)}{\exp\left(\frac{EE_{NH}}{k_b \cdot T_e}\right)} = 0.17 \times \frac{n_{e>5.48\ eV}}{n_{e>3.68\ eV}} \qquad \text{II.10}$$

P probability of electron impact excitation

n_e electron density

T_e electron temperature

k_b Boltzmann constant

The ratio of the electron density with the required energy for the excitation to NO($A^2\Sigma^+$) and NH($A^3\Pi$) can be presented by the fraction of electrons, assuming a Maxwell-Boltzmann energy distribution, which results in an excitation factor of 0.0331 for NO($A^2\Sigma^+$) excitation compared to NH($A^3\Pi$). It has to be noted that the considered corona model corrected for quenching processes is valid for low ionization degree plasmas with only electron impact excitation mechanisms. Additional excitation processes can lead to overestimation of the

excited states density in the corona model. However, a model including a complete set of population processes would require a collisional-radiative model, which is not yet available in literature for mixtures such as used in our work.

For the experiments described in Chapter VI, a Horiba iHR550 spectrometer with UV 250 nm blazed grating of 2400 g/mm (Chapter VIII, Materials, Table 13, entry 36) and a Zolix Omni750 spectrometer with 500 nm blazed grating of 3600 g/mm equipped with a linear fiber optics array slit (Chapter VIII, Materials, Table 13, entry 37) is used, for the experiments axial and perpendicular to the plasma, respectively.

3. Chemical diagnostics

The following techniques are used to qualitatively and quantitatively determine chemical species in the gas phase and in aqueous solutions. They are supplementary techniques or complementary depending on the species of interest. Note, OES can and was also used as a chemical diagnostics tool, but was discussed in the previous section.

3.1. Gas phase

3.1.1. FTIR spectroscopy

Quantification of IR active species. Fourier transform spectroscopy is an absorption spectroscopy technique using a broad band light source. Absorption techniques measure the intensity decrease of light, in this case IR light, passing through a medium. The Fourier transform aspect refers to the use of a Michelson interferometer with one movable mirror, which converts the light into an interferogram. A Fourier transform converts the interferogram into an actual spectrum. Together with a CCD camera, this enables simultaneous recording of all wavelengths, an increase in the signal-to-noise ratio and high

spectral resolution[191]. The FTIR spectrum is a chemical fingerprint for ground state molecules that absorb IR light (i.e. vibrational transitions) and can be used to identify and quantify chemical species in a sample. The so-called Lambert-Beer law shows the signal intensity decreases as a function of the path length through the medium:

$$I(\nu) = I_0(\nu)\exp\left(-\sum_j n_j \sigma_j(\nu) \times L\right) \qquad \text{II.11}$$

with $I(\nu)$ the intensity after passing through the medium, $I_0(\nu)$ the intensity before passing, n_j the density of the absorbing species j, $\sigma_j(\nu)$ the absorption Cross-section of a transition of species j and L the length. Homogeneous distribution of the species is assumed[173]. In practice, often the area under the curve is used when talking about the intensity.

In Chapters IV and VI, a Matrix-MG2 Bruker FTIR (5 m optical path) is used. Two methods are employed for quantification: Bruker's database and Beer's law based on the absorption Cross-sections from the HITRAN database[192] as described below. The deviation between methods was found to be <3%. The concentration of gaseous HNO2 is calculated through Beer's law only, using the absorbance Cross-section reported by Barney et al.[193]. Though for NO, NO_2 and N_2O the concentration is determined through both Beer's law and the Bruker system, all concentrations reported are determined using Beer's law, for consistency in Chapter VI. In Chapter IV, only the values directly from the Bruker's database are reported, because all species discussed in that work are present in the database. Since the average deviation between the two methods is <3% (based on:

$\frac{1}{n}\sum_{i=1}^{n}\frac{|c_{Bruker}-c_{Beer}|}{c_{Bruker}}$, for the conditions measured) there is no significant difference in the results, nor the discussion.

Beer's law. The concentrations are determined by measuring a reference signal from a gas mixture with a known concentration of the species of interest and *via* Beer's law as follows[194]:

$$n_j = \frac{ln(I(v)/I_0(v))}{\sigma_j(v)\cdot L}\times\left(\frac{10^{12}}{n}\right) \qquad \text{II.12}$$

where $ln(I(v)/I_0(v))$ is the measured absorbance ($A(v)$) as a function of wavenumber (v), $\sigma_j(v)$ is the absorption Cross-section of species j as a function of v in cm^2 $molecule^{-1}$, and L is the length of the absorbance pathway [in cm]. The last term in the brackets performs the unit conversion from cm^{-3} to ppm, where n is the gas density at 323 Kelvin (the temperature in the gas cell).

Figure 10 shows the theoretical absorbance peaks for NO, NO_2, N_2O, NH_3, HNO_3, HNO_2 and O_3 as reported in the HITRAN database[192].

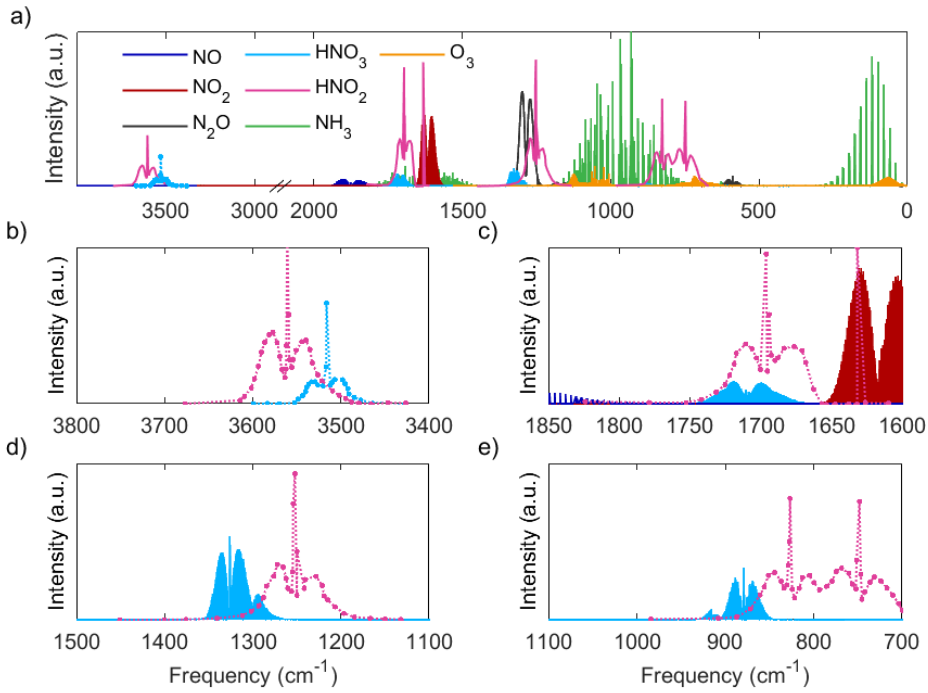

Figure 10 (a) Overview of absorption bands from NO, NO_2, N_2O, HNO_3, HNO_2, NH_3 and O_3; (b) HNO_2 and HNO_3 bands in the 3400 – 3800 cm^{-1} region; (c) HNO_2, HNO_3, NO and NO_2 bands in the 1550 – 1850 cm^{-1} region; (d) HNO_2 and HNO_3 bands in the 1100 - 1500 cm^{-1} region; (e) HNO_2 and HNO_3 bands in the 700 - 1100 cm^{-1} region. All simulated spectra were from the HITRAN database[192], except for HNO_2 and the HNO_3 region (3700 – 3800 cm^{-1}) annotated with dashed lines, which are digitized from Pipa et al.[195] based on literature values[196,197].

3.2. Liquid phase

3.2.1. UV-VIS spectroscopy

Quantification of (derived) UV-VIS active species. UV-VIS spectroscopy is a light absorption-based technique, however, contrary to FTIR, it looks at the absorption of UV and visible light. Molecules of interest are therefore often converted into a molecule with a clear absorption maximum in the UV-VIS range, i.e. a chromophore. The behaviour of the light spectrum before and after the medium can also

be described by Lambert-Beer's law, most often used in the following form:

$$A(\nu) = ln\left(\frac{I_0(\nu)}{I\ (\nu)}\right) = \varepsilon\ \times\ c\ \times\ L \qquad \text{II.13}$$

where A is the measured (dimensionless) absorbance as a function of the wavelength, $I(\nu)$ the intensity after passing through the medium,$I_0(\nu)$ the intensity before passing, ε the extinction coefficient in $L.mol^{-1}.cm^{-1}$ or molar absorptivity, c the concentration in $mol.L^{-1}$ and L the path length in cm^{-1}. Logically this resembles eq. II.12, both written using the constants and quantities and their respective units as commonly used for each method.

In practice, both the area under the curve and the absorption maximum can be used in combination with a calibration curve and a blank or reference spectrum. In this thesis, only UV-VIS spectroscopy in liquid is used. De-ionized H_2O is used to prepare all solutions. Background absorbance and evaporation are accounted for in the final concentration values. All calibration curves and discussion on the test selectivity can be found in Appendix A and B, on pg. IX-247 and IX-249 , respectively. Details on the materials can be found in Chapter VIII, Materials, Table 13, entries 1 - 20.

The procedures used are as follows:

HNO_3/NO_3^- and HNO_2/NO_2^-. The concentrations of NO_3^- and NO_2^- are measured using the Nitrate/nitrite Kit based on a Griess essay with nitrate reductase enzyme in Chapter V,[198–200] and for NO_2^- using the Griess essay in Chapter VI. In general, this essay is based on the following two step reaction, where an azo dye chromophore is formed:

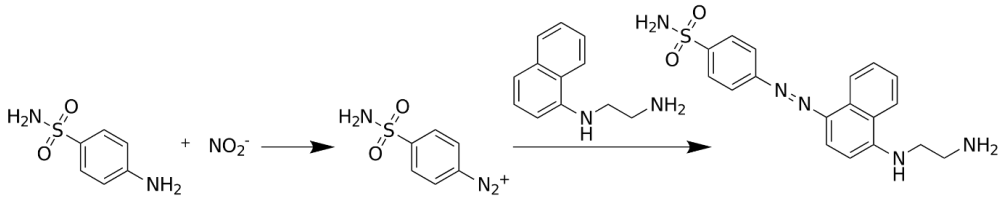

Figure 11 Griess reaction for the quantification of nitrite.

Nitrate/nitrite Kit protocol. For NO_2^--detection, 100 µL of NO_2^--containing H_2O solution is mixed with 50 µL of Griess reagent 1 and 50 µL of Griess reagent 2, and incubated for 6 min. Samples are measured in a 96 flat-bottom well plate using a BIO-RAD iMark microplate reader at 540 nm. For NO_3^--detection, 80 µL of NO_3^--containing H_2O solution is mixed with 10 µL of nitrate reductase and 10 µL of nitrate reductase cofactor and incubated for 1 h at room temperature. by doing so, all NO_3^- is converted into NO_2^-, which is measured. The amount of NO_3^- is calculated as the difference of the two values obtained. The calibration is performed using solutions of $NaNO_2$ (provided in the kit).

Griess essay protocol. Griess reagent is made mixing 1 g sulphanilamide, 0.1 g naphtylethylenediamine, 2.3 mL phosphoric acid (85%) and 97.7 mL H_2O. 1 mL of Griess reagent is mixed with 1 mL of the NO_2^--containing H_2O solution; after 10 min of incubation in the dark, the absorbance is measured at the peak maximum of 540 nm within 30 min after colour development. The calibration was performed using solutions of $NaNO_2$. Background absorbance is accounted for in the final concentration values.

NH_3. NH_3 concentrations are measured using the indophenol blue reaction[134,201]. In general, this essay is based on the following reaction:

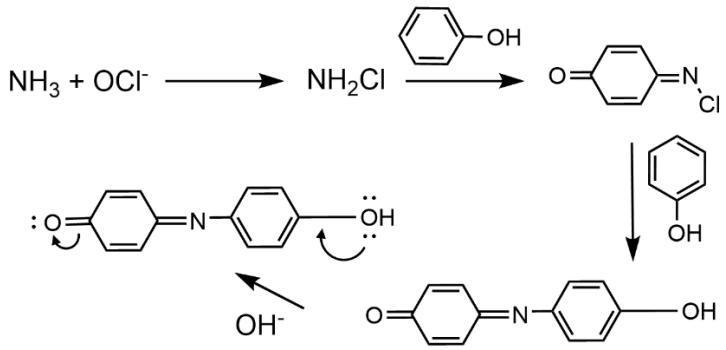

Figure 12 Indophenol blue reaction for the quantification of NH3.

Protocol. Though the above reaction is followed in all likeliness, the kit does not specify the reagents provided. 140 µL of Chromogen A (from the NH_3 kit) is mixed with 140 µL of the NH_3-containing H_2O solution; after 30 min of incubation, 70 µL of Chromogen B is added; after another 30 min of incubation, 140 µL of Chromogen C is added, and the resulting mixture was incubated for 2 h. The absorbance was measured at the peak maximum of 637 nm.

H_2O_2. H_2O_2 is measured using titanium(IV)sulphate with the addition of NaN_3[198–200]. Adding NaN_3 first to the treated solution is necessary to avoid the destruction of H_2O_2 by reaction with NO_2^-(R II.4), instead NO_2^- reacts away via R II.5. The chromophore is formed through reaction of H_2O_2 with Ti^{4+} ions, forming a yellow peroxytitanium(IV) complex (R II.6) [200].

$$NO_2^- + H_2O_2 + H^+ \rightarrow NO_3^- + H_2O + H^+ \quad \text{R II.4}$$

$$3N_3^- + NO_2^- + 4H^+ \rightarrow 5N_2 + 2H_2O \quad \text{R II.5}$$

$$Ti^{+4} + H_2O_2 + 2H_2O \rightarrow \mathbf{H_2TiO_4} + 4H^+ \quad \text{R II.6}$$

Protocol. Immediately after plasma treatment, 50 µL of 80 mM NaN_3 solution, 200 µL H_2O_2 containing H_2O and 50 µL of 0.1 M $K_2TiO(C_2O_4)_2 \cdot 2H_2O$ is mixed and analyzed by UV-VIS absorption using a spectrophotometer at 400 nm.

NH_2OH. NH_2OH is assessed by colourimetry via reduction of Fe(III) to Fe(II) and subsequent complexation with 1,10-phenanthroline.[202] NH_2OH is oxidized to N_2O by Fe(III) ($NH_4Fe(SO_4)_2$, FAS), and Fe(III) is reduced to Fe(II) (R II.7 - R II.8)[203]. Next, the chromophore ferroin complex – tris(1,10-phenanthroline)iron(II) sulfate – is formed by coupling 1,10-phenanthroline to Fe(II) (Figure 13) [202].

$$Fe(NH_2OH)^{3+} \rightarrow Fe^{2+} + H_2NO^{\cdot} + H^+ \qquad \text{R II.7}$$

$$Fe^{3+} + H_2NO^{\cdot} \rightarrow Fe^{2+} + HNO + H^+ \qquad \text{R II.8}$$

$$2H_2NO^{\cdot} \rightarrow N_2 + 2H_2O \qquad \text{R II.9}$$

$$2HNO \rightarrow N_2O + H_2O \qquad \text{R II.10}$$

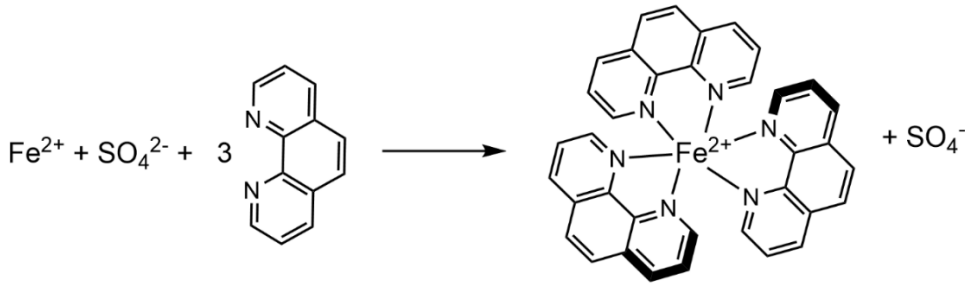

Figure 13 Tris(1,10-phenanthroline)iron(II) sulfate complex formation, for the quantification of NH2OH.

Protocol. 1.2 mL of the NH_2OH-containing solution is mixed with 100 µL of a 5:6 mixture of 1 M CH_3COONa and 1 M CH_3COOH, to buffer the solution at pH 4.8. Then, 100 µL of 4 mM $NH_4Fe(SO_4)_2 \cdot 12H_2O$ in 0.1 M HCl is added. After the solution is vigorously stirred for 2 min, 100 µL of 1,10-phenanthroline in 0.1 M HCl is added, and the resulting mixture is incubated for 30 min. The absorbance is measured at the peak maximum of 510 nm.

NH_2NH_2. NH_2NH_2 was assessed via formation of an azo-dye in a reaction with 4-dimethylaminobenzaldehyde forming a chromophore azo-dye[204].

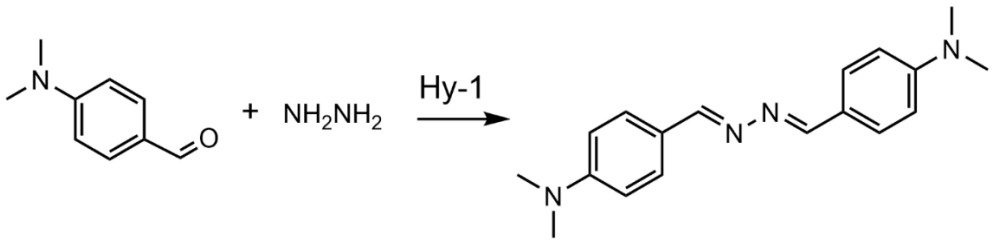

Figure 14 Dimethylaminobenzaldehyde formation reaction for the quantification of NH_2NH_2. The unspecified Hy-1 reagent from the kit is most likely hydrochloric acid.

Protocol.1 mL of the NH_2NH_2-containing solution is mixed with 100 µL of the Hy-1 reagent from the Spectroquant Hydrazine Test Kit, and incubated for 10 min. The absorbance was measured at the peak maximum of 458 nm.

A UV-VIS Thermo Fischer Genesys 6 spectrophotometer using Hellma quartz cuvettes with a 10 mm path length and Shimadzu UV mini 1240 spectrometer are used in Chapter V and VI, respectively (Chapter VIII, Materials, Table 13, entries 38 and 39, respectively).

4. pH and temperature measurements

Ambient and liquid temperature, and pH values are measured using an Extech Instruments TM100 thermometer and a Mettler Toledo MP255 pH meter, respectively (Chapter VIII, Materials, Table 13, entries 41 and 40, respectively).

5. Kinetic isotope effect

The kinetic isotope effect (KIE) is used in Chapter V to investigate the role of liquid vs. gaseous water using heavy water (D_2O) as a reactant. Isotopically labeled molecules show lower reaction rates compared to their non-labeled counterparts due to their higher bond dissociation energy. Indeed, the heavier the molecule or atom, the lower the

frequency of vibration and the smaller the zero point energy in the potential energy surface. This does not change the energy potential surface itself, hence only the reaction rate is affected. For example, R-D conversion will be slower than R-H conversion, due to $E_D > E_H$[205]. The KIE is most pronounced when the change in mass between the isotopes is largest, meaning isotopic labeling of H-containing molecules with D will have the largest change in rate, known as the deuterium effect.

6. Computational models

6.1. Reality in an unreal box

A computational model is a theoretical representation of a system or object through mathematical expressions, e.g. describing known physical and chemical laws or theories.

6.1.1. Why do we need models?

Plasma is a complex mix of chemistry and physics. Therefore, it is often challenging to separate the different effects at play, which makes elucidation of the chemistry and physics difficult. A model simulates (a part of) the process taking place, allowing us to gain a deeper understanding. Modelling shows a number of advantages that make it an excellent complementary method to purely experimental work; here we give three main examples. Firstly, one does not necessarily have to perform all the experiments of interest, e.g. small changes in the setup can be screened first within the model before practical implementation. Secondly, modelling allows us to look into the underlying physics and chemistry in a way that is rarely possible through experiments alone, e.g. looking at the individual reactions. Thirdly, one can decouple effects with much more ease, e.g. by setting up a model for an

experiment that would not be easily available in practice.
Modelling can therefore accelerate fundamental and applied research and even open up new paths that were not possible before.

6.1.2. Predictive vs. explanatory models

A model is made with the application in mind: predictive models and explanatory models are discriminated. The former aims to provide good predictions for future outcomes by using associations between predictors and the outcome variable. The variables used in predictive models are based on association, not statistical significance or scientific meaning. A predictive model can to a certain extent be used as a substitute for direct measurement and experimentation.
Explanatory models aim to gain insight and elucidate the underlying physics and chemistry by analysing multiple, simultaneous, physical or chemical phenomena. In this case, the outcome of the model is a consequence of the phenomena that are (not) included in the model. By comparing its outcome to experimental results and/or similar phenomena, one can verify the validity of the model and use it to elucidate the role of the phenomena included within the model. The models presented in this thesis are considered explanatory models.

6.1.3. A simplified presentation of reality

All models are a simplified representation of reality, designed for a specific use. To realize achievable models with feasible calculation times, the complexity of the reality we are trying to represent is always reduced by (1) approximating an aspect or phenomenon through the use of a simplified version and (2) making assumptions that allow us to neglect certain phenomena. Such simplifications are either well-founded in the physics or made out of necessity to allow for feasibility

or because a certain aspect of the system is unknown. In both cases, approximations and assumptions are kept in the back of our mind during construction, validation and analysis. For example, as shown in Figure 15, let's say we are simulating an apple in a music-filled room and want to study the influence of the room temperature on the apple: to start this study the apple could (1) be approximated as a sphere with apple properties, like density and heat conductivity and (2) we can neglect the music that is playing in the background, the notes on the wall and the woodcarving detail of the door and windows, as we know it does not influence the apple and the phenomenon we like to study, temperature.

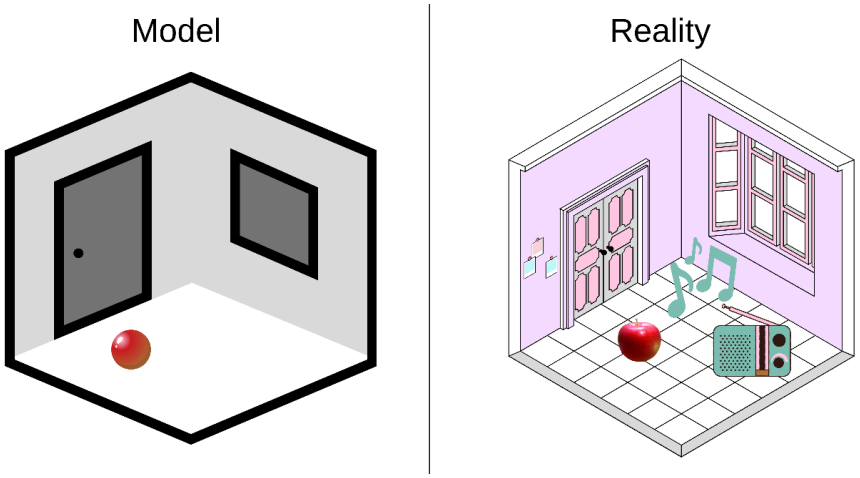

Figure 15 Example of a model (left) compared to the more detailed reality (right) of an apple in a room.

6.1.4. Different fit for each approach

Depending on the phenomena of interest and boundary conditions such as infrastructure, time and availability of data, a suitable model type is used. Common distinction is made between 0D – 1D – 2D and 3D models, typically going from low to high complexity when looking at the physics/chemistry involved.

Choosing a model type is often a balance between calculation time and comprehensiveness, though this is not the only aspect that should be taken into account. Added complexity also complicates reliable model construction and convolutes error identification. Moreover, a thorough knowledge of the underlying physics and chemistry, allows for well-founded simplifications resulting in a less complex model that attains the same insight. Lastly, simplification of one aspect, e.g. physics, can allow for the elaborate description of another aspect, e.g. chemistry, as is done in the 0D model explained below.

Ultimately, the model type should be decided carefully and cannot be done without sufficient knowledge of the phenomena we want to study. The theoretical background on the model types used are discussed below. A description of the specific model used in this thesis is given in Chapter IV section 3.

6.2. 0D Chemical kinetics model

A zero-dimensional (0D) kinetic model describes the chemistry of a process as a function of time without spatial variations or transport of species. It is most convenient for describing complex chemistry, i.e. a large set of reactions, while keeping the computational load low.

The basis for the 0D model is the continuity equation, which contains the chemical kinetics. As input - be it initial or as a function of time - one needs a set of data related to the reactions and species included in the model and information on the plasma properties, like power and gas temperature. Though a number of secondary properties can be calculated in the 0D model, the main output is species densities as a function of time.

6.2.1. The continuity equation

The zero-dimensional (0D) chemical kinetics model - or 0D model in short - used in Chapter IV is based on the code ZDPlasKin. Herein, the species densities are obtained as a function of time by numerically solving a set of continuity equations (R I.22) for the individual species included in the model (see Table 7):

$$\frac{dn_i}{dt} = \sum_j \left[\left(a_{ij}^R - a_{ij}^L \right) k_j \prod_l n_l^L \right] \qquad \text{II.14}$$

The equation represents mass conservation, where n_i is the density of species i, a_{ij}^R and a_{ij}^L are the right and left stoichiometric coefficients species i in reaction j, and n_l is the is de density of the reacting species, for the following general reaction:

$$aA + bB\ (+\Delta H) \xrightarrow{k_j} cC + dD\ (+\Delta H) \qquad \text{II.15}$$

Here, A, B, C and D are the different species and a, b, c and d are their respective stoichiometric coefficients. ΔH represents the enthalpy of reaction j. The reaction rate coefficients, k_j, of the heavy particle reactions are expressed in $cm^3.s^{-1}$ or $cm^6.s^{-1}$ for two-body or three-body reactions, respectively. k_j is either constant or dependent on the gas temperature. The rate coefficients of the electron impact reactions are calculated according to the following equation:

$$k_i = \int_{\varepsilon_{th}}^{\infty} \sigma_i(\varepsilon) v(\varepsilon) f(\varepsilon) d\varepsilon \qquad \text{II.16}$$

ε is the electron energy (usually in eV), ε_{th} is the minimum threshold energy needed to induce the reaction, $v(\varepsilon)$ is the velocity of the electrons, $\sigma_i(\varepsilon)$ is the Cross-section of collision i, and $f(\varepsilon)$ is the electron energy distribution function (EEDF) (Elastic collisions are also included in the model: in this case, the lower limit of the integration

equals 0). To calculate the EEDF and the rate coefficients of the electron impact reactions, the code has a built-in Boltzmann solver, BOLSIG+[206]. The electric field (E) is calculated from a given power density, using the so-called local field approximation[178], meaning the effect of non-local electrons is neglected when solving the electron energy equation, i.e. spatial variations are excluded[175]:

$$E = \sqrt{\frac{P}{\sigma}} \qquad \text{II.17}$$

P is the input power density (W m^{-3}) and σ is the plasma conductivity ($A.V^{-1}.m^{-1}$), expressed as[178]:

$$\sigma = e\, n_e\, \mu_e \qquad \text{II.18}$$

where n_e is the electron number density and μ_e the electron mobility.

6.2.2. The chemistry set

A reaction set for use in a 0D model consists of (1) electron impact reactions where the reaction rate coefficients can be calculated through the cross-sections and (2) heavy particle reactions, where the reaction rate coefficients necessary for the continuity equation are either constant or depend on the gas temperature. Both the reaction rate coefficients and cross-sections can be found in literature, with notable examples such as, among others, Atkinson et al.[207–210], Kossiyi et al.[211], Tsang et al.[212,213], and databases such as the NIST chemical kinetics database[176] - for reaction rate coefficients - and LxCat[214] and Phys4Entry[215] - for Cross-section data. Furthermore, a reaction set can be expanded, as done in this thesis with an elaborate description of vibrational kinetics, which in case of the presented works includes: N_2 and O_2, i.e. N_2 and O_2 electron impact vibrational excitations, N_2-N_2, O_2-O_2 and N_2-O_2 vibrational-vibrational (VV) exchanges and N_2-N_2, N_2-

O_2, O_2-N_2, O_2-O_2, N_2-N, O_2-O and N_2-O vibrational-translational (VT) relaxations. 24 vibrational levels for N_2 and 15 levels for O_2 are included. The calculation of reaction rate coefficients related to these reactions are explained below.

Often there are multiple sources available for a coefficient related to a reaction. The most appropriate constant can be chosen based on, a.o., whether the constant was based on experiments or modelling, whether it is valid for the specific experimental conditions under study (most commonly gas temperature and pressure), whether the finding was recent and/or confirmed by other sources. The list of reactions, their reaction rate coefficients and cross-sections are presented in Appendix C, pg. IX-251, where we refer to last Appendix, pg. IX-288, for the full list. This chemistry set was first validated in a previous work related to my master thesis[216], which is discussed in Appendix D, pg. IX-252.

A few concepts and methods should be explained alongside the chemistry set.

Scaling laws and distribution functions. The included species can have different energies depending on how they are rotationally, vibrationally and electronically excited. For example, in the case of N_2 molecules, the total number density is distributed among the different energy states commonly described by a distribution function, which gives the probability of finding a molecule of a certain (in this case) vibrationally excited state (also see section 4.6). One can look at this group of species - with a certain distribution function associated with it - as one species, or one can consider each individual state as a separate species. In this thesis, the latter approach is used. Excited species typically show different kinetic behaviour, which means it is important for them to be included as such within the 0D model.

Electron impact reactions with excited species. In the model described in Chapter IV, the Cross-sections for the electron impact reactions involving excited species on the left-hand side were shifted over the difference in the threshold energies when a separate Cross-section for that excited species was not available in literature.

Reactions with vibrationally excited species. As explained in the introduction, vibrationally excited species can facilitate certain reactions by lowering their activation energy by $\alpha\,\mathrm{E_v}$[54]:

$$k_R(E_v, T_0) = k_{R_0} \exp\left(-\frac{E_a - \alpha E_v}{T_0}\right)\theta(E_a - \alpha E_v) \qquad \text{II.19}$$

with $\mathrm{E_v}$ the energy of the vibrational level of the species being considered, α the efficiency with which the vibrational energy is used, k_{R_0} the pre-exponential factor and θ the Heaviside function ($\theta(x - x_0) = 1$ when $x > 0$; and $\theta(x - x_0) = 0$ when $x < 0$). In a plasma, where vibrationally excited species are overpopulated compared to the equilibrium case, it is thus important to take these types of reactions into account.

VT and VV exchanges. The reaction rate coefficient expressions of the VT relaxations and VV exchanges between N_2-N_2, O_2-O_2, N_2-O_2 are calculated using the Forced Harmonic Oscillator (FHO) model proposed by Adamovich et al.[217]. This method offers a semi-classical non-perturbative analytical solution for VT and VV transitions of diatomic molecules by averaging the VT and VV probabilities ($\mathrm{P_{VT}}$ and $\mathrm{P_{VV}}$) over the one-dimensional Boltzmann distribution.

$$\mathrm{P_{VT}(i \to f)} = \frac{(\mathrm{n_s})^{\mathrm{s}}}{(\mathrm{s!})^2} \cdot \varepsilon^{\mathrm{s}} \cdot \exp\left(-\frac{2\mathrm{n_s}}{\mathrm{s}+1}\varepsilon\right) \qquad \text{II.20}$$

$$P_{VV}(i_1, i_2 \to f_1, f_2) \cong \frac{\left[n_s^{(1)} n_s^{(2)}\right]^s}{(s!)^2} \cdot \left(\frac{\rho_\varepsilon^2}{4}\right)^s \cdot \exp\left[-\frac{2 n_s^{(1)} n_s^{(2)}}{s+1} \frac{\rho_\varepsilon^2}{4}\right] \quad \text{II.21}$$

with $s = |i - f|$, $n_s = \left[\frac{\max(i,f)!}{\min(i,f)!}\right]^{1/s}$. ρ_ε and ε are collision- and potential-specific parameters.

Table 5 Vibrational-vibrational exchanges and vibrational-translational relaxations for N_2 (as an example) and the rate coefficient expressions.

Reaction	Rate coefficient
$N_2(v_i) + M \rightarrow N_2(v_i - 1) + M$	$Z \cdot \left(\frac{m}{kT}\right) \int_0^\infty P_{VT}(\bar{v}) \cdot \exp\left(\frac{-mv^2}{2kT}\right) vdv$
$N_2(v_i) + N_2(v_j) \rightarrow N_2(v_i - 1) + N_2(v_j + 1)$	$Z \cdot \left(\frac{m}{kT}\right) \int_0^\infty P_{VV}(\bar{v}) \cdot \exp\left(\frac{-mv^2}{2kT}\right) vdv$

M represents any neutral molecule in the plasma.
v_i and v_j are the vibrational levels of N_2 (0-24).
Z is the collision frequency and v is the particle velocity.

The reaction rate coefficients of the VT relaxations between N_2-N are based on quasi-classical calculations that are reproduced through a fit as proposed by Esposito et al.[218], for the following general reaction:

$N_2(v) + N \rightarrow N_2(w) + N$, with $v > w$

All the relevant trends in the reaction rate coefficient are taken into consideration by using an additive model into the exponential argument of the reaction rate coefficient, as shown in the following expression (valid for $v = 1 - 66$ and $\Delta v = 1 - 30$):

$$k(v, T, \Delta v) = \exp\left(a_1(v, \Delta v) + \frac{a_2(v, \Delta v)}{T} + \frac{a_3(v, \Delta v)}{T^2} + \frac{a_4(v, \Delta v)}{T^3} + a_5(v, \Delta v) \cdot \ln(T)\right) \quad \text{II.22}$$

where

$$a_i(v, \Delta v) = z_{i0}(\Delta v) + z_{i1}(\Delta v)v + z_{i2}(\Delta v)v^2 + z_{i3}(\Delta v)v^3 + z_{i4}(\Delta v)v^4 \quad \text{II.23}$$

$$z_{ij}(\Delta v) = b_{ij} + c_{ij}\Delta v \quad \text{II.24}$$

for which the parameters are reported in[218].

Similarly, the reaction rate coefficients of the VT relaxations between O_2-O are based on quasi-classical calculations that have been reproduced through a fit as proposed by Esposito et al.[219], for the following general reaction:

$$O_2(v) + O \rightarrow O_2(w) + O, \text{ with } v > w \qquad \text{II.25}$$

The reaction rate coefficient is then determined based on the following expression:

$$k(T, v, \Delta v) = DegF \cdot \exp\left(a_1(v, \Delta v) + \frac{a_2(v, \Delta v)}{\ln(T)} + a_3(v, \Delta v) \cdot \ln(T)\right) \qquad \text{II.26}$$

where Δv is $(v - w)$

$$a_i(v, \Delta v) = b_{i1}(\Delta v) + b_{i2}(\Delta v) \cdot \ln(v) + \frac{b_{i3}(\Delta v) + b_{i4}(\Delta v)v + b_{i5}(\Delta v)v^2}{10^{21} + \exp(v)} \qquad \text{II.27}$$

$$b_{ij}(\Delta v) = c_{ij1} + c_{ij2} \cdot \ln(\Delta v) + c_{ij3} \cdot \Delta v \cdot \exp(-\Delta v) + c_{ij4} \cdot \Delta v \cdot \Delta v \qquad \text{II.28}$$

The coefficients c_{ijk} are generated using a linear least squares method and are reported in[219] where the degeneracy factor (DegF) is also explained.

6.2.3. 0D to quasi-1D: plug flow reactor model

Every time progression in the 0D model can be translated into position progression by means of the gas flow velocity, which can be either set or calculated. This transforms a time-dependent 0D model (“batch reactor”) into a quasi-1D model (“plug flow reactor”), where the plasma characteristics vary as a function of the distance travelled by the gas. In this way, the spatial variations can be taken into account to a certain extent without increasing the computational load. Chapter IV, section 3, discusses the transformation specifically for the plasma device presented in this thesis. One can either use a set gas flow velocity to perform this transformation or calculate the gas flow velocity within the setup using a computational fluid dynamics model.

6.3. Computational fluid dynamics model

Computational fluid dynamics (henceforth CFD) describes fluid flows through numerical analysis. In Chapter IV, a CFD model is used as an input into the 0D model to effectively transform time-dependent calculations of the chemistry into position-dependent calculations.

6.3.1. Geometry and meshing

A CFD simulation starts with the geometry of the system, usually in 2D or 3D. This computational volume is appropriately discretized, i.e. meshed, to obtain an accurate and feasible numerical solution for the nonlinear equations computed. Meshing takes the equations and transforms their continuous form into a system of algebraic difference equations, creating a number of cells that cover the entire simulation domain[220].

6.3.2. Boundary and initial conditions

The simulated volume is bounded by set conditions based on assumptions that simplify the problem or by known conditions. In other words, boundary conditions take into account how the simulated space interacts with the environment. The initial conditions specify the known starting conditions and/or initial guesses for parameters to start iterations for steady-state simulations[220].

6.3.3. Solver

To solve the set of differential equations, an appropriate solver is chosen, including smoothers and tolerances in order to achieve a solution or facilitate a solution in a more reasonable time.

6.3.4. $k-\epsilon$ model

In Chapter IV, the $k-\epsilon$ model, which is part of the Reynolds-averaged Navier Stokes (RANS) family, is used to describe the turbulent flow. Next to the conservation equations, two transport equations are solved: the turbulent kinetic energy (κ) and the rate of dissipation of the turbulent kinetic energy (ϵ). The $k-\epsilon$ model is well-suited to describe problems with relatively small pressure gradients and is the most commonly used model to describe turbulent flow[220]. For a more elaborate discussion on this type of model in a comprehensible way, we suggest Computational Fluid Dynamics for Engineers by Anderson et al.[220].

III. CHARACTERIZATION OF THE SOFT JET

This Chapter gives an overview of the characterization of the plasma source used in Chapters IV - VI and is based on the following published works:

Vervloessem, E., Gromov, M., De Geyter, N., Bogaerts, A., Gorbanev, Y., & Nikiforov, A. (2023). NH_3 and HNO_x formation and loss in nitrogen fixation from air with water vapor by non-equilibrium plasma. *ACS Sust. Chem. Eng.*, 11, 4289-4298. DOI:10.1021/acssuschemeng.3c00208

Vervloessem, E., Gorbanev, Y., Nikiforov, A., De Geyter, N., & Bogaerts, A. (2022). Sustainable NO_x production from air in pulsed plasma: elucidating the chemistry behind the low energy consumption. *Green Chem.*, *24*, 916–929. DOI:10.1039/d1gc02762j

Gorbanev, Y., Vervloessem, E., Nikiforov, A., & Bogaerts, A. (2020). Nitrogen fixation with water vapor by non-equilibrium plasma: toward sustainable ammonia production. *ACS Sust. Chem. Eng.*, *8*, 2996–3004. DOI:10.1021/acssuschemeng.9b07849

In Chapters IV - VI*, a plasma source named the Soft Jet is used. This Chapter gives an overview of the properties and characteristics of the Soft Jet. Knowing the temperature of the plasma, how much energy it consumes and what it looks like can help us better understand the chemistry we study in the next Chapters. Also, understanding a plasma source inside-out is crucial in making a good model of it.*

In short, the Soft Jet is a pulsed plasma source. Meaning it quickly turns on and off for short periods of time. The temperature of the plasma is fairly high (1450 °C), but thanks to the short pulses it feels close to room temperature to the touch. Furthermore, this jet only needs a small amount of power to operate.

1. Soft Jet: a pulsed non-equilibrium plasma

In this thesis, we applied a plasma jet typically used in biomedical applications, such as anti-cancer therapy[221] and the synthesis of anti-bacterial nanomaterials[222]. Figure 16 shows a picture of the Soft Jet (left) and a schematic (right).

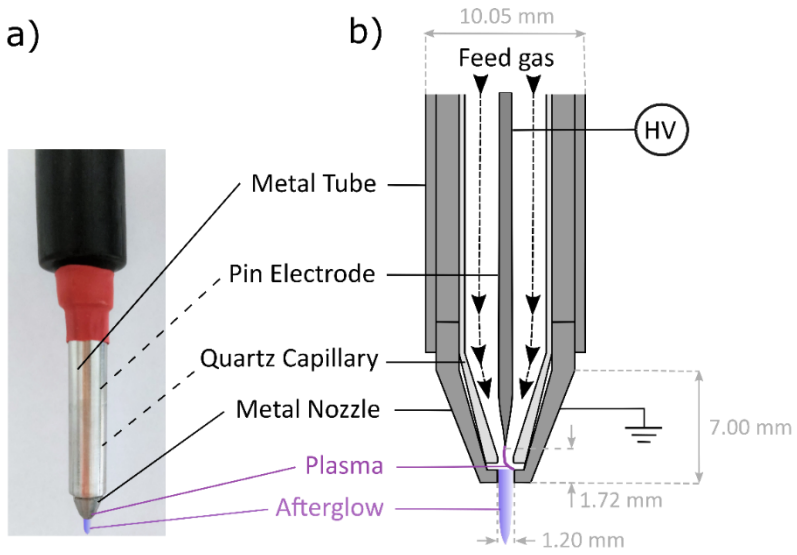

Figure 16 (a) Side view of the Soft Jet. The dashed lines indicate parts that are located on the inside. The plasma effluent (afterglow) is manually drawn in purple as it would not be clearly visible in a picture. (b) Schematic of the inside of the Soft Jet, with the most important dimensions. The dashed arrow lines indicate the gas flow direction through the jet.

The jet comprises a powered needle electrode ringed by a quartz capillary (outer diameter 5 mm; inner diameter 2 mm), contained in a metal tube. The feed gas is supplied into the capillary and leaves the jet via the nozzle tip screwed on top.

The plasma is ignited inside a small cavity between the needle and the nozzle (inner diameter 0.7 mm, volume ca. 0.4 mm^3), with the nozzle

serving as the ground electrode, and the quartz tube as a dielectric spacer.

The plasma is generated by connecting the secondary windings of a high frequency transformer to the system of electrodes separated by a small dielectric spacer. The voltage and current waveforms are close to sinusoidal, and are governed by the primary winding and the transformer characteristics, and high capacitance of the source, respectively (see section 2). Taking into account the shape of the discharge (see section 2.2 below), we consider the discharge mechanism to be similar to the phenomena occurring during the formation of a low current spark[223]. In short, the plasma operates in a pulsed spark mode.

2. Pulsing behaviour and power calculation

The voltage and current waveforms and time-resolved imaging are used to calculate the power going into the plasma and to accurately describe the source in the model presented in Chapter IV.

2.1. Voltage and current waveforms

Figure 17 shows the voltage and current (V-I) characteristics of the Soft Jet at three relevant time-scales: (a) long, (b) for a typical gas residence time at 1 L/min, and (c) short, showing the V-I characteristics.

(a) The long time-scale shows the pulse trains (26.3 ms) with pulse-off time in-between (149.9 ms), meaning the pulse train has a frequency of 6 Hz.
(b) Shows a representation of a typical residence time of a gas molecule in the plasma (here for 1 L/min), if it were to enter during a pulse train. During this residence time (0.2 ms), the molecules

experience ca. 30 pulses (at 1 L/min) within one pulse train. (c) One pulse train (26.3 ms; panel a) contains 4420 pulses, with each period of 11.9 µs containing 2 pulses (which can be recognised as peaks). The duration of one pulse is 0.74 µs, with an interpulse duration of 5.21 µs. The frequency of one such period (two peaks) is 84 Hz.

We tested different gas compositions and concluded that the V-I characteristics, and hence the power calculations, are virtually independent of the gas composition for N_2, humid N_2, air and humid air. We therefore use the same diagnostics results for all gas compositions discussed in this thesis.

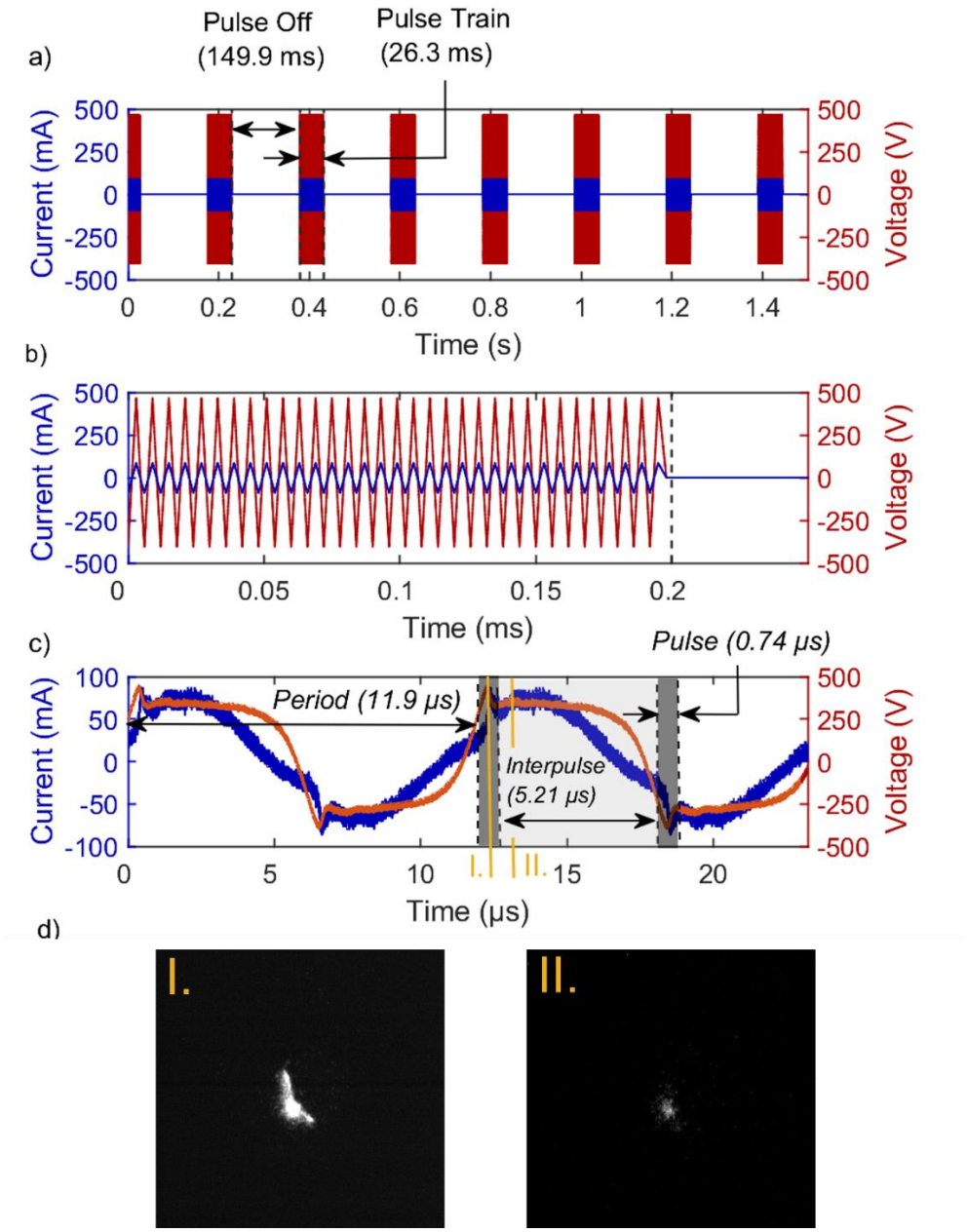

Figure 17 Measured V-I characteristics of the Soft Jet in dry air at three different time-scales: (a) long; (b) for the typical residence time of a gas molecule in the plasma; (c) short, shows V-I characteristics within one pulse train. The pulse (dark grey) and interpulse (light grey) are annotated; and (d) ICCD camera frames ca. at timepoint I. and II. indicated by orange lines on panel c (see Figure 18).

2.2. Time-resolved imaging of the plasma

The plasma was visualized using an ICCD camera at different time points during one period, with 100 ns exposure time (Figure 18). The time indication on the frames is shown in relation to the voltage crossing the zero value (0 µs). Two low current sparks are generated at 4.4 and 9.6 µs. The intensity (i.e. brightness on the images) of the signal decreases with time, until the next spark. The visible zone of low light intensity appearing in between sparks corresponds to the afterglow emission.

If these frames are put next to the V-I characteristics, we can conclude that plasma is only ignited during the small peaks in current and voltage. As an illustration, two ICCD frames are shown on Figure 17c and d, one within the peak (I.) and one right after (II.).

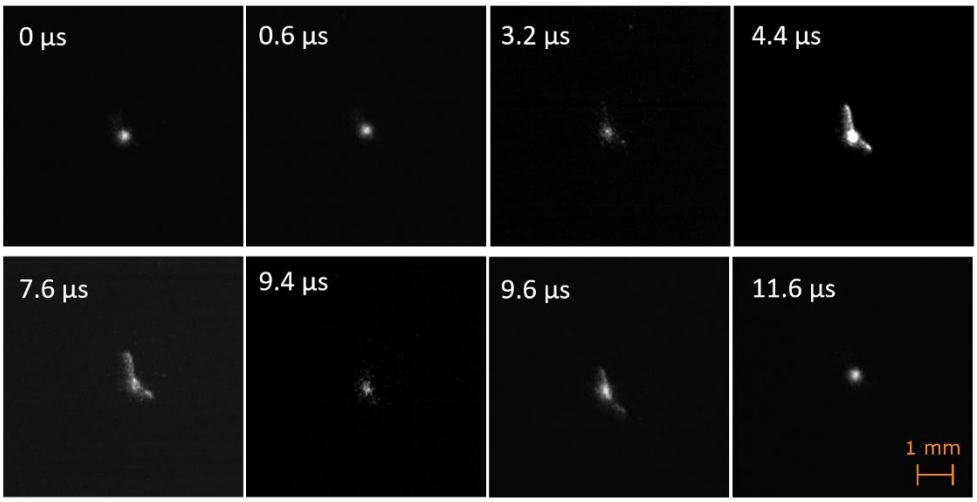

Figure 18 Time-resolved imaging of the plasma discharge obtained using an ICCD camera with a 100 ns exposure time. Time indication on the frames is shown in relation to the voltage crossing the zero value. The camera lens surface was perpendicular to the effluent. Plasma conditions: 0.7 L/min N_2 with 100% H_2O vapor saturation.

2.3. Power calculation

Because of the spark type nature of the plasma, the plasma is formed only during the peak of the voltage and current waveform, as seen in Figure 17c and d. Hence, this corresponds to the discharge power, which is deposited into the plasma, whereas the sinusoidal shape of the current and voltage waveforms correspond to a displacement current, i.e. power that does not go into the plasma[224]. Note, it is the *plasma power* that is used to calculated the energy consumption in the following Chapters.

The integration of the peak in this power profile, corresponding to the V-I peaks (i.e. the sharp peak above the sinusoidal-like shape in Figure 17c) gives an energy of ca. $4 \cdot 10^{-6}$J, which, when divided by the duration of the peak (0.74 µs), yields a power value (in W) corresponding to the time-averaged power within the peak. This way, the *average peak power* of two peaks within the same period was found to be 5.11±0.35 W. For a volume of 0.39 cm^3, this results in a peak power density of 13 $kW \cdot cm^{-3}$ (i.e. the power density for the 0.74 µs duration of the pulse).

The measured power of one pulse, i.e. the *peak power*, does not equal the power put into the plasma overall. Indeed, as explained in the previous section, there is a pulse train only 14.9% of the time (6 Hz) and within this pulse train there is only a pulse 12.4% of the time (84 Hz). Hence, the total duty cycle of the plasma is merely 1.86% (12.4% × 14.9%), i.e. the time a plasma is present. With a peak power of 5.11 W, this means the plasma power of the Soft Jet is 0.1 W. This power is used to calculate the ECs in the following Chapters. The peak power and the pulse characteristics are used in the model (Chapter IV). Chapter II on Methodology explains the different viewpoints for power calculation, here, we used the approach that is custom in plasma

research: considering only the power that goes into the plasma to evaluate the EC.

The asymmetry of the V-I profiles shown in Figure 17c can be explained by a higher power deposition in the positive half-period of the applied voltage. Such effect of voltage polarity on the discharge behaviour is often observed in plasmas[225] and can be explained by charge accumulation in the discharge gap leading to asymmetry of the V-I waveforms.

3. Gas temperature

On a macroscopic scale, the Soft Jet is close to room temperature, as can be seen on an IR frame of the Soft Jet's outer casing (

Figure 19a) and the outer casing's temperature as a function of the plasma operation time and gas composition (

Figure 19b). The nozzle temperature increases mildly as a function of time, saturating within 10 min, likely due to reaching a thermal equilibrium with the surrounding atmosphere and the passing feed gas. Based on the energy deposited within one pulse, the plasma temperature is very likely much higher. Therefore, we looked at the gas temperature (3.1) in the plasma and after the plasma (3.2) in more detail.

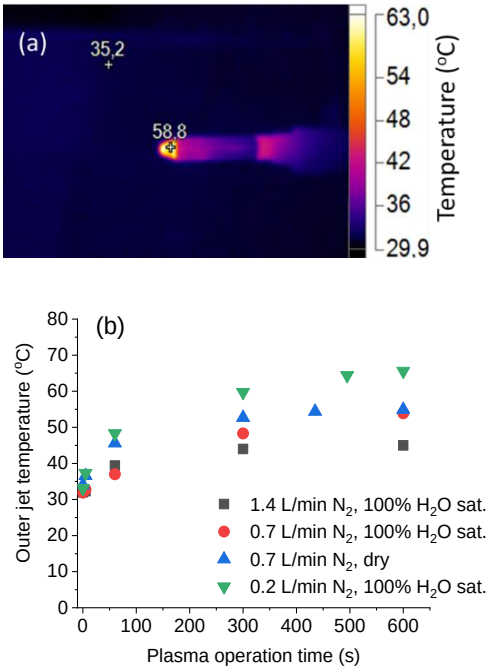

Figure 19 (a) A typical image obtained for the temperature measurements of the outer casing of the plasma jet performed by imaging with an IR camera. (b) The Soft Jet's outer casing temperature as a function of the operation time, at 0.2; 0.7 and 1.4 L/min and 100% humidity and dry conditions in N_2.

3.1. Arc temperature

Analysis of the OES spectra allows us to estimate the temperature of the plasma during a pulse. The methodology used is explained in Chapter II on Methodology, section 2.4 of this thesis. In short, the rotational temperature measured via OES can be used as an indicator of the translational temperature or the gas temperature (T_g).

OES is a spatially- and time-averaged measurement which allows us to measure the plasma core temperature (T_g in the arc) by a line of sight looking into the Soft Jet. The arc emission is much higher compared to the afterglow emission, this means the contribution of the emission from the afterglow in the gas temperature estimations was

very low or even negligible. Based on these measurements, the arc temperature, i.e. the T_g, within a pulse is 1750 ± 150 K.

3.2. Afterglow and plasma effluent temperature

The temperature outside of the jet nozzle was mapped using Rayleigh-scattering spectroscopy (RSS) using the methodology explained in Methodology section 2.3. The spectra are taken perpendicular to the jet, meaning there is no contribution of the arc emission.

Table 6 The average temperature of the plasma effluent at different distances from the nozzle, gas flow rates (FR), at 0 or 100% relative humidity (rel. hum.) and the corresponding effluent width, as measured by RSS.

Distance from the jet (mm)	**FR (L/min)**	**H_2O rel. hum. (%)**	**Effluent width (mm)** *± 0.2 mm*	**Effluent T (K)** *± 10 K*	**Entry**
1.2	0.2	-	1.2	381	1
1.2	0.35	-	1.0	364	2
1.2	0.7	-	0.9	349	3
1.2	1.4	-	0.8	320	4
1.2	0.2	100	1.1	393	5
1.2	1.4	100	0.9	330	6
3.4	0.2	-	1.8	345	7
3.4	0.35	-	1.6	348	8
3.4	0.7	-	1.3	325	9
3.4	1.4	-	1.0	308	10
3.4	0.2	100	1.8	346	11
3.4	1.4	100	1.0	315	12

Table 6 shows the average temperature of the plasma effluent at 1.2 and 3.4 mm from the nozzle, at 0.2 – 1.4 L/min and 100% relative humidity for some select conditions. The temperatures range from T_{room} to ca. 400 K, with the lowest flow rate, logically, reaching the highest temperature. The temperature drops quickly as the distance from the nozzle increases (1.2 – 3.4 mm); at 3.4 mm, the temperature does not go above 350 K. Interesting to note is that under conditions of high relative humidity (entries 5-6 and 11-12) the effluent temperature differs by maximum 10 K compared to their dry counterparts, which is within the error margin of the technique.

Note that OES and RSS are used complementary: RSS is used to determine the temperature of the plasma jet effluent, while OES spectra were mostly collected from the very bright region located directly inside the plasma jet nozzle corresponding to the active discharge region. The IR camera is used as a supplementary technique to RSS. The above values indicate that the Soft Jet is a non-equilibrium, non-thermal plasma.

Lastly, the temperature of both the plasma arc and the effluent was higher than room temperature, thus clearly indicating that the H_2O introduced into the feed gas as vapor in Chapters V and VI remains in the gas phase throughout the whole plasma reactive system (0 – 100% relative humidity).

4. Summary

In Chapters IV - VI, we use a so-called Soft Jet plasma, a pulsed spark plasma with a peak power of 5.11 W and a duty cycle of 1.89%. The plasma is only formed during the power pulse, meaning the plasma power equals 0.1 W. The high power deposited in one pulse results in

a high gas temperature of 1750 ± 150 K in the plasma. The time-averaged temperature of the jet, however, does not exceed 400 K and drops to near room temperature a few mm from the outlet. This means we are working with a non-equilibrium, non-thermal plasma.

The plasma power is used to calculate the energy consumption of NF species synthesis, in Chapters IV - VI. Details on the pulse characteristics, peak power, gas temperatures in the plasma, the afterglow and beyond are used in the model (Chapter IV), next to providing useful background information on the plasma source to help us in our understanding of its behaviour.

IV. SUSTAINABLE NO_X PRODUCTION FROM AIR IN PULSED PLASMA: ELUCIDATING THE CHEMISTRY BEHIND THE LOW ENERGY CONSUMPTION

This Chapter was published as:

Vervloessem, E., Gorbanev, Y., Nikiforov, A., De Geyter, N., & Bogaerts, A. (2022). Sustainable NO_x production from air in pulsed plasma: elucidating the chemistry behind the low energy consumption. *Green Chem.*, *24*, 916–929. DOI:10.1039/d1gc02762j

This Chapter studies the pulsed plasma source described in Chapter III. Pulsing means that the plasma is essentially turned on and off very quickly while we let air pass through the plasma. We see that the air passing through the plasma (i.e. O_2 (oxygen) and N_2 (nitrogen)) is converted into NO_x, a fixed form of nitrogen and something we can use to make fertilizers. Interestingly, we notice this plasma does not transform a lot of air into NO_x, however, it is able to convert air at a very low energy cost, meaning most of the electricity going into the plasma is used to convert air into NO_x, instead of being wasted. Keeping the energy cost low is very important for industrial applications, therefore, it is interesting to know how this plasma is able to use the energy so efficiently. One hypothesis is that the fast on-off switching of the plasma plays a crucial role.

To look into this, we develop a computer model of the plasma. We can send virtual air into this model and observe what happens to it chemically, i.e. what reactions occur. Now we can answer questions such as: "What reactions are taking place a lot?" And: "Does the fast on-off switching of the plasma indeed help in converting air into NO_x in a more energy-efficient way?".

From the model we conclude that indeed, the fast on-off switching of the plasma helps in using the energy more efficiently. We know this by looking into the numerous reactions that take place in the plasma in detail and analyzing their role in making NO_x molecules.

This is another step towards a more sustainable way to make fertilizers. This specific plasma is not suitable for industrial application, but we can use the knowledge from this study to help us develop other plasmas that might be a bit closer to real-life application, i.e. a better way to make fertilizers.

1. Introduction

In this Chapter, we present a combined computational and experimental study of a pulsed plasma operating in air – the so-called Soft Jet[123,226], discussed in the previous Chapter. The pulsing plasma (i.e. plasma with pulsed power) is attractive because pulsing helps to reach the VT non-equilibrium at atmospheric pressure[58,227,228], required to achieve the theoretical minimum EC for plasma-based NO_x production of 0.2 MJ/mol [15,229], as explained in the Introduction, section 5.2.1. To date, no dedicated study – neither experimental not computational – has been performed to elucidate the underlying mechanisms of NO_x formation induced by pulsing plasmas in dry air.

The first aim of this Chapter is to (1) address the applicability of plasma technology, by discussing how detailed insights in the underlying mechanisms can be used to improve the NO_x yield and EC in plasma-based NF. The additional aim is to (2) gain step-wise insight into wet plasma-based NF by studying the source first in its *simplest* form, before adding H_2O in the next two Chapters.

2. Experimental

In this Chapter, the Soft Jet is supplied with compressed dry air (Chapter VIII, Materials, Table 13, entry 22), and the gas flow rate is controlled by a mass flow controller (MFC) (Chapter VIII, Materials, Table 13, entry 42) ranging from 0.4 to 2.0 L/min. The pulse characteristics of the plasma are discussed in Chapter III, to which will be referred often in this Chapter.

2.1. Analysis of the plasma-treated gas

The plasma-treated gas (consisting of the products and unconverted gas) was analyzed by FTIR (Chapter VIII, Materials, Table 13, entry 43), enabling quantitative analysis of the concentrations of NO, NO_2, N_2O_5, N_2O and O_3. Details on this method can be found in section 3.1.1, of the Methodology Chapter. Spectra were obtained with an average of 50 scans with a resolution of 0.5 cm^{-1}. The experiments were performed in triplicates for each flow rate and the average was taken over a 15 min measurement period, chosen to stabilize the FTIR measurements. The system was flushed thoroughly with air for at least 15 min in between measurements. The reported concentrations and error bars are the weighted average of this set of three measurements.

2.2. Energy consumption

Using the plasma power (P), calculated in the previous Chapter and the total NO_x concentration, the EC was calculated according to eq. IV.1. The EC is expressed in MJ/mol N, where mol N is the amount of nitrogen fixed.

$$EC\ \left[\frac{MJ}{mol\ N}\right] = \frac{P[W]}{mol\ of\ NO_x\ produced\ per\ second\ [mol/s]} \cdot \frac{1}{10^6[J/MJ]} \quad \text{IV.1}$$

3. Model description

3.1. Quasi-1D plasma-kinetics model

To gain insight into the gas phase chemistry taking place in the Soft Jet, we developed a quasi-1D chemical kinetics model within the Zero-Dimensional (0D) plasma kinetics solver, ZDPlasKin[230]. The model calculates, among other, the NO_x concentration and reveals the

underlying mechanisms. The densities of the various plasma species are obtained as a function of time by numerically solving the continuity equation for each species included in the model (Table 7) taking into account the production and loss terms by the chemical reactions (see Chapter III on Methodology). This type of modelling allows to describe an extensive chemistry without extreme computational load. An overview of the included reaction types and the full set of reactions can be found in Appendix C, pg. IX-251, and the last Appendix, pg. IX-288, respectively. This chemistry set was extensively developed and validated in previous work, related to my master thesis [216]. A discussion on the validation can be found Appendix D, pg. IX-252. After critical review of the literature, one reaction rate coefficient (k) in Appendix Table 4, pg. IX-290 (annotated in bold) was updated to a more recent k value from a reliable source.

3.2. 0D to quasi-1D model

To account for spatial variations, the time dependence of the model ("batch reactor") is transformed into a spatial dependence ("plug flow reactor") using a gas velocity profile through the Soft Jet, as explained in section 6.2.3 of the Methodology. This velocity profile is determined by CFD calculations. General information on CFD can be found in section 6.3 of the Methodology, while information on the CFD model of the Soft Jet is given in Appendix E, pg. IX-256. The plasma characteristics thus vary as a function of the distance travelled by the gas through the Soft Jet. In essence, this transforms the time-dependent 0D model into a quasi 1D model.

Table 7 Species included in the model.

N_2 species	
Neutral ground state molecules and atoms	N_2, N
Ions	N^+, N_2^+, N_3^+, N_4^+
Vibrationally excited molecules	$N_2(v_1 - v_{24})$
Electronically excited molecules or atoms	$\mathrm{N_2(A^3\Sigma_u^+)}, \mathrm{N_2\left(B^3\Pi_g\right)}, \mathrm{N_2(C^3\Pi_u)}$ $\mathrm{N_2\left(a'^1\Sigma_u^-\right)}, N(2D), N(2P)$
N_xO_y species	
$NO, N_2O, NO_2, NO_3, N_2O_5, N_2O_3, N_2O_4, NO^+, N_2O^+, NO_2^+, NO^-, N_2O^-$	
O_2 species	
Neutral ground state molecules and atoms	O_2, O_3, O
Ions	$O^-, O_2^-, O_3^-, O_4^-, O^+, O_2^+, O_4^+$
Vibrationally excited molecules	$O_2\ (v_1 - v_{15})$
Electronically excited molecules or atoms	$O\ (1D), O\ (1S), \mathrm{O_2(a^1\Delta)}$, $\mathrm{O_2(b^1\Sigma^+)}$ and a combination of three states, i.e. $\mathrm{O_2(A^3\Sigma^+, C^3\Delta, c^1\Sigma^-)}$ at a threshold energy of 4.5 eV.

3.3. Applying the quasi-1D model to the Soft Jet

Figure 20 shows a schematic description of the quasi-1D model. The species follow the blue line, through the plasma (orange), wherein the molecules experience the pulse train, into the afterglow and outside of the jet until steady state is reached. Hence, the model follows a volume element, moving through the plasma and the afterglow. The number of pulses a species experiences depends on the gas flow rate, and thus the residence time in the plasma: a longer residence time means the gas encounters more pulses (320 pulses at a gas flow rate of 0.1 L/min; 15 pulses at 2.0 L/min). The gas temperature profile and the power profile as a function of time, as experienced by the molecules, were used as input in the model to simulate the pulses, and are plotted in

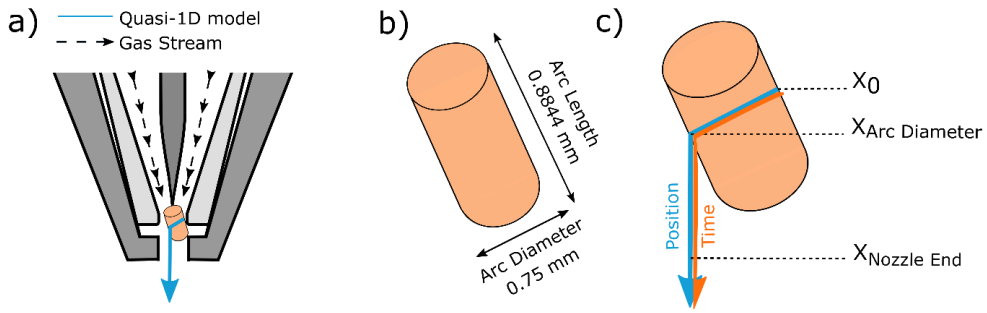

Figure 20 Schematic description of the geometry considered in the quasi-1D model. The dashed lines in (a) indicate the gas flow, the blue lines in (a, c) indicate the region of the simulation. (a) Soft Jet, with the plasma arc represented as a cylinder. (b) Dimensions of this plasma arc cylinder. (c) Schematic explanation of the quasi-1D model: the gas enters the plasma arc region at X_0 and leaves the arc at $X_{Arc\ Diameter}$, after which it continues its way through the nozzle and in the afterglow.

Figure 21a. Together they define the pulsed behaviour of the jet and the conditions inside and outside of the jet. The following sections discuss how these profiles were constructed and what they look like. Figure 21c shows the calculated electron temperature (T_e), electron density (n_e) and reduced electric field (E/N) as calculated by the model and can be rationalized as follows. At the beginning of the pulse (approx. 0 µs) a large amount of energy is deposited, resulting in a high E/N, with high energy electrons (high T_e). n_e is low, as not many electrons have been produced yet. As high energy electrons start colliding during the pulse, more electrons are freed, hence n_e increases, however, the power put into the system stays constant throughout the pulse, meaning T_e decreases as the same energy is divided amongst more electrons (0 – 0.74 µs). Right after the pulse E/N plummets as the power input is halted, on the other hand T_e is still able to rise further for about 0.5 µs, because of the electrons present and T_g is still relatively high. During the interpulse (0.74 – 6 µs) the parameters are governed by (1) the T_g which decreases throughout the interpulse

from 1750 – 330 K. Higher gas temperature, means more scattering and therefore lower electron mobility (μ_e) and vice versa. (2) The plasma conductivity, which is directly proportional to n_e and μ_e and (3) in turn determines the electric field strength ($E = \sqrt{P/\sigma}$). As an example, the increase in E/N towards the end of the interpulse takes place because the T_g drops at constant power input, which results in a higher μ_e, which increases the plasma conductivity and therefore the E/N.

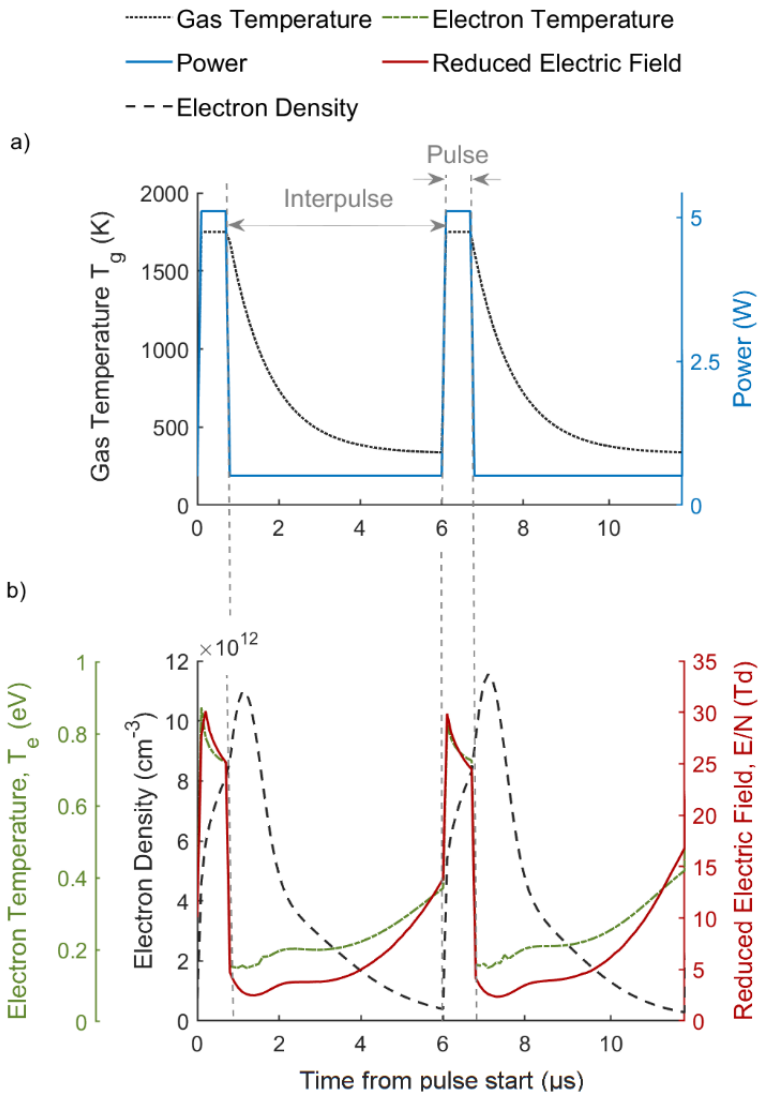

Figure 21 (a) Input plasma parameters in the model, i.e., gas temperature and power for two pulses. (b) Calculated plasma characteristics, i.e., electron temperature, electron density and reduced electric field, as calculated in the model, for air composition (80/20 N_2/O_2) and feed gas flow rate 1 L/min. The vertical grey dashed lines indicate the pulse and interpulse times.

3.3.1. Power profile – in plasma

The power deposited in the plasma, considering that the plasma is only formed during the peak (= one pulse) of the voltage waveform corresponds to 5.11 W for the duration of the pulse. This was calculated based on the V-I profiles as explained in Chapter III. In between the pulses (i.e. the so-called interpulse period), the power was set to 10% of the peak power. Although the interpulse power (density) is not known, we know that the power does not reach zero in the interpulse period. Therefore, we assumed that the interpulse power is 10% of the peak power. This assumption also significantly improves the robustness of the calculations, as going to zero power, on the small timescale that is necessary for the Soft Jet's calculations, makes the model crash, unless very small timesteps are used, resulting in much too long calculation times. Also 1, 5 and 15% were considered, balancing computational restrictions and physics, as well as to map the influence of this choice. We infer the difference is small enough to support the discussion and conclusions below.

Note that making elaborate speculations about the exact shape of the interpulse power profile would not affect the calculation results, but would only impede the model operation and interpretation. Therefore, we decided upon a constant interpulse power, that includes the known characteristics of the power, preventing that the results interpretation would become ambiguous.

3.3.2. Temperature profile – in plasma

The gas temperature profile in the plasma is based on OES measurements by a line of sight looking straight into the Soft Jet and is virtually independent of flow rate. We chose OES as the only way to measure the discharge temperature, due to geometric constraints.

OES is a well-established technique for monitoring the plasma temperature [126,172,231,232], and the spectral band used is representative for the gas temperature under the conditions of our experiments [172] (see section 2.4.1, Methodology). The temperature during the pulse, i.e. the gas temperature of the plasma arc is 1750 ± 150 K. This was found to be the same within error margin (ca. 150 K), for the entire range of flow rates investigated (0.2 – 2.0 L/min). There are a variety of possible processes, including heat exchange, arc elongation, possible arc constriction and even rotation that could result in a change of gas temperature of the plasma as the gas flow changes. Based on the OES measurements, we can conclude that these processes are not dominant, or counteract each other, and therefore do not influence the gas temperature of the plasma to a degree which would be experimentally observable. One possible explanation is as follows: the constant gas temperature is representative of the fact that there are a number of mechanisms of gas heating at play. Indeed, as the flow rate increases, the arc compresses but also elongates, resulting in a constant energy deposition in the arc. The arc elongation does not significantly increase the voltage due to the low power dissipation and low resistivity of the discharge. Note, the change in flow could result in other more elaborate changes in arc dynamics, such as rotation, which influences the heat transfer as well. The full detailed study of the arc dynamics would require either full-scale 3D modelling or direct optical access to the arc region, which is not possible in the current configuration of the plasma reactor. To evaluate the sensitivity of the modelling results to changes in the input temperature, the upper (1900 K) and lower (1600 K) limit were ran as well in the 0D model. There

was no significant influence on the main mechanisms within this temperature range.

As the interpulse gas temperature could not be measured directly due to the small timescale of the pulses, the gas temperature during the interpulse period was set to an exponential decay to 330 K, in accordance with the average gas temperature measured by Rayleigh scattering in the afterglow (see Chapter III, section 3). This approximation was found valid through a sensitivity test described in the Appendix section F, pg. IX-259.

3.3.3. Power and temperature profile – outside plasma

The plasma zone with the pulse train is followed by an afterglow, i.e. outside of the jet nozzle, where post-plasma reactions can take place. In this region the power was set to zero and the gas temperature profile for each flow rate was calculated based on Rayleigh-gas temperature measurements by line of sight perpendicular to the Soft Jet (See Chapter III, section 3.2). In reality, the temperature decrease in the afterglow is flow rate dependent and likely due to the change of heat transfer at higher flow rates, which is governed by the interplay between elongation and restriction of the arc. Indeed, as the flow rate increases, the afterglow temperature decreases. In the model, this is approximated by one temperature profile, based on the available experimental data. The full approach is explained in Appendix G, pg. IX-260.

Note that the methods used for temperature measurements of the plasma arc (OES) and the afterglow (Rayleigh scattering) are complementary: due to geometrical constraints, Rayleigh scattering cannot be applied to study the arc, while OES cannot be used to study

the gas temperature in the afterglow due to very low (almost negligible) emission of the afterglow.

Due to the short pulse duration, the time-averaged temperature of the jet never exceeds 390 K. This means that even though on a microscopic the temperature drops from 1750 K to room temperature over 10 mm, on a macroscopic scale this temperature drop is due to the cooling through heat exchange with surrounding cooler gas and is not as substantial (i.e., approximately from 390 – 330 K with T_{room} = 308 K). This temperature drop agrees well with the literature reports on this phenomenon[155,233].

The thermal diagnostics provide us sufficient information on the temperature behaviour in the plasma and in the afterglow, allowing to model a large chemistry set without solving for the heat balance in the model itself. This is a justified but considerate simplification to gain more insight into the underlying chemistry, while keeping the computational resources feasible. Although not needed in the Quasi-1D model, a full heat balance would provide interesting insight. However, it is a topic of a separate study, outside the scope of this thesis.

3.3.4. Treatment fraction

Due to the pulsing nature of the Soft Jet and its geometry, only a fraction of the gas is treated by plasma. This is included in the model, which considers only a fraction of the gas being plasma-treated by a pulse train, while the other molecules do not pass through the actual plasma zone. In practice, we have accounted for this by multiplying the calculated reactive plasma species densities by the effective treatment fraction of 3.0%, as estimated from the experiments. This estimation

was made as follows:

There are three options for the gas molecules moving through the Soft Jet. These options determine whether a gas molecule is plasma-treated or not, i.e. what is the effective treatment fraction:

(1) The gas molecule moves through the plasma zone when plasma is on, i.e. it is plasma-treated during the pulse train. This case applies to approximately 14.9% of the molecules, based on the duty cycle of the pulse train (i.e., 26.3/(149.9 + 26.3)), see Chapter III, section 2. Note, this duty cycle should not be mistaken with the duty cycle of the entire system (1.9%), as explained in the Methodology.

(2) The remainder of the gas molecules move through the plasma zone untreated (pulse-off time; ca. 85.1% calculated from 149.9/(149.9 + 26.3)).

(3) Besides the duty cycle of the pulse train, also the physical dimensions and shape of the ignited plasma play a role in determining the effective treatment fraction. If the gas molecule moves alongside the plasma, it cannot be plasma-treated, regardless of the plasma ignition state. ICCD camera images of the plasma, discussed in Chapter III, section 2.2, show what fraction of the cavity is taken up by the plasma. Based on this, we estimated that ca. 20% of the gas moving through the cavity during plasma-on time (case 1) is actually plasma-treated. From these 2D images of a 3D arc, it is only possible to estimate the fraction. However, this estimation does not influence the underlying mechanisms or other insights gained from the model, as it only decreases the plasma-treated fraction, not the way in which the gas is treated.

The effective treatment fraction is calculated by multiplying the duty cycle of the pulse train (case 1) with the fraction of the cavity that is taken up by plasma (case 3) and amounts to 3.0% (20% x 14.9%).

In practice, only case (1) is modelled, i.e. molecules moving through the Soft Jet when the plasma is on. Afterwards, the calculated densities of the various reactive plasma species (i.e., electrons, various ions, radicals, excited molecules) are multiplied by the effective treatment fraction (3.0%) to obtain the effective calculated species densities. Indeed, the remainder of the molecules move through untreated by the plasma, hence they are not converted into reactive plasma species.

4. Results and discussion

4.1. NO_x production and energy consumption

The Soft Jet produces NO and NO_2 at every flow rate investigated (0.4 – 2.0 L/min). As the flow rate increases, the NO concentration drops, due to the shorter residence time of the gas in the plasma (Figure 22; dotted green curve). The NO_2 concentration remains approximately constant, but is considerably lower than the NO concentration at all flow rates. It is known from previous studies of NO_x production in plasma that NO_2 is formed from NO[62,216]. As the equilibrium between NO and NO_2 is reached more quickly than the time needed to initially form NO, the NO/NO_2 ratio is lower at high flow rates (short residence time) compared to low flow rates (long residence time).

The FTIR spectra confirm there is no production of O_3, N_2O_5, N_2O_3, N_2O and NO_3 at the investigated flow rates. In other words, we see a good selectivity towards NO/NO_2, which can be used directly for fertiliser and base chemical production.

The minimum EC in the Soft Jet of 0.42 ± 0.03 MJ/(mol N) is reached

at 1.5 L/min. Indeed, because the concentration stays constant between 1.2 and 1.5 L/min, even though the residence time is shorter at higher flow rates, a minimum in the EC is reached (Figure 22; orange curve), corresponding to a maximum NO_x production rate of 28.4 ± 0.4 mg/h (See Appendix H, pg. IX-263, for the production rates at all gas feed flow rates). To the best of our knowledge, such a low EC – close to the theoretical minimum EC of 0.2 MJ/(mol N) (cf. Introduction) – has never been reported up to now in atmospheric-pressure plasmas. In the next section, we discuss these results in the framework of the state of the art.

The calculated NO_x concentration (Figure 22; full black curve) as a function of flow rate is in good agreement with the experimental data (dotted black curve), both in trend and absolute values. The calculated NO_2 concentration is underestimated (< 1 ppm at all investigated flow rates), however rather than tuning the reaction rate coefficients to account for this underestimation, we prefer using only reliable scientific works that investigated reaction rate coefficients. Indeed, we do not know what exact (combination of) reaction rate coefficients might be slightly over- or underestimated, and tuning the rate constants in order to reach a better agreement would therefore not have a strong scientific basis. In any case, we only compare the total NO_x concentration, because the oxidation of NO into NO_2 can still occur after the plasma or in the gas tubing to the FTIR, which is not included in the model.

Finally, just like in the experiments, there is no production of O_3, N_2O_5, N_2O_3, N_2O and NO_3 in the model. This means our model can predict the chemistry of the Soft Jet fairly well, in a wide range of flow rates, and therefore can be used to gain a deeper understanding of the mechanisms that lie at the base of this very energy-efficient NO_x

production (see section 4.3 *Mechanisms of Energy-efficient NO_x Production in Pulsed Plasma*).

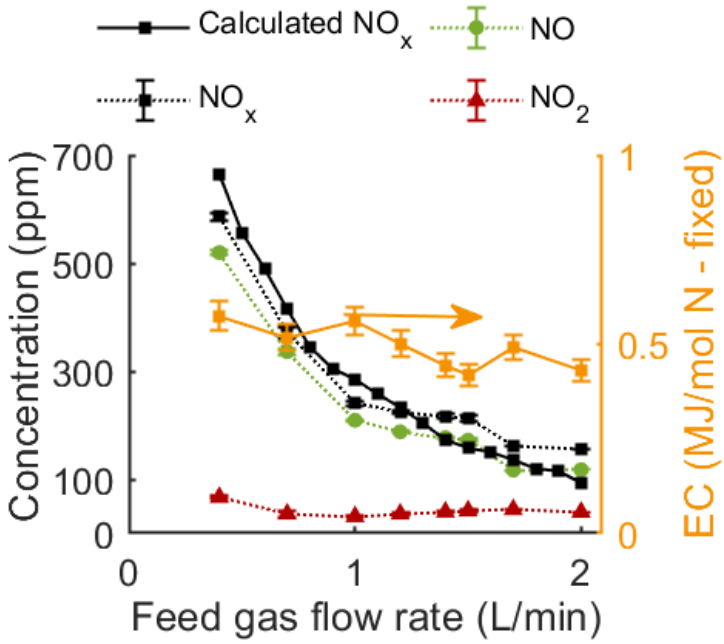

Figure 22 NO, NO_2 and total NO_x (dashed lines) concentration as measured by FTIR, calculated total NO_x concentration (black; full line) and measured EC (orange; right y-axis) as a function of the feed gas flow rate. Error bars are plotted but are barely visible at most flow rates.

4.2. Comparison with the state of the art

As mentioned above, to our knowledge the EC obtained in our Soft Jet is by far the lowest value reported in literature for plasma-based NO_x production at atmospheric pressure. The NO_x or NO concentrations and associated EC reported in various plasma types in literature are summarised and discussed in full-length in section 5.2 of the Thesis Introduction, specifically Table 1. The best performing setups to date reach EC's around 2 MJ/mol (Table 1, entries 20 - 25), while the Soft Jet shows an EC ¼ of that.

The very low EC reached with our Soft Jet shows that values close to

the theoretical minimum EC for plasma-based NO_x production at atmospheric pressure can be achieved in practice. Although the Soft Jet as is cannot be used in most applied settings directly, because of the rather low NO_x concentration achieved, the knowledge about the low EC close to the theoretical minimum is highly beneficial, as properties of the Soft Jet that lie at the base of this low EC can be used to inform further research. As mentioned in the Introduction of this thesis, around the time of publication another work was published by Britun et al. in a spark type plasma, achieving near-the-limit energy costs as well, effectively confirming our results.

4.3. Mechanisms of energy-efficient NO_x production in pulsed plasma

In literature, the positive influence of pulsed plasma in N_2 fixation (either due to arc rotation[62,80] or by pulsing the power[58], like the Soft Jet) [38,70,75,234] has been reported, and to a certain extent their physical characteristics have been studied[228,235–237]. However, because the reported plasma reactors are so different in performance and type, isolating the function of pulsing and determining whether or not and how significantly it enhances the energy efficiency of NO_x formation is challenging. Therefore, the knowledge of pulse-driven chemistry is very limited[238,239]. Our model allows us to elucidate the underlying mechanisms for our pulsed plasma source, which will provide us general insight in the role of pulsing for reaching the most energy-efficient plasma-based NO_x formation.

4.3.1. Conditions for energy-efficient NO_x production

To understand the benefits of pulsing, we remind the reader, in short, about the difference between thermal and non-thermal plasmas. In

thermal plasmas, the heavy species (gas molecules, radicals,…) and electrons are in thermal equilibrium (i.e., same temperature), and a large fraction of the input energy (plasma power) is lost to gas heating. The high gas temperature ($T_g \sim 10^4$ K) not only increases the EC, but can also impede effective gas conversion by destroying the products formed[15]. In “warm“ (or quasi-thermal) plasmas, the electron temperature (around 1 eV) is higher than the temperature of the heavy species, but the latter still can reach several thousands of Kelvin[37]. This electron temperature is ideal for efficient vibrational excitation of N_2 molecules[41,44], which is the most efficient path for dissociation and for energy-efficient NO_x formation through the vibrationally-enhanced Zeldovich mechanism (Introduction, section 5.2.1). On the other hand, the relatively high gas temperature reduces the vibrational population by vibrational-translational (VT) relaxation, i.e., collisions of the vibrational levels with ground state molecules, causing further gas heating.[58,80] Finally, in non-thermal plasmas, the gas temperature remains near room temperature, but the electron temperature is several eV, so the energy put into the plasma is used for gas conversion instead of gas heating[44]. However, the electron temperature is typically too high for efficient vibrational excitation of N_2 molecules.

The holy grail in energy-efficient plasma-based NO_x production is thus to find plasma conditions which generate an electron temperature around 1 eV. This typically corresponds to a reduced electric field (i.e., ratio of electric field over gas number density; E/N) up to 50 Td. These conditions are most suitable for N_2 vibrational excitation (Appendix I, pg. IX-264). At the same time, the gas temperature should be kept low, to maintain a high vibrational population of the N_2 molecules. Such

conditions are more easily achieved at low pressures, where collisions (including VT relaxation) are less prominent (see also the best values in Table 1 in the Introduction of this thesis, for low-pressure plasmas). However, by pulsing the plasma power[58,66,227,228], the same conditions may be reached at higher (e.g., atmospheric) pressure, because the time during the pulses is too short for considerable gas heating[58]. This eliminates the need for low-pressure equipment, which significantly reduces the process cost[44].

Due to its pulsing regime, the Soft Jet obviously meets the requirements of this holy grail for energy-efficient NO_x production, exactly by the combination of high vibrational excitation and limited gas temperature (strong VT non-equilibrium; see Introduction, section 4.4). This is clearly revealed from the model. Indeed, the calculated reduced electric field is around 30 Td, resulting in an electron temperature around 0.7 – 1.0 eV in the pulses, for the various conditions investigated (see Figure 21b for the condition of 1 L/min feed gas flow rate). As mentioned above, these values of reduced electric field and electron temperature are ideal for transferring most of the electron energy to N_2 vibrational excitation[41]. In addition, the electron number density is around 10^{13} cm^{-3} during the pulses (see also Figure 21a), which is fairly high, and thus also beneficial for strong vibrational excitation.

Finally, the gas temperature, while being high (1750 K) during the pulses, reduces to near room temperature in between the pulses (interpulse period; see Figure 21a), and the time for VT relaxation during the pulses is too short for significant vibrational depopulation. Hence, a strong VT non-equilibrium is reached, important for splitting the strong triple bond of N_2: the vibrationally excited N_2 molecules can

more easily overcome the energy barrier of NO_x formation through the non-thermal Zeldovich mechanism (R IV.1 and R IV.2, further below), as discussed above. The degree of N_2 vibrational excitation will be discussed in next section.

4.3.2. Influence of pulsing on the vibrational excitation of N_2 and O_2

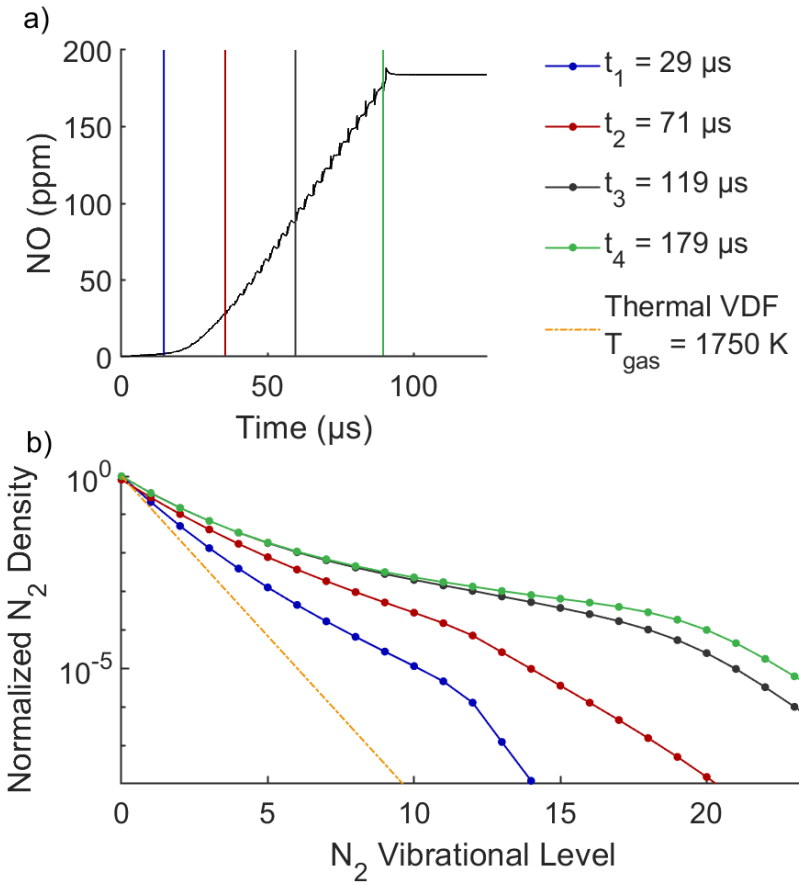

Figure 23 (a) Calculated NO concentration (black curve) as a function of time, during its residence time in the plasma (at 1 L/min), encountering a train of pulses, and (b) calculated VDF of N_2 taken in the middle of each pulse, for four different time points, as indicated by the vertical coloured lines in (a). The thermal VDF at 1750 K is also plotted.

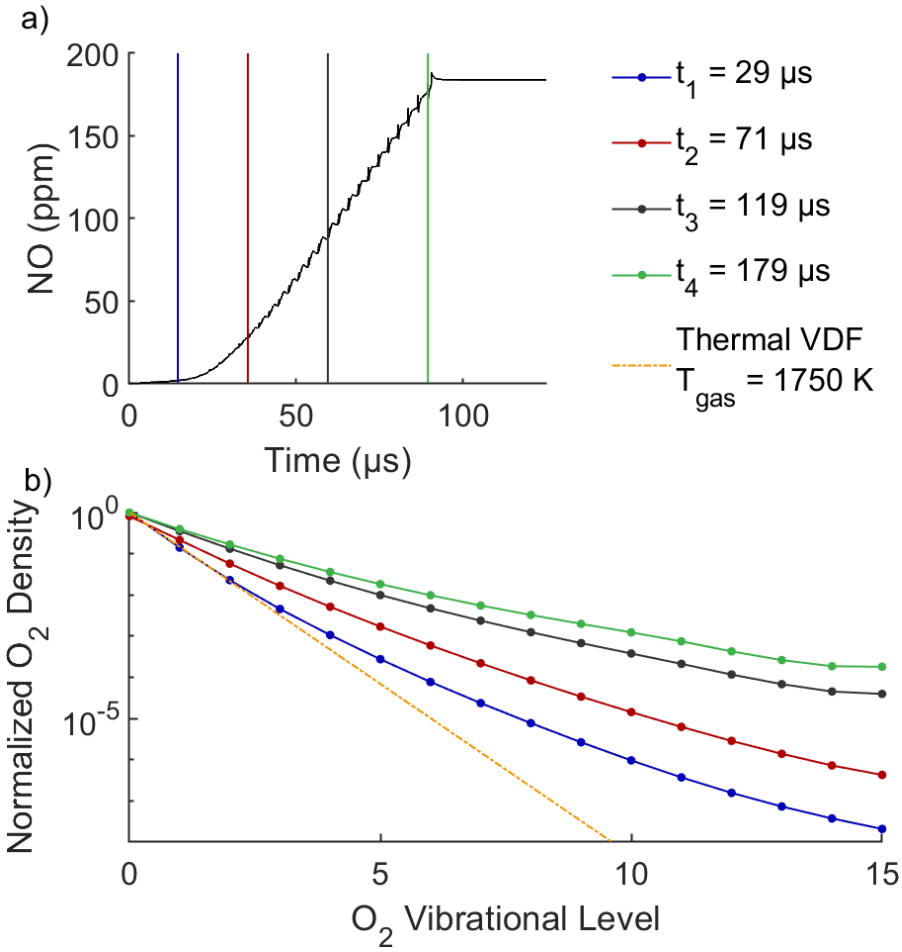

Figure 24 (a) Calculated NO concentration (black curve) as a function of time, during its residence time in the plasma (at 1 L/min), encountering a train of pulses, and (b) calculated VDF of O_2 taken in the middle of each pulse, for four different time points, as indicated by the vertical coloured lines in (a). The thermal VDF at 1750 K is also plotted.

Figure 23a shows the calculated NO concentration as a function of time, as formed during the train of pulses, within the gas residence time in the plasma (Figure 23a; black curve), as well as the calculated vibrational distribution function (VDF) of N_2 (Figure 23b) at the time points indicated in Figure 23a. The VDF shows how the energy is distributed among the vibrationally excited levels of a molecule, by

plotting the relative density of each level (normalised to the ground state). An introduction to VDFs was given in section 4.6 of the Introduction.

In case of VT equilibrium, the VDF exhibits a Boltzmann distribution, dictated by the gas temperature (orange dashed line in Figure 23b). The calculated N_2 VDF in the Soft Jet, however, clearly deviates from the thermal Boltzmann distribution. As time increases, the VDF builds up to higher populations of the higher vibrational levels (see plateau in Figure 23b), significantly above the Boltzmann distribution, i.e. a strong VT non-equilibrium is reached. Inside the pulses, due to the relatively high gas temperatures, VT relaxation will also occur to some extent, but the rate of VT relaxation drops drastically when the temperature drops after the pulses[217]. This allows for a longer lifetime of the vibrationally excited states and hence a build-up of the VT non-equilibrium (or plateau formation in the VDF of N_2) over the time of multiple pulses, as clearly illustrated in Figure 23b.

A reminder: It is generally known that the most energy-efficient pathway to NO_x is via the non-thermal Zeldovich mechanism promoted by vibrational excitation[37,41,44,59,62,69], as was discussed in the Introduction of this thesis. (Reactions R IV.1 and R IV.2; where g and v stand for the ground state and the vibrationally excited states of the molecule, respectively. The mechanism inherently includes the thermal Zeldovich mechanism.)

$$O_2(v,g) + N \rightarrow NO + O \qquad \text{R IV.1}$$

$$N_2(v,g) + O \rightarrow NO + N \qquad \text{R IV.2}$$

Our model reveals that in the Soft Jet on average >99% of NO is formed through vibrationally excited N_2. However, not every vibrational level contributes equally. The exact contribution of each level depends on (i)

the energy level (i.e., the higher the level, the more the activation energy for the Zeldovich mechanism is reduced), and (ii) the population density of that level (and as is clear from Figure 23b, the lower vibrational levels have a higher population density). Figure 25 shows the contribution of the various N_2 vibrational levels to the rate of R IV.1 and R IV.2, for different times in and after one pulse. N_2(v12) has the highest contribution, both during the pulse and the interpulse time. Indeed, the N_2(v12) population is sufficiently high (see plateau in the VDF of N_2) and the activation energy is reduced to zero. The densities of the vibrational levels above v12 are (significantly) lower, while the lower N_2(v) levels require a higher activation energy for R IV.1 and R IV.2. Note that pulsing is mainly beneficial for increasing the population of N_2(v). Indeed, the VT relaxation rate constant of O_2 is higher than for N_2 at 300 K ($k_{VT\ O2} = 5.10^{-18}$ $cm^3.s^{-1}$ vs $k_{VT\ N2} = 10^{-18} – 10^{-19}$ $cm^3.s^{-1}$)[55] and the reaction rate coefficient for electron impact vibrational excitation of O_2 is lower than for N_2 above electron temperatures of 0.6 eV[41,55]. This results in a Boltzmann-distributed (though elevated) VDF for O_2(v) (Figure 24). A lower degree of O_2(v) is, however, not a problem in plasma-based NO_x formation, as the production of O atoms is not the limiting process. Indeed, N_2 has a much higher dissociation energy compared to O_2 (9.79 eV vs 5.15 eV).

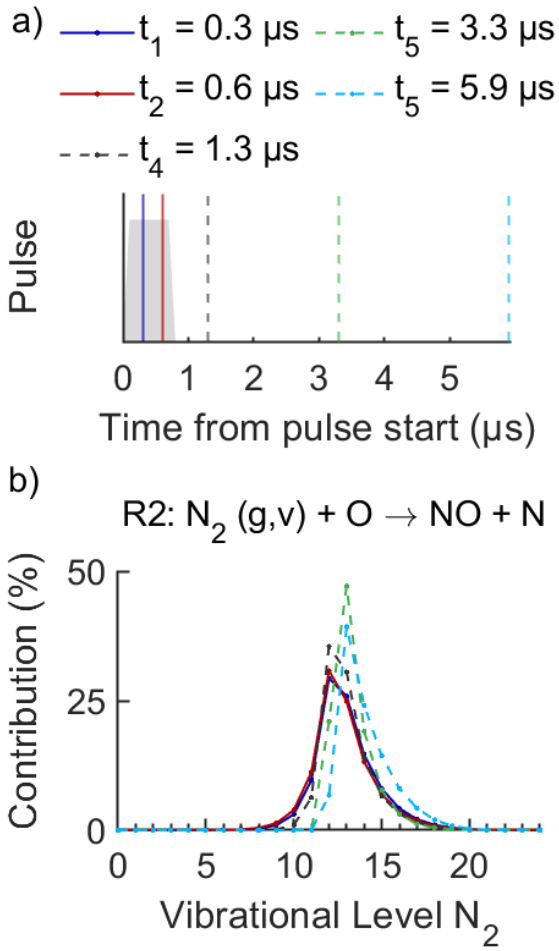

Figure 25 Contribution of each N_2 vibrational level to the rate of R2 (b), for different time points specified in (a), both during the pulse (solid lines) and during the interpulse time (dashed lines).

Our model reveals that the density of O atoms is at least of the same order of magnitude as the density of N atoms (see next section). We should therefore focus especially on the non-equilibrium in the VDF of N_2 instead of O_2. Interesting to note, even though only a fraction of the gas passes through the arc, this is enough to produce an adequate amount of vibrational population for the formation of NO_x. The model shows how pulsing enables such high vibrational population. A

sufficiently high vibrational population (be it Boltzmann or non-Boltzmann distributed), combined with a low treatment fraction is not unique to the Soft Jet, a number of other plasma setups produce a significant amount of NO_x while working with a small treatment fraction[41,62,216].

4.4. NO_x formation and loss mechanisms during pulse and interpulse

The most important formation and loss processes of NO (including oxidation to NO_2), as revealed by our model, are listed in Table 8. Their calculated reaction rates are plotted and discussed in detail in the last Appendix, pg. IX-288. Here, we present two sequential pulse-interpulse cycles, as a representative case study to explain the main reaction mechanisms in the pulses and during the interpulse times; depicted in Figure 26. Panel (a) illustrates the reaction analysis, i.e., the importance of the two steps of the (non-thermal) Zeldovich mechanism (N1 and N2), as a function of time during the pulse and interpulse period. Green represents the forward reaction (net NO production), while black corresponds to the back reaction (net NO loss). Panel (b) shows the corresponding densities of NO, NO_2, N and O in the same time-scale, as calculated in the model.

Table 8 Main reactions for the formation and loss (F,L) of NO. The net reactions (N), as they occur for either NO formation or loss (including oxidation to NO_2), are denoted in grey. Note that N1, N2 and N3 are net formation reactions for NO, while N4 is a net loss reaction.

	Reaction	**Process**	
NO Formation	$N + O_2(g,v) \rightarrow NO + O$	F1	
	$O + N_2(g,v) \rightarrow NO + N$	F2	
NO Loss	$NO + O \rightarrow O_2 + N$	L1	
	$NO + N \rightarrow N_2 + O$	L2	
NO ↔ NO_2	$NO_2 + O \rightarrow NO + O_2$	F3	
	$NO + O_2 \rightarrow NO_2 + O$	L3	
	$NO_2 + M \rightarrow NO + O + M$	F4	
	$NO + O + M \rightarrow NO_2 + M$	L4	
Net reactions	$N + O_2(g,v) \rightleftharpoons NO + O$	N1	= F1 – L1
	$O + N_2(g,v) \rightleftharpoons NO + N$	N2	= F2 – L2
	$NO_2 + O \rightleftharpoons NO + O_2$	N3	= L3– F3
	$NO + O + M \rightleftharpoons NO_2 + M$	N4	= F4 – L4

(g) and (v) denote the molecules in the ground state vs vibrational levels, respectively. Note that F2 can also occur from electronically excited N_2, but our model reveals that its contribution is only significant at early times (7 - 11 % until ca. 35 µs), afterwards its contribution drops to zero (10^{-30} %). M stands for any neutral molecule.

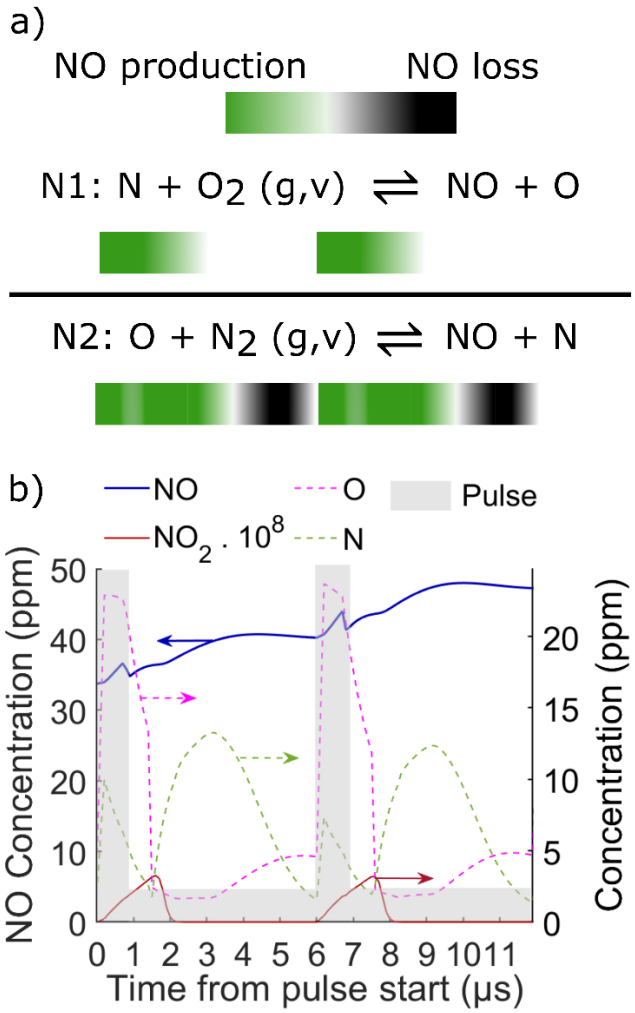

Figure 26 (a) Importance of N1 and N2 as a function of time during two pulses and interpulse times, as indicated by a gradient scale (green = forward reaction, i.e., net NO production; black = backward reaction, i.e., net NO loss; white = no net production or loss). A darker shade indicates a higher net rate, both in the forward or backward direction. (b) Corresponding concentration of NO, NO_2, N and O for the same two pulses. The NO concentration is shown on the left y-axis, while the other species concentrations are shown on the right y-axis. Note, the NO_2 concentration has been multiplied by 10^8 for better visibility.

Our model reveals that the non-thermal Zeldovich mechanism promoted by vibrational excitation is the main mechanism for NO formation (N1 and N2; see Table 8); see detailed analysis in Appendix J, pg. IX-265. It should be noted that the reactions with highest rate, overall, are the oxidation of NO to NO_2 (N3 in Table 8) and vice versa (N4), which produce a limited amount of NO_2 (< 1 ppm at all investigated flow rates). However, they do not contribute to the initial NO_x formation, and are therefore not shown in Figure 26.

N1 is mainly important during the pulses, due to the high gas temperature. Its rate rises during successive pulses because more N atoms become available. Thanks to the strong VT non-equilibrium (see Figure 23b), N_2 dissociation is not the limiting step. Indeed, Figure 25 shows that the N and O concentrations are of the same order of magnitude.

After the pulses, the rate of N1 gradually drops to zero due to the strong temperature drop, which reduces the reaction rate coefficient (k) with a factor 10^6 (see Appendix K, pg. IX-268). Note, however, that the rate of N1 does not drop below zero (which would correspond to NO loss) during the interpulse time. This is an interesting aspect that will be discussed in more detail in the next section.

The rate of N2 shows roughly the same trend as for N1 during the pulses, due to the high gas temperature. After the pulse, however, the rate rises further, even though the rate coefficient drops due to the lower temperature (see Appendix K, pg. IX-268). This is because $N_2(v)$ builds up a strong VT non-equilibrium during the interpulse time, and additionally an abundance of O atoms is produced during and right after the pulse (through N1; see dashed pink curve in Figure 25b). Subsequently, the rate of N2 drops below zero, corresponding to net

NO loss. Species availability is the determining factor at this stage. Indeed, during the second half of the interpulse period, less O atoms are available due to the drop in the rate of N1, and the N atoms are now preferably used for the back reaction of N2. Important to note is that the negative rate of N2 never exceeds the positive rate (i.e., production of NO). Hence, while the NO production slows down and the NO concentration drops slightly near the end of the interpulse time, the NO concentration at the end of the pulse-interpulse cycle is still higher than in the beginning of the pulse, demonstrating that the NO concentration gradually builds up as a function of time, as is also clear from Figure 23a above.

In general, we can conclude that the two steps of the non-thermal Zeldovich mechanisms dominate the NO production. They occur at high rates during the pulses, and gradually become negligible (for N1) or occur in the backward direction (for N2) during the interpulse period, but overall, they lead to a steady rise in NO concentration as a function of time.

4.5. How pulsing assists NF at low energy consumption

The next sections discuss the specific lessons learned from the above reaction analysis, that can be applied to plasma-based N_2 fixation more in general. Our Soft Jet plasma obviously results in very low EC, and this is clearly attributed to the pulsing.

4.5.1. Exploiting the VT non-equilibrium of N_2

The pulse train builds up the $N_2(v)$ population during the pulses via electron impact vibrational excitation and vibrational-vibrational (VV) exchanges between vibrationally excited N_2 and O_2 molecules. At the

same time, the temperature drop in between the pulses prevents two things: (1) It prevents loss of vibrational energy caused by VT relaxation. Indeed, low temperature plasma-based chemistry aims to minimise energy losses through gas heating (hence through VT relaxation) to maximise the selective input of energy into molecules for chemical reaction through for example vibrational excitation. (2) It prevents N_2-O_2 VV exchanges. The latter was found to be a limiting mechanism for energy-efficient NO_x production in a gliding arc plasmatron[216]. Indeed, because O_2-O_2 VT relaxation is faster than N_2-N_2 VT relaxation[217], the N_2-O_2 VV exchanges connect the vibrational energy of N_2 to a sink of O_2-O_2 VT relaxation. A more detailed explanation of this can be found in Appendix L, pg. IX-269. However, in our Soft Jet plasma, due to the temperature drop after the pulses, the O_2-O_2 VT relaxation rate drops and this vibrational sink is limited, hence decreasing the loss of energy into heat that would be caused by VT relaxation.

If power pulsing is properly adapted in the design of other plasma sources, their EC could also be minimised. In order to use pulsing in the most optimal way, a balance has to be found between pulse-on and pulse-off times and the associated treatment fraction. Indeed, when the pulse is off for a longer time to ensure cooling, the gas can obviously not be treated and will therefore not be converted. The pulse characteristics are clearly the underlying reason for the low EC of the Soft Jet, but the limited treatment fraction is also why the NO_x concentration is low compared to other plasma types. Modelling can help in this regard: by changing the pulse characteristics, an optimum between both should be found.

4.5.2. Suppressing the back reactions of the Zeldovich mechanism

Next to promoting the N_2 vibrational population, the other main challenge in plasma-based NO_x formation is limiting the back reactions of the Zeldovich mechanism (L1 and L2 in Table 8) to prevent NO_x destruction. In continuous plasmas, which operate at constant temperature, this is not straightforward, because both the back and forward reactions are promoted at higher temperatures. However, their temperature dependence is not exactly the same, and we can exploit this in pulsed plasmas, due to the temperature drop in between the pulses. The rate coefficients of the Zeldovich reactions are plotted as a function of the gas temperature in Appendix K, pg. IX-268.

Another point of attention, specifically for the Zeldovich mechanism, is that both forward reactions (F1 and F2) and their back reactions (L1 and L2) compete for the same species. For instance, the O atoms are used for NO formation (F2) and for NO loss (L1). By pulsing the plasma, the temperature dependence of the corresponding reaction rate coefficients can be used to selectively limit the loss reaction (L1). Indeed, the rate coefficients of both the forward and back reaction of N1 increase with temperature, but the temperature dependence for L1 is much more pronounced (see Appendix K, pg. IX-268). Therefore, the drop in temperature in the interpulse period essentially limits the back reaction. In addition, while the rate coefficients of both L1 and F2 are more temperature-dependent than for L2 and F1 (Appendix Figure 13, Appendix K, pg. IX-268), the rate of F2 is significantly enhanced by the rise in $N_2(v)$ population during the interpulse period, and therefore the O atoms are preferable consumed in F2 (NO production) as opposed to L1 (NO loss).

In the case of N2, suppressing the back reaction (L2) is more challenging, as its rate coefficient is temperature-independent and relatively high compared to the other reactions at play in the Zeldovich mechanism (Appendix K, pg. IX-268). The rate coefficient of the forward reaction would only be greater than that of the back reaction above 13200 K. This means that a drop in temperature does not favour one reaction over the other, but instead, it is more a matter of reactive species availability (O and N_2(g,v)). Thus, based only on the rate coefficients, N2 would benefit from a high temperature (and not from the temperature drop after the pulses), but it is also strongly promoted by a high N_2(v) population, which is more pronounced at lower temperature. Hence, a balance between these factors needs to be found to fully exploit pulsing in order to maximise energy-efficient NO_x production in plasma.

4.6. Economic viability of plasma-based NO_x production

When discussing plasma-based N_2 fixation, the comparison with the HB process is commonly made, based on production rate and EC of NF species. However, the inherent differences between the HB process and plasma-based NF are substantial, and plasma-based processes offer other advantages, because they are electricity-based, flexible, and they can operate on a small scale for decentralisation, as explained in the Introduction of this thesis. Therefore, a direct comparison with the HB process regarding production rate and EC is not a great indicator of whether or not plasma-based NF is economically viable[44]. To answer the latter, Rouwenhorst et al. performed a techno-economic analysis (TEA) on plasma-based NO_x

production,[37] and Anastasopoulou et al. carried out a Life Cycle Assessment (LCA) of plasma-based NO production[240]. The TEA was benchmarked against a small scale electrolysis-based HB process followed by an Ostwald process (100 t HNO_3/day) [37]. The LCA considers the “cradle to factory gate”, i.e. starting from raw materials up to HNO_3 production. It is benchmarked against the conventional HNO_3 process, including the steam reforming [240].

The TEA concluded that plasma-based NO_x production for HNO_3 synthesis will become a highly competitive alternative to electrolysis-based HB combined with the Ostwald process, if the EC can be reduced to 0.7 MJ/(mol N)[37]. This is mainly due to the low capital expenditure of plasma-based conversions[37]. The lowest theoretical EC limit of plasma-based NO_x production is 0.2 MJ/(mol N),[229] while the EC of NH_3 synthesis via the Haber-Bosch process is at least two times higher (0.48 MJ/(mol N))[44]. This potential is a large driving force in plasma-based NO_x production research[229]. However, in practice such a low EC had not yet been reported in atmospheric-pressure plasmas, before the work presented in this Chapter.

Likewise, the LCA encourages plasma-based NF research by stating that plasma demonstrates strong capabilities in becoming a viable alternative to the current HNO_3 production process, provided that certain optimization steps are considered, such as the use of renewable energy and at least either 10% NO yield, tail gas recycle or energy recovery, as well as a combination of those methods[240]. When assumed the process is electricity-based, HB is below the nitric acid market value at production capacities above 200 t HNO_3, while plasma-based processes are already commercially viable at 10 t HNO_3 and above. This means, for example, that in areas where the production

cost is high, such as remote locations, electricity-driven processes can become favourable at higher electricity cost.

This Chapter demonstrates that plasma-based NO_x production can meet the first prerequisite, based on the TEA, namely an EC below 0.7 MJ/(mol N). By combining knowledge from a pulsed plasma source, like the Soft Jet, with other well-performing atmospheric-pressure plasma setups, such as a Rotating Gliding Arc plasma (5.4 % NO_x; 2.5 MJ/(mol N); Table 1, entry 23)[62], we believe it is attainable to meet the second prerequisite, based on the LCA, regarding the NO_x yield as well.

5. Conclusions

In this Chapter, we presented a pulsed power plasma source (Soft Jet) operating at atmospheric-pressure with dry air as feed gas, for NO_x production at a very low energy consumption (EC) of 0.42 ± 0.03 MJ/(mol N). This is the lowest EC reported for plasma-based NO_x production at atmospheric pressure to date.

To gain insight into the underlying mechanisms of this record-low EC, we developed a chemical kinetics model, which provides very good agreement with the experiments at the full range of flow rates (0.4 – 2.0 L/min) and can thus be used for reaction analysis. The model pinpoints the specific aspects of pulsed plasma power, that allow for such a low EC.

Our reaction analysis indeed illustrates that pulsing is the key for energy-efficient plasma-based NO_x production, by the drop in gas temperature in between the pulses, which affects the rates of the forward and back reactions of the Zeldovich mechanism in a delicate

way, and also enhances the N_2 vibrational population, crucial for the (most efficient) non-thermal Zeldovich mechanism.

The exact pulse and interpulse times appear to be critical for finding a balance between the drop in temperature and the fraction of gas treated by the plasma (pulses). In the Soft Jet, this ratio of pulse and interpulse times appears to be nearly ideal for energy-efficient NO_x formation, as evidenced by the unprecedented low EC, as compared to other studies in literature. On the other hand, the NO_x concentrations obtained are very low (0.02 %), attributed to a limited fraction of gas passing through the plasma, and this might also be improved by a somewhat shorter interpulse period.

While this Soft Jet plasma is thus not suitable for practical applications due to the low NO_x production, the concepts revealed in our study will be very useful for other plasma devices, which exhibit a larger fraction of gas passing through the plasma, and which can hopefully be further improved by a careful selection of the pulse and interpulse times, based on the insights obtained in our study.

In terms of economic viability, we demonstrated that it is possible with pulsed plasma to almost reach the theoretical minimum EC of plasma-based NO_x formation, and to meet the required EC (of 0.7 MJ/(mol N)) for plasmas to be competitive with the electrolysis-based HB and Ostwald process for HNO_3 synthesis, as recently defined in a TEA by Rouwenhorst et al.[37].

Additionally, when the insights from our work about the influence of pulsed plasma on the EC can be combined with other well-performing atmospheric-pressure plasma setups, such as a Rotating Gliding Arc plasma (5.4 % NO_x; 2.5 MJ/(mol N))[62], we believe it is realistic to meet

the second prerequisite (based on a LCA), regarding the NO_x yield as well.

Sustainable generation of *reactive* nitrogen (like NO_x) is paramount and plasma-based processes are promising in this field, as they are electricity-driven, and can easily be switched on-off, i.e. they can easily be coupled to fluctuating renewable electricity, providing grid stabilisation and peak shaving, and they are suitable for small-scale decentralised fertiliser production. In this Chapter, we showed that pulsed plasmas can be the key for such energy-efficient sustainable fertiliser and base chemical production.

Now that we have gained a deeper understanding of the chemistry taking place in dry air, we are ready to move towards adding H_2O in the next Chapter. We add H_2O both as a liquid and as a vapor, in order to elucidate both of their roles in the formation of NF species.

6. Use of the Soft Jet in other works: Plasma Nitrogen Oxidation Coupled with Catalytic Reduction to Ammonia (PNOCRA)

In a collaboration with ir. Lander Hollevoet and prof. dr. ir. Johan Martens of the Center for Surface Chemistry and Catalysis: Characterization and Application Team at KULeuven, the results in this Chapter were used as the NO_x source in a joint paper, of which I am second author, titled “Energy-efficient small-scale ammonia synthesis process with plasma-enabled nitrogen oxidation and catalytic reduction of absorbed NO_x”[102]. A so-called PNOCRA (Plasma-NO_x and catalytic reduction to ammonia) system was developed to convert air into NH_3 via a combination of plasma and catalytic reduction using a lean NO_x trap (LNT). The total energy cost of the PNOCRA process is ca. 2.1 MJ

mol/NH_3, making PNOCRA the least energy consuming small-scale ammonia production process at mild conditions demonstrated so far.

V. NITROGEN FIXATION WITH WATER VAPOR BY NON-EQUILIBRIUM PLASMA: TOWARDS SUSTAINABLE AMMONIA PRODUCTION

This Chapter was published as:

Gorbanev, Y., Vervloessem, E., Nikiforov, A., & Bogaerts, A. (2020). Nitrogen fixation with water vapor by non-equilibrium plasma: toward sustainable ammonia production. *ACS Sust. Chem. Eng.*, *8*, 2996–3004. DOI:10.1021/acssuschemeng.9b07849[h]

[h] This work was led by Dr. Yury Gorbanev. My work included the characterization of the Soft Jet together with Dr. Gorbanev (under close supervision and practical guidance of Dr. Anton Nikiforov), which was first published under this work and later used and expanded on in the works presented in Chapters IV and VI.

In the previous Chapter, we used a plasma to convert air (nitrogen and oxygen) into NO_x, a fixed form of nitrogen (N) that we can use in fertilizers. Now that we know a lot more about the chemistry that takes place in the plasma, we can make it a bit more complicated by adding water (H_2O) into the plasma as well. With H_2O in the mix (N_2 + O_2 + H_2O), one can make both NO_x and NH_3, which can be combined into ammonium nitrate, a good basis for fertilizer. In the industry as well as in many research papers, H_2 or hydrogen gas is used as a H source, however, H_2 is energy intensive to be produced. Currently the industry uses methane (CH_4), the main component in natural gas, i.e., a fossil fuel, to make H_2. Therefore, researchers are looking for another way to add H to a reaction mixture. Water (H_2O), containing 2 H's, is a very good candidate, because it is abundant and sustainable.

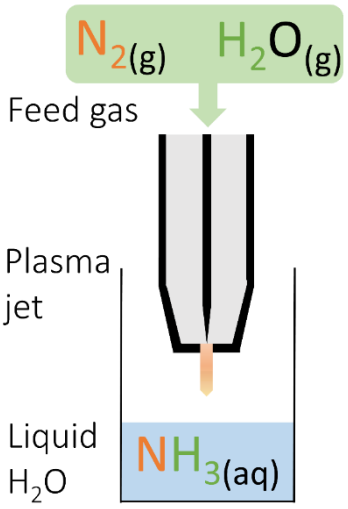

Figure 27 Schematic illustration of the concept of this chapter. A plasma is put above liquid water (H_2O). Using N_2 and H_2O (vapor) in the plasma, we measure ammonia (NH_3) in the liquid water. It is the water from the gas phase (green) that is used to form NH_3 (H in green).

Naturally, a lot of other plasma researchers have also had this idea of using water. Plasmas have been put on top of water in many different ways and even inside water, all to make sure the plasma reacts with the H_2O molecule. There is one large question that is not solved yet: what is the best way to use water in combination with plasma? As a gas, i.e. water vapor? Or as a liquid, e.g. a petri dish filled with water?

Most plasma researchers have suggested liquid water plays and important role.

In this Chapter, we look more deeply into that question, by adding water both as a vapor and as a liquid.

Based on a series of tests we believe ammonia (NH_3) is mainly formed from water vapor and not liquid water, as was suggested by some other researchers. Recently, however, our conclusion was confirmed by another group of researchers. This makes us even more confident in the fact that NH_3 is indeed formed through H_2O(vapor) + N_2 + O_2 and not H_2O(liquid) + N_2 + O_2.

This is interesting because (1) we have shown that one can make fertilizers from water and air, (2) we know more about how water is used as a source of hydrogen, and (3) it is more complicated to analyze experiments with both a liquid and a gas: now we can focus on the gas phase alone to study the chemistry in more detail. We will do so in the next Chapter.

1. Introduction

In the literature overview of this thesis, we concluded that it has been generally accepted that increasing the contact between H_2O and the plasma-produced species increases the NF capacity of the plasma. However, there is no consensus on what phase, i.e. liquid vs gaseous water vapor, is most beneficial. Liquid[105,130,131,134], gas[137] and gas+liquid[105,134] have all three been proposed as playing an important role in the underlying chemistry. Most of these works suggested that liquid water, or more precisely, the plasma-liquid interface is the most important, however, in these studies the liquid surface was the main H_2O source. Recent insights suggest that most of the reactive chemistry in plasma-liquid systems occurs in the gas (vapor) phase[199,241].

In the previous Chapter, we showed that the Soft Jet produces NO_x from dry air at a very low EC, and elucidated the underlying mechanism. Together with the diagnostics from Chapter III, we have a good grasp on this plasma source. Furthermore, because the Soft Jet is a relative flexible system in terms of inlet gas possibilities, it is a good source for studying the role of gas vs liquid H_2O.

In this Chapter, we used for the first time this Soft Jet, i.e., a non-equilibrium atmospheric-pressure plasma, operated with N_2 and air containing H_2O vapor, in contact with liquid H_2O. We studied the induction of chemical products in the liquid phase as a function of H_2O vapor saturation of the feed gas, with special focus on NH_3 selectivity and production rate. In addition, to understand the underlying mechanisms, we evaluated the role of H_2O vapor in the feed gas and liquid H_2O by excluding the direct plasma-liquid interaction, and by

discriminating between H_2O introduced with the feed gas and from the liquid sample, using isotopically labelled (D_2O) molecules.

2. Experimental

2.1. plasma setup design

In this Chapter, the plasma jet was connected to an N_2 or air gas cylinder (Chapter VIII, Materials, Table 13, entries 24 and 25). Partial saturation (i.e., % saturation) of the feed gas with H_2O vapor was achieved via splitting the N_2 flow. The H_2O content in N_2 was thus controlled by the flow rate of N_2 passing through a Drechsel flask filled with H_2O (Figure 28). It was previously shown that a gas flow rate up to 2 L/min allows full saturation of the gas with H_2O vapor[128]. The gas flow was regulated using two MFCs equipped with a microcomputer controller (Chapter VIII, Materials, Table 13, entry 44). The total N_2 flow rate was varied from 0.2 to 1.4 L/min. The concentration of H_2O vapor is quoted in % of the relative saturation at 19-21 ^oC (ambient temperature during the experiments), and in mol% as calculated from the relative saturation[128,242]. We refer to Chapter III for details on the plasma source, i.e. the Soft Jet.

2.2. nitrogen fixation experiments

In a typical experiment, 5 mL of de-ionized H_2O was put in a glass reaction vessel and exposed to plasma for 10 min. The distance between the liquid surface and the plasma jet was 5 mm (Figure 28). We also performed air-free experiments, for which the glass reaction vessel and the jet were positioned inside a gas-tight reactor[199,243] to exclude the possible interference of ambient air. The reactor was flushed for 3 min with the feed gas, and then the plasma was ignited for 10 min (Figure 28b). When performing experiments without a direct

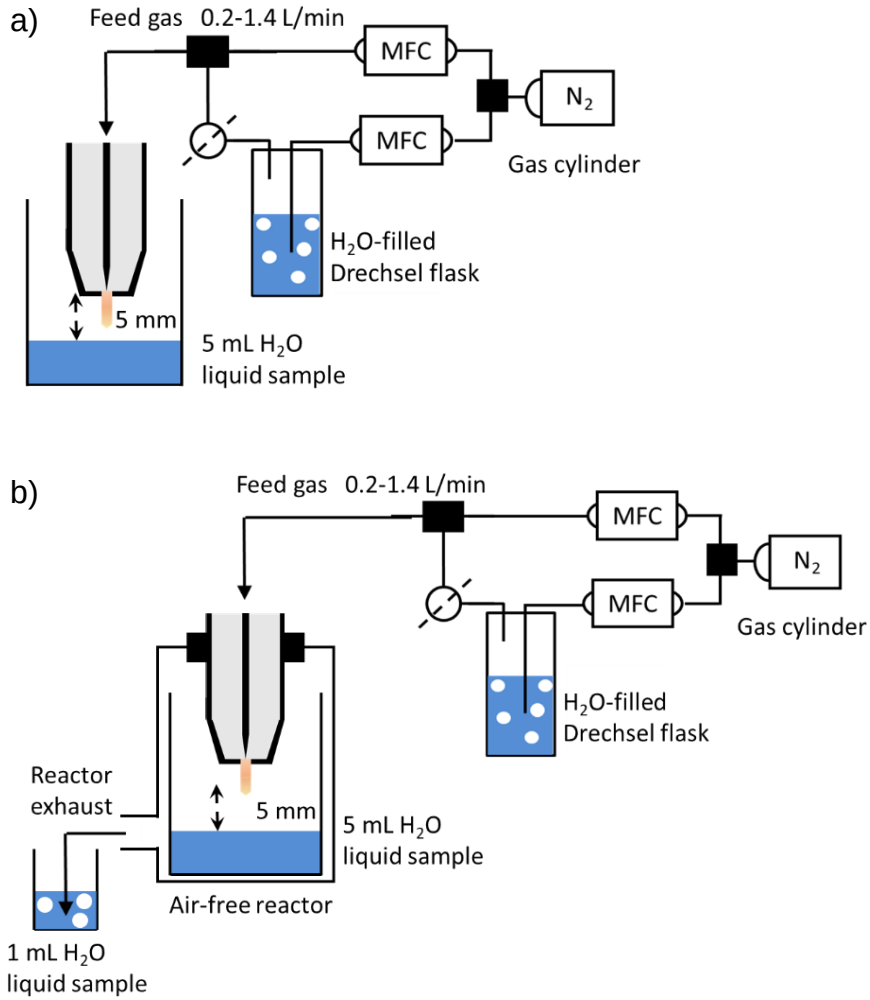

Figure 28 Experimental setups used in this Chapter. (a) plasma jet in direct contact with liquid contained in a glass reaction vessel, (b) air free reactor setup.

plasma-liquid contact, a glass tube (length ca. 330 mm, inner diameter 5 mm, outer diameter 7 mm) was pushed towards the plasma jet to cover the jet nozzle. The opposite end of the glass tube (inner diameter 1 mm, outer diameter 2 mm) was positioned 2 mm above the H_2O surface (5 mL) contained in a reaction vessel (see further below, Figure

33). Immediately after plasma exposure, the samples were collected and frozen until further analysis.

2.3. Liquid analysis

The concentrations of all chemical compounds were measured by colourimetry as explained in the Methodology, section 3.2.1, to which we refer for more details. NH_3 concentrations were measured using the indophenol blue reaction[134,201]. NH_2OH was assessed by colourimetry via reduction of Fe(III) to Fe(II) and subsequent complexation with 1,10-phenanthroline[202], and NH_2NH_2 via formation of an azo-dye in a reaction with 4-dimethylaminobenzaldehyde[204]. The concentrations of NO_3^- and NO_2^- were measured using the Nitrate/Nitrite Kit based on the Griess method with nitrate reductase enzyme, and H_2O_2 was measured using titanium(IV) sulfate with the addition of NaN_3[198–200]. The calibration curves and an analysis of the selectivity of the used methods are found in Appendix A and B, on pg. IX-247 and IX-249 respectively. Ambient and liquid temperature, and pH values were measured (Chapter VIII, Materials, Table 13, entries 41 and 40, respectively) and all measured concentrations were quoted after correction for evaporation of the solvent in each case. The error bars represent standard deviation values between three measurements.

3. Results and discussion

3.1. NH_3 production in a system comprised of N_2 plasma with H_2O vapor and with liquid H_2O

We studied the production of various compounds in liquid by exposing a liquid H_2O sample to the plasma jet effluent for 10 min at several feed gas flow rates (Figure 29). The minimal flow rate of 0.2 L/min was

chosen to avoid the heat-up of the gas (see Chapter III, section 3.2) to temperatures which would lead to thermal evaporation of the plasma-exposed water, and therefore a potential loss of NH_3 due to its decreased solubility at elevated temperatures[242]. The maximal flow rate obtainable with the equipment used was 1.4 L/min. In all our experiments, the liquid samples remained at room temperature or slightly above (21±3 ^{o}C), due to the relatively low temperature of the plasma effluent at 5 mm from the nozzle and the cooling down of liquid due to evaporation. Using liquid water has several purposes. Firstly, it demonstrates the possibility of using H_2O as a benign solvent for the storage of nitrogen fixation products in our experiments. Secondly, it enables facile measurements of the generated products by spectrophotometric analysis of the liquid samples. Finally, we studied the role of liquid H_2O in nitrogen fixation (*vide infra*).

NH_3 and NO_2^-/NO_3^- are the products of nitrogen fixation with H_2O molecules. H_2O can react with e.g. N atoms to produce •NH and •OH radicals, as proposed by Haruyama et al.[134] Besides, H_2O also forms •OH and H via e.g. direct electron impact[244] or reacting with UV photons of plasma[136]. •OH can further recombine into H_2O_2[244]. H_2O_2 is thus one of the products in a N_2/H_2O plasma system, and must be acknowledged in the overall nitrogen fixation process.

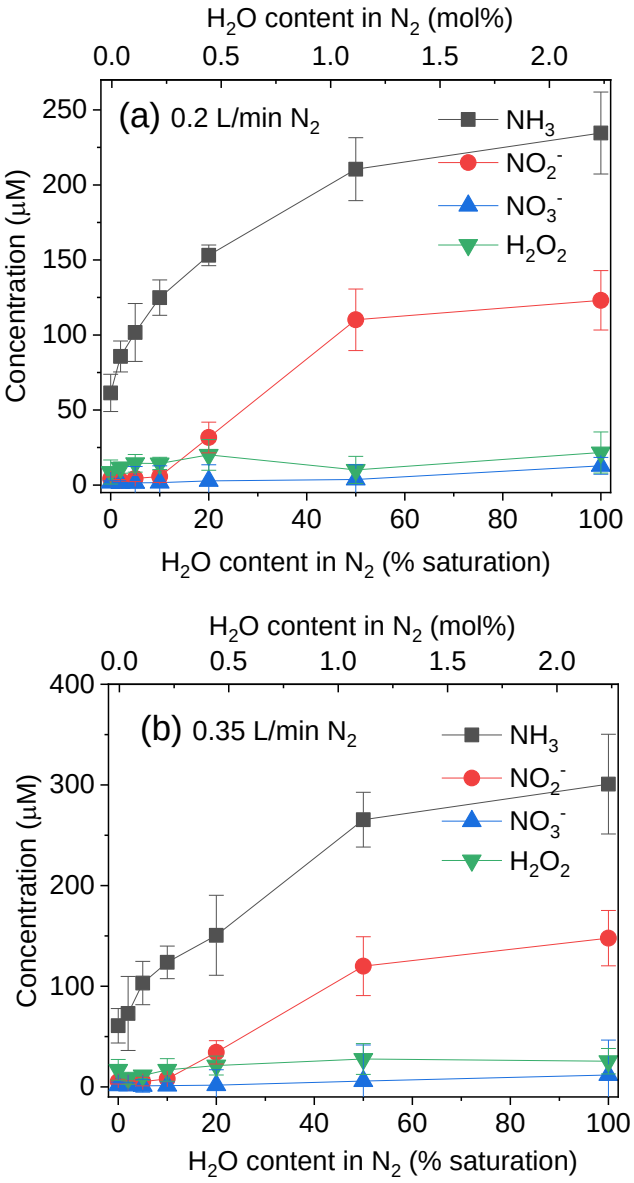
H2O content in N2 (mol%)
0.0
0.5
1.0
1.5
2.0
(a) 0.2 L/min N2
NH3
NO2-
NO3-
H2O2
Concentration (μM)
0
50
100
150
200
250
0
20
40
60
80
100
H2O content in N2 (% saturation)
H2O content in N2 (mol%)
0.0
0.5
1.0
1.5
2.0
(b) 0.35 L/min N2
NH3
NO2-
NO3-
H2O2
Concentration (μM)
0
100
200
300
400
0
20
40
60
80
100
H2O content in N2 (% saturation)

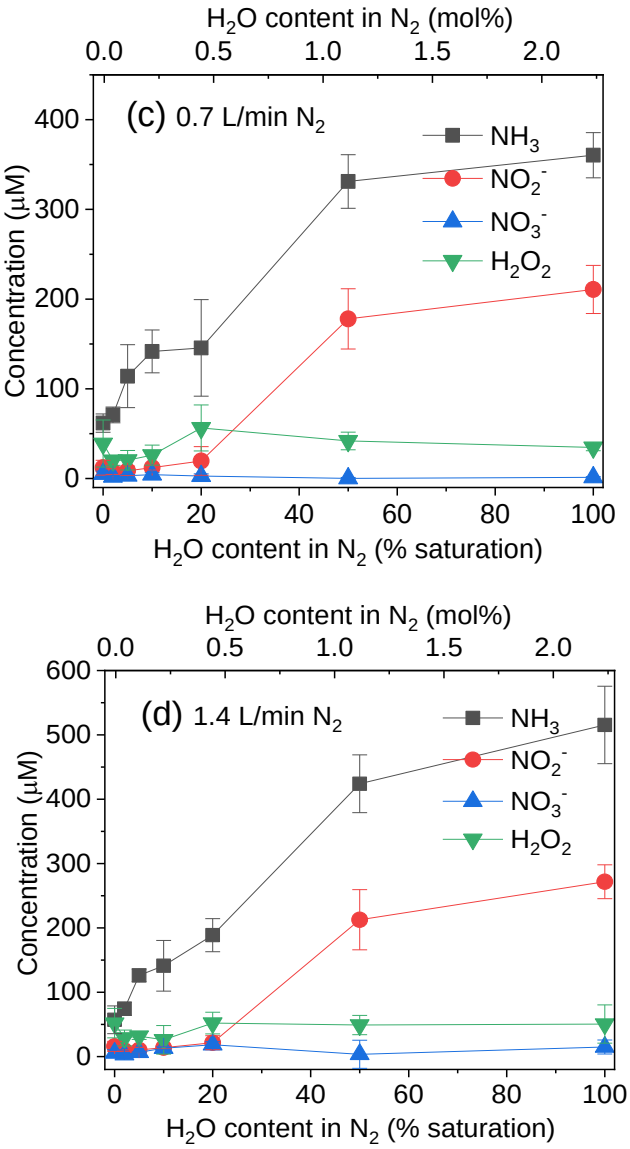

Figure 29 Concentration of produced NH_3, NO_2^-, NO_3^-, and H_2O_2 in liquid H_2O for different N_2 flow rates (a-d), as a function of H_2O vapor saturation.

In our experiments, the NO_3^- and H_2O_2 amounts slightly increase up to 20% H_2O saturation, but remain the same at ca. 20-100% H_2O saturation, while the concentrations of NH_3 and NO_2^- keep increasing upon higher H_2O saturation. Interestingly, the yields of NH_3 and NO_2^- /NO_3^- (i.e., total conversion of N_2) increase with increasing gas flow rate, but not proportionally. For example, at 50% H_2O saturation, the concentration of produced NH_3 increases from ca. 200 μM to 400 μM for gas flow rates rising from 0.2 to 1.4 L/min. Similarly, the concentration of NO_2^- is 125 μM and 225 μM for 0.2 and 1.4 L/min. This is attributed to the reduced residence time of the feed gas within the plasma ignition region, while the plasma frequency remains the same (Chapter III, Section 2.1). Therefore, a lower feed gas flow rate is preferable for a higher conversion.

In spite of the higher production at higher H_2O vapor content (50-100%, see Figure 30), the selectivity towards NH_3 decreases at high contents of H_2O vapor at all flow rates, down to 60-70%, compared to 70-80% with dry N_2 (Figure 29). However, at low H_2O vapor content (approx. 2-10% saturation) it increases compared to the dry N_2 feed gas, and it is around 90% with any of the N_2 flow rates. Remarkably, with 0.2 L/min of N_2 gas and 5% H_2O vapor saturation, the selectivity towards NH_3 is ca. 96% (Figure 29a, Appendix M, pg. IX-272). In other words, the introduction of small amounts of H_2O vapor yield both a higher NH_3 production rate and a higher selectivity. Larger amounts of H_2O vapor further increase the production rate, albeit with lower selectivity.

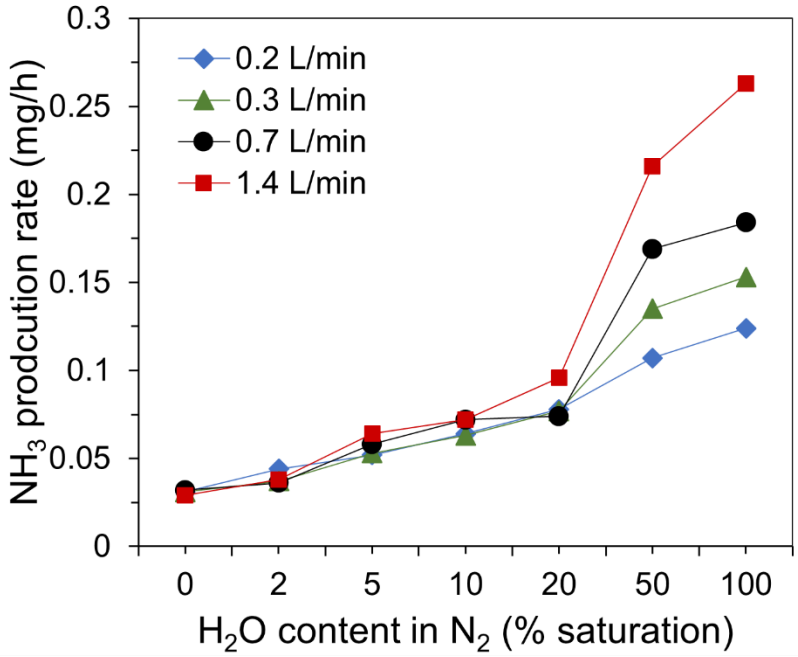

Figure 30 NH_3 production rate for different N_2 flow rates, as a function of H_2O vapor saturation.

Nonetheless, the introduction of H_2O vapor into the plasma feed gas clearly had two main effects: (i) increased total N_2 conversion (with all H_2O vapor contents) compared to dry N_2 interacting with liquid H_2O, and (ii) increased selectivity towards NH_3 (at low H_2O vapor content).

We also calculated the EC (as explained in Appendix N, pg. IX-274), yielding values in our non-catalytic, H_2-free plasma system of 95-118 MJ/mol NH_3 at 0.2 L/min N_2 and 5-10% H_2O vapor saturation (i.e., the conditions giving the highest NH_3 selectivity). This is in the range of plasma-catalytic processes using N_2 and pure H_2, reporting values from ca. 2 to 600 MJ/mol NH_3[44,101]. It is worth noting that despite the low energy cost of H_2 production e.g. from H_2O via electrolysis (<1 MJ/mol[245]), the produced H_2 must be stored and delivered into a reactive system, and H_2 storage is a bottleneck and potentially a 'showstopper' for an H_2 economy[246]. In contrast, we demonstrate the

possibility of the direct, ‘one-pot’ synthesis of NH_3 from the gases N_2 and H_2O.

Furthermore, the calculated energy consumption of total N_2 fixation was 92-105 MJ per mol of converted N_2 for the conditions specified above, and only 15 MJ/mol for the conditions which afforded the highest total concentration of NH_3 and NO_2^-/NO_3^- (1.4 L/min N_2, 100% H_2O saturation), albeit at somewhat lower selectivity.

We also assessed the energy efficiency of the process. For this, we calculated the ΔG values for a hypothetical reaction of N_2 with H_2O leading to NH_3 under the conditions which afford the highest NH_3 selectivity (i.e., $2N_2 + 6H_2O \rightarrow 3O_2 + 4NH_3$, see Mechanistic considerations below). ΔG was calculated for two ‘envelope’ temperature values (298 K and 1623 K/1350 ^oC as the lowest and highest possible temperatures in our system, see Chapter III, Table 6 and the partial pressures of the products and reactants calculated from the conversion and yield values (Appendix A, pg. IX-247). The detailed description of the ΔG calculation is found in Appendix O, pg. IX-274. In short, based on the energy consumption obtained in our work (around 100 MJ/mol) and the ΔG of ca. 1 MJ/mol, we achieve an energy efficiency of ca. 1% for NH_3 production. Thus, it is clear that there is still room for improvement via e.g. optimization of the reaction parameters or the plasma setup. However, as stated by Chen et al., although using H_2O as a feedstock is slightly more energy demanding than H_2, avoiding the HB and using milder conditions for NH_3 production can become overall energetically favorable[247].

Besides NH_3, NO_3^-/NO_2^-, and H_2O_2, we also analyzed the solutions for NH_2OH and NH_2NH_2, potential products of the complex chemistry in N_2/H_2O plasmas[248] (see Methodology, section 3.2.1, and Appendix B,

pg. IX-249 for details on the procedure). We detected no NH_2OH or NH_2NH_2 under all conditions investigated, but we stress that only assessing the full range of the possible N_2 fixation products allows evaluating the production selectivity. We acknowledge that a separation of NH_3, NO_2^- and NO_3^- may result in an extra energy cost. However, (i) under optimized conditions the selectivity in our case was over 95%, and (ii) the separation is possible via e.g. electrophoresis[249]. Therefore, both the N_2 fixation, and the product separation comply with the concept of electrification of chemical industry[10,41,250].

We also studied the production of the chemical compounds over time under representative conditions: minimal and maximal gas flow rate, low and high vapor saturation. Within the experimental time frame (10 min), the accumulation of all compounds was practically linear (Appendix P, pg. IX-275), indeed allowing comparison of production rates. This suggests that despite the pH increase (max. up to 8-8.5 under all conditions), NH_3 was continuously induced in the plasma-exposed water, and remained dissolved in it. This was also confirmed by an experiment in which the jet and the reaction vessel with H_2O were contained inside a gas-tight reactor[199,243], with the reactor exhaust passing through a second H_2O sample (Figure 28b). We did not observe any detectable amounts of NH_3, NO_3^-/NO_2^-, or H_2O_2 in the second sample, confirming that all (or most) products of N_2 fixation remained in the plasma-exposed solution.

It must be acknowledged that using a reactor with static (i.e., non-moving) liquid can have diffusion-related limitations[251], such as accumulation of the products in the upper layers of the liquid, and associated dominance of secondary reactions in the liquid phase. While we did not observe a decrease of the rate of absorption of the N_2

fixation products in our experiments, a potential alternative in future investigations would be a reactor where the gaseous plasma would be in contact with a flowing liquid[252].

The production rate under all conditions remained rather low, as is common for N_2/H_2O plasma systems (Table 2). The highest production rate observed corresponds to the highest flow rate of N_2 (1.4 L/min) at 100% relative humidity, as discussed above, reaching a maximum of 0.263 mg/h (see Appendix A, pg. IX-247 for the full list of calculated production rate values). While the NH_3 production rate in our work is somewhat lower than in some of the other studies reported in literature for N_2 plasma in contact with H_2O, the advantage of our setup is the simple design, i.e., open reactor with no additional electrolytic or UV components, which of course add in the NH_3 production. In addition, the NH_3 selectivity and energy consumption in our work is generally better than the values reported in literature (see Table 2).

3.2. Mechanistic considerations

To understand the pathways leading to NH_3, we can consider several possibilities, as discussed in the Introduction of this thesis. N_2 molecules can be converted in the plasma into electronically or vibrationally excited states (e.g. N_2*, $N_2(v)$), N_2^+ ions, and N atoms, as shown by Sakakura et al.[135] These species further interact with H_2O (or H and •OH generated from H_2O by plasma), forming first •NH and ultimately NH_3[134–136]. On the other hand, H atoms (again generated from H_2O via interaction with plasma) can also directly interact with N_2 molecules, also yielding NH_3[141]. As for the plasma action, the key reactions are direct electron impact excitation and dissociation of N_2 and H_2O[244,248]. Additionally, UV irradiation from plasma may assist in dissociation of H_2O into H and •OH[134,136].

Our experiments suggest that the reaction regimes can be divided into three main groups, depending on the H_2O saturation of the N_2 gas. In **the first regime**, dry N_2 reacts with the plasma-exposed H_2O. At higher flow rates of N_2, nearly equal amounts of NH_3 and H_2O_2 are formed (Figure 29c and d), suggesting interaction of e.g. N atoms with H_2O to produce •NH and •OH, and further recombination of •OH into H_2O_2. Here, the plasma can interact with the liquid phase H_2O molecules as suggested in literature[134–136]. However, it has also been suggested that plasma interacts first with a vapor layer immediately above the liquid surface[105,251,253]. This agrees with our previous results, by Gorbanev et al., where they experimentally demonstrated that the plasma effluent does not interact directly with the liquid, but instead reacts with the vapor above the solvent[128]. More precise evaluations require physicochemical modelling.

The second regime (2-10% H_2O saturation) yields NH_3 with high selectivity. The absence of extra amounts of H_2O_2 suggests that another species potentially formed from O in H_2O in this regime is O_2, or possibly N_2O, which were not analyzed in this study. N_2O, however, could react with •OH to be transformed back into N_2[213].

The third regime (N_2 saturation with H_2O vapor of 20% and above) exhibits the formation of NH_3 and NO_2^-+NO_3^- in a ratio close to 2:1. This regime is possibly controlled by the initial formation of NH_3 (similarly to the second regime), and its further oxidation. However, Sakakura et al. proposed that this could be due to the reactions of N with H_2O and/or H (from H_2O) leading to NH_3, and N with •OH (from H_2O) leading to NO_2^-/NO_3^-[135].

Thus, in all three regimes the formation of the reduced product NH_3 is accompanied by the formation of an oxidized one, the nature of which

likely depends on the regime (i.e., NO_2^-/NO_3^- (from N_2), H_2O_2 or O_2 (from H_2O)). In any regime, H_2O is a key component since it is the only source of H for NH_3. The interaction of plasma with H_2O in the feed gas and H_2O exposed to the effluent is an important parameter of the described reactive system.

3.3. Influence of ambient air on NH_3 production

The use of an air-free gas-tight reactor in which the gaseous atmosphere consisted only of the feed gas (N_2+H_2O) and the solvent vapor (H_2O) allowed us to evaluate the influence of the ambient atmosphere on NH_3 synthesis. Generally, in plasmas with an active effluent (i.e., containing high energy species, such as electrons), the chemistry is strongly affected by the composition of gas in contact with the effluent[241,251]. Ambient air can diffuse into the effluent, altering the production of chemical species[200,244]. However, comparing the experiments in the reactor and the open reaction vessel revealed no significant differences in product concentrations (Figure 31), probably due to the high gas velocity, reasonably short distance between jet and liquid, and the walls of the reaction vessel reducing the air diffusion. This emphasizes the facile use of our experimental setup for NH_3 production, and its independence from the surrounding air eliminates the need for an air-free reactor[136,141].

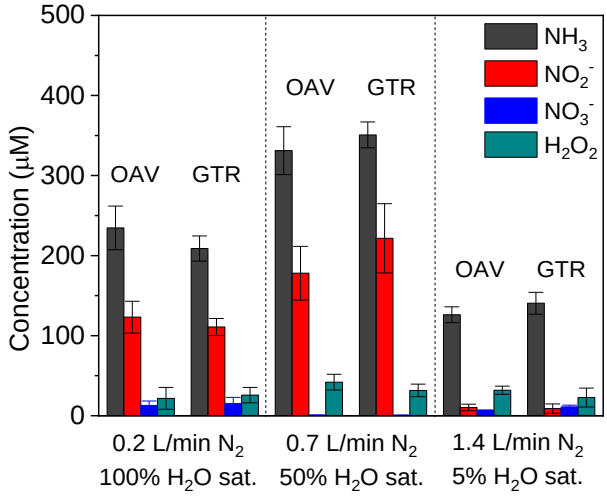

Figure 31 Concentration of produced NH_3, NO_3^-, NO_2^-, and H_2O_2 in liquid H_2O in open atmosphere in a reaction vessel (OAV) and in an air-free, gas-tight reactor (GTR), at three representative plasma conditions.

3.4. NH_3 production when using air as the feed gas

Using air instead of N_2 as the feed gas expectedly provided very different results. With dry air, detectable amounts of NH_3 were produced only with 0.7-1.4 L/min flow rate (Figure 32). Introducing H_2O vapor into the plasma feed gas, we observed higher NH_3 formation under all conditions. It was higher at higher flow rates, like in the N_2 plasma (Figure 29). However, the amount of produced NH_3 was ca. 6 times lower than in the N_2 plasma with the same flow rates. For instance, the concentration of produced NH_3 in H_2O with a gas flow rate of 0.2 L/min was ca. 40 and 240 μM with the air and N_2 plasma, respectively (see Figure 31a and Figure 32). Moreover, the NH_3 selectivity dropped drastically when using air plasma. In all cases, the total concentration of NO_3^- and NO_2^- produced by air plasma was 5-6 times higher than the concentration of NH_3 (see Figure 32), reducing

the NH_3 selectivity to values below 15-20%. Nonetheless, the total yield of all products of nitrogen fixation evidently increased upon addition of H_2O vapor with air as feed gas, as well as with N_2, making the process more efficient. However, the results strongly indicate that N_2 as plasma feed gas is required to achieve high NH_3 selectivity.

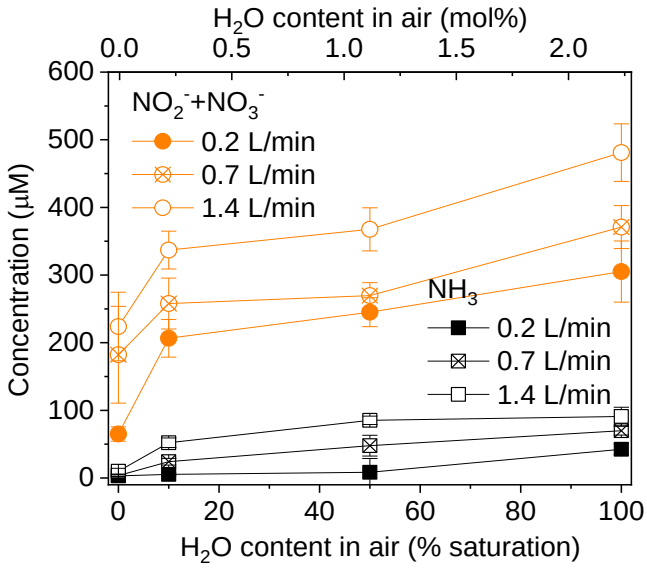

Figure 32 Concentration of produced NH_3 and $NO_2^-+NO_3^-$ in liquid H_2O from air plasma, as a function of H_2O vapor saturation.

3.5. Contribution of H_2O-vapor and plasma-exposed H_2O to NH_3 formation

Because this, at the time of publication, was the first work describing the use of H_2O vapor in the plasma feed gas, we needed to elucidate whether (1) the gaseous plasma effluent interacted with the plasma-exposed H_2O, or (2) NH_3 was produced from H_2O vapor. This is one of the main open questions in wet plasma-based NF literature. To evaluate the first option, the distance between the plasma jet and the liquid has to be increased to exclude interaction with the liquid. This could result in a potential loss of NH_3 due to the effluent dissipation into

the gas phase instead of delivering NH_3 into the liquid (the increase of the effluent width, and hence the decrease of the gas velocity, within the 5 mm distance from the jet is shown in Table 6, of Chapter 3.2). To avoid a drastic drop in the gas velocity, we performed experiments in which the tip of the plasma jet was inserted in a glass tube (see Experimental section). The opposite end of the glass tube (inner diameter 1 mm) was positioned 2 mm above the liquid (Figure 33). Plasma was ignited with N_2 and H_2O vapor as the feed gas. The total distance from the plasma jet was ca. 300 mm.

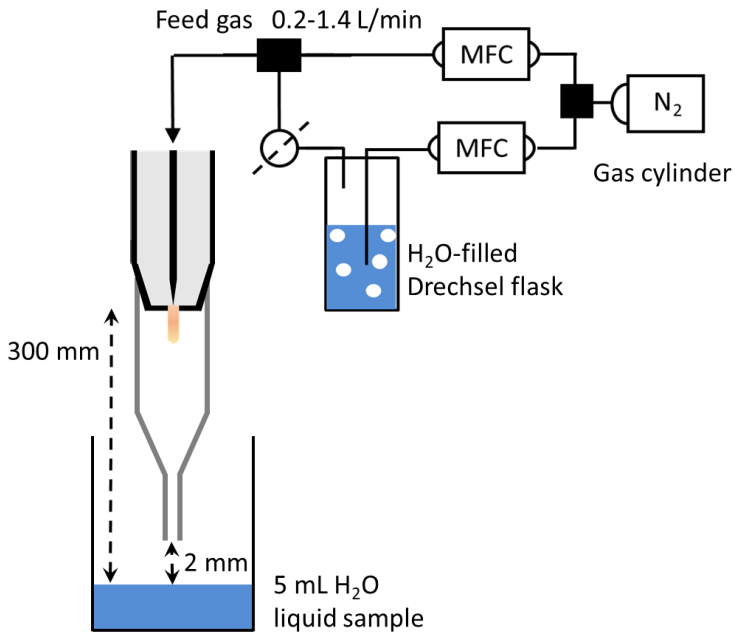

Figure 33 Experimental setup with the glass tube, eliminating the direct plasma-liquid interaction.

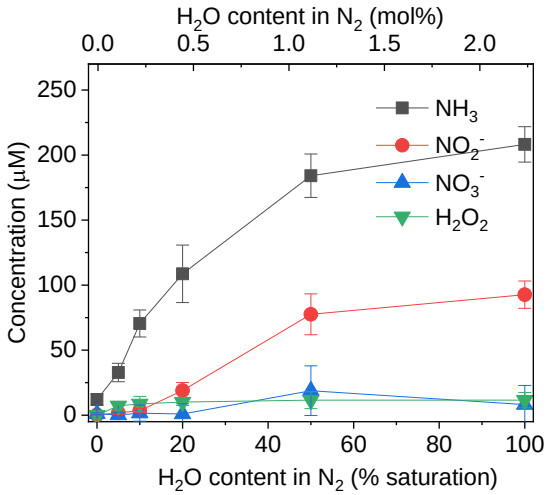

Figure 34 Concentration of produced NH_3, NO_3^-, NO_2^-, and H_2O_2 in liquid H_2O, with 0.2 L/min N_2, as a function of H_2O vapor saturation, when using a glass tube to increase the distance between plasma jet and liquid without a drop in gas velocity.

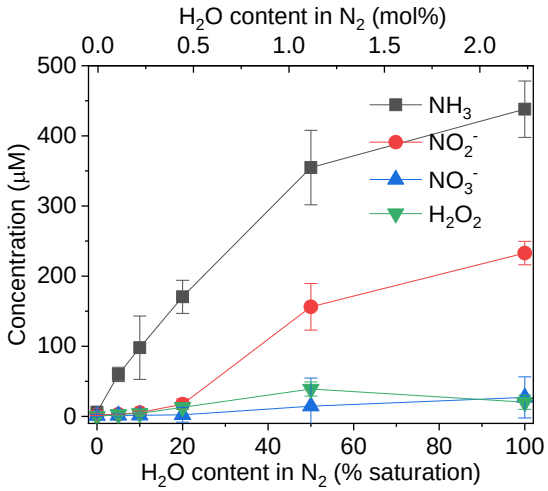

Figure 35 Concentration of the produced NH_3, NO_3^-, NO_2^-, and H_2O_2 in liquid H_2O with 1.4 L/min N_2, as a function of H_2O vapor saturation. Liquid volume 5 mL, distance from plasma jet to liquid 300 mm, exposure time 10 min. This Figure corresponds to Figure 34, but at a higher flow rate.

Comparing Figure 34 and Figure 29a, it is seen that the concentration of NH_3 and NO_3^-/NO_2^- are slightly lower than the values in H_2O exposed

to plasma at 5 mm distance, at all H_2O saturation values (5-100%). For example, at 50% H_2O saturation, the NH_3 concentrations are ca. 190 μM at 300 mm distance, compared to 210 μM at 5 mm distance. At the same time, the NH_3 selectivity remains practically the same, suggesting similar reaction pathways. The H_2O_2 concentrations were substantially lower here, suggesting that most H_2O_2 was formed via interaction of the effluent with the plasma-exposed H_2O. In other words, H_2O_2 is largely formed via recombination of •OH formed from plasma-exposed H_2O upon interaction with the plasma effluent, while NH_3, NO_3^-, and NO_2^- are mainly formed upon reaction of N_2 molecules (or excited species) with H and •OH originating from H_2O vapor in the feed gas, rather than from the plasma-exposed liquid H_2O.

A notable difference, however, was observed for dry N_2. Here, virtually no NO_3^-/NO_2^- or NH_3 were detected. This is expected, because no H-source was present in the system. The considerable production of NH_3 with dry N_2 at 5 mm (Figure 29) suggests that the plasma effluent does interact with H_2O of the solvent under those conditions. With increasing H_2O content in the plasma feed gas, this interaction becomes less pronounced. We hypothesize that this is due to the lower density of electrons and excited N_2 molecules and atoms in the effluent with high H_2O vapor admixtures in the feed gas[241,244]. Still, even at 100% saturation of the feed gas, the NH_3, NO_3^- and NO_2^- concentrations were slightly lower with no effluent-solvent interaction (i.e., lower at 300 mm than at 5 mm), indicating that these products are also formed to a minor extent from the plasma-exposed liquid H_2O.

At high flow rate the interaction of the plasma effluent with the liquid H_2O is more probable. However, we observed similar effects with 1.4 L/min (see Figure 35 and Figure 29d). The addition of H_2O vapor to the

feed gas reduces the effect of the effluent interaction with the molecules of the plasma-exposed H_2O, but does not eliminate it completely. This suggests that in our plasma jet, most of the chemistry leading to NH_3 (and NO_2^-/NO_3^-) formation occurs in the gas phase plasma, via reactions of the feed gas components, with only a minor contribution from the H_2O molecules of the solvent, either liquid or evaporated.

3.6. Using isotopically H_2O/D_2O to distinguish between the role of gaseous vs liquid H_2O

This hypothesis was further confirmed by experiments with isotopically labelled water (Chapter VIII, Materials, Table 13, entry 21). The theoretical background used in the interpretation of these results, i.e. the kinetic isotope effect, is discussed in the Methodology, section 5. We used: 1) D_2O liquid sample exposed to H_2O vapor plasma; 2) H_2O liquid exposed to D_2O vapor plasma; and 3) D_2O liquid exposed to D_2O vapor plasma (Figure 36). This was done to distinguish between the water vapor in the feed gas, and water of the exposed sample. The results were compared with the data with H_2O liquid and H_2O vapor (added as dashed lines in Figure 36).

When the liquid was changed to D_2O but the plasma feed gas contained H_2O vapor, the NH_3 and $NO_3^-+NO_2^-$ concentrations remain virtually the same as with liquid H_2O. This means that both the NH_3 production rate and selectivity were the same. Switching from H_2O to D_2O introduces the primary kinetic isotope effect (KIE)[254], which could lead to potentially different concentrations of the N_2 fixation products. Indeed, a reactive system comprised of D_2O vapor and exposed D_2O liquid yielded lower NH_3 and $NO_3^-+NO_2^-$ concentrations, although the selectivity remained the same.

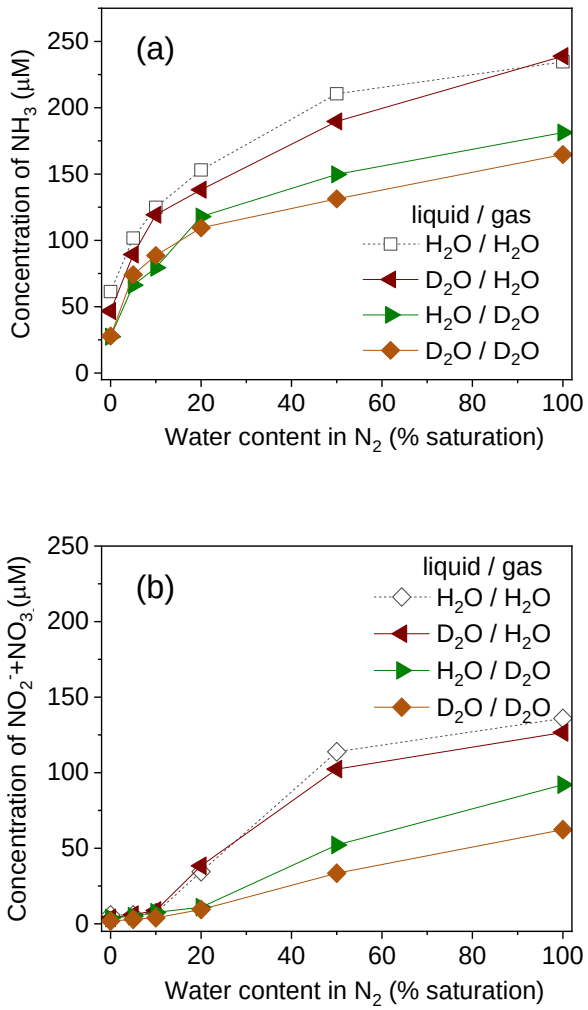

Figure 36 Concentration of produced (a) NH_3 and (b) NO_2^-+NO_3^- in liquid water, as a function of water vapor saturation, with 0.2 L/min N_2 flow rate, for different combinations of liquid/gas H_2O/D_2O. Results for 1.4 L/min can be found in Appendix Q, pg. IX-276.

This was in agreement with previous studies on plasmas with isotopically labelled water[199,241], and the work of Haruyama et al.[134]. When liquid H_2O sample was exposed to D_2O vapor-containing N_2 plasma, the concentrations of both NH_3 and NO_2^-/NO_3^- decreased compared to the H_2O liquid/H_2O vapor conditions (again, with the same selectivity), but they were slightly higher than those in the case of D_2O liquid/D_2O vapor. With D_2O liquid/H_2O vapor, the difference was probably too small to be observed. Nonetheless, these data confirm that liquid H_2O participates in the NH_3 and NO_3^-+NO_2^- production to some (minor) extent, as we hypothesized above (*vide infra*), but that water (H_2O or D_2O) introduced as vapor component plays a much larger role than the plasma-exposed liquid.

4. Conclusions

We present here for the first time, at the time of publication, a green NH_3 synthesis process, based on non-catalytic nitrogen fixation by non-equilibrium plasma using H_2O vapor instead of H_2. Since then, a few H_2O vapor studies have been published, though limited[122,137]. Interestingly, Toth et al. also suggested H_2O played a more limited role compared to what had previously been suggested in literature [130,131,134,135]. We used the Soft Jet, which is a very simple plasma setup, for a straightforward on-spot generation of NH_3 in a benign solvent (H_2O), avoiding more complex air-free plasma chambers. We assess the formation of the full range of possible N_2 fixation products, which is required to evaluate the selectivity of NH_3 formation. We evaluated the selectivity and applicability of the colorimetric analytical techniques used to measure the concentrations of the N_2 fixation products in H_2O. We studied the selectivity and rate of NH_3 production as a function of the added H_2O vapor content in the plasma feed gas operated at

different flow rates. Excellent selectivity of NH_3 formation (up to 96%) and increased production rate compared to dry N_2 in contact with liquid H_2O (up to 0.064 mg/h) were achieved under conditions with low amounts of H_2O vapor saturation of the N_2 feed gas. With higher H_2O vapor contents, the selectivity was lower (ca. 60-85%), but the combined yield of all N_2 fixation products (i.e., NH_3, NO_3^-, NO_2^-) increased. Similarly, the total N_2 fixation product yield increased when air was used instead of N_2, but the selectivity towards NH_3 was drastically lower when compared to the N_2 feed gas. Thus, in terms of total N_2 fixation efficiency, higher levels of H_2O vapor saturation of the plasma feed gas were beneficial, as they increased the overall N_2 conversion. Notably, the energy consumption of the presented catalyst-free and H_2-free plasma system (around 100 MJ/mol for NH_3, or 15 MJ/mol for total N_2 fixation) are in the range of reported values of plasma-assisted catalytic NH_3 production, but with the additional advantage of using H_2O vapor and absence of catalyst.

Experiments without direct plasma-liquid interaction and with isotopically labelled water were performed to study the contribution of H_2O vapor in the feed gas, and liquid H_2O. The results show some interaction of plasma effluent with the plasma-exposed H_2O, but the role of this interaction decreases dramatically when H_2O vapor is introduced into the N_2 feed gas.

Therefore, using H_2O vapor admixtures in N_2 can result in both higher NH_3 selectivity and production rate. At the same time, it reduces the need to use liquid water as a reagent, enabling the use of plasma setups without a direct plasma-liquid interaction. Future studies in this field, including optimization of the plasma setup and development of computational models, can shed more light on the mechanisms leading

to NH_3 and other N_2 fixation products. This can further enhance the energy efficiency, selectivity, and yield outcomes.

In the next Chapter, we look at the formation of NF species in the gas phase in more detail. Knowing that NH_3 is mainly formed in the gas phase allows us to focus only on the gas phase instead of both the gas and liquid phase, which simplifies the problem and helps to elucidate the first steps in NH_3 formation. Secondly, it opens up more possibilities in terms of gas phase diagnostics and analysis like FTIR.

VI. NH_3 FORMATION AND LOSS IN NITROGEN FIXATION FROM AIR WITH WATER VAPOR BY NON-EQUILIBRIUM PLASMA

This Chapter was published as:

Vervloessem, E., Gromov, M., De Geyter, N., Bogaerts, A., Gorbanev, Y., & Nikiforov, A. (2023). NH_3 and HNO_x formation and loss in nitrogen fixation from air with water vapor by non-equilibrium plasma. *ACS Sust. Chem. Eng.*, 11, 4289-4298. DOI:10.1021/acssuschemeng.3c00208

In the previous Chapter, we showed that (1) we can make the basis of fertilizers (from the molecules NH_3 and HNO_x) from water and air (or nitrogen) and (2) these molecules are mainly formed from chemical reactions with water in the gas phase (water vapor) and not water in the liquid phase.

In this Chapter, we are interested in studying how these molecules, NH_3 and HNO_x, are formed. Thanks to our experiments in the previous Chapter, we know that the molecules are mainly formed in the gas phase, and therefore we will be focussing on the gas phase alone.

Our experiments suggest that NH_3 is produced in the gas phase, as we expected. However, further away from the plasma we do not measure NH_3 anymore. We hypothesize that NH_3 is destroyed on its way to the detection device, meaning we are losing the NH_3 we made in the plasma. This is an important finding. If we can prevent losing NH_3 like this, more NH_3 can be produced in the same plasma.

1. Introduction

In the previous Chapter, we have shown that H_2O can also be used for the production of NH_3 from mixtures of N_2 and H_2O vapor, and even more interestingly, from air (N_2 and O_2) and water vapor (i.e., humid air), with accumulation of the produced NH_3 in liquid water[140]. However, plasma-based studies that have looked at N_2/H_2O vapor and air/H_2O vapor (i.e., without liquid water) are very scarce[140,255] (see Introduction, Table 2). Hence, more insight into the gas phase formation of NH_3 with water vapor is needed, to understand how NH_3 production can be achieved in both N_2 and air plasma using H_2O as a hydrogen source.

In air/H_2O and N_2/H_2O mixtures, the formation of HNO_x is also of interest. As explained in the Introduction of this thesis, the majority of fertilizers are ammonium salts produced from NH_3 and its oxidation product HNO_3, which is commercially synthesized through the Ostwald process using HB-made NH_3 as feedstock[23]. The direct synthesis of HNO_x alongside NH_3 could therefore result in a more streamlined production process[37].

This Chapter studies the selectivity of plasma-based NF in air and N_2 discharges at a relative humidity up to 100% at 20 °C (room temperature), i.e. up to 2.4 mol% H_2O. The same pulsed plasma jet, i.e. the Soft Jet, is used. In summary, we first characterized the Soft Jet in Chapter III, then, in Chapter IV we studied the plasma in dry air and used it in combination with quasi-1D modelling to elucidate the underlying mechanism responsible for the record-low EC that it showed for NO_x production from air. In Chapter V, we then used this plasma jet to demonstrate that the gaseous H_2O present in the feed gas (and not the liquid H_2O) plays a major role in NF. Work by Toth et al. confirmed

this finding later on [137]. Moreover, we showed that both dissolved NH_4^+ and NO_x^- were formed when H_2O vapor was added to the plasma feed gas (N_2 or air).

In the present Chapter, we elaborate on this topic, investigating the fundamentals behind the one-step NF process from gaseous N_2/air and H_2O via gas phase diagnostics: FTIR and OES to elucidate the formation mechanisms of the H_2O-based NH_3.

2. Experimental

2.1 plasma setup design

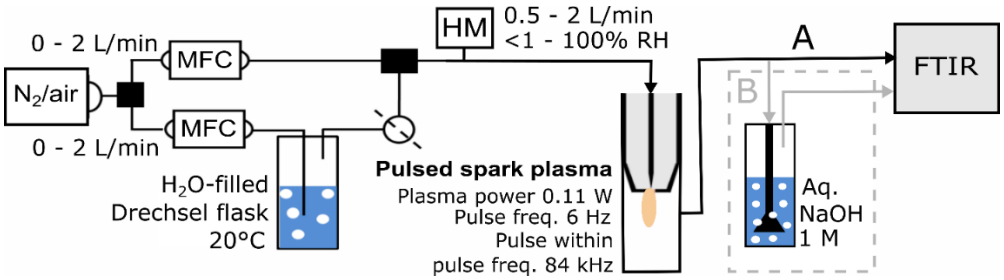

Figure 37 Experimental setup used in this Chapter. Line A shows the setup where the effluent goes straight to the FTIR. Line B shows the setup where the effluent first passes a base washer, indicated in dashed grey. The latter is only used when specified in the text.

In this Chapter, the Soft Jet was operating either in synthetic air (N_2 + O_2), or pure N_2 (Chapter VIII, Materials, Table 13, entries 22 and 23, respectively). The gas flow rate was regulated using two MFCs (Chapter VIII, Materials, Table 13, entry 42). Partial saturation of the supplied feed gas with H_2O vapor was achieved by splitting the main gas flow and passing its fraction through a water-filled bubbler[128,199]. The resulting gaseous H_2O concentration in the flow was monitored with a humidity meter (Chapter VIII, Materials, Table 13, entry 45). The

feed gas flow rate was 0.5 or 2 L/min. All tubing in the setup was Swagelok PTFE[i] (diameter ¼ inch). The concentration of H_2O vapor was varied, and will be shown in both molar percentage (<0.1 to 2.4 mol%) and relative humidity at 20 °C (<1 to 100%). We explicitly note that even with no added H_2O vapor, the feed gas contained residual humidity, hence the absence of the zero value humidity. The effluent of the plasma jet was contained within a quartz reservoir (ca. 30 mL volume), the exhaust of which was connected to the FTIR spectrometer, as shown in Figure 37 (length ca. 50 cm).

2.2 Downstream gas phase analysis

N-containing stable gaseous products were measured employing FTIR (Chapter VIII, Materials, Table 13, entry 43); using an average of 50 scans, all gas from the setup plasma was directed to the FTIR). Quantitative measurements of NO, NO_2 and N_2O were performed using Bruker's database and Beer's law based on the absorption cross-sections from the HITRAN database[256]. The deviation between both methods was found to be <3%. The concentration of gaseous NH_3 and HNO_2 were calculated through Beer's law only, using the absorbance cross-section reported by Barney et al.[193]. Further details are discussed in Methodology, section 3.1.1.

2.3 OES analysis of the plasma-produced species

The NO ($A^2\Sigma^+–X^2\Pi$; 226.94 nm), NH ($A^3\Pi–X^3\Sigma$; 336.0 nm), and N_2 ($C^3\Pi–B^3\Pi$; Second Positive System; 337 nm) transitions[175] were measured as shown in Figure 9 (Methodology, section 2.4). We

[i] Polytetrafluorethylene.

performed measurements (i) axially in the plasma (Figure 9a), as well as (ii) space-resolved perpendicularly to the plasma effluent (Figure 9b). The spectrometers used and their details can be found in Chapter VIII, Materials, Table 13, entries 36 and 37. In the axial position, the presented results were corrected for quenching by H_2O, O_2 and N_2, the sensitivity at different wavelengths, and the difference in the electron impact excitation coefficients for the NO($A^2\Sigma^+$) and NH($A^3\Pi$) states. This means that the intensities of NO($A^2\Sigma^+$) and NH($A^3\Pi$) bands at different gas mixtures can be compared directly after the performed calculations, i.e. as a function of the humidity. The measured intensities can be correlated to ground state NH and NO densities when assuming that excitation to these states occurs predominantly through electron impact. This approach is based on the approximations explained in the Methodology section 2.4.2. The computational corrections and normalization based on both experimental data and calculated values can be found in the same section.

3 Results and discussion

3.1 Net production of NH_3, NO_x and HNO_x downstream

First, we studied the production of various stable compounds in the gas phase using FTIR, using the setup shown in Figure 38, without base washer, hence following line A. Figure 38a and b show the NH_3 and HNO_2 concentration in N_2 at 0.5 L/min and 2 L/min gas flow rate. The results of similar experiments, but with humid air, are shown in Figure 38c and d, where besides NH_3 and HNO_2 also NO and NO_2 were detected. At all conditions tested, the N_2O_5, NO_3, O_3 and HNO_3 concentrations were below the limit of detection. The highest observed

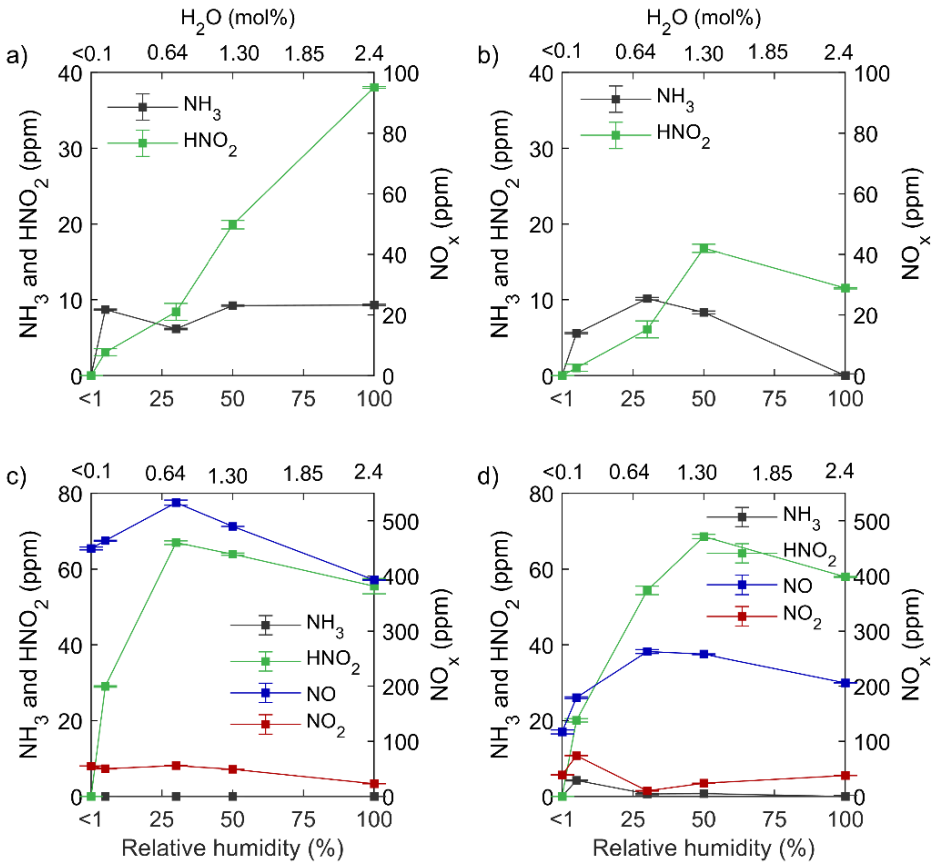

Figure 38 Concentration of NH_3, HNO_2 (left y-axis), and NO_x (right y-axis) in the gas phase as a function of feed gas humidity. (a) N_2, 0.5 L/min; (b) N_2, 2 L/min; (c) air, 0.5 L/min; (d) air, 2 L/min.

N_2O concentration did not exceed 2 ppm, and was thus considered negligible. An overview of the FTIR bands of interest is presented in Figure 10. Describing the detailed reaction mechanisms for HNO_x, NO, NO_2 and NH_3, as well as their interplay, requires dedicated computational studies based on a chemical kinetics model, which can take into account large reaction sets, while incorporating the plasma parameters (e.g., power density) as input. In Chapter IV, we did this for a much simpler chemical system consisting only of dry air[87], where we discussed how reverse reactions of the Zeldovich mechanism can be

suppressed and the vibrational non-equilibrium can be promoted through the use of pulsed power and resulting pulsed temperature. A complete computational model with added H_2O would be much more complex, and was outside the scope of the present Chapter. However, based on our general insights obtained from our other models, data from literature, and our present experimental data, we can hypothesize the following mechanisms/pathways.

In this discussion, we first focus briefly on the mechanisms for NO and NO_2 and then more elaborately on the possible pathways of nitrogen fixation, leading to the production of HNO_2, HNO_3, and NH_3.

3.1.1 NO_x production pathways

In brief, in humid N_2 the dominating mechanism for NO and NO_2 formation is the extended Zeldovich mechanism (see R VI.1 in Table 9), as discussed by Gromov et al.[145], because H_2O is the sole oxygen source. However, the concentrations of NO and NO_2 were below 1 ppm for the whole range of used H_2O content (<1-100% relative humidity)), likely because all NO_x reacted further to form HNO_2, as seen in Figure 38a and b.

On the other hand, in humid air where O_2 is readily available, the NO_x concentration is not only dramatically higher than in humid N_2 (where NO_x concentration was <1 ppm), but is up to 4 times higher than the HNO_2 concentration (e.g., 69 ppm HNO_2, 254 ppm NO_x at 50% relative humidity and 2 L/min; Figure 38d). In this scenario, NO_x formation is guided by both the traditional non-thermal (R VI.2 and R VI.3) and the extended Zeldovich mechanisms (R VI.1) shown in Table 9.

Table 9 (Extended) Zeldovich reactions, their corresponding reaction rate coefficients and relevant temperature ranges.

Reaction	Rate coefficients [a]	Temperature range (K)		Ref
$N + OH \rightarrow NO + H$	4.7×10^{-17}	300–2500	R VI.1	257
$O_2 + N \rightarrow NO + O$	$4.47 \times 10^{-12} \times e^{-27188/RT}$	298–5000	R VI.2	257
$N_2 + O \rightarrow NO + N$	$3.01 \times 10^{-10} \times e^{-318000/RT}$	1400–4000	R VI.3	257

[a] Unit: $cm^3/(molecules \cdot s)$ for two-body reactions, and $cm^6/(molecules^2 \cdot s)$ for three-body reactions. T is the gas temperature.

3.1.2 NH_3 and HNO_x production pathways

As a common trend in both humid N_2 and humid air, when the H_2O content of the feed gas increases, the HNO_2 concentration initially rises, as more H and O become available through H_2O dissociation into H atoms and OH radicals. In N_2 feed gas, since NO is produced predominantly from OH (formed through water dissociation), we observe a continuous increase in HNO_2 concentration with increasing humidity, for 0.5 L/min (Figure 38a), while at 2 L/min, a maximum is reached at 50% relative humidity (Figure 38b). In air, the highest HNO_2 concentration (around 70 ppm) is measured between 25 and 50% relative humidity (Figure 38c and d). Note that the chemistry of the system becomes more complex in humid air compared to humid N_2, rendering a detailed discussion on the mechanisms too speculative. However, a plausible hypothesis why in both N_2 and air, instead of HNO_2 rising until 100% humidity, its concentration decreases at higher H_2O vapor content (i.e., 50–100% for 2 L/min in air and N_2, and 25–100% for 0.5 L/min in air), will be given further down below.

Because H_2O is the sole H source in humid N_2, one could expect the NH_3 concentration to rise with increasing H_2O vapor content as well. However, in the present study, the gas phase NH_3 concentration instead stays constant around 10 ppm at humidity above 5% (N_2, 0.5 L/min; Figure 38a) or even starts dropping after reaching a maximum of ca. 10 ppm at 25% humidity (N_2, 2 L/min; Figure 38b). At the same time, in air, despite being H_2O present as an H source, no NH_3 is detected, except for one condition (air, 2 L/min, 5% humidity; Figure 38d). This is counterintuitive, because in Chapter V we observed NH_3 accumulation in liquid when the plasma effluent was placed above a

water surface, and NH_3 was measured in PTW (as NH_4^+)[140]. Additionally, we confirmed in our previous work that most H in the formed NH_3 came from the gaseous H_2O, with only a minor contribution of liquid H_2O to the formation of NH_3. This clearly indicated that NH_3 should be formed in the gas phase of the plasma system, although it is not detected by the downstream FTIR analysis in this work.

Moreover, HNO_3 (detected in PTW as NO_3^-) was not detected by FTIR in the gas phase under any of the conditions tested. We propose that the reasons are as follows. (i) Gaseous HNO_3 is mainly formed from NO_2 via reaction with OH[36] (see also Table 10 below), however NO_2 is not detected in humid N_2 (Figure 39a and b), and in humid air it is present in low concentrations (much lower than NO) (Figure 39c and d). Furthermore, (ii) we hypothesize the formation of NH_4NO_3 and its precipitation out of the gas phase, as described by Zhu et al.[114]. The latter hypothesis was supported by the observed accumulation of white dust during our experiments (see below). Still, we need an in-situ plasma gas phase analysis to elucidate the presence of NH_x species created by the plasma from N_2 and H_2O in both air and nitrogen feed gas, as shown below.

To investigate the near-simultaneous decrease of NH_3 and HNO_2 at high relative humidity (especially for humid N_2 at 2 L/min; Figure 38b), and the absence of detected NH_3 in air when switching from a humid gas-liquid system (Chapter VI) to a pure humid gas system (Figure 38c and d), we studied the chemical species in the plasma and in the plasma afterglow by means of OES (Figure 9a and b). OES is a widely used analytical technique for qualitative and quantitative plasma analysis. It measures the light emission from state transitions in a non-intrusive way, allowing qualitative insight into (short lived) species in

the plasma itself and right after the plasma, before potential downstream reactions take place[258].

3.2 OES shows NH and NO are produced in the plasma

First, we analyzed the gas composition immediately inside the plasma. This was done by placing the OES spectrometer axially to the plasma jet (see Figure 9a).

The direct OES data provide the intensity of the signals related to the density of excited species. After the necessary corrections (described in the Methodology, section 2.4) we can correlate the intensity of the bands of the excited states NH($A^3\Pi$) and NO($A^2\Sigma^+$) to their ground state density, taking into account the approximations behind the corona model applied. This means the resulting corrected data in Figure 39 are representative of the NH and NO ground state concentrations in the plasma. It has been shown that NH is predicative of and correlates with the concentration of NH_3 [107,109,110]. In (humid) N_2 the trend of the NO($A^2\Sigma^+$) intensity (Figure 39a and b) follows the gas phase HNO_2 concentration with increasing H_2O content, suggesting NO is directly involved in HNO_2 formation (Figure 38a and b).

On the contrary, in (humid) N_2, the NH trend (based on the NH($A^3\Pi$) intensity) and the NH_3 trend (measured downstream) show opposite behavior at high humidity (50–100% H_2O content; see Figure 38a and b). I.e. inside the plasma the NH generation continues rising throughout the whole humidity range, corresponding to the increase in H_2O (and hence H), as shown in Figure 39a and b, while NH_3 decreases or plateaus after 50% humidity. Most importantly, the results with (humid) air not only show the presence of NH($A^3\Pi$), but also its increase with

increasing H_2O vapor content (Figure 39c and d), contrary to the lack of NH_3 in the gas phase downstream (see Figure 38c and d). This clearly demonstrates that the NH_3 precursor NH is produced in the plasma, both in humid N_2 and air. This discrepancy in the NH behavior compared to NH_3 suggests that NH_3 is “lost” after the plasma, before the downstream FTIR analysis. To obtain insights in the aforementioned pathway of NH_3 decomposition, we used spatially resolved emission spectroscopy, perpendicularly to the plasma effluent (Figure 9). For these conditions we also measured $N_2(C^3\Pi–B^3\Pi)$ (see below), and found a correlation between NO and the excited state of N_2. Indeed, next to ground state and vibrationally excited N_2, electronically excited N_2 also plays a role in the main formation reactions of NO, i.e. the Zeldovich mechanism (R VI.2 and R VI.3, Table 9)[87].

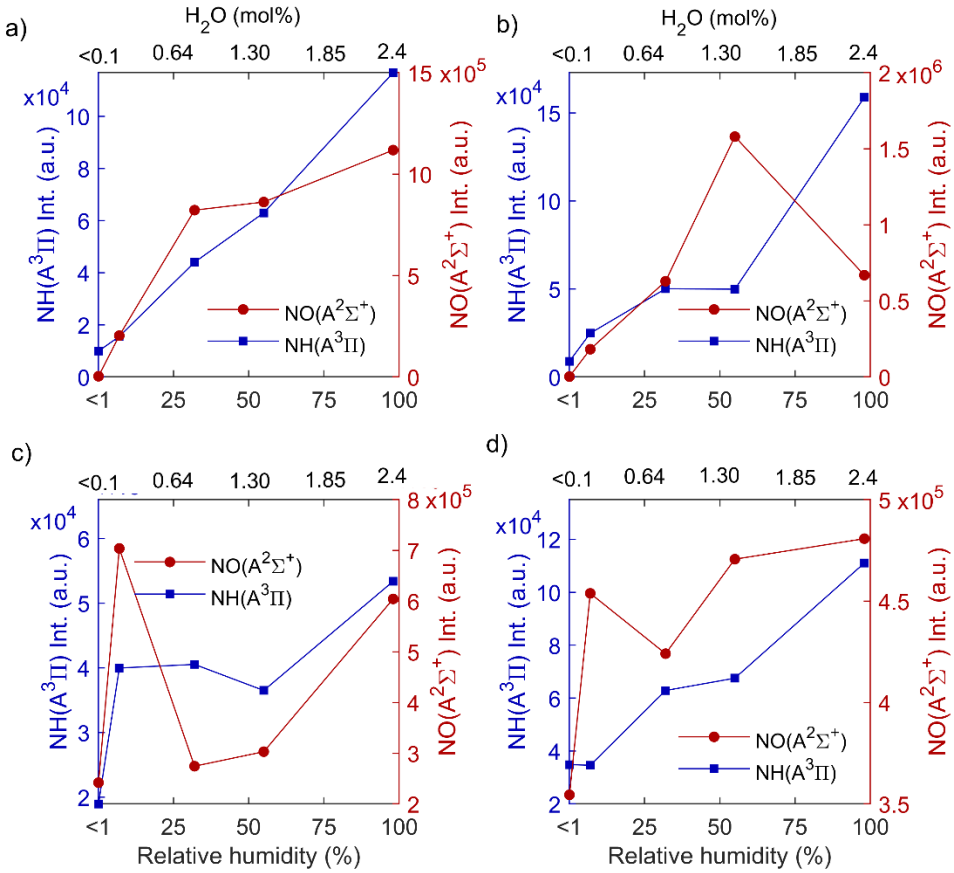

Figure 39 NH($A^3\Pi$) (left y-axis) and NO($A^2\Sigma^+$) (right y-axis) intensities in the plasma as a function of feed gas humidity. (a) N_2, 0.5 L/min; (b) N_2, 2 L/min; (c) air, 0.5 L/min; (d) air, 2 L/min.

3.3 NH presence in the afterglow

In the afterglow, the following state transitions were observed: NH($A^3\Pi$–$X^3\Sigma$), N_2($C^3\Pi$–$B^3\Pi$) and NO($B^2\Pi$–$X^2\Pi$). The NO($A^2\Sigma^+$–$X^2\Pi$) transition was below the limit of detection in the afterglow under the conditions studied, however, the NO($B^2\Pi$–$X^2\Pi$) transition is visible in the 338–340 nm region for some conditions. Figure 40 shows typical emission spectra (334–340 nm) along the plasma jet stream measured at a distance from 1 to 10 mm from the jet's outlet (or nozzle), for 5%

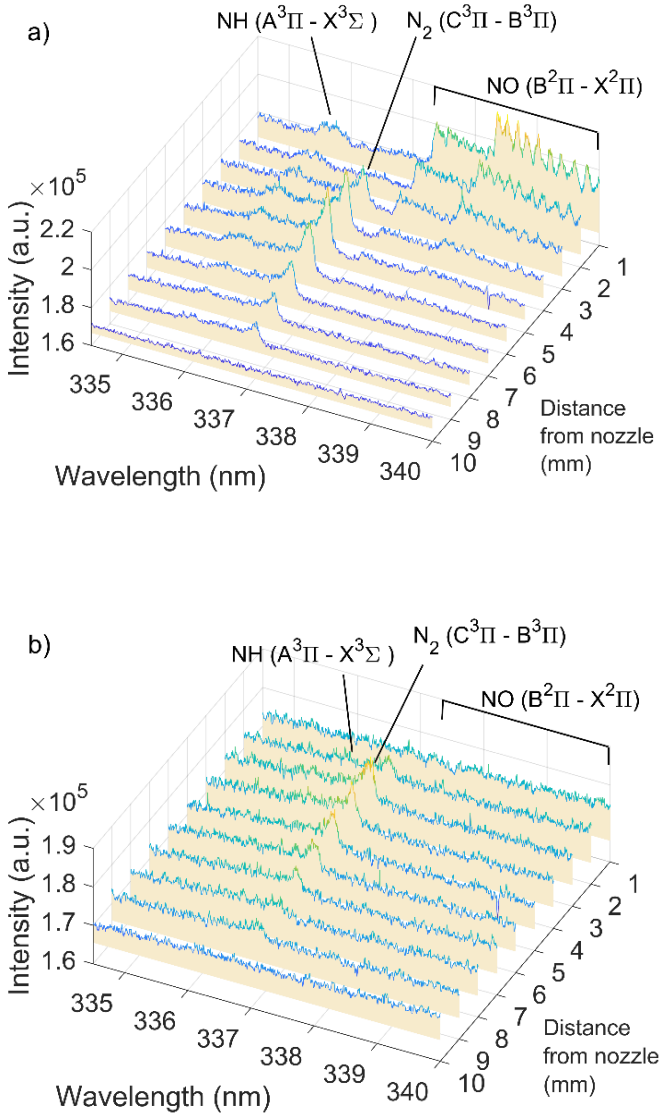

Figure 40 Emission spectra (334–340 nm) as a function of distance from the jet nozzle (1–10 mm), for 5% relative humidity at 2 L/min, in N_2 (a) and air (b).

relative humidity in N_2 and air, at 2 L/min. Spectra for all other conditions (N_2 and air, 0.5 and 2 L/min, from <1 to100% relative humidity) are found in Appendix R, pg. IX-277. It is worth noting that $N_2(C^3\Pi–B^3\Pi)$ was also observed in the axial OES. However, there its presence is non-informative. In contrast, the space-resolved

perpendicular OES allowed us to draw conclusions on the relationship between various chemical species present in the plasma afterglow.

While no direct correlation between NO($B^2\Pi$–$X^2\Pi$) and either NH($A^3\Pi$) and N_2($C^3\Pi$) was found, the obtained data allowed us to draw conclusions on the relationship between NH($A^3\Pi$) and N_2($C^3\Pi$). At all conditions, NH($A^3\Pi$) correlates strongly with the presence of N_2($C^3\Pi$) in the plasma and in the afterglow. Indeed, next to vibrationally excited N_2, electronically excited N_2 also plays a role in the splitting of N_2, which is a necessary step in NH formation[87].

Interestingly, at low humidity (5–30%) in N_2, another excited state, N_2($B^2\Pi$), is formed through high energy electrons, and is effectively quenched at higher H_2O concentrations and at higher O_2 fractions[259]. This is the reason why the NO($B^2\Pi$) emission is visible only in N_2 gas, and only at low humidity (Figure 40a; see also Appendix R, Appendix Figure 17k, 17q and to a lesser extent 17l and 17r, pg. IX-277). NH($A^3\Pi$) is observed in N_2 even when only trace amounts of H_2O vapor are present (see Appendix R, Appendix Figure 17k and 17p, pg. IX-277), due to the relatively low excitation energy needed for NH ground state excitation (3.68 eV)[190], and because there is only a small amount of strong quenchers present (i.e. H_2O) for NH($A^3\Pi$)[182,186] in the feed gas.

As discussed above, no NH_3 was detected in the gas phase downstream when humid air was used as feed gas. At the same time, we have measured NH_3 in liquid when the plasma was placed above liquid water[140] and we observe by OES the formation of NH($A^3\Pi$), an indicator for NH_3, when humid air is used, both in the plasma and in the afterglow.

3.4 NH_3 and HNO_x loss through salt formation and decomposition

To explain this discrepancy, we considered that NH_3 can form salts with HNO_x and looked at the most commonly reported pathways for the formation and decomposition of NH_4NO_x (summarized in Table 10, R VI.4-R VI.11)[260–262]. It is known from the selective catalytic reduction process (SCR) that NO_x and HNO_x can react with NH_3, which facilitates their conversion into N_2 and H_2O via NH_4NO_2 and NH_4NO_3 intermediates. Unlike in SCR, in plasma synthesis, the formation of NH_4NO_2 is undesirable as it decomposes back to N_2 and H_2O at room temperature and atmospheric pressure[263]. On the other hand, NH_4NO_3 is more stable and requires higher temperatures to undergo decomposition (R VI.10)[261,264,265]. The formation of NH_4NO_x has been observed in plasma systems as well, e.g. in a DBD which focuses on NH_3 oxidation[266,267].

In our experimental setup, the residence time between the plasma and the FTIR (0.07 and 0.3 s for 2 and 0.5 L/min, respectively) is sufficient to allow complete conversion of NH_3 and HNO_2 into NH_4NO_2 (assuming reaction R VI.6). Indeed, the timescale for loss of NH_3 (drop in concentration from 50 ppm to 0.1 ppm) would be around 0.1 s, making NH_4NO_2 formation a plausible pathway in this system.

Table 10 Relevant reactions, and corresponding reaction rate coefficients and relevant temperature ranges, for the formation and decomposition of NH_4NO_x.

Reaction	Rate coefficient [a] /Equilibrium constant (R9) [b]	Temperature range		Ref
$NO + OH + M \rightarrow HNO_2 + M$	$7.52 \times 10^{-31} (T/300)^{-2.4}$	200–400 K	R VI.4	210
$NO_2 + OH + M \rightarrow HNO_3 + M$	$1.63 \times 10^{-30} (T/300)^{-2.9}$	300–600 K	R VI.5	268
$HNO_2 + NH_3 \rightarrow [NH_4NO_2]$	3.65×10^{-18}	298 K	R VI.6	269
$HNO_2 + NH_4NO_3 \rightarrow [NH_4NO_2] + HNO_3$	n/a		R VI.7	262
$[NH_4NO_2] \rightarrow N_2 + 2H_2O$	n/a (unstable)	<400 K	R VI.8	263
$NH_3(g) + HNO_3(g) \leftrightarrow NH_4NO_3(s)$	$2.46 \times 10^{10} \times (118.87 - 24084/T - 6.025 \times \ln(T))$	265–305 K	R VI.9	270
$NH_4NO_3 \rightarrow N_2O + 2H_2O$ [c]	$10^{6.7} \times e^{-86/RT}$, $10^{14} \times e^{-207/RT}$	350–600 K	R VI.10	271
$NH_4NO_3 + NO \rightarrow NO_2 + NH_4NO_2$	n/a		R VI.11	262,272

M is any neutral molecule and T is the gas temperature

[a] Unit: $cm^3/(molecules \cdot s)$ for two-body reactions, and $cm^6/(molecules^2 \cdot s)$ for three-body reactions.

[b] Unit: $molecules^2/cm^6$

[c] In the temperature range 530 - 560 K, 98% of the irreversible decomposition of NH_4NO_3 occurs via this reaction[273]. However, in NO rich conditions R8 is more favourable[262].

Therefore, we hypothesize that downstream from the plasma in our system HNO_2 reacts with NH_3 to form NH_4NO_2, which rapidly decomposes into N_2 and H_2O (R VI.6-R VI.8)[264,274]. We note that NH_4NO_2 can also be formed through HNO_3 as an intermediate (R VI.7). However, we assume this pathway to be negligible in our experiments because we observe HNO_3 neither in the gas nor in the liquid.

Another plausible explanation is the precipitation of NH_4NO_3, which has also been described in SCR systems and as a direct product in plasma systems[261,264,265]. However, in the case of N_2 as feed gas, formation of NH_4NO_3 is unlikely: this would require HNO_3 being present, but we detected HNO_3 neither in the gas phase (in this Chapter) nor in PTW in the previous Chapter of this thesis[140]. Therefore, we infer that while in humid air plasma the loss of NH_3 is possible through NH_4NO_3 (R VI.9, R VI.10 and R VI.11) and NH_4NO_2 (R VI.6, R VI.7, R VI.8 and R VI.11), in N_2 plasma the loss of NH_3 at higher humidity levels, as seen in Figure 38a and b, occurs almost solely through NH_4NO_2.

To confirm our hypothesis about NH_4NO_x, we performed an in-line removal of HNO_2 (and possibly HNO_3) immediately after plasma by adding a Drechsel flask with 1M aqueous solution of NaOH (see Figure 37, following line B, i.e. including the base washer). This basic medium completely dissolves gaseous HNO_x, while hindering the solvation of gaseous NH_3 which thus passes further downstream, as was shown in the case of N_2 with H_2O vapour[130]. Figure 41 shows the effect of HNO_x removal on the FTIR spectra, reflected in the NH_3 concentration measured in the gas phase downstream from plasma. When an alkaline medium is added to trap HNO_2, the concentration of NH_3 in humid air goes from non-detectable (cf. also Figure 38c and d) to clearly detectable (Figure 41). Specifically, at 2 L/min air, 100% RH, we

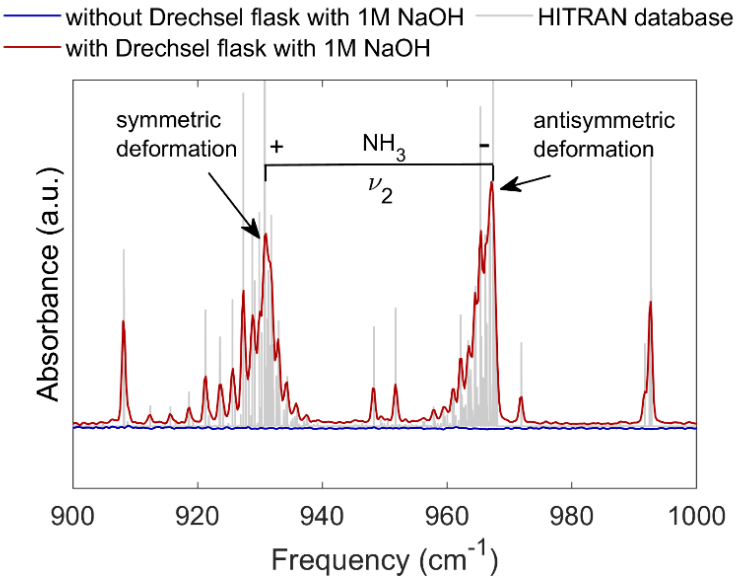

Figure 41 FTIR spectra of the NH_3 ν_2 deformation region, with and without HNO_x removal by NaOH, at 100% relative humidity in air, 2 L/min. The symmetric and antisymmetric deformations of NH_3 are shown, together with the simulated NH_3 spectrum in this range as obtained from the HITRAN database[192].

measured a NH_3 concentration of ca. 50 ppm in the gas phase. This fully supports our above hypothesis.

Thus, we demonstrate for the first time that NF from air with H_2O vapor proceeds via a pathway towards NH_3 as well as NO_x/HNO_x, but this can be overlooked because of the product loss downstream due to side reactions leading to NH_3 decomposition.

These data are consistent with the drop in HNO_2 and NH_3 concentrations at a H_2O content above 30% relative humidity (Figure 38). Once HNO_2 and NH_3 are produced simultaneously, NH_4NO_2 starts being formed and further decomposes, thus effectively decreasing the net HNO_2 and NH_3 production. In air, the concentrations of the generated HNO_x are certainly higher than in N_2, due to the presence of O_2 and associated oxidative pathways. At the same time, in air the

concentration of NH_3 is likely lower due to the larger contribution of competing reactions with the excited N_2 molecules (i.e., oxidative versus reductive NF). As a result, some (but not all) NH_3 and some HNO_x are likely lost due to the NH_4NO_x formation when N_2 is the feed gas, while virtually all NH_3 is lost when using air.

This effect appears to be slightly different at 0.5 L/min in N_2 (Figure 38a). Even though the NH_3 concentration plateaus instead of rises upon increasing humidity, both HNO_2 and NH_3 do not drop (as is the case with other high humidity conditions, Figure 38b and d), and HNO_2 even shows a rising trend until 100% humidity. While the specific reasons for this are unclear at this point, we propose that the adverse effect of NH_4NO_x formation is still present, because otherwise the continuous rise of NH_3 concentrations should be observable. This question presents an important point for further research aimed at decreasing this loss mechanism, next to the use of an in-line HNO_2 removal.

However, as mentioned above, NH_4NO_2 is not the only salt formed from NH_3 and HNO_x. In our experiments, we observed the build-up of a fine white powder in the quartz tube used during the OES experiments, Qualitative analysis of the powder via the indophenol blue reaction (described elsewhere[134,201]) demonstrated that the cation of the salt was indeed NH_4^+[24,47]. A negative Griess reagent test[275] excluded the presence of NO_2^-. This is in agreement with NH_4NO_2 not being a stable product at atmospheric pressure and room temperature[263] (Table 10). Therefore, we conclude that the anion was likely NO_3^-, in agreement with Zhu et al.[114], who observed NH_4NO_3 dust formation after operating plasma which contained both NH_3 and NO_x. We note, however, that the amount of solid formed after weeks of our experiments (at different flow

rates and humidity values) was in the range of mg. This is due to the (likely) very low amount of HNO_3 formed in our plasma[122]. Indeed, although low concentrations of HNO_3 would be expected in our experiments because substantial amounts of NO_2 are produced in the gas phase with air plasma, no HNO_3 was detected. Hence, it is reasonable to conclude that all formed HNO_3 reacted with NH_3 to form NH_4NO_3. Interestingly, when liquid H_2O was used to accumulate the NF products, both NO_3^- and NH_4^+ were detected in PTW with air plasma. In case of a close liquid surface, NH_4NO_3 did not precipitate out of the gas phase due to the short flight time to the liquid surface. Liquid water prevents decomposition via dissolution; the coordination of ions with water molecules in solution stabilizes the ions and inhibits decomposition reactions.

Furthermore, a semi-quantitative assessment of the relative loss pathways in this case was performed, with humid air. We performed the experiment with 2 L/min of air, 100% RH, for 3 h, during which we observed precipitate deposition on the tubing. After this, a gravimetric analysis of the precipitate was performed by washing the precipitate off the walls of the tubing. After evaporation of water, the mass of the accumulated precipitate was found to be below 5 mg. As shown above, by introducing the alkaline washer, 50 ppm of NH_3 was “recovered” under these conditions (we note once again that the alkaline washer is not selective, and removes HNO_x rather than only HNO_2 or only HNO_3). This amounts to ca. 74 nmol/s of NH_3. From the stoichiometry of NH_4NO_3 formation, we conclude that after 3 h the amount of precipitate would constitute 64 mg if all of it was NH_4NO_3 – which is not the case. Thus, the relative contribution of the NH_4NO_3 pathway to NH_3 loss does

not exceed 10%. Therefore, even in the humid air plasma, most of NH_3 is lost via the generation and subsequent decomposition of NH_4NO_2.

3.5 Energy consumption and production rate

Although performance optimization is not the focus of this Chapter, we also assessed the energy consumption (EC) and the production rate (PR) of NF in our experiments. Using the plasma power (P) and the total (H)NO_x concentration, the EC was calculated according to eq. VI.1. The EC is expressed in MJ/(mol N), where mol N is the amount of nitrogen fixed.

$$EC\left(\frac{MJ}{mol}N\right) = \frac{P(\mathrm{W})}{mol\ of\ (\mathrm{H})NO_x\ produced\ per\ second\ \left(\frac{mol}{s}\right)} \times \frac{1}{10^6\ \left(\frac{J}{MJ}\right)} = \\ = \frac{P\ (W) \times\ 10^6 \times 60\ \left(\frac{s}{min}\right) \times\ 22.4\ \left(\frac{L}{mol}\right)}{(C_{HNO2} + C_{NO2} + C_{NO} + C_{NH3})\ (\mathrm{ppm}) \times Flow\ rate\ \left(\frac{L}{min}\right) \times 10^6 \left(\frac{J}{MJ}\right)} \qquad \text{VI.1}$$

Table 11 Average energy consumption (EC) of nitrogen fixation, based on the plug power and the plasma power.

Flow rate (L/min)	**Relative Humidity (%)**	**EC* (MJ/(mol N fixed) *Plug power***		**EC* (MJ/(mol N fixed) *Plasma power***	
		Air	N_2	Air	N_2
0.5	<0.1	5.54	-	0.58	-
	5	5.40	238.01	0.57	25.10
	30	5.03	192.28	0.53	20.28
	50	4.79	78.25	0.51	8.25
	100	6.12	59.22	0.65	6.25
2	<0.1	4.45	-	0.47	-
	5	3.37	106.03	0.36	11.18
	30	2.93	43.13	0.31	4.55
	50	2.18	22.03	0.23	2.32
	100	2.70	60.76	0.29	6.41
2**	100	2.24	-	0.24	-

*We note that the EC and PR values shown are not compensated for the losses due to the NH_4NO_2 decomposition and NH_4NO_3 precipitation because the experiments with the alkaline washer were not performed for every condition used.

**Results with alkaline washer included in EC.

In Table 11, we present the EC calculated based on the *plasma power* (0.11 W) and based on the *plug power* for the so-called *plug-to-NO_x* EC (1.04 W; see Chapter 2.3). The plasma power, which is used to support the sustaining of the discharge, can be one factor of magnitude lower than the plug power. Comparing both results gives different information on the state of the art in plasma-based NF. (1) Looking at the EC based on the plug power, even the lowest EC we observed is still ca. 4 times higher than the EC of Haber-Bosch, which is 0.48 MJ/(mol N). Nonetheless, plasma has the advantage of being able to use renewable electricity, because of its fast switch on/off capacity, and is therefore promising for distributed fertilizer production. Based on this, we infer that plasma processes should be used as an auxiliary technology, rather than substituting the current industrial state-of-the-art entirely, with the current performance. (2) The difference between the EC based on the plug power and the plasma power shows that the overall EC can be drastically improved by optimization of the power supply system. The engineering challenge is to design a power system where power efficiency is optimized, which is however out of the scope of this thesis.

The production rate (PR) of the various products (x), and the conversion of N_2 in our system was calculated as shown in eq. VI.2 and VI.3:

$$PR_x\left(\frac{mg}{h}\right) = \frac{C_x\ (\text{ppm}) \times Flow\ rate\ \left(\frac{L}{min}\right) \times 60\ \left(\frac{min}{h}\right)}{22.4\ \left(\frac{L}{mol}\right) \times 10^3} \times \text{M}_\text{x}\ \left(\frac{g}{mol}\right)\ (\text{S11}) \qquad \text{VI.2}$$

$$N_2\ conversion\ (\%) = \frac{(C_{HNO2} + C_{NO2} + C_{NO} + C_{NH3})\ (\text{ppm})}{N_2\ fraction\ in\ the\ feed\ gas\ (\text{ppm}) \times 2} \times 100\%\ (\text{S12}) \qquad \text{VI.3}$$

The data presented in Table 12 demonstrate that numerical values of PR are different for different conditions, as follows from the different selectivity towards different products (see Figure 38 above).

Table 12 Flow rate, production rate and N_2 conversion at all experimental conditions reported in this Chapter.

Flow Rate (L/min)	**Relative Humidity (%)**	**Production rate (mg/h)**								**N_2 conversion (%)**	
		Air				**N_2**				**Air**	**N_2**
		NO	**NO_2**	**NH_3**	**HNO_2**	**NO**	**NO_2**	**NH_3**	**HNO_2**		
0.5	<0.1	18	3.4	-	-	-	-	-	-	0.032	-
	5	17	2.7	-	1.8	-	-	0.20	0.19	0.032	0.00059
	30	18	2.7	-	4.2	-	-	0.14	0.53	0.035	0.00073
	50	19	2.9	-	4.0	-	-	0.21	1.3	0.037	0.0018
	100	15	1.7	-	3.5	-	-	0.21	2.39	0.029	0.0024
2	<0.1	19	9.9	-	0.0	-	-	0.00	0.00	0.010	-
	5	23	11	-	5.1	-	-	0.51	0.26	0.013	0.00033
	30	23	11	-	14	-	-	0.92	1.5	0.015	0.00081
	50	37	6.1	-	17	-	-	0.76	4.2	0.020	0.0016
	100	29	5.3	-	15	-	-	0.00	2.9	0.016	0.00058

For example, at 2 L/min of N_2, 100% relative humidity, the main product is HNO_2 (with a PR of 2.9 mg/h). Under the same conditions but in air, NO is the main product (with a PR of 29 mg/h). The relative improvement in a hypothetical scenario when NH_3 and HNO_2/HNO_3 are not lost in our experiments was evaluated. Let us consider example conditions of humid air plasma operated at 2 L/min, 100% RH, i.e. the same conditions at which the experiment with the HNO_x-removing washer was performed. Here, we detect 50 ppm of NH_3, which means also 50 ppm HNO_x was lost. The overall concentration of NF products without accounting for the NH_4NO_x loss is ca. 300 ppm (see Figure 38), which becomes 400 ppm when NH_4NO_x is not lost. Therefore, the relative decrease in EC, and the relative increase in PR, when the product loss is avoided amounts to ca. 30%. Using liquid water as a reservoir to accumulate the nitrogen fixation products can aid in this. Taken together, these data clearly suggest that using liquid H_2O in proximity to the plasma zone is beneficial: it increases the total net accumulation of the NF products, because it reduces or even eliminates the loss of NH_4NO_x. Other ways to counter the adverse effect of NH_4NO_x decomposition could be by engineering ways to effectively scavenge before decompositions via for example a bubbling setup, sprays or flowing liquid and by focussing on improving the selectivity towards one product, while maintaining total NF through for example the use of a catalyst. Dedicated studies are necessary to evaluate these or develop new approaches.

4 Conclusions

We studied the pathways of nitrogen fixation in humid N_2 and humid air plasma using OES and FTIR. We revealed that the increased NH emission, as well as NH ground state density, strongly correlates with the water vapor content in both N_2 and air plasmas, indicating that the reduction nitrogen fixation pathway (towards NH_3 formation) takes place in both gas mixtures.

We show for the first time that NH_3 is produced in air plasma in non-negligible quantities (in the same order of magnitude as HNO_2, and only an order of magnitude lower than NO and NO_2 combined). However, in both air and N_2, this nitrogen fixation pathway is strongly affected by the presence of HNO_2 and HNO_3.

In humid air, the formation of both NH_4NO_3 and NH_4NO_2 likely occurs. Although both of these can decrease the process efficiency downstream, part of NH_3 remains in fixated form as precipitated NH_4NO_3. In contrast, in humid N_2 we ascribe the loss pathway exclusively to NH_4NO_2, which is unstable and decomposes to N_2 and H_2O, decreasing the overall nitrogen fixation efficiency.

In summary, this Chapter shows that (1) the selectivity of nitrogen fixation in air and N_2 plasmas can be controlled by changing the humidity of the feed gas, (2) NH_3 production can be achieved in both N_2 and air plasma using H_2O as a hydrogen source, and (3) the adverse effects of NH_4NO_2 formation hinder the net production, and therefore the overall efficiency, of the plasma-based nitrogen fixation process. The latter means that, under conditions where HNO_2 and NH_3 are produced simultaneously, it is important to suppress the reverse process (via decomposition of NH_4NO_2). This can be performed

through an in-line removal of HNO_2 from the gas mixture, or by using PTW to accumulate all nitrogen fixated products simultaneously without losses.

VII. GENERAL CONCLUSIONS AND OUTLOOK

N-based fertilisers are paramount to support our still-growing world population. Current industrial N_2 fixation is heavily fossil fuel-dependent, and therefore, a lot of work is put into the development of fossil-free pathways. Plasma-based NF is one technology that fits better in the sustainable world we are trying to achieve.

Throughout this thesis, we took into account the knowledge gaps identified in the plasma-based NF state of the art.

1. We de-coupled the problem for pathway elucidation by (i) first thoroughly characterizing the plasma that was used throughout this thesis, (ii) focussing on a simple dry system before adding water and (iii) studying the role of liquid vs gaseous water before moving on to a more detailed pathway elucidation.
2. In the dry system, we enabled more detailed elucidation by including modelling.
3. We branched out to another way of adding water to the system, i.e. water vapor, and dedicated a study to elucidating the role of gaseous H_2O vs liquid H_2O, including the liquid surface.
4. We focussed on analyzing species in both the gas and the liquid phase.

The following research questions were answered:

In **Chapter IV**, we discussed a pulsed plasma source that showed a near-the-theoretical-energy-limit EC for NO_x production from air.

What underlying mechanism are at the base of the low energy consumption achieved in the Soft Jet, a pulsed low-temperature source?

Based on the reaction analysis of a validated quasi-1D model, we can conclude that pulsing is indeed the key factor for energy-efficient NO_x-formation. The model shows that it is mainly the strong temperature drop in between pulses which (1) affects the forward and backward rate of the Zeldovich mechanism, such that a.o. the back reactions are limited and (2) enhances the N_2 vibrational population, responsible for energy-efficient NO_x production.

In **Chapter V**, we added H_2O vapor to the feed gas of the Soft Jet above a H_2O surface and measured excellent selectivity towards NH_3 in humid N_2 and even observed NH_3 production in humid air.

What is the role of liquid vs gaseous H_2O in wet plasma-based NH_3 formation?

We studied the role of H_2O vapor and of the plasma-exposed liquid H_2O in NF by using isotopically labelled water to distinguish between these two sources of H_2O and by increasing the plasma-liquid surface distance. We showed that added H_2O vapor, and not liquid H_2O, is the main source of H for NH_3 generation. This can be taken into account in future wet plasma-based NF designs by focussing on increasing the water vapor content in the plasma.

In **Chapter V** and **Chapter VI**, we looked more closely into the pathways towards NF species.

What are the important chemical pathways towards plasma-based NF species (NH_3/(H)NO_x) in a wet environment?

Though this question remains open, this thesis adds to the current state of the art. The conclusions on the pathways can be summarized as follows.

Both **Chapter V** and **Chapter VI** showed that the selectivity of plasma-based NF in humid air and humid N_2 can be controlled by changing the humidity in the feed gas. Those Chapters also showed that NH_3 production can be achieved in both N_2 and air plasmas using H_2O as a H source. In **Chapter V**, we identified that for our plasma system, water vapor is the main H source for NH_3 production. Additionally, in **Chapter VI**, we identified a significant loss mechanism for NH_3 and HNO_2 that occurs in systems where these species are synthesized simultaneously, i.e. downstream from the plasma, HNO_2 reacts with NH_3 to form NH_4NO_2, which decomposes into N_2 and H_2O. This reduces the effective NF when not properly addressed, and should therefore be considered in future works aimed at optimizing plasma-based NF.

If we look at the state of the art including this thesis, the following areas could use focus.

1. It would be important to validate our results further in other plasma setups and to attempt to apply the knowledge presented in this thesis for performance enhancement. Specifically, the following is proposed.

   The near-the-theoretical-energy-limit EC described in **Chapter**

IV has been confirmed in a similar plasma by other authors, however transferring this knowledge to another design, with the focus on improving the NO_x yield has not been attempted. A plasma with modulating pulse settings would be appealing for this kind of study. Next, expanding the gas phase model presented in **Chapter IV** to one containing H_2O vapor would be highly beneficial. Including liquid H_2O is more challenging, however, as stated before, it is advantageous to first elucidate the gaseous system, opposed to a multi-phase one. Furthermore, the role of gas vs liquid H_2O as suggested by us in **Chapter V** has been implied in other works as well, nonetheless, due to the complexity of plasma-liquid systems this should be explored further. We should investigate the universality of gaseous H_2O being a more advantageous H source compared to liquid H_2O by studying a larger variety of humid air and humid N_2 plasmas, with the focus on NF. Furthermore, we should explore more ways to increase the H_2O vapor fraction in the plasma and study the influence of high H_2O vapor content. On the other hand, we identified a decomposition pathway via NH_4NO_x in **Chapter VI**. Trapping the NF product in water was proposed as a way to reduce this loss pathway, potentially giving liquid H_2O a vital role again, though not as H source. As Gromov et al. also suggest a loss of efficiency in the presence of liquid H_2O, the balance between the two factors should be studied and other innovative methods could be explored to avoid this pathway. Avoiding contact or close proximity between the plasma and the liquid might even be enough.

2. When the underlying chemistry of wet plasma-based NF has been more established and the advantages and disadvantages have been mapped, we can look for synergies with other NF fields. Indeed, the state of the art illustrated that plasma in combination with electrochemistry and catalysis improves the performance of NF, however, further advancement beyond exploration is more challenging to achieve if the separate processes are not properly elucidated.
3. Wet plasma-based NF is in an earlier research stage compared to dry plasma-based NF, nonetheless is it important to also focus on the technological aspects of this application. While this field is fundamental in nature, it does exist relatively close to applied research due to the need for an alternative NF process in the near future. By coupling back to techno -economic and life cycle analysis as well as industry, we can ensure a steady course during exploration and elucidation of wet plasma-based NF.

In conclusion, this thesis adds further to the current state of the art of plasma-based NF both in the presence of H_2O and in dry systems.

VIII. MATERIALS

Table 13 A list of the chemicals and equipment used in this thesis.

Chemical	Formula	details	Supplier	Entry
Nitrate/nitrite colorimetric Assay Kit			Cayman Chemicals	1
Potassium nitrate	KNO_3	99%	Alfa Aesar	2
Griess Essay				3
Sulphanilamide				4
naphtylethylenediamine				5
Sodium nitrite	$NaNO_2$	98%	Alfa Aesar	6
Phosphoric acid		85%		7
LabAssay Ammonium kit			Fujifilm Wako Pure Chemical Corporation	8
Hydrogen peroxide	H_2O_2	30 wt%	Sigma	9
NaN_3		(≥98%)	Sigma	10
$K_2TiO(C_2O_4)2•2H_2O$		1 M (≥98%)	Sigma	11
H_2SO_4		97%	Sigma	12
NH_2OH		50 wt%	Sigma	13
1,10-phenanthroline		≥99%	Sigma	14
CH_3COONa			Sigma	15
CH_3COOH		100%	Sigma	16
$NH_4Fe(SO_4)_2•12H_2O$		≥99%	Sigma	17
HCl		37%	Sigma	18
Spectroquant Hydrazine Test Kit			VWR	19
NH_2NH_2 . H_2O			VWR	20
D_2O		99.9%	Sigma Aldrich	21
Gasses				
Air	Last Chapter	Chapter IV and VI, 99.999%	Air Liquide Alphagaz 1	22
N_2	Last Chapter	Chapter IV and VI, 99.999%	Air Liquide Alphagaz 1	23
N_2		Chapter V, 99.999%	Praxair	24
Air		Chapter V, 99.999%	Praxair	25

Equipment	Details	Supplier	Type	Entry
Voltage probe		Tektronix	P6015A	26
Current probe		Pearson	Current monitor 2877	27
Oscilloscope		Le Croy	WaveSurfer 64Xs	28
IR camera		Fluke	TiS45	29
ICCD camera	532 nm filter	Hamamatsu	C8484	30
Pulsed laser	wavelength 532 nm, pulse energy 12 mJ, repetition rate 10 Hz, pulse duration 8 ns	Litron	Nano-S Nd:YAG laser	31
Delay generator		SRS	DG535	32
Spectrometer	300-390 nm	Avantes	AvaSpec-3048	33
Halogen lamp (calibration)	250-2400 nm	Hamamatsu	D2 L7293	34
Power supply lamp		Hamamatsu	C9598	35
Spectrometer	UV 250 nm blazed 2400 g/mm grating (Used axial)	Horiba	iHR550	36
Spectrometer	500nm blazed grating of 3600g/mm with linear fiber optics array slit (Used perpedicular)	Zolix	Omni750	37
UV-VIS Spectrometer	Using Hellma quartz cuvettes	Thermo Fischer	Genesys 6	38
UV-VIS Spectrometer		Shimadzu	UV mini 1240	39
pH meter		Mettler Toledo	MP255	40
Thermometer		Extech Instruments	TM100	41
MFC	Chapter IV and VI	Bronkhorst	EL-FLOW® F-201CV	42
FTIR		Bruker	Matrix-MG2	43
MFC	Chapter V	Brooks Instruments	0254	44
Humidity meter		Testo	445	45

IX. APPENDIX

A. Calibration curves

These calibration curves are used for the liquid analysis explained in Methodology section 3.2.1, which is used in the experiments described in Chapter V and VI.

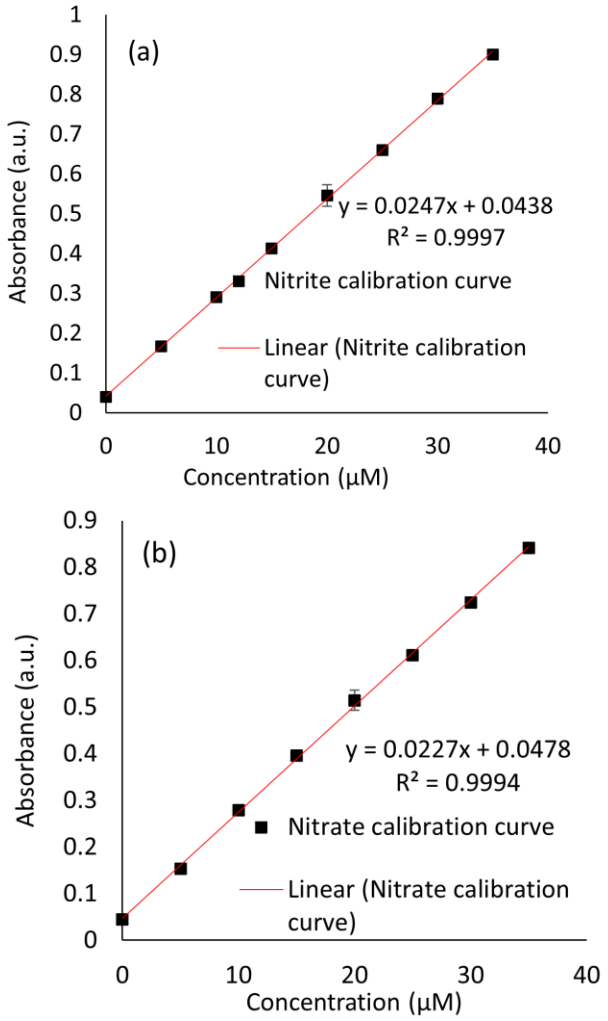

Appendix Figure 1 Calibration curves for the measurement of (a) NO_2^- and (b) NO_3^- in liquid H_2O samples.

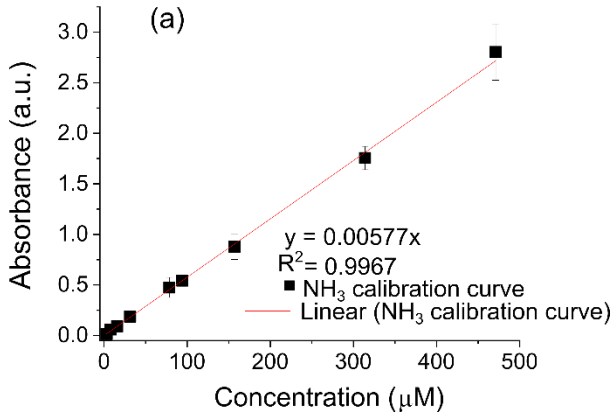

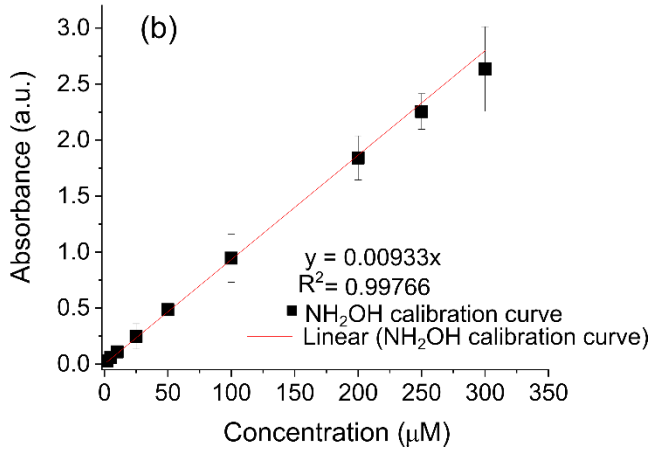

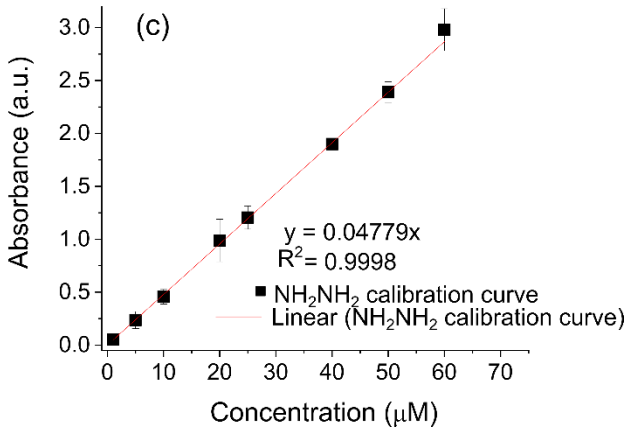

Appendix Figure 2 Calibration curves for the measurement of (a) NH_3, (b) NH_2OH and (c) NH_2NH_2 in liquid H_2O samples.

B. Selectivity of NH_3, NH_2OH and NH_2NH_2 colorimetric measurements in plasma-exposed water

Related to the liquid analysis explained in Methodology section 3.2.1, and used in the experiments described in Chapter V and VI, we performed extensive tests to determine the influence of possible other N_2 fixation and plasma-H_2O interaction products on the selectivity of the UV-VISUV-VIS spectrophotometric analysis used. We cross-tested each of the species: NH_3, NH_2OH, and NH_2NH_2, together with NO_2^-, NO_3^-, and H_2O_2 (i.e., all possible long-lived species in the plasma-exposed H_2O). NO_2^- was added as $NaNO_2$ (Chapter VIII, Materials, Table 13, entry 6), and NO_3^- as KNO_3 (Chapter VIII, Materials, Table 13, entry 2).

NH_3 analysis selectivity with the LabAssay Ammonium kit.

The calibration curve of NH_3 in absence of any other species is shown in Appendix Figure 2a. Of all tested species, only NH_2OH and NH_2NH_2 exhibited a potential to directly interfere with the colorimetric analysis: they both produced an absorbance peak with a maximum at 637 nm. NH_2OH gave much stronger interference than NH_2NH_2. Here, a 1 mM concentration of commercial NH_2NH_2 gave an absorption signal of ca. 0.040 a.u. This would correspond to 7 µM of NH_3 (Appendix Figure 2a). Therefore, unless NH_2NH_2 is produced in very large quantities, its interference can be disregarded. At the same time, NH_2OH gave much stronger absorption values, as shown in Appendix Figure 3. Therefore, NH_2OH concentrations must be measured, and included in the calculation of NH_3 concentrations. However, we note that in our experiments we did not observe any NH_2NH_2 or NH_2OH in H_2O after plasma exposure.

The overall analysis is based on the modified method developed by Ito et al.[276]. NH_3 is converted to dioxydiphenylamine (DODPA) via the reaction with phenol and $Na[Fe(CN)_5NO]$. DODPA is further oxidized to indophenol blue by ClO^-. H_2O_2 and NO_2^- in the plasma-exposed H_2O could react with ClO^- [277], which is added as one of the chromogens in the kit. However, ClO^- is added in a large excess, making the chosen method suitable for our experiments.

NH_2OH analysis selectivity. The only interference was from H_2O_2. However, the absorbance signal at 510 nm created in the analysis method by 1 mM H_2O_2 was ca. 0.051 a.u., corresponding to 5.5 µM NH_2OH (Appendix Figure 2). In all our experiments, the concentration of H_2O_2 did not exceed ca. 50 µM (see Figure 29 - Figure 32 in Chapter V). In any case, we did not detect any absorbance peaks at 510 nm when analysing the plasma-exposed H_2O solutions. However, NH_2OH can react with NO_2^-[278]. Thus, although we cannot exclude that some NH_2OH can be produced in situ during the plasma exposure, it is lost in a reaction with NO_2^-.

We explicitly note that the selectivity reported in our work is based on the final concentrations of the N_2 fixation products in H_2O, after plasma exposure.

***NH_2NH_2 analysis selectivity with the Spectroquant Hydrazine Test Kit*.** We did not observe any detectable analysis interferences for NH_2NH_2. Furthermore, in all experiments we did not observe the induction of an absorbance peak at 458 nm, i.e., no NH_2NH_2 was detected.

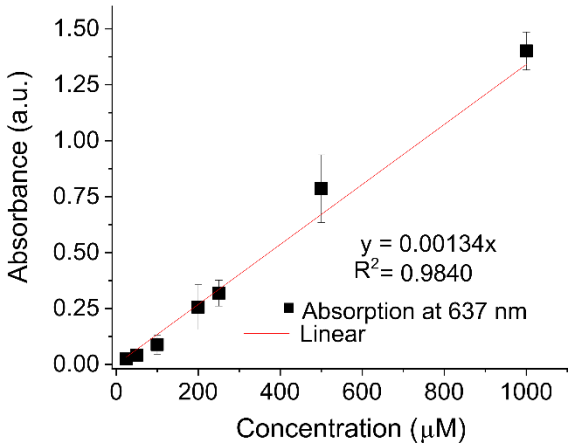

Appendix Figure 3 Absorption signal at 637 nm produced by various concentrations of NH_2OH using the LabAssay Ammonium Kit.

C. Chemistry set

This Appendix discusses the chemistry set used in Chapter IV, first introduced in the Methodology, section 6.2.2.

The set of reactions is based on a (revised) compilation of reactions reported in previous work based on my master thesis[59]. The set contains an elaborate description of the vibrational kinetics of N_2 and O_2, i.e. N_2 and O_2 electron impact vibrational excitations (e-V), N_2-N_2, O_2-O_2 and N_2-O_2 vibrational-vibrational (VV) exchanges and N_2-N_2, N_2-O_2, O_2-N_2, O_2-O_2, N_2-N, O_2-O and N_2-O vibrational-translational (VT) relaxations. 24 vibrational levels for N_2 and 15 levels for O_2 are included. Next to vibrational exchanges, the set includes electron impact, neutral-neutral, neutral-ion and ion-ion reactions. The species taken into account in the model are listed in Table 7 of Chapter IV. This includes neutral molecules in the ground state, vibrationally and electronically excited states, various radicals, positive and negative ions, and electrons. Appendix Table 3 lists all electron impact reactions.

Most of these reactions are treated by energy-dependent Cross-sections. Appendix Table 4 lists the neutral-neutral reactions and the corresponding rate coefficient expressions. For certain reactions, the rate coefficients of the vibrationally excited species are determined according to the Fridman-Macheret model, in which the activation energy is reduced by $\alpha\, E_v$, where α is the vibrational efficiency to lower the activation barrier and E_v is the vibrational energy. For those reactions, the α parameter is given in the last column of Appendix Table 4 (see also Methodology, Chapter II, section 6.2.2). Appendix Table 5 to Appendix Table 7 list the electron-ion recombination, ion-neutral and ion-ion reactions and the corresponding rate coefficients, respectively. Appendix Table 8 lists the optical transitions.

This chemistry set was extensively developed and validated in our previous work[216]. After critical review of the literature, one reaction rate coefficient (k) in Appendix Table 4 (annotated in bold) was updated to a more recent k value from a reliable source. The Tables can be found at the end of the Appendix (section T).

D. Validation of the chemistry set in the GAP

The chemistry set used in Chapter IV is based on the validated set used in previous work related to my master thesis[59] and can be found in Appendix S. To test the reliability and robustness, the chemistry set was validated for different gas compositions possible with a N_2-O_2 chemistry set, from 0/1 N_2/O_2 to 1/0 N_2/O_2 fractions, in a reverse vortex flow gliding arc plasmatron (GAP) developed by Nunally et al. at Drexel University[279]. In a classical GA reactor, an arc discharge is created between two electrodes by applying a potential difference. Subsequently, this arc glides along the electrodes dragged by a gas

flow. The GAP, on the other hand, has a very different design. It is a cylindrical GA reactor in which the gas flows in the reactor through tangential inlets, creating a vortex, and an arc is formed between the reactor body (cathode potential) and outlet (anode).

Appendix Figure 4a shows the modelled NO_x concentration as a function of the N_2 fraction in the feed gas compared to the experimental ones, as well as the yield and energy cost (Appendix Figure 4b and c).

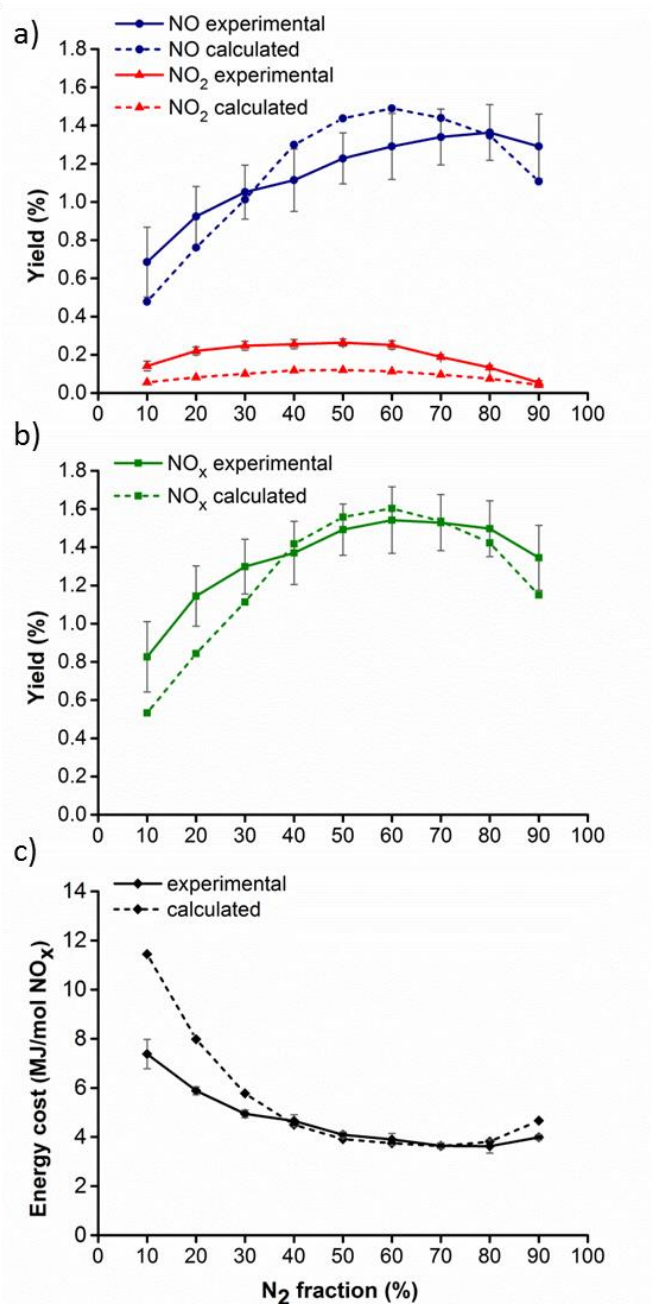

Appendix Figure 4 Experimental (solid lines) and calculated (dashed lines) yield of NO (blue) and NO_2 (red) (a), total NO_x yield (b), and energy cost (c), as a function of N_2 fraction in the feed gas, for a gas flow rate of 10 L/min, a pressure of 1.25 bar and a power ranging from 365 to 458 W.

Appendix Figure 4a shows the experimental and calculated NO (blue) and NO_2 (red) yields as a function of N_2 fraction in the gas mixture, for a gas flow rate of 10 L/min and a pressure of 1.25 bar. All experiments were repeated three times to determine the measurement uncertainty. The experimental NO yield increases upon increasing N_2 fraction, until it reaches a maximum value of 1.4% at 80% N_2, after which the yield drops slightly. The calculated NO yield (dashed blue curve) follows the experimental trend, but shows a maximum at 60% N_2. Indeed, according to the model, both N_2 and O_2 molecules must be present at almost equal amounts for the highest NO production. Still, the highest yield is reached at slightly higher N_2 than O_2 fractions, as in the experiments, but the parabolic trend is more pronounced than in the experiments. This results in a calculated NO yield at 40 - 60% N_2 to be slightly above the range of the experimental error bars. The reason for this discrepancy is not yet fully understood, but might be attributed to certain reaction rates that can be slightly over- and/or underestimated in our model. However, we did not want to tune our rate coefficients to reach an exact agreement without scientific basis. Nevertheless, in general, the calculated results show good agreement with the experiments, keeping in mind the complex chemistry and the approximations inherent to a 0D model (see section 6.2).

The trends of the calculated and experimental NO_2 yields are in very good agreement. The calculated NO_2 yield, however, is underestimated by a factor two. Considering the complexity of the chemistry included in the model, it is reasonable to conclude that our model adequately describes the plasma chemistry, in spite of the above-mentioned discrepancies, and can therefore be used to

elucidate the underlying mechanisms in a N_2 - O_2 gas mixture in this reactor.

Provided the chemistry set is revised critically for the source we are modelling in this thesis, we can use this chemistry set and code as a base, even though the presented validation was performed for another type of plasma (GAP). The above discussion also provides a common and realistic view of the error range and acceptability with regards to model-experiment agreement. Indeed, depending on the model type the extent of the agreement criteria between the simulated and measured date can vary. Though large differences in absolute values can certainly indicate a lacking or incorrect implementation of the chemistry, trends are providing much more information on the reliability of a chemical kinetics model.

E. CFD model of the Soft Jet

This Appendix discusses the CFD model used in Chapter IV, section 3.2, to transform the 0D model into a quasi-1D model.

The Soft Jet is cylindrically symmetrical, and its 2D geometry, considered in the CFD simulations, is shown in Appendix Figure 5. The 1D velocity profiles through the Soft Jet (Appendix Figure 6) are used to accurately transform the time-dependent simulation of the 0D model into a position-dependent one (quasi-1D model). The CFD calculations are performed until steady state is reached for each inlet flow rate, by means of a 2D axisymmetric turbulent gas $\kappa - \varepsilon$ model built in COMSOL Multiphysics.[280] The turbulent flow model results are used as input into the 0D model. It is independent of the plasma chemistry, i.e. we assume the flow is independent of the heat produced by the plasma or by changes in the gas composition due to chemical reactions. This is a valid assumption, as the spatially averaged gas temperature does

not exceed 350 K; hence, the influence of the gas heating on the flow behaviour is small compared with the background flow, and the conversion is too limited (<< 1 %) to cause any significant changes to the gas composition, and thus to the physico-chemical properties of the flow.

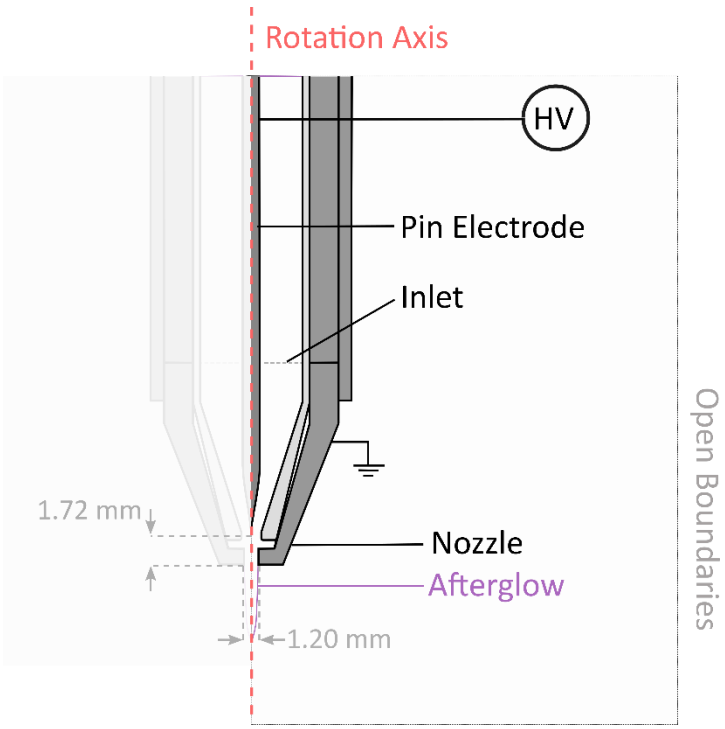

Appendix Figure 5 Geometry of the Soft Jet, used in COMSOL for the CFD calculations. The indication of the afterglow shape is used to ensure proper meshing around the outlet.

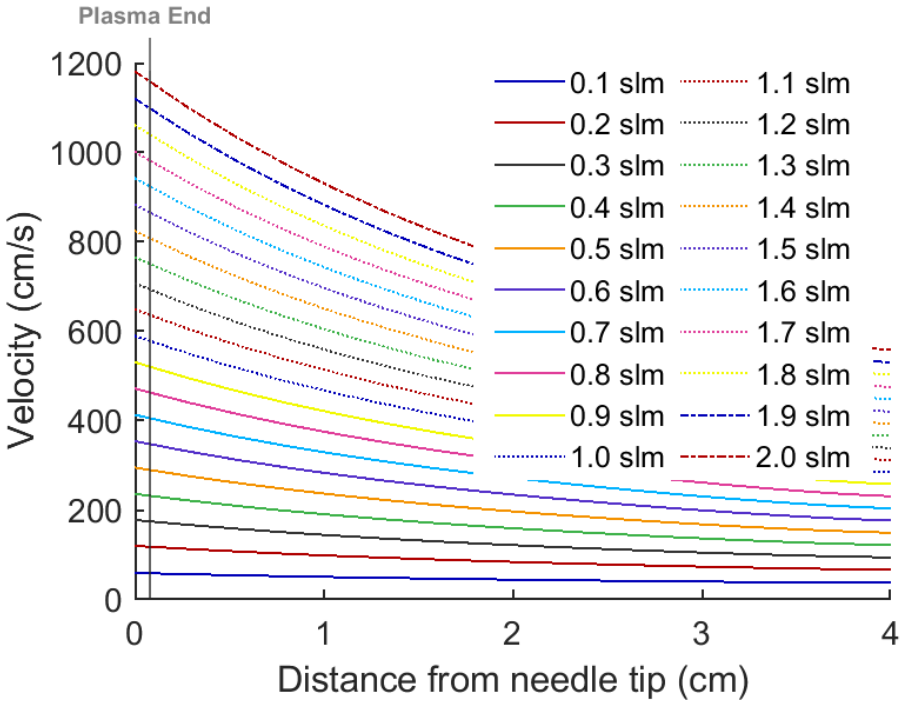

Appendix Figure 6 Axial gas velocity calculated via CFD simulations as a function of distance from the needle tip, for inlet flow rates of 0.1 – 2.0 L/min. The plasma end is indicated by the grey line (0.075 cm).

Based on these calculations, the residence time in the plasma ranges from 2 ms to 94 µs, for inlet flow rates ranging from 0.1 to 2.0 L/min, respectively.

The radial-component of the gas velocity at the nozzle edge is << 0.1 m/s for all flow rates. Hence, we can safely assume that short-lived reactive species do not come in contact with ambient air before they are destroyed, and thus mixing with ambient air at the nozzle does not have to be included in the quasi-1D model.

F. Interpulse gas temperature profile

This Appendix discusses how the interpulse temperature profile (used in Chapter IV, section 3.3.2) was determined in detail.

The temperature during the pulse, i.e. the temperature of the plasma arc, was measured to be 1750 $\pm$ 150 K and coincides with the power peak. During the interpulse, an exponential decay to 330 K is set in accordance with the average gas temperature measured by Rayleigh scattering in the afterglow (Table 6; section 3.2, Chapter III) The shape of the temperature decay in between pulses was estimated based on a sensitivity study where we tested four different profiles, shown in Appendix Figure 7: a slow linear drop (profile 1), an exponential drop (profile 2), a fast linear drop (profile 3) and a straight vertical drop after the pulse ends (profile 4). Profiles 1 and 4 act as limiting cases to estimate the influence of the temperature drop on the modelling results. The modelling results do not differ significantly for the different interpulse temperature profiles. We therefore chose the more intuitive profile 2, which is exponential.

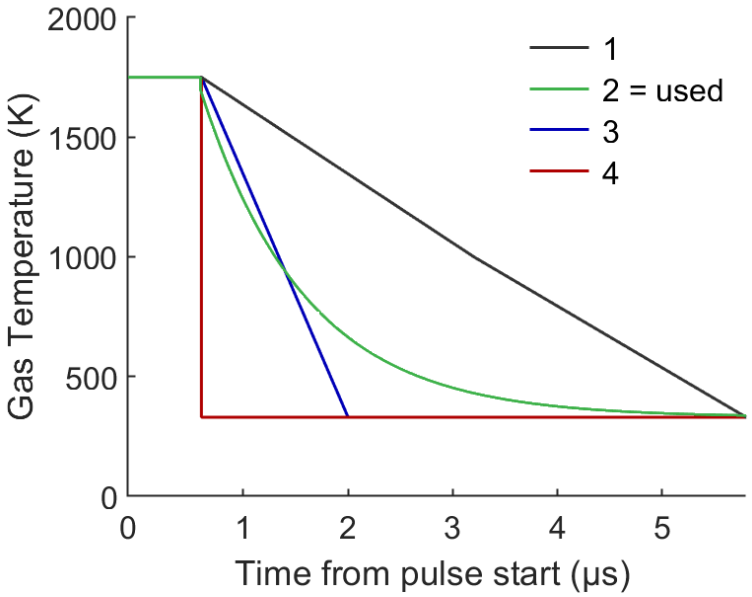

Appendix Figure 7 Four options of gas temperature as a function of time from the pulse start until the start of a new pulse, considered in the model: (1) slow linear drop, (2) exponential drop, (3) fast linear drop and (4) instantaneous drop.

G. Afterglow gas temperature profile

This Appendix discusses how the gas temperature profile in the afterglow was set, used in Chapter IV, section 3.3.3.

Finally, after the pulse train, the species move into the post-plasma zone, where the gas temperature (T_g) rapidly decreases to room temperature and the power was set to zero (no plasma). The gas temperature was calculated from Rayleigh scattering measurements at two distances from the nozzle tip (1.2 and 3.4 mm) and four different flow rates (0.2; 0.35; 0.7; and 1.4 L/min) as described in Chapter III, section 3.2. Next to these data points, the gas temperature in the plasma arc (1740 K; 0 mm, obtained from OES; see Chapter III, section 3.1) and the temperature of the room (308 K; position of 10 mm) are also known. We used these four experimental data points to fit an

exponentially decreasing curve for the four different flow rates (0.2; 0.35; 0.7; and 1.4 L/min; see Appendix Figure 8), based on four parameters: $T_g = a \cdot \exp(-b \cdot x) + c \cdot \exp(-d \cdot x)$, with x = the distance from the nozzle tip. Because of the strong difference in temperature between the plasma and the temperature at 10 mm from the nozzle (308 K) the temperature profiles in the afterglow are very alike for the four flow rates (0.2; 0.35; 0.7 and 1.4 L/min). For the other flow rates between 0.1 and 2.0 L/min an average fit (Appendix Figure 8; black dashed line) was used, based on the experimental data points. To validate this approximation to reality (i.e. a different temperature decay for each flow rate), we compared the calculated densities obtained when using the fitted temperature profile based on the experimental data for that specific flow rate with the average fit. There was no significant difference between both approaches, so it is a valid assumption to use the average fit for all flow rates.

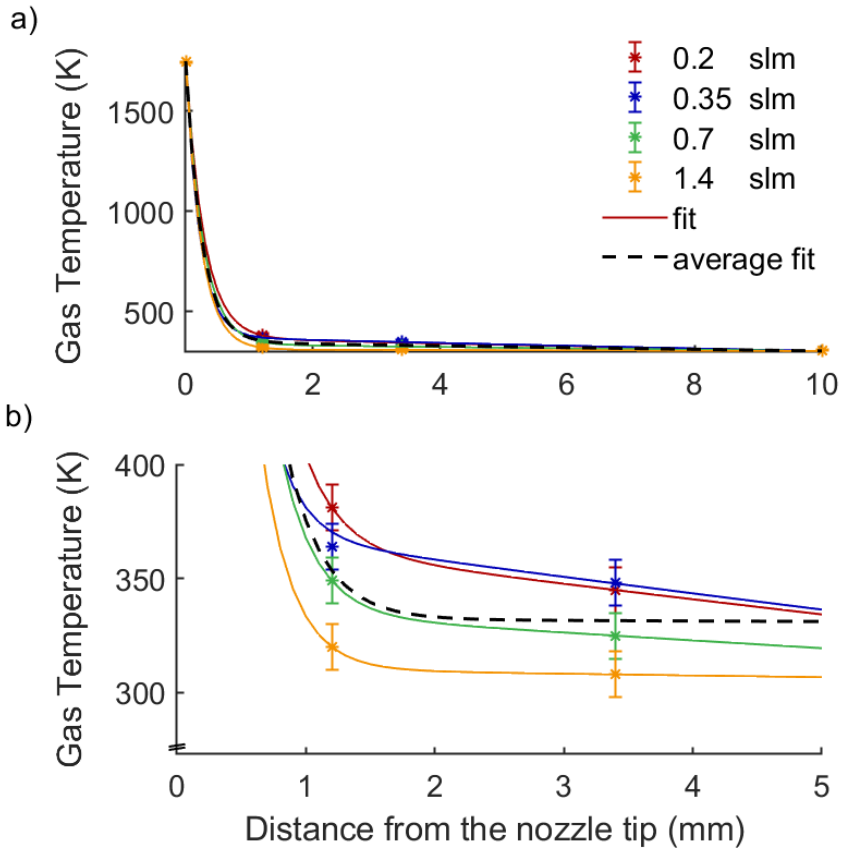

Appendix Figure 8 Gas temperature in the afterglow as measured by Rayleigh scattering experiments at 0.2, 0.35, 0.7 and 1.4 L/min (stars), as a function of distance from the nozzle tip, as well as the temperature in the plasma (0 mm; 1750 K) and room temperature (10 mm; 308 K). (a) Entire temperature profile from the plasma region until the simulation end (10 mm). (b) Zoomed into the points measured by Rayleigh scattering.

Measuring the temperature in the afterglow with a thermocouple is not possible. Indeed, it resulted in broadening of the plasma effluent, and in plasma arcing onto the thermocouple (see Appendix Figure 9), rendering the measurements invalid.

Appendix Figure 9 shows the normal plasma effluent, in the absence of a thermocouple (a), as well as the broadening of the plasma effluent

(b) and the arcing (c) onto the thermocouple, rendering the measurements invalid.

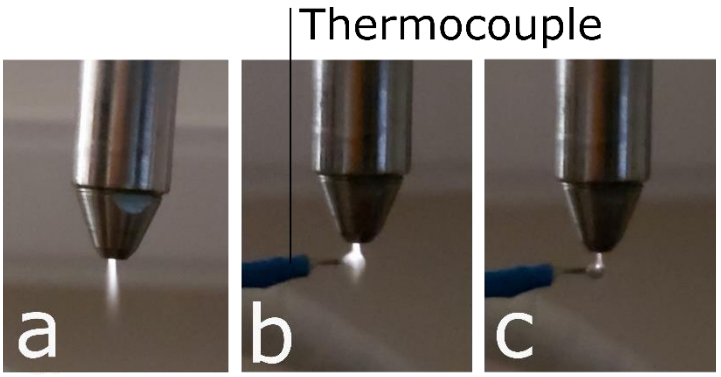

Appendix Figure 9 (a) The Soft Jet in operation, (b) with a thermocouple placed in the afterglow to measure the temperature: the gas dynamics are changed significantly, resulting in widening of the afterglow shape and (c) with a thermocouple placed closer to the nozzle tip: arc formation is visible onto the thermocouple.

H. NO_x Production rate

Appendix Figure 10 shows the NO_x production rates discussed in Chapter IV, section 4.1.

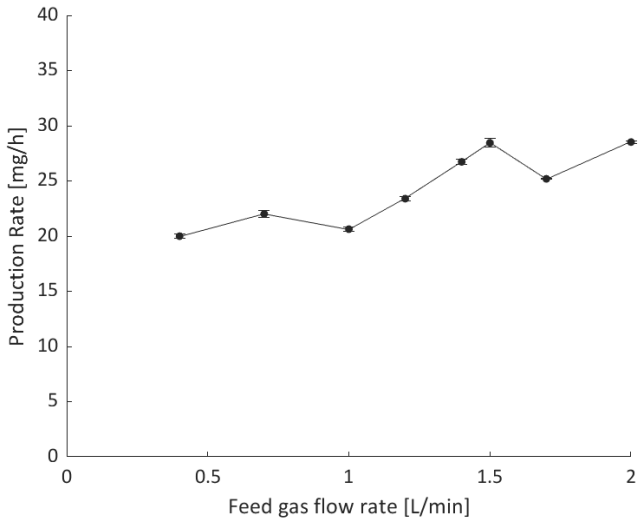

Appendix Figure 10 NO_x Production rate as a function of the feed gas flow rate.

I. Energy transfer due to electron impact reactions

In Chapter IV, section 4.3.1 we state that reduced electric fields up to 50 Td are most suitable for promoting vibrational excitation. This is shown in Appendix Figure 11, where we plot the electron energy loss fraction as a function of the reduced electric field for different excitation channels as calculated through BOLSIG+ [206].

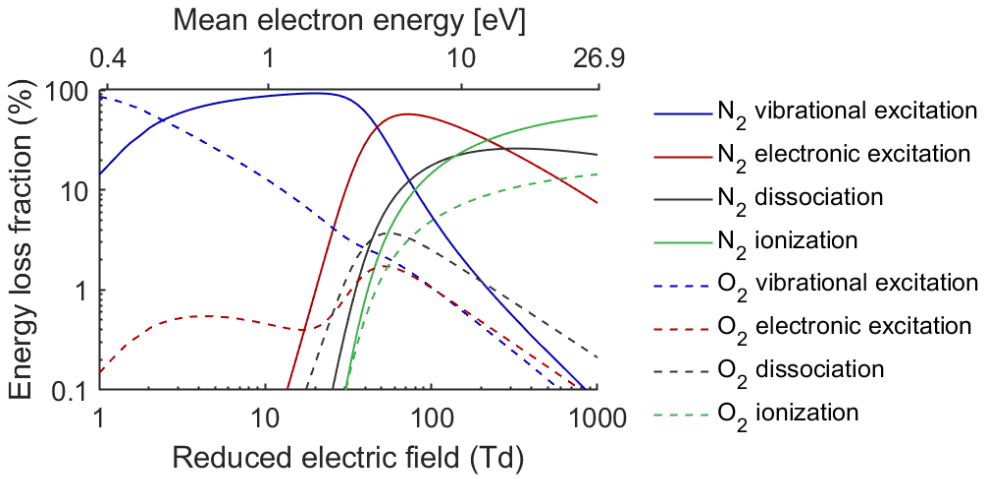

Appendix Figure 11 The electron energy loss to various electron impact processes as a function of the reduced electric field (bottom x-axis) and the mean electron energy (top x-axis) at 80/20 N_2/O_2 gas composition and 1750 K.

J. Extended reaction analysis

In Chapter IV, section 4.4, the formation and loss mechanisms in the Soft Jet are discussed. This Appendix gives a more detailed analysis of the mechanisms for three points in the residence time within the plasma, as is annotated on Appendix Figure 12d.

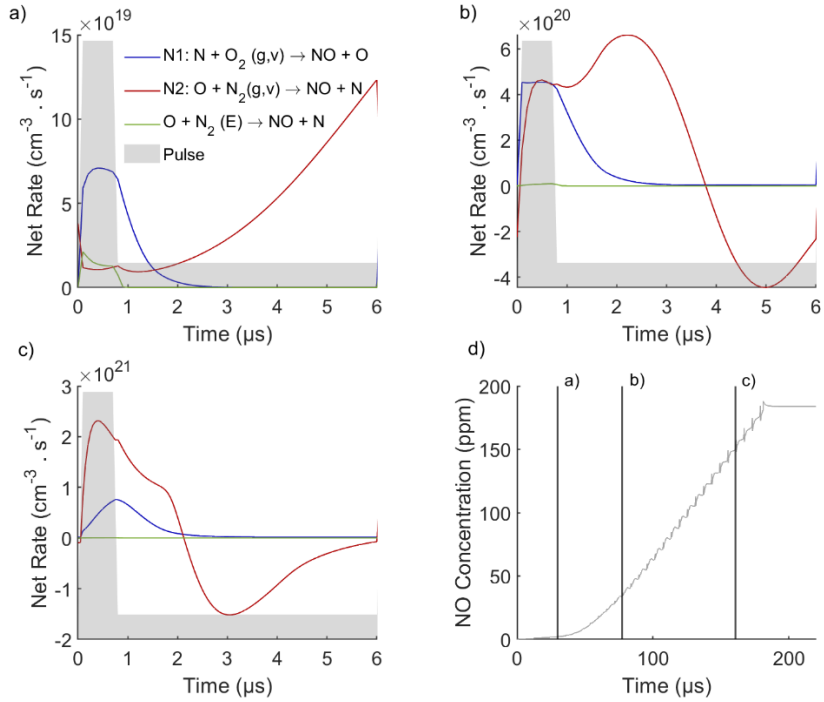

Appendix Figure 12 (a, b, c) Net reaction rates of the most important NO production reactions as a function of time during one pulse and interpulse time. A negative rate means that the reaction occurs in the opposite direction, i.e., as NO loss reaction. Panel (d) shows the time points in the pulse train, during the gas residence time in the plasma (at 1 L/min), with the associated NO concentration as a function of time: (a) Beginning, (b) middle, (c) end of the residence time. The x-axis of (a), (b) and (c) always starts at the beginning of a pulse.

The time- and space-averaged reaction rates were calculated for all formation and loss processes of NO and NO_2, as listed in Table 8, Chapter IV. The results are plotted in Appendix Figure 12. Panels a, b

and c present the reaction analysis of the main NO_x formation reactions as a function of time for one pulse – interpulse cycle, at the beginning, middle and end of the residence time in the plasma, as annotated by the three vertical lines in panel d. Throughout the whole residence time, the non-thermal Zeldovich mechanism promoted by vibrational excitation is the main mechanism for NO formation (blue and red curve; N1 and N2; see also Table 8). Note that the reactions with highest rate, overall, are the oxidation of NO to NO_2 (N3) and vice versa (N4), which occur throughout the whole residence time and produce a limited amount of NO_2 (< 1 ppm at all investigated flow rates). However, they do not contribute to the initial NO_x formation, and are therefore not plotted in Appendix Figure 12. In the following, we describe the mechanism in more detail.

(a) In the beginning, there are only small amounts of reactive species (N and O atoms, and N_2 and O_2 vibrationally excited levels) present, so the first pulses are predominantly governed by the temperature dependence of the reaction rate coefficients (k). Note that for this reason the net reaction rates increase overall with residence time in the plasma (from a → b → c), as reactive species densities increase but the temperature remains constant. The rate of N1 (Appendix Figure 12; blue curve) is higher than for N2 (red curve) during the pulse, because its rate constant is higher at higher temperature (hence in the pulse), and it drops after the pulse, due to the drop in temperature. At the same time, the rate of N2 rises, due to the rising population of N_2 vibrationally excited states during the interpulse.

At short residence times, N2 from N_2(E) (green curve) also plays a small role. Its contribution drastically reduces compared to the vibrationally promoted reactions, as the population of the vibrational

states increases throughout the residence time, while the population of $N_2(E)$ does not.

(b, c) At longer residence time, the gas mixture contains a significant amount of N and O atoms, as well as vibrationally excited N_2 and O_2 molecules, and this affects the reaction behaviour.

(b) R1 still reaches its maximum rate during the pulse and slowly drops after the pulse. The maximum is clearly higher, because the N atoms are abundant now, and the reaction is not limited anymore by the energy-intensive splitting of N_2 (to produce N atoms), due to the strong VT non-equilibrium. On the other hand, the rate of N2 first increases and then drops below 0 from the middle till the end of the interpulse. Indeed, during the first part of the interpulse, the O atom density is still high and the $N_2(v)$ density increases. However, after 2 μs, the back reaction of N2 becomes more and more important compared to the forward reaction, so around 3.8 μs, there is net destruction of NO via L2. Indeed, the rate coefficient of this back reaction is temperature-independent, while the rate coefficient of the forward reaction decreases due to the lower temperatures. This back reaction was not yet important in the beginning (Appendix Figure 12), because of the low concentration of N atoms at that stage.

(c) At the end of the residence time, N2 is now the dominant reaction in the pulse due to the high density of higher vibrationally excited N_2. The maximum rate of N1 has moved to the end of the pulse. Indeed, N1 relies on N2 for the production of N atoms, so its maximum is reached after the maximum of N2. As N1 cannot compete anymore for the N atoms at low temperature (low k), the rate of L1 increases earlier in the interpulse. As the O atoms are thus consumed by L1, there is no maximum for R2, and its net rate gradually decreases until it becomes

negative (net loss of NO).

Both in (b) and (c) the destruction of NO diminishes near the end of the interpulse (red curve returns to 0), due to the increasing population of $N_2(v)$ throughout the interpulse.

K. Rate coefficient plots for the Zeldovich mechanism

The reaction rate coefficients of the Zeldovich mechanism as a function of temperature, referred to in Chapter IV, section 4.4, are shown in Appendix Figure 13.

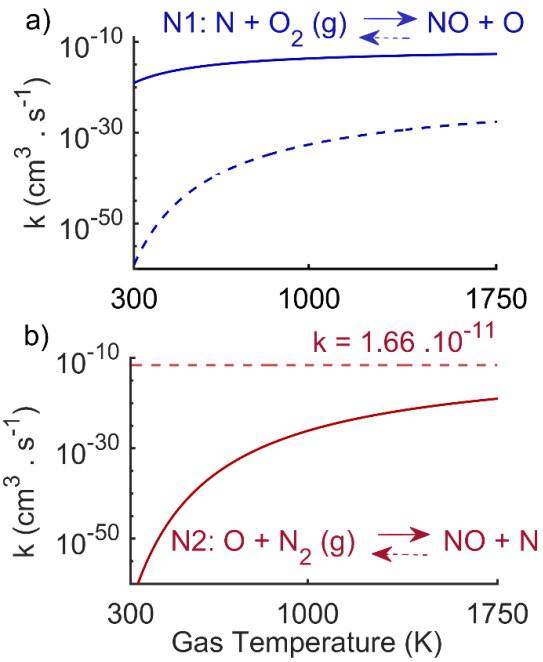

Appendix Figure 13 Reaction rate coefficient (k) for the forward (full) and backward (dashed) reaction of (a) N1 and (b) N2, as a function of gas temperature. Note the y-axes on both panels are on a log scale.

L. The effect of O_2 on the VDF of N_2: the ambivalent role of the vibrational kinetics

In previous work, related to my master thesis (reference [59]), a similar quasi-1D model was used to describe a gliding arc plasmatron (GAP). Because one phenomenon discussed in that paper is of relevance to the discussion in Chapter IV, section 4.5.1, it is explained here. From the reaction analysis in that paper it can be concluded that the vibrational kinetics are important for NO_x production in the GAP, therefore it is interesting to investigate the vibrational populations in more detail. On the one hand, vibrational-induced dissociation is known to be the most energy-efficient pathway, because low-energy electrons populate the lowest vibrational levels by electron impact excitation, and gradually the higher levels are populated by vibrational-vibrational (VV) exchanges, i.e., so-called ladder climbing, until dissociation takes place from the highest vibrational levels. On the other hand, however, these simulations reveal the vibrational kinetics can also play a limiting role in the NO_x production. We call this the ambivalent role of the vibrational kinetics.

Vibrational-vibrational (VV) exchanges do not only take place between different N_2 molecules and between different O_2 molecules, but also upon collision between N_2 and O_2 molecules. As the O_2 vibrational levels are more easily depopulated, the VV exchange between N_2 and O_2 vibrationally excited molecules results in a depopulation of the N_2 vibrational levels, and in a net population of the O_2 vibrational levels. This is clear from Appendix Figure 14, showing the comparison of the VDFs of N_2 and O_2 with (full curves) and without (dashed curves) these VV exchanges. We plot the results for a 50/50 N_2/O_2 gas feed ratio, to

illustrate most clearly the effect of these VV exchanges. If the $N_2 – O_2$ VV exchanges are taken into account, the vibrational levels of N_2 are less populated than when they are not included, while for O_2 the opposite is true. Thus, the O_2 vibrational levels depopulate the N_2 vibrational levels through $N_2 – O_2$ VV exchanges.

This process explains why the maximum in NO formation in the GAP is reached at a N_2 fraction above 50%, while based on the stoichiometry it would be expected at equal fractions of N_2 and O_2. Indeed, at higher N_2 fractions, the depopulation of the N_2 vibrational levels (upon collision with O_2 molecules) is more limited and the vibrational ladder climbing, aiding the Zeldovich mechanism for NO formation (see above), is better promoted.

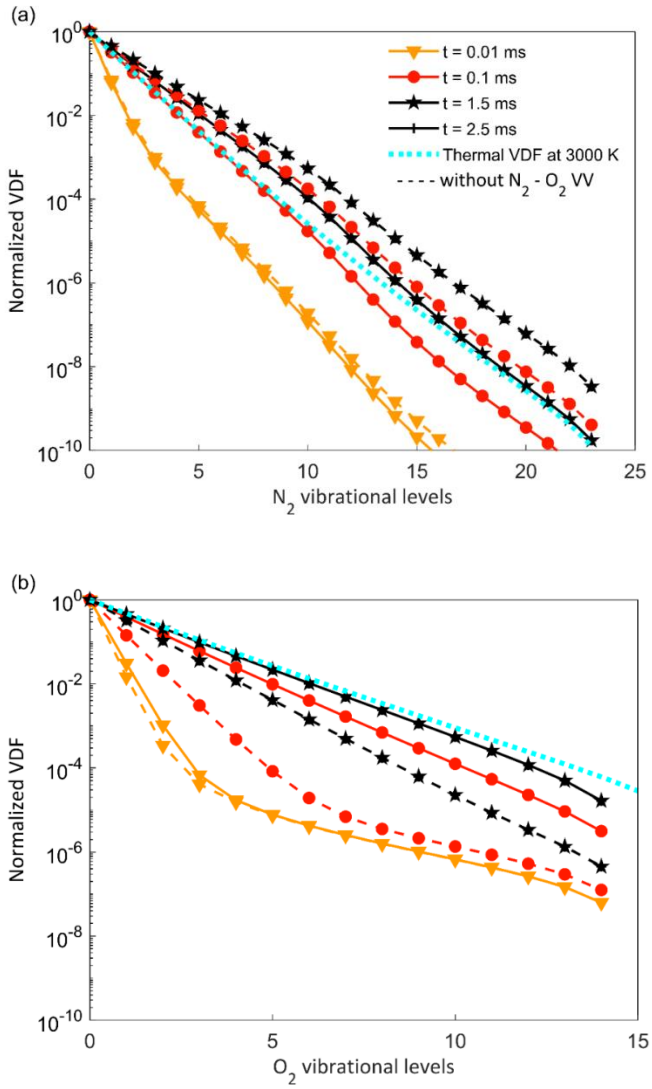

Appendix Figure 14 Normalized vibrational distribution function (VDF) of N_2 (a) and O_2 (b) at different times in the plasma for a 50/50 N_2/O_2 plasma in a GAP. The solid and dashed curves represent the VDFs of a chemistry set that includes and excludes N_2 –O_2 VV exchanges, respectively (see next section). The black full lines (representing t = 1.5 and 2.5 ms) are on top of one another, as well as the black dashed lines, indicating that the VDFs of N_2 and O_2 reach steady state already after 1.5 ms. For comparison, the thermal VDF at 3000 K is also plotted as a dotted blue curve.

M. Rate and selectivity of NH_3 production and conversion of N_2

Appendix Table 1 is referred to in Chapter V, section 3.1.

Appendix Table 1 Rate and selectivity of NH_3 production, and conversion of N_2, by the plasma jet as a function of H_2O vapor content at different gas flow rates.

Feed gas flow rate (L/min)	H_2O vapor saturation (%)	NH_3 production rate (mg/h)	NH_3 selectivity (%)*	N_2 conversion (%)**	Entry
0.2	-	0.031	88	0.0004	1
	2	0.044	95	0.0006	2
	5	0.052	96	0.0007	3
	10	0.064	95	0.0008	4
	20	0.078	86	0.0011	5
	50	0.107	65	0.0020	6
	100	0.124	63	0.0023	7
0.35	-	0.031	86	0.0002	8
	2	0.037	93	0.0003	9
	5	0.053	94	0.0004	10
	10	0.063	93	0.0005	11
	20	0.077	81	0.0007	12
	50	0.135	68	0.0014	13
	100	0.153	65	0.0016	14

0.7	-	0.032	78	0.0001	15
	2	0.036	88	0.0001	16
	5	0.058	91	0.0002	17
	10	0.072	89	0.0003	18
	20	0.074	87	0.0003	19
	50	0.169	65	0.0009	20
	100	0.184	63	0.0010	21
1.4	-	0.029	73	0.0001	22
	2	0.038	86	0.0001	23
	5	0.064	88	0.0001	24
	10	0.072	84	0.0001	25
	20	0.096	83	0.0002	26
	50	0.216	66	0.0006	27
	100	0.263	64	0.0007	28

*Calculated as $\frac{\mathrm{C(NH3)\ mol/L}}{\mathrm{C(NH3+NO2-+NO3-)\ mol/L}} \times 100\ \%$.

**Calculated as $\frac{\mathrm{C(NH3+NO2-+NO3-)\ mol/L}}{10\ \mathrm{min}} \times \frac{5\ \mathrm{mL}}{1000\ \mathrm{mL/L}} \times 24.5\ \mathrm{L/mol} \times \frac{1}{\mathrm{FR\ L/min}} \times 100\%$,

where FR is the flow rate of the gas. This is based on the assumption that all N_2 fixation products are converted into NH_3, NO_2^-, or NO_3^-.

N. Energy consumption calculation

This energy calculation is used in Chapter V, section 3.1.

The power deposited in the plasma (DP) was 0.1 W (Chapter III, Section 2.3). The conditions which allow highest NH_3 selectivity were 0.2 L/min N_2, with 5-10% H_2O vapor saturation. Under these conditions, the production rate (PR) of NH_3 was 0.052-0.064 mg/h (Appendix Table 1). The energy consumption (EC) is calculated as $\mathrm{EC\,(J/mol)} = \frac{\mathrm{DP\ (W)}}{\mathrm{PR\ (mg/h)}} \times 3600\left(\frac{\mathrm{s}}{\mathrm{h}}\right) \times 17000\left(\frac{\mathrm{mg}}{\mathrm{mol}}\right)$. Under the conditions mentioned above, EC was 95-118 MJ/mol NH_3. This is in essence the same formula as used in Chapter IV, adapted for the measurements in liquid.

O. Calculation of ΔG values

This Appendix discusses the calculation of ΔG values which are used in the discussion of Chapter V, section 3.1.

The values of ΔG for the reaction $2N_2 + 6H_2O \rightarrow 3O_2 + 4NH_3$ were calculated as shown below using data from literature[281]. The calculation was based on the following assumptions: 1) the reactions occur in the gas phase, with all reactants and products in the gaseous state; 2) C_p is constant within the used temperature range; 3) partial pressures of the products were estimated from the stoichiometry of the reaction and the conversion values of N_2 (see Appendix Table 1). The values of ΔG were calculated for two 'envelope' conditions: 298 K, and the highest measured temperature in our plasma system (1623 K). The ΔG values at all other possible temperature values belong to this range. At 298 K, $\Delta G^0 = \Delta G_f^0\,(NH_3)\times 4 - \Delta G_f^0\,(H_2O)\times 6 + RT\ln K$ = ca. 1.2 MJ/mol, where $K = P_{O2}^3 \times P_{NH3}^4 / (P_{H2O}^6 \times P_{N2}^2)$. At other temperatures, ΔH_f and S values of each compound were calculated as $\Delta H_f^0 + C_p\Delta T$, and S^0 +

$C_p \ln(T/298)$, respectively. ΔG was calculated as $\Delta H_f - T \times \Delta S + RT\ln K$. At 1750 K, ΔG is 0.9 MJ/mol.

P. Concentration of nitrogen fixated species as a function of time

In Chapter V, section 3.1., we state the accumulation of all compounds in the liquid was practically linear. This is shown in Appendix Figure 15.

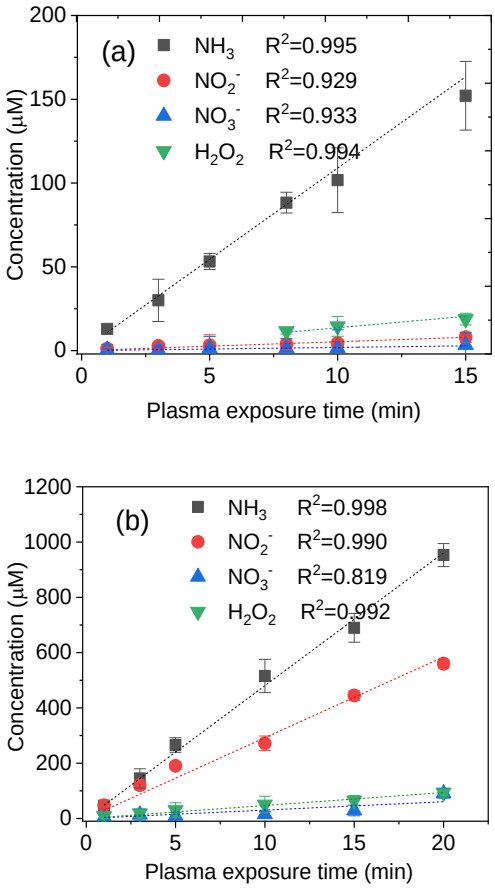

Appendix Figure 15 Concentration of the produced NH_3, NO_2^-, NO_3^-, and H_2O_2 in liquid H_2O as a function of plasma exposure time. Plasma conditions: (a) 0.2 L/min N_2, 5% H_2O vapor saturation; (b) 1.4 L/min N_2, 100% H_2O vapor saturation. Liquid volume 5 mL, distance from plasma jet to liquid 5 mm. R^2 values are given for linear $y=kx$ fittings.

Q. H_2O/D_2O results for 1.4 L/min

As referred to in the caption of Figure 36, Chapter V, section 3.6, Appendix Figure 16 below shows the effect of using D_2O/H_2O in the species production for 1.4 L/min.

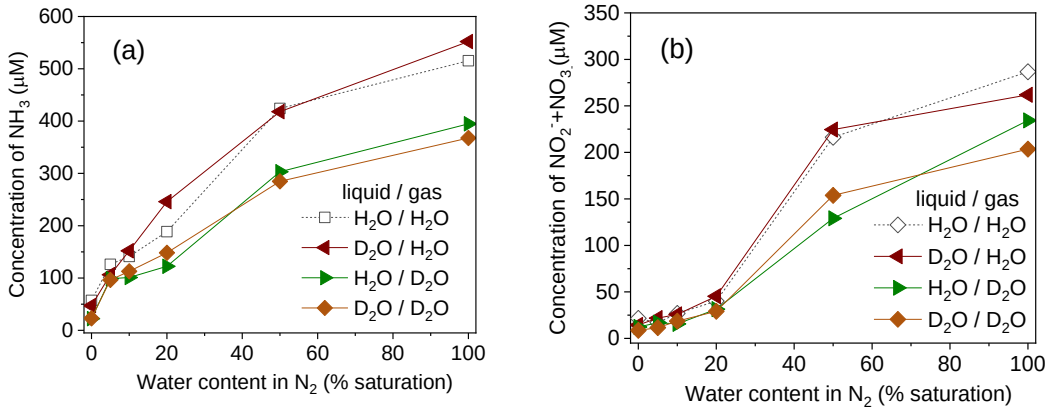

Appendix Figure 16 Concentration of NH_3, NO_3^-, NO_2^-, as a function of water vapor saturation, with 1.4 L/min N_2 flow rate. (a) NH_3 concentration; (b) total NO_2^-+NO_3^- concentration. Liquid volume 5 mL, distance from plasma jet to liquid 5 mm, exposure time 10 min. Experimental data with H_2O liquid and H_2O vapor were added here as dashed lines for comparison. This figure corresponds to Figure 36, Chapter V, section 3.6, but at a higher flow rate.

R. OES spectra recorded perpendicular to the plasma effluent

Appendix Table 2 Overview of the waterfall plot conditions and their respective Figure numbers.

Gas	**Air**									
Flow rate (L/min)	0.5					2				
Relative humidity at 20°C (%)	<1	5	30	50	100	<1	5	30	50	100
Appendix Figure 17	**a**	**b**	**c**	**d**	**e**	**f**	**g**	**h**	**i**	**j**
Gas	**N_2**									
Flow rate (L/min)	0.5					2				
Relative humidity at 20°C (%)	<1	5	30	50	100	<1	5	30	50	100
Appendix Figure 17	**k**	**l**	**m**	**n**	**o**	**p**	**q**	**r**	**s**	**t**

Appendix Figure 17 Emission spectra (334–340 nm) as a function of the distance from the jet nozzle (1–10 mm). The full list of the experimental conditions (Appendix Figure 17a – Appendix Figure 17t) is shown in Appendix Table 2 above.

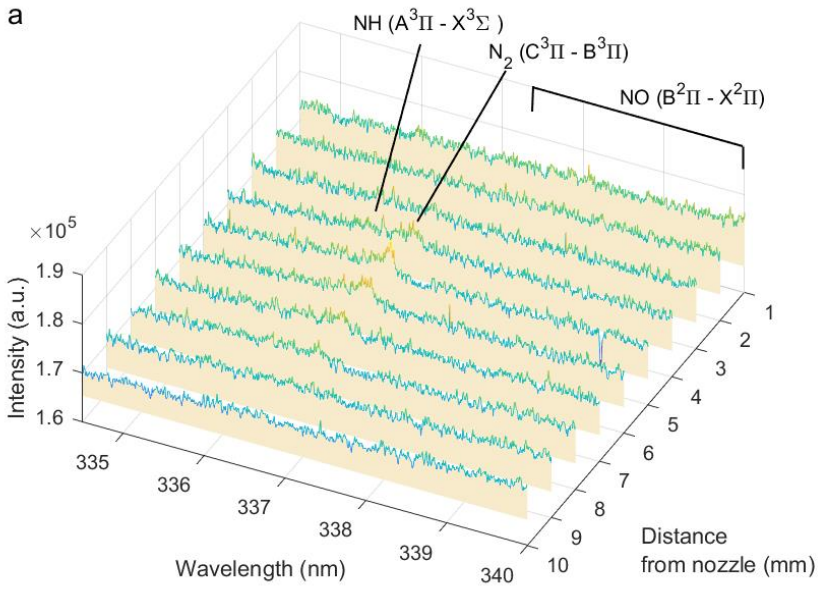

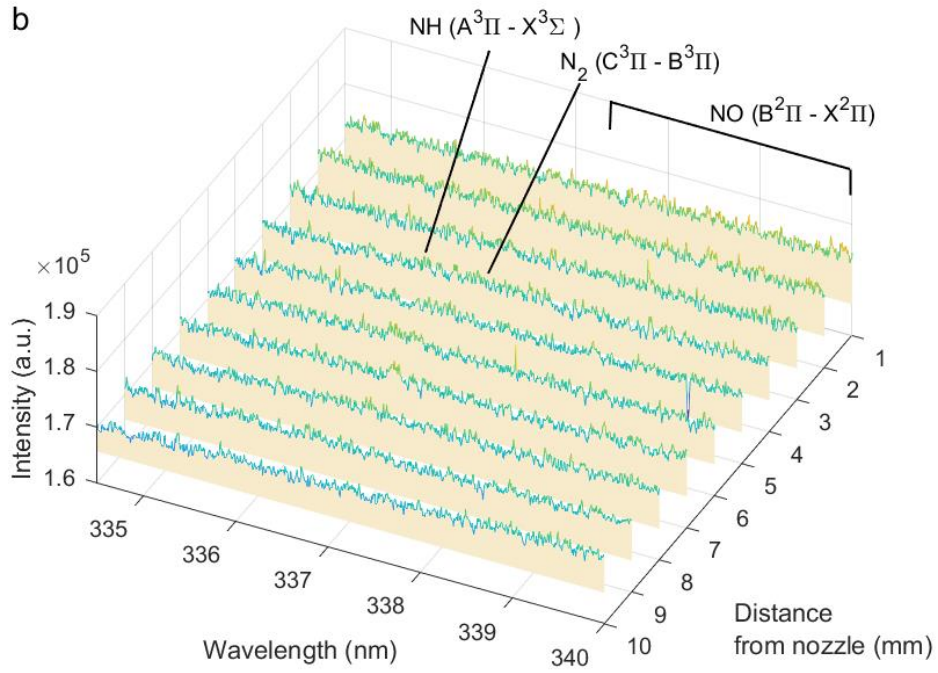
b
NH ($A^3\Pi$ - $X^3\Sigma$)
N_2 ($C^3\Pi$ - $B^3\Pi$)
NO ($B^2\Pi$ - $X^2\Pi$)
$\times 10^5$
Intensity (a.u.)
1.9
1.8
1.7
1.6
335
336
337
338
339
340
Wavelength (nm)
1
2
3
4
5
6
7
8
9
10
Distance
from nozzle (mm)

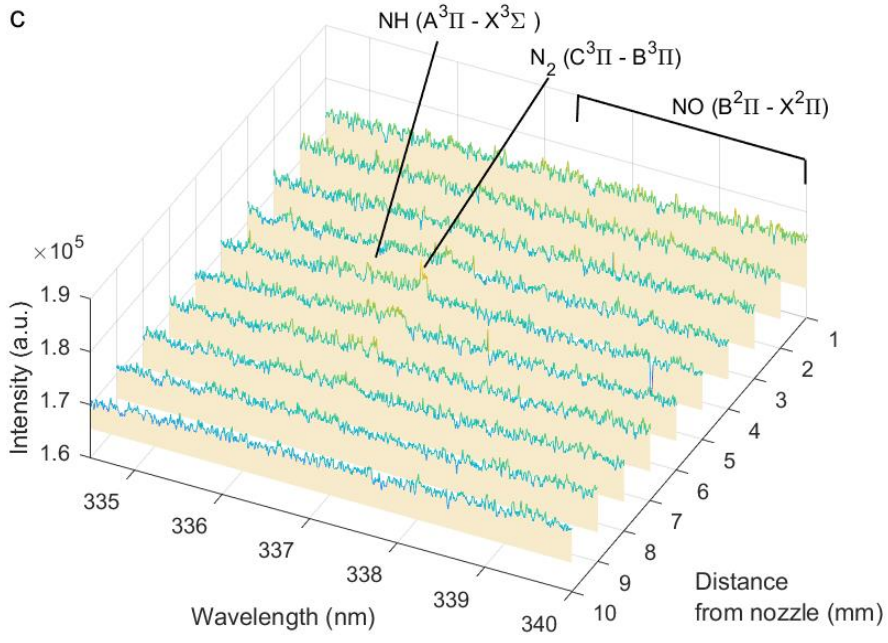
c
NH ($A^3\Pi$ - $X^3\Sigma$)
N_2 ($C^3\Pi$ - $B^3\Pi$)
NO ($B^2\Pi$ - $X^2\Pi$)
$\times 10^5$
Intensity (a.u.)
1.9
1.8
1.7
1.6
335
336
337
338
339
340
Wavelength (nm)
1
2
3
4
5
6
7
8
9
10
Distance
from nozzle (mm)

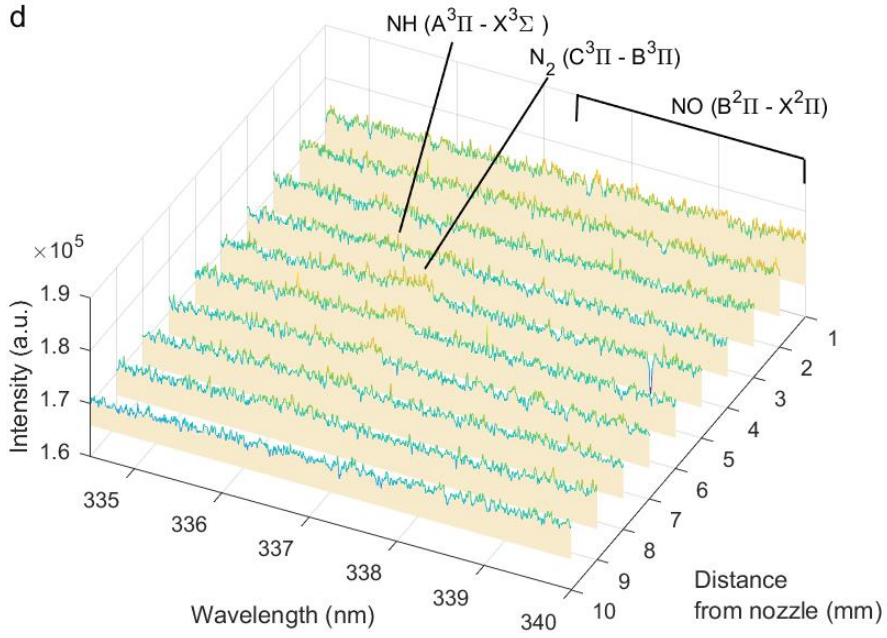
d
NH (A3Π - X3Σ)
N2 (C3Π - B3Π)
NO (B2Π - X2Π)
×10^5
1.9
1.8
1.7
1.6
Intensity (a.u.)
335
336
337
338
339
340
Wavelength (nm)
1
2
3
4
5
6
7
8
9
10
Distance
from nozzle (mm)

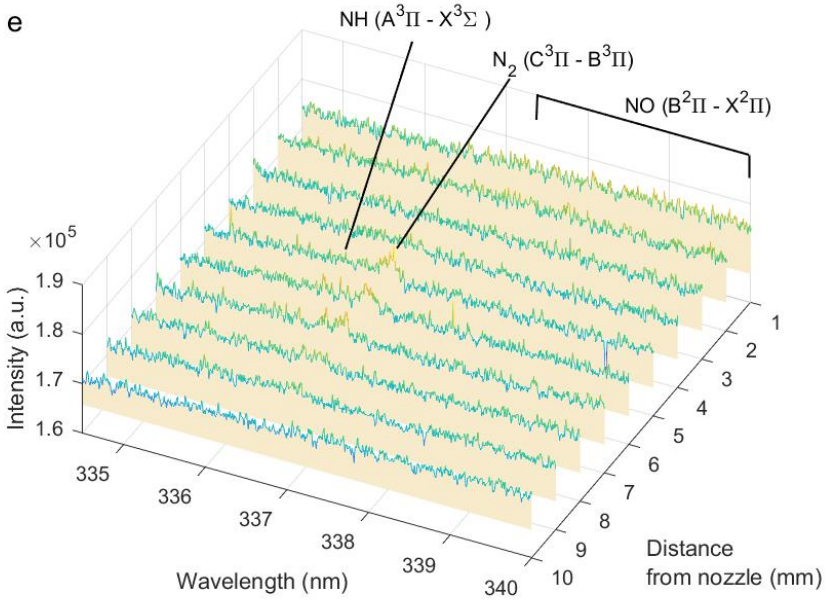
e
NH (A3Π - X3Σ)
N2 (C3Π - B3Π)
NO (B2Π - X2Π)
×10^5
1.9
1.8
1.7
1.6
Intensity (a.u.)
335
336
337
338
339
340
Wavelength (nm)
1
2
3
4
5
6
7
8
9
10
Distance
from nozzle (mm)

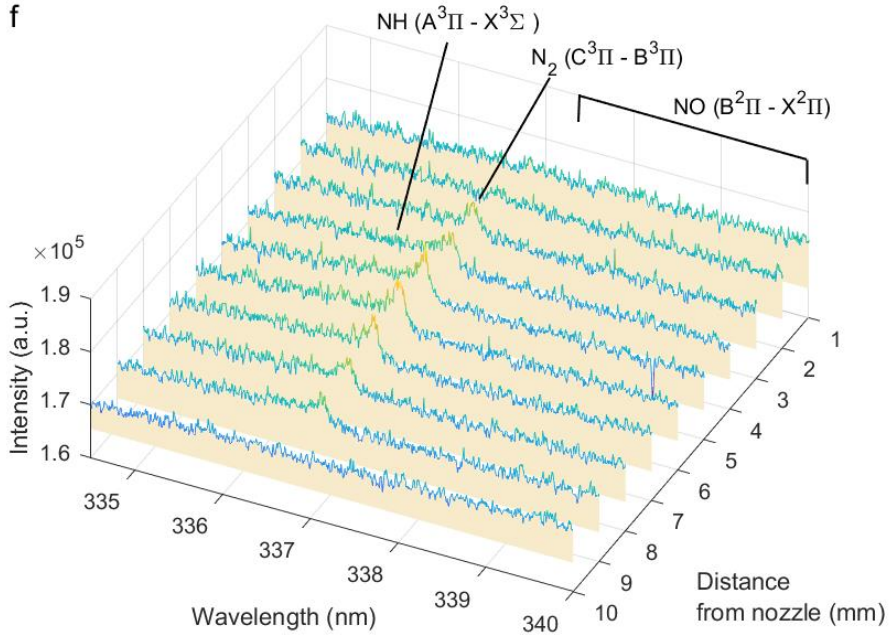
f
NH (A3Π - X3Σ)
N2 (C3Π - B3Π)
NO (B2Π - X2Π)
×10^5
1.9
1.8
1.7
1.6
Intensity (a.u.)
335
336
337
338
339
340
Wavelength (nm)
1
2
3
4
5
6
7
8
9
10
Distance
from nozzle (mm)

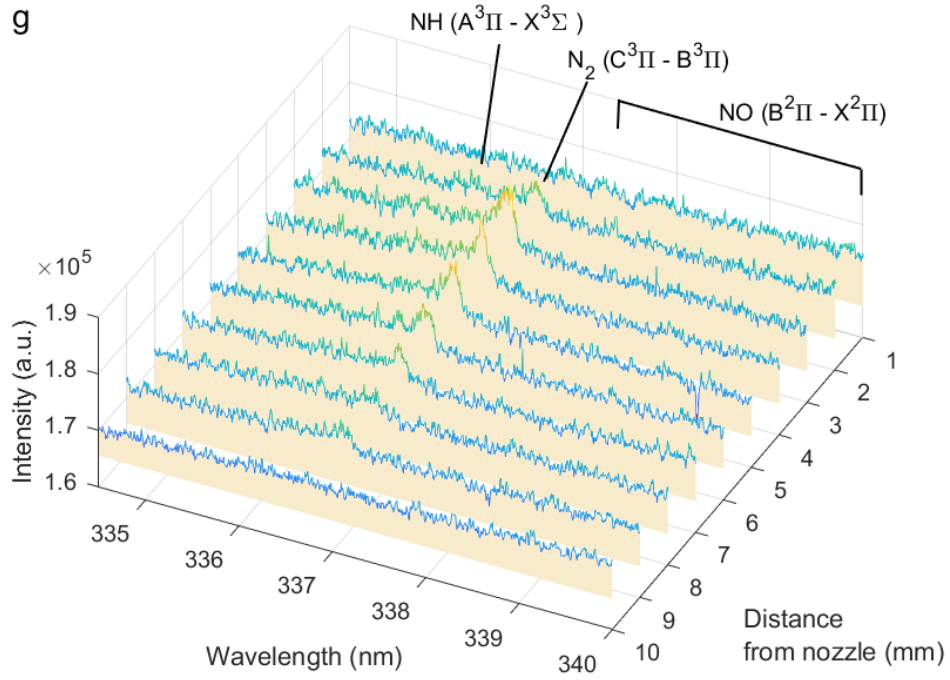
g
NH (A3Π - X3Σ)
N2 (C3Π - B3Π)
NO (B2Π - X2Π)
×10^5
1.9
1.8
1.7
1.6
Intensity (a.u.)
335
336
337
338
339
340
Wavelength (nm)
1
2
3
4
5
6
7
8
9
10
Distance
from nozzle (mm)

h

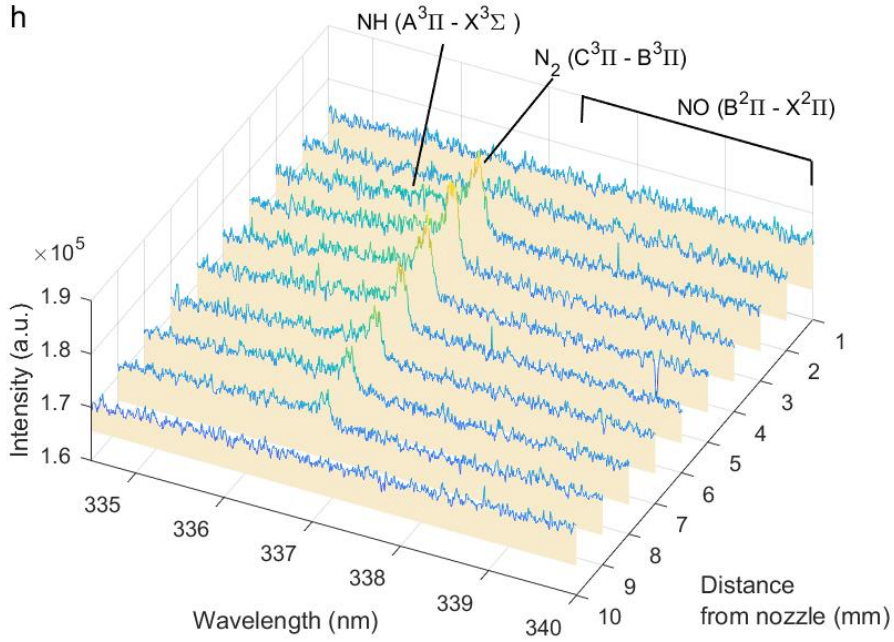
NH ($A^3\Pi$ - $X^3\Sigma$)
N_2 ($C^3\Pi$ - $B^3\Pi$)
NO ($B^2\Pi$ - $X^2\Pi$)
$\times 10^5$
Intensity (a.u.)
1.9
1.8
1.7
1.6
335
336
337
338
339
340
Wavelength (nm)
1
2
3
4
5
6
7
8
9
10
Distance
from nozzle (mm)

i

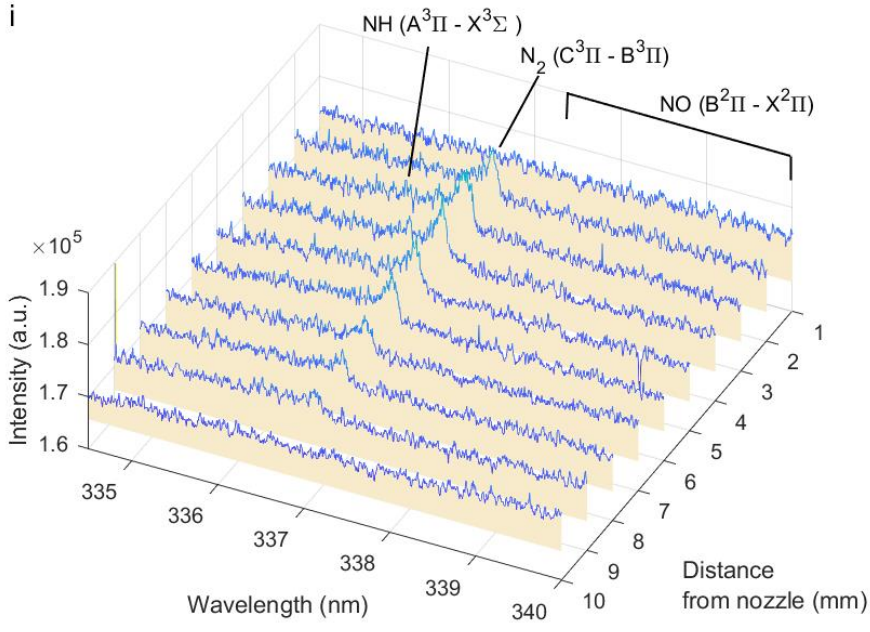
NH ($A^3\Pi$ - $X^3\Sigma$)
N_2 ($C^3\Pi$ - $B^3\Pi$)
NO ($B^2\Pi$ - $X^2\Pi$)
$\times 10^5$
Intensity (a.u.)
1.9
1.8
1.7
1.6
335
336
337
338
339
340
Wavelength (nm)
1
2
3
4
5
6
7
8
9
10
Distance
from nozzle (mm)

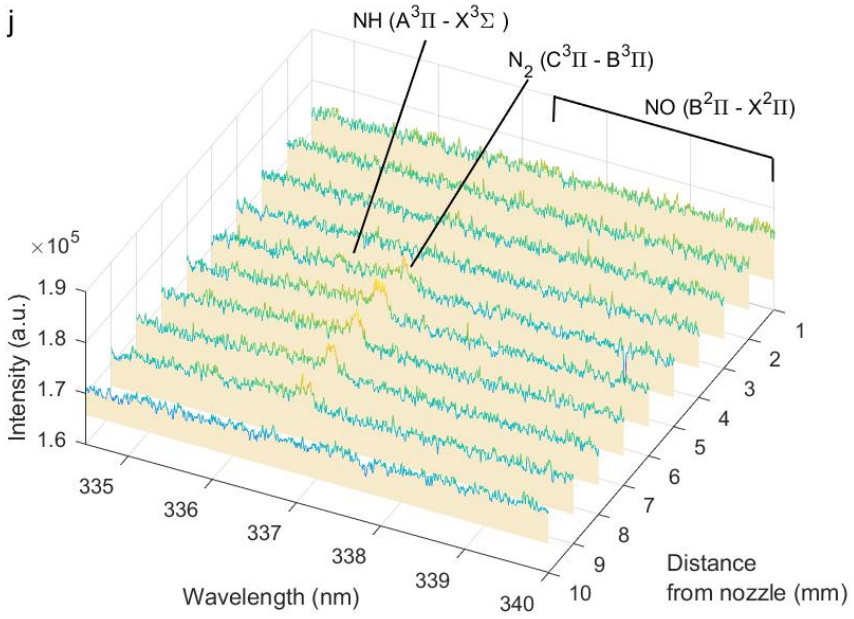
j
NH (A3Π - X3Σ)
N2 (C3Π - B3Π)
NO (B2Π - X2Π)
×10^5
Intensity (a.u.)
1.9
1.8
1.7
1.6
335
336
337
338
339
340
Wavelength (nm)
1
2
3
4
5
6
7
8
9
10
Distance
from nozzle (mm)

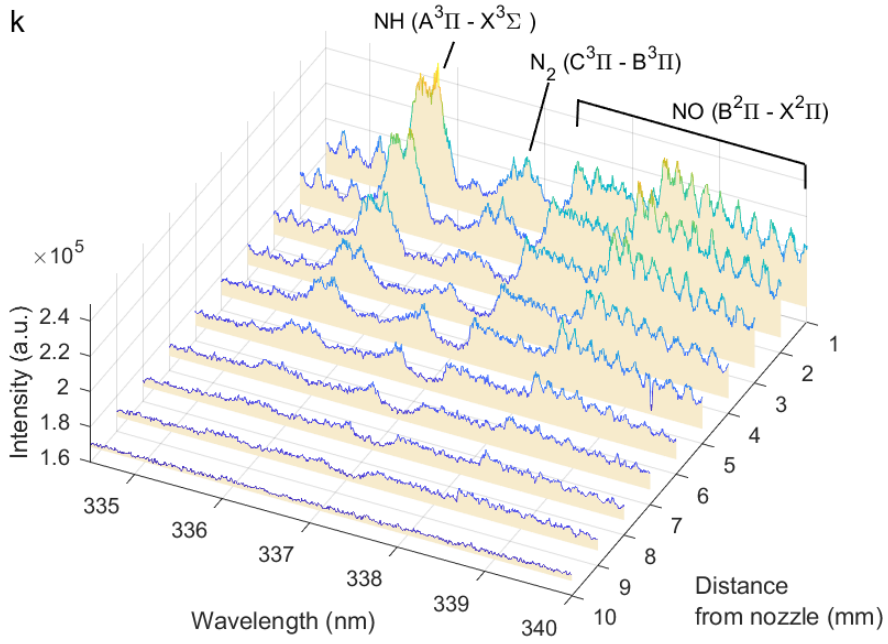
k
NH (A3Π - X3Σ)
N2 (C3Π - B3Π)
NO (B2Π - X2Π)
×10^5
Intensity (a.u.)
2.4
2.2
2
1.8
1.6
335
336
337
338
339
340
Wavelength (nm)
1
2
3
4
5
6
7
8
9
10
Distance
from nozzle (mm)

l

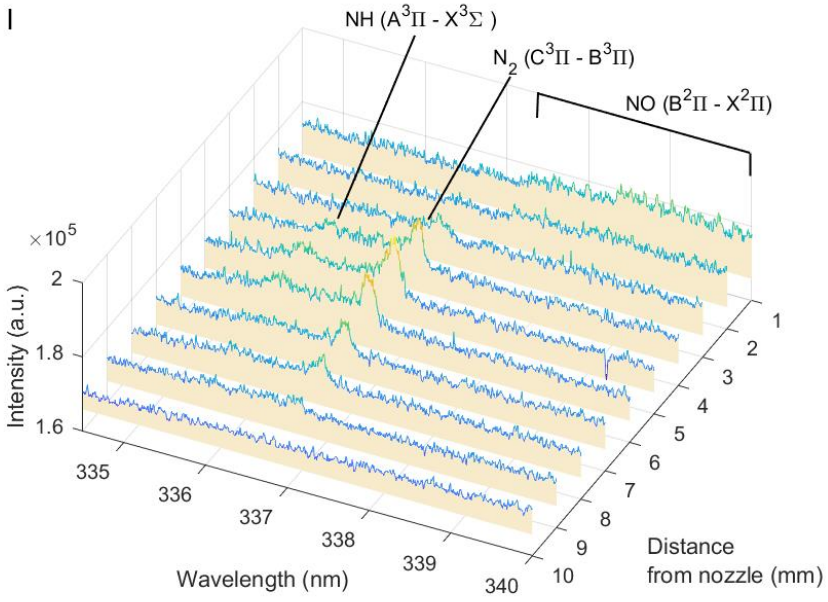
NH (A3Π - X3Σ)
N2 (C3Π - B3Π)
NO (B2Π - X2Π)
×10^5
2
1.8
1.6
Intensity (a.u.)
335
336
337
338
339
340
Wavelength (nm)
1
2
3
4
5
6
7
8
9
10
Distance
from nozzle (mm)

m

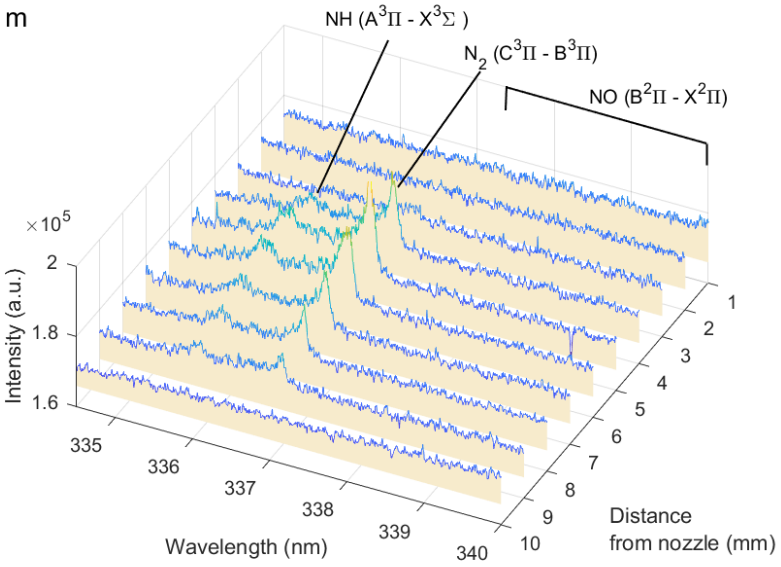
NH (A3Π - X3Σ)
N2 (C3Π - B3Π)
NO (B2Π - X2Π)
×10^5
2
1.8
1.6
Intensity (a.u.)
335
336
337
338
339
340
Wavelength (nm)
1
2
3
4
5
6
7
8
9
10
Distance
from nozzle (mm)

n

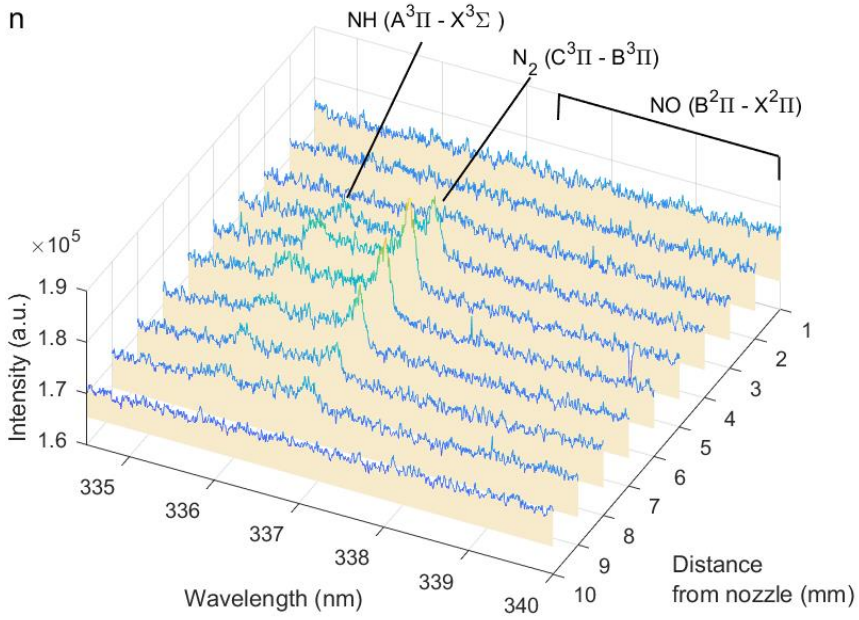
NH ($A^3\Pi$ - $X^3\Sigma$)
N_2 ($C^3\Pi$ - $B^3\Pi$)
NO ($B^2\Pi$ - $X^2\Pi$)
$\times 10^5$
Intensity (a.u.)
1.9
1.8
1.7
1.6
335
336
337
338
339
340
Wavelength (nm)
1
2
3
4
5
6
7
8
9
10
Distance
from nozzle (mm)

o

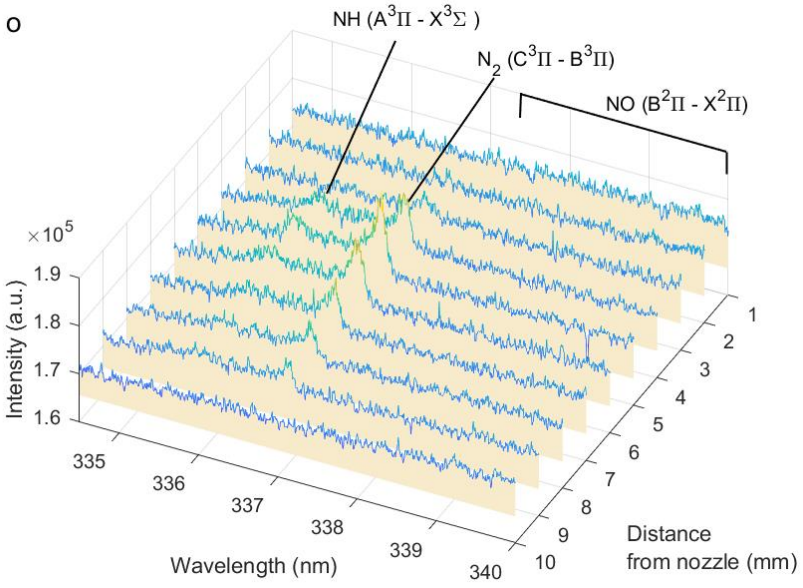
NH ($A^3\Pi$ - $X^3\Sigma$)
N_2 ($C^3\Pi$ - $B^3\Pi$)
NO ($B^2\Pi$ - $X^2\Pi$)
$\times 10^5$
Intensity (a.u.)
1.9
1.8
1.7
1.6
335
336
337
338
339
340
Wavelength (nm)
1
2
3
4
5
6
7
8
9
10
Distance
from nozzle (mm)

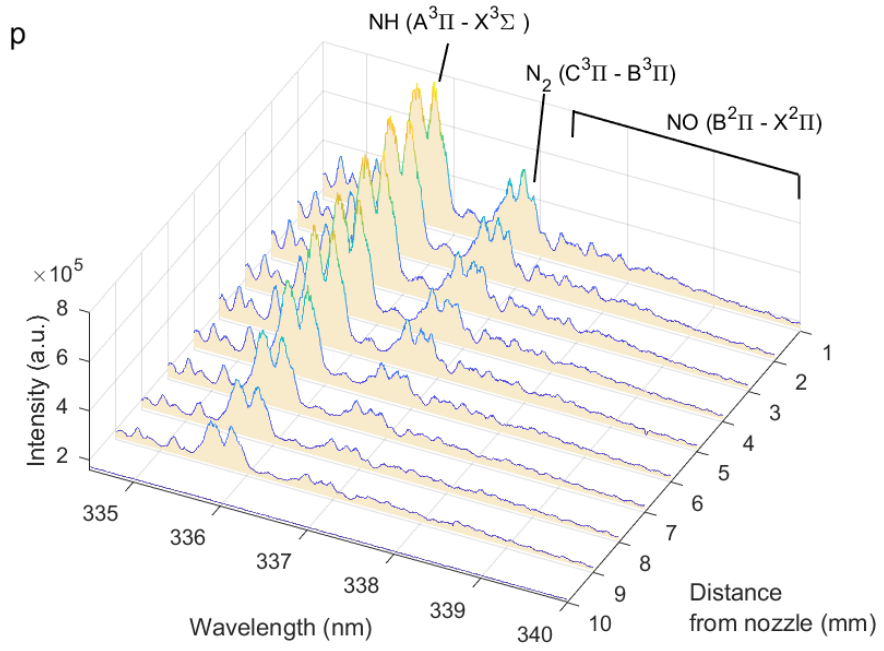
p
NH (A3Π - X3Σ)
N2 (C3Π - B3Π)
NO (B2Π - X2Π)
×10^5
Intensity (a.u.)
8
6
4
2
335
336
337
338
339
340
Wavelength (nm)
1
2
3
4
5
6
7
8
9
10
Distance
from nozzle (mm)

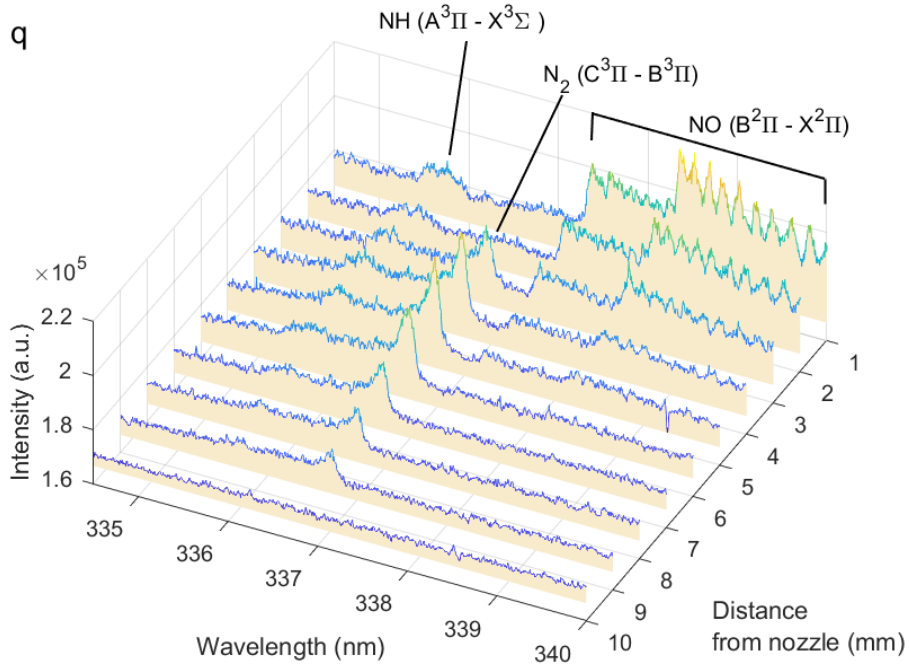
q
NH (A3Π - X3Σ)
N2 (C3Π - B3Π)
NO (B2Π - X2Π)
×10^5
Intensity (a.u.)
2.2
2
1.8
1.6
335
336
337
338
339
340
Wavelength (nm)
1
2
3
4
5
6
7
8
9
10
Distance
from nozzle (mm)

r

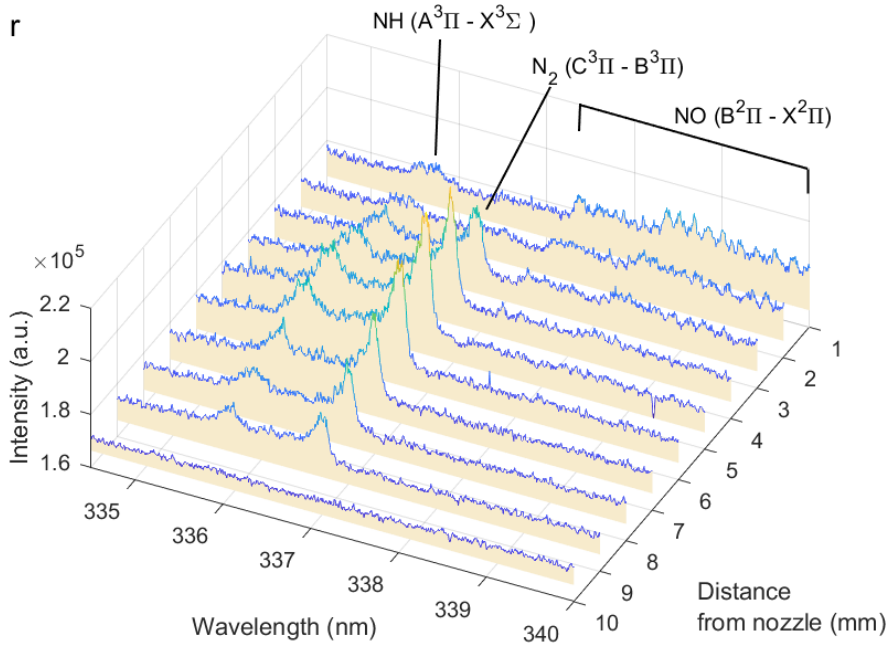
NH (A3Π - X3Σ)
N2 (C3Π - B3Π)
NO (B2Π - X2Π)
×10^5
2.2
2
1.8
1.6
Intensity (a.u.)
335
336
337
338
339
340
Wavelength (nm)
1
2
3
4
5
6
7
8
9
10
Distance
from nozzle (mm)

s

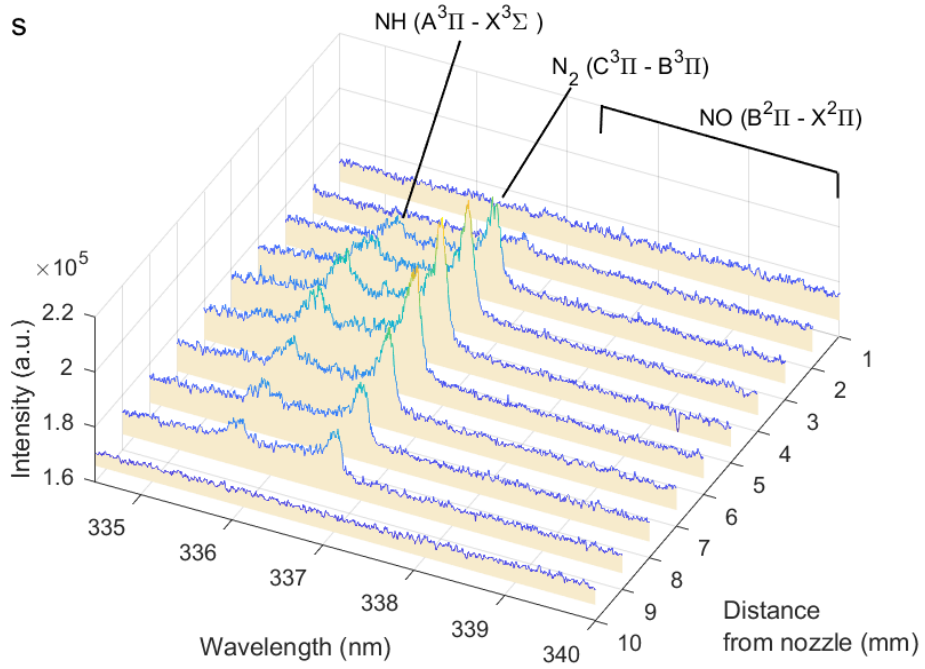
NH (A3Π - X3Σ)
N2 (C3Π - B3Π)
NO (B2Π - X2Π)
×10^5
2.2
2
1.8
1.6
Intensity (a.u.)
335
336
337
338
339
340
Wavelength (nm)
1
2
3
4
5
6
7
8
9
10
Distance
from nozzle (mm)

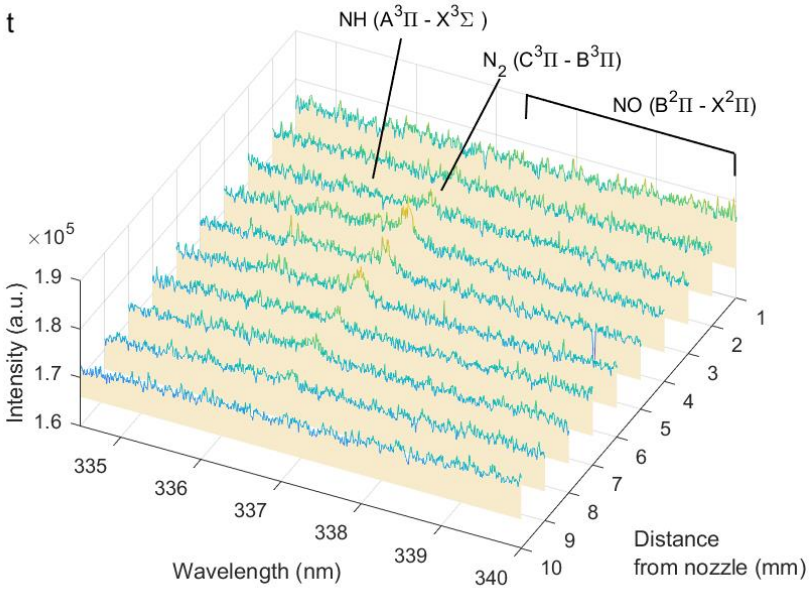
t
NH (A3Π - X3Σ)
N2 (C3Π - B3Π)
NO (B2Π - X2Π)
×10^5
1.9
1.8
1.7
1.6
Intensity (a.u.)
335
336
337
338
339
340
Wavelength (nm)
1
2
3
4
5
6
7
8
9
10
Distance
from nozzle (mm)

S. List of reactions and rate coefficients

Appendix Table 3 – Appendix Table 8 lists the reactions and their rate coefficients as used in Chapter IV. Discussion on the chemistry set construction can be found in Chapter II, section 6.2.2

Appendix Table 3 Electron impact reactions implemented in the model for atomic and molecular nitrogen and oxygen species as well as NO_x species. The list includes vibrational excitation and de-excitation, electronic excitation and de-excitation, direct and dissociative ionization, dissociation, and direct and dissociative attachment reactions. When the rate coefficient is not specified, these reactions are treated by energy-dependent cross sections. The rate coefficients are expressed in $cm^3\ s^{-1}$ or $cm^6\ s^{-1}$ for binary or ternary reactions, respectively.

Reaction	Rate Coefficient	Ref.	Note
$e^- + N_2 \leftrightarrow e^- + N_2(v)$		282	
$e^- + N_2(v) \leftrightarrow e^- + N_2(v')$		283	
$e^- + N_2(g,v) \rightarrow e^- + N_2(E_x)$		284	a, b, c
$e^- + N_2(E_x) \rightarrow e^- + N_2$		284	b
$e^- + N_2(g,v) \rightarrow 2e^- + N_2^+$		285	a
$e^- + N_2(E_x) \rightarrow 2e^- + N_2^+$		285	b,c
$e^- + N \rightarrow 2e^- + N^+$		214	
$e^- + N_2(g,v) \rightarrow 2e^- + N^+ + N$		286	a
$e^- + N_2(g,v) \rightarrow e^- + N + N$		284	a, c
$e^- + N_2(E_x) \rightarrow e^- + N + N$		284	b, c
$e^- + N \rightarrow e^- + N(E_x)$		284	d
$e^- + O_2 \leftrightarrow e^- + O_2(v)$		283	
$e^- + O_2(v) \leftrightarrow e^- + O_2(v')$		287	
$e^- + O_2(g,v) \rightarrow e^- + O_2(E_x)$		284	a, c, e
$e^- + O_2(E_x) \rightarrow e^- + O_2$		284	e

$e^- + O_2(g,v) \rightarrow 2e^- + O_2^+$		285	a, c
$e^- + O_2(E_x) \rightarrow 2e^- + O_2^+$		288	e, c
$e^- + O \rightarrow 2e^- + O^+$		284	
$e^- + O_2(g,v) \rightarrow 2e^- + O + O^+$		289	a, c
$e^- + O_2(E_x) \rightarrow 2e^- + O + O^+$		289	e,c
$e^- + O_3 \rightarrow 2e^- + O + O_2^+$		290	
$e^- + O_3 \rightarrow e^- + O^+ + O^- + O$		291	
$e^- + O_2(g,v) \rightarrow e^- + O + O$		284	a
$e^- + O_3 \rightarrow e^- + O_2 + O$		290	
$e^- + O_2(g,v) \rightarrow O + O^-$		284	a, c
$e^- + O_2(g,v) + M \rightarrow O_2^- + M$		292	a, c, f
$e^- + O_3 \rightarrow O^- + O_2$		285	
$e^- + O_3 \rightarrow O + O_2^-$		285	
$e^- + O_3 + M \rightarrow O_3^- + M$	5×10^{-31}	293	f
$e^- + O + M \rightarrow O^- + M$	1×10^{-31}	294	f
$e^- + NO \rightarrow 2e^- + NO^+$		286	
$e^- + NO_2 \rightarrow 2e^- + NO_2^+$		295	
$e^- + N_2O \rightarrow 2e^- + N_2O^+$		296	
$e^- + N_2O \rightarrow e^- + N_2 + O$		297	
$e^- + N_2O \rightarrow e^- + N_2 + O(1D)$		297	
$e^- + N_2O \rightarrow e^- + NO + N$		297	
$e^- + NO \rightarrow O^- + N$		286	
$e^- + N_2O \rightarrow N_2 + O^-$		296	
$e^- + NO_2 \rightarrow NO_2^-$	1×10^{-11}	298	
$e^- + NO_2 \rightarrow O^- + NO$	1×10^{-11}	299	
$e^- + NO + M \rightarrow NO^- + M$	8×10^{-31}	299	f
$e^- + N_2O + M \rightarrow N_2O^- + M$	6×10^{-33}	299	f

[a] For any species indicated with (g,v), g and v stand for its ground and vibrationally excited state, respectively.

[b] $N_2(E_x)$ represents the electronically excited states: $N_2(A^3\Sigma_u^+)$, $N_2(B^3\Pi_g)$, $N_2(C^3\Pi_u)$ and $N_2\left(a'^1\Sigma_u^-\right)$.
[c] The cross sections of the reactions involving excited species on the left hand side are shifted over the difference in the threshold energies.
[d] $N(E_x)$ represents the electronically excited states of atomic N: $N(2D)$ and $N(2P)$.
[e] $O_2(E_x)$ represents the electronically excited states: $O_2(a^1\Delta)$, $O_2(b^1\Sigma^+)$ and a combination of three states, i.e. $O_2(A^3\Sigma^+, C^3\Delta, c^1\Sigma^-)$ at a threshold energy of 4.5 eV.
[f] M represents any neutral molecule.

Appendix Table 4 Neutral-neutral reactions included in the model and the corresponding rate coefficient expressions. Tg is the gas temperature in Kelvin. The rate coefficients are expressed in $cm^3\ s^{-1}$ or $cm^6\ s^{-1}$ for binary or ternary reactions, respectively. For certain reactions, the rate coefficients of the vibrationally excited species are determined according to the Fridman-Macheret model in which the activation energy is reduced by $\alpha\, E_v$, where α is the vibrational efficiency to lower the activation barrier and E_v is the vibrational energy. For those reactions, the α parameter is given in the last column.

Reaction	Rate coefficient	Ref.	Note
$N_2(g,v) + M \rightarrow N + N + M$	$8.37 \times 10^{-4} \times \left(\frac{T_g}{298}\right)^{-3.5} \times \exp\left(-\frac{113710}{T_g}\right)$	300	a, b $\alpha = 1$
$N + N + M \rightarrow N_2 + M$	$1.38 \times 10^{-33} \times \exp\left(\frac{502.978}{T_g}\right)$	301	b
$N + N \rightarrow N_2^+ + e^-$	$2.7 \times 10^{-11} \times \exp\left(-\frac{6.74\times10^4}{T_g}\right)$	299	
$N + N + N \rightarrow N_2(A^3\Sigma_u^+) + N$	1.0×10^{-32}	299	
$N + N + N \rightarrow N_2(B^3\Pi_g) + N$	1.4×10^{-32}	299	
$N + N + N_2 \rightarrow N_2(A^3\Sigma_u^+) + N_2$	1.7×10^{-33}	299	
$N + N + N_2 \rightarrow N_2(B^3\Pi_g) + N_2$	2.4×10^{-33}	299	
$N(2D) + M \rightarrow N + M$	2.4×10^{-14}	302	b
$N(2P) + N \rightarrow N(2D) + N$	1.8×10^{-12}	299	
$N(2P) + N_2 \rightarrow N + N_2$	2.0×10^{-18}	299	
$N_2\left(a'^1\Sigma_u^-\right) + N \rightarrow N_2 + N$	2.0×10^{-11}	302	
$N_2\left(a'^1\Sigma_u^-\right) + N_2 \rightarrow N_2 + N_2$	3.7×10^{-16}	302	

$N_2\left(a'^1\Sigma_u^-\right) + N_2 \rightarrow N_2\left(B^3\Pi_g\right) + N_2$	1.9×10^{-13}	299	
$N_2\left(a'^1\Sigma_u^-\right) + N_2\left(a'^1\Sigma_u^-\right) \rightarrow N_2^+ + N_2 + e^-$	5.0×10^{-13}	302	
$N_2\left(a'^1\Sigma_u^-\right) + N_2\left(a'^1\Sigma_u^-\right) \rightarrow N_4^+ + e^-$	1.0×10^{-11}	299	
$N_2\left(a'^1\Sigma_u^-\right) + N_2(A^3\Sigma_u^+) \rightarrow N_4^+ + e^-$	4.0×10^{-12}	299	
$N_2(A^3\Sigma_u^+) + N \rightarrow N_2 + N(2P)$	$4.0 \times 10^{-11} \times \left(\frac{300}{T_g}\right)^{0.667}$	299	
$N_2(A^3\Sigma_u^+) + N \rightarrow N_2 + N$	2.0×10^{-12}	299	
$N_2(A^3\Sigma_u^+) + N_2 \rightarrow N_2 + N_2$	3.0×10^{-16}	299	
$N_2(A^3\Sigma_u^+) + N_2\left(a'^1\Sigma_u^-\right) \rightarrow N_2^+ + N_2 + e^-$	1.0×10^{-12}	302	
$N_2(A^3\Sigma_u^+) + N_2(A^3\Sigma_u^+) \rightarrow N_2 + N_2(A^3\Sigma_u^+)$	2.0×10^{-12}	302	
$N_2(A^3\Sigma_u^+) + N_2(A^3\Sigma_u^+) \rightarrow N_2 + N_2\left(B^3\Pi_g\right)$	3.0×10^{-10}	299	
$N_2(A^3\Sigma_u^+) + N_2(A^3\Sigma_u^+) \rightarrow N_2 + N_2(C^3\Pi_u)$	1.5×10^{-10}	299	
$N_2\left(B^3\Pi_g\right) + N_2 \rightarrow N_2 + N_2$	2.0×10^{-12}	299	
$N_2\left(B^3\Pi_g\right) + N_2 \rightarrow N_2(A^3\Sigma_u^+) + N_2$	3×10^{-11}	299	
$N_2(C^3\Pi_u) + N_2 \rightarrow N_2 + \left(a'^1\Sigma_u^-\right)$	1.0×10^{-11}	299	
$O_2(g, v) + M \rightarrow O + O + M$	$\left(\frac{3.0\times10^{-6}}{T_g}\right) \times \exp\left(\frac{-59380}{T_g}\right)$		a $\alpha = 1$
$O + O + M \rightarrow O_2 + M$	$5.21 \times 10^{-35} \times \exp\left(\frac{900}{T_g}\right)$	303	b
$O + O_3 \rightarrow O_2 + O_2$	$8.0 \times 10^{-12} \times \exp\left(-\frac{2056}{T_g}\right)$	304	
$O + O_2(g, v) + M \rightarrow O_3 + M$	$1.34 \times 10^{-34} \times \left(\frac{T_g}{298}\right)^{-1.0}$	305	a, b
$O_3 + M \rightarrow O_2 + O + M$	$7.16 \times 10^{-10} \times \exp\left(-\frac{98120}{R_g T_g}\right)$	306	b, c

$O + O_2(E_x) + M \rightarrow O_3 + M$	$1.34 \times 10^{-34} \times \left(\frac{T_g}{298}\right)^{-1.0}$	305	b, d, e
$O + O_3 \rightarrow O_2 + O_2(a^1\Delta)$	$2.0 \times 10^{-11} \times \exp\left(-\frac{2280}{T_g}\right)$	299	
$O_2(a^1\Delta) + O \rightarrow O_2 + O$	7.0×10^{-16}	299	
$O_2(a^1\Delta) + O_2 \rightarrow O_2 + O_2$	$3.8 \times 10^{-18} \times \exp\left(-\frac{205}{T_g}\right)$	299	
$O_2(b^1\Sigma^+) + O \rightarrow O_2(a^1\Delta) + O$	8.1×10^{-14}	299	
$O_2(b^1\Sigma^+) + O \rightarrow O_2 + O(1D)$	$3.4 \times 10^{-11} \times \left(\frac{T_g}{300}\right)^{-0.1} \times \exp\left(-\frac{4200}{T_g}\right)$	299	
$O_2(b^1\Sigma^+) + O_2 \rightarrow O_2 + O_2(a^1\Delta)$	$4.3 \times 10^{-22} \times \left(T_g\right)^{2.4} \times \exp\left(-\frac{281}{T_g}\right)$	299	
$O_2(b^1\Sigma^+) + O_3 \rightarrow O_2 + O_2 + O$	2.2×10^{-11}	299	
$O_2(a^1\Delta) + O_3 \rightarrow O_2 + O_2 + O(1D)$	$5.2 \times 10^{-11} \times \exp\left(-\frac{2840}{T_g}\right)$	299	
$O_2(a^1\Delta) + O_2(a^1\Delta) \rightarrow O_2 + O_2(b^1\Sigma^+)$	$7.0 \times 10^{-28} \times \left(T_g\right)^{3.8} \times \exp\left(\frac{700}{T_g}\right)$	299	
$O(1D) + O \rightarrow O + O$	8.0×10^{-12}	299	
$O(1D) + O_2 \rightarrow O + O_2$	$6.4 \times 10^{-12} \times \exp\left(-\frac{67}{T_g}\right)$	299	
$O(1S) + O \rightarrow O(1D) + O(1D)$	$5.0 \times 10^{-11} \times \exp\left(-\frac{300}{T_g}\right)$	299	
$O(1S) + O_2 \rightarrow O + O_2$	$1.3 \times 10^{-12} \times \exp\left(-\frac{850}{T_g}\right)$	299	
$O(1S) + O_2 \rightarrow O + O + O$	3.0×10^{-12}	299	
$O(1S) + O_2(a^1\Delta) \rightarrow O + O + O$	3.2×10^{-11}	299	
$O(1S) + O_2(a^1\Delta) \rightarrow O(1D) + O_2(b^1\Sigma^+)$	2.9×10^{-11}	299	
$O(1S) + O_2 \rightarrow O + O_2(A^3\Sigma^+, C^3\Delta, c^1\Sigma^-)$	$3.0 \times 10^{-12} \times \exp\left(-\frac{850}{T_g}\right)$	299	f
$N + O_2(g, v) \rightarrow O + NO$	$2.36 \times 10^{-11} \times \exp\left(-\frac{44230}{R_g T_g}\right)$	307	a, c

			$\alpha = 0.24$
$O + N_2(g, v) \rightarrow N + NO$	$3.01 \times 10^{-10} \times \exp\left(-\frac{318000}{R_g T_g}\right)$	257	a, c $\alpha = 1$
$O_3 + N \rightarrow NO + O_2$	$5.0 \times 10^{-12} \times \exp\left(-\frac{650}{T_g}\right)$	304	
$O_3 + NO \rightarrow O_2 + NO_2$	$2.5 \times 10^{-13} \times \exp\left(-\frac{765}{T_g}\right)$	299	
$O_3 + NO_2 \rightarrow O_2 + NO_3$	$1.2 \times 10^{-13} \times \exp\left(-\frac{2450}{T_g}\right)$	298	
$NO_3 + O_3 \rightarrow NO_2 + O_2 + O_2$	1.0×10^{-17}	308	
$N + NO \rightarrow O + N_2$	1.66×10^{-11}	309	
$N + NO_2 \rightarrow O + O + N_2$	9.1×10^{-13}	299	
$N + NO_2 \rightarrow O + N_2O$	3.0×10^{-12}	299	
$N + NO_2 \rightarrow N_2 + O_2$	7.0×10^{-13}	299	
$N + NO_2 \rightarrow NO + NO$	2.3×10^{-12}	299	
$O + NO \rightarrow N + O_2$	$7.5 \times 10^{-12} \times \left(\frac{T_g}{300}\right) \times \exp\left(-\frac{19500}{T_g}\right)$	299	
$\mathbf{O + NO_2 \rightarrow NO + O_2}$	$\mathbf{5.5 \times 10^{-12} \times \exp(\frac{188}{T_g})}$	310	**i**
$O + N_2O \rightarrow NO + NO$	$1.5 \times 10^{-10} \times \exp\left(-\frac{14090}{T_g}\right)$	299	
$O + N_2O \rightarrow N_2 + O_2$	$8.3 \times 10^{-12} \times \exp\left(-\frac{14000}{T_g}\right)$	299	
$O + NO_3 \rightarrow O_2 + N_2$	1.0×10^{-11}	299	
$NO + NO \rightarrow N + NO_2$	$3.3 \times 10^{-16} \times \left(\frac{300}{T_g}\right)^{0.5} \times \exp\left(-\frac{39200}{T_g}\right)$	299	
$NO + NO \rightarrow O + N_2O$	$2.2 \times 10^{-12} \times \exp\left(-\frac{32100}{T_g}\right)$	299	
$NO + NO \rightarrow N_2 + O_2$	$5.1 \times 10^{-13} \times \exp\left(-\frac{33660}{T_g}\right)$	299	

$NO + N_2O \rightarrow N_2 + NO_2$	$4.6 \times 10^{-10} \times \exp\left(-\frac{25170}{T_g}\right)$	299	
$NO + NO_3 \rightarrow NO_2 + NO_2$	1.7×10^{-11}	299	
$NO_2 + NO_2 \rightarrow NO + NO_3$	$4.5 \times 10^{-10} \times \exp\left(-\frac{18500}{T_g}\right)$	299	
$NO_2 + NO_2 \rightarrow NO + NO + O_2$	$3.3 \times 10^{-12} \times \exp\left(-\frac{13500}{T_g}\right)$	299	
$NO_2 + NO_3 \rightarrow NO + NO_2 + O_2$	$2.3 \times 10^{-13} \times \exp\left(-\frac{1600}{T_g}\right)$	299	
$NO_3 + NO_3 \rightarrow O_2 + NO_2 + NO_2$	$4.3 \times 10^{-12} \times \exp\left(-\frac{3850}{T_g}\right)$	299	
$NO + O_2(g, v) \rightarrow O + NO_2$	$2.8 \times 10^{-12} \times \exp\left(-\frac{23400}{T_g}\right)$	299	a $\alpha = 1$
$NO + NO + O_2(g, v) \rightarrow NO_2 + NO_2$	$3.3 \times 10^{-39} \times \exp\left(-\frac{4410}{R_g T_g}\right)$	210	a, c $\alpha = 0.2$
$NO_2 + O_2(g, v) \rightarrow NO + O_3$	$2.8 \times 10^{-12} \times \exp\left(-\frac{25400}{T_g}\right)$	299	a $\alpha = 0.2$
$NO_3 + O_2(g, v) \rightarrow O_3 + NO_2$	$1.5 \times 10^{-12} \times \exp\left(-\frac{15020}{T_g}\right)$	299	a $\alpha = 0.8$
$NO + O \rightarrow NO_2$	$3.01 \times 10^{-11} \times \left(\frac{T_g}{300}\right)^{-0.75}$	213	
$NO_2 + NO + M \rightarrow N_2O_3 + M$	$3.09 \times 10^{-34} \times \left(\frac{T_g}{300}\right)^{-7.70}$	304	b
$NO_2 + NO_2 + M \rightarrow N_2O_4 + M$	$1.4 \times 10^{-33} \times \left(\frac{T_g}{300}\right)^{-3.8}$	304	b
$NO_2 + NO_3 + M \rightarrow N_2O_5 + M$	$3.7 \times 10^{-30} \times \left(\frac{300}{T_g}\right)^{4.10}$	210	b
$N + O + M \rightarrow NO + M$	$1.0 \times 10^{-32} \times \left(\frac{300}{T_g}\right)^{0.5}$	299	b

$N_2(g,v) + O + M \rightarrow N_2O + M$	$3.9 \times 10^{-35} \times \exp\left(-\frac{10400}{T_g}\right)$	299	b
$N_2O + M \rightarrow N_2 + O + M$	$1.20 \times 10^{-9} \times \exp\left(-\frac{240000}{R_g T_g}\right)$	299	b, c
$NO_2 + M \rightarrow NO + O + M$	$9.4 \times 10^{-5} \times \left(\frac{T_g}{298}\right)^{-2.66} \times \exp\left(-\frac{311000}{R_g T_g}\right)$	213	b, c
$NO_3 + M \rightarrow NO + O_2 + M$	$2.51 \times 10^{-14} \times \exp\left(-\frac{10230}{R_g T_g}\right)$	311	b, c
$NO + M \rightarrow N + O + M$	$8.7 \times 10^{-9} \times \exp\left(-\frac{75994}{T_g}\right)$	299	b
$N_2O_3 + M \rightarrow NO + NO_2 + M$	$1.91 \times 10^{-7} \times \left(\frac{T_g}{298}\right)^{-8.7} \times \exp\left(-\frac{40570}{R_g T_g}\right)$	304	b, c
$N_2O_4 + M \rightarrow NO_2 + NO_3 + M$	$1.3 \times 10^{-5} \times \left(\frac{T_g}{298}\right)^{-3.8} \times \exp\left(-\frac{53210}{R_g T_g}\right)$	304	b, c
$N_2O_5 + M \rightarrow NO_2 + NO_3 + M$	$2.1 \times 10^{-11} \times \left(\frac{300}{T_g}\right)^{-3.5} \times \exp\left(-\frac{91460}{R_g T_g}\right)$	299	b, c
$NO + O_2(g,v) + M \rightarrow NO_3 + M$	$5.65 \times 10^{-41} \times \exp\left(-\frac{1750}{R_g T_g}\right)$	312	a, b, c
$NO + O_2(E_x) + M \rightarrow NO_3 + M$	$5.65 \times 10^{-41} \times \exp\left(-\frac{1750}{R_g T_g}\right)$	312	b, d
$N + N + NO \rightarrow N_2(A^3\Sigma_u^+) + NO$	1.7×10^{-33}	299	
$N + N + NO \rightarrow N_2(B^3\Pi_g) + NO$	2.4×10^{-33}	299	
$N + N + O \rightarrow N_2(A^3\Sigma_u^+) + O$	1.0×10^{-32}	299	
$N + N + O \rightarrow N_2(B^3\Pi_g) + O$	1.4×10^{-32}	299	
$N + N + O_2 \rightarrow N_2(A^3\Sigma_u^+) + O_2$	1.7×10^{-33}	299	
$N + N + O_2 \rightarrow N_2(B^3\Pi_g) + O_2$	2.4×10^{-33}	299	
$N(2D) + N_2O \rightarrow NO + N_2$	3.5×10^{-12}	299	
$N(2D) + NO \rightarrow N_2 + O$	1.8×10^{-10}	299	

$N(2D) + O \rightarrow N + O(1D)$	4.0×10^{-13}	299	
$N(2D) + O_2(g, v) \rightarrow NO + O$	5.2×10^{-12}	299	a
$N(2P) + NO \rightarrow N_2(A^3\Sigma_u^+) + O$	3.0×10^{-11}	299	
$N(2P) + O \rightarrow N + O$	1.0×10^{-12}	299	
$N(2P) + O_2(g, v) \rightarrow NO + O$	2.6×10^{-15}	299	a
$N_2\left(a'^1\Sigma_u^-\right) + NO \rightarrow N_2 + N + O$	3.6×10^{-10}	299	
$N_2\left(a'^1\Sigma_u^-\right) + O \rightarrow NO + N$	3.0×10^{-10}	257	
$N_2\left(a'^1\Sigma_u^-\right) + O_2(g, v) \rightarrow N_2 + O + O$	2.8×10^{-11}	299	a
$N_2(A^3\Sigma_u^+) + N_2O \rightarrow N_2 + N + NO$	1.0×10^{-11}	299	
$N_2(A^3\Sigma_u^+) + NO \rightarrow N_2 + NO$	6.9×10^{-11}	299	
$N_2(A^3\Sigma_u^+) + NO_2 \rightarrow N_2 + O + NO$	1.0×10^{-12}	299	
$N_2(A^3\Sigma_u^+) + O \rightarrow N_2 + O(1S)$	2.1×10^{-11}	299	
$N_2(A^3\Sigma_u^+) + O \rightarrow NO + N(2D)$	7.0×10^{-12}	299	
$N_2(A^3\Sigma_u^+) + O_2(g, v) \rightarrow N_2 + O + O$	$2.0 \times 10^{-12} \times \left(\frac{T_g}{300}\right)^{0.55}$	299	a
$N_2(A^3\Sigma_u^+) + O_2 \rightarrow N_2 + O_2(a^1\Delta)$	$2.0 \times 10^{-13} \times \left(\frac{T_g}{300}\right)^{0.55}$	299	
$N_2(A^3\Sigma_u^+) + O_2 \rightarrow N_2 + O_2$	2.54×10^{-12}	299	
$N_2(A^3\Sigma_u^+) + O_2(g, v) \rightarrow N_2O + O$	$2.0 \times 10^{-14} \times \left(\frac{T_g}{300}\right)^{0.55}$	299	a
$N_2\left(B^3\Pi_g\right) + N_2O \rightarrow N_2 + N + NO$	0.58×10^{-10}	313	
$N_2\left(B^3\Pi_g\right) + N_2O \rightarrow N_2 + N_2 + O$	0.58×10^{-10}	313	
$N_2\left(B^3\Pi_g\right) + O \rightarrow NO + N$	3.0×10^{-10}	257	
$N_2(C^3\Pi_u) + O \rightarrow NO + N$	3.0×10^{-10}	257	
$N_2(C^3\Pi_u) + O_2(g, v) \rightarrow N_2 + O + O$	3.0×10^{-10}	299	a
$NO + O_2(E_x) \rightarrow O + NO_2$	$2.8 \times 10^{-12} \times \exp\left(-\frac{23400}{T_g}\right)$	299	d, g
$NO_3 + O_2(E_x) \rightarrow O_3 + NO_2$	$1.5 \times 10^{-12} \times \exp\left(-\frac{15020}{T_g}\right)$	299	d, h

$O(1D) + N_2 \rightarrow N_2 + O$	2.3×10^{-11}	[299]	
$O(1S) + N \rightarrow O + N$	1.0×10^{-12}	[299]	
$O(1S) + N_2(g, v) \rightarrow O + N_2(g, v)$	1.0×10^{-17}	[299]	
$O_2(a^1\Delta) + N \rightarrow NO + O$	$2.0 \times 10^{-14} \times \exp\left(-\frac{600}{T_g}\right)$	[299]	
$O_2(a^1\Delta) + N_2(g, v) \rightarrow O_2 + N_2(g, v)$	3.0×10^{-21}	[299]	
$O_2(a^1\Delta) + NO \rightarrow O_2 + NO$	2.5×10^{-11}	[299]	
$O_2(b^1\Sigma^+) + N_2 \rightarrow O_2(a^1\Delta) + N_2$	$1.7 \times 10^{-15} \times \left(\frac{T_g}{300}\right)^{1.0}$	[299]	
$N_2(B^3\Pi_g) + NO \rightarrow N_2(A^3\Sigma_u^+) + NO$	2.4×10^{-10}	[299]	
$N_2(B^3\Pi_g) + O_2(g, v) \rightarrow N_2 + O + O$	3.0×10^{-10}	[299]	a

[a] For any species indicated with (g, v), g and v stand for its ground and vibrationally excited state, respectively.
[b] M represents any neutral molecule.
[c] $R_g = 8.3144598\ J.K^{-1}.mol^{-1}$ is the universal gas constant.
[d] $O_2(E_x)$ represents the two electronically excited states: $O_2(a^1\Delta)$ and $O_2(b^1\Sigma^+)$.
[e] The rate coefficient is assumed to be equal to that of $O + O_2 + M \rightarrow O_3 + M$.
[f] $O_2(A^3\Sigma^+, C^3\Delta, c^1\Sigma^-)$ is a combination of three electronic excited states at a threshold energy of 4.5 eV.
[g] The rate coefficient is assumed to be equal to that of $NO + O_2 \rightarrow O + NO_2$.
[h] The rate coefficient is assumed to be equal to that of $NO_3 + O_2 \rightarrow O_3 + NO_2$.
[i] The reaction rate coefficient for this reaction has been changed compared to our previous work. Before $k = 9.05 \times 10^{-12} \times \left(\frac{T_g}{298}\right)^{-0.52}$ from [310] was used. The updated reaction rate coefficient was found to be more appropriate after critical review of the literature.

Appendix Table 5 Electron-ion recombination reactions included in the model and the corresponding rate coefficient expressions. T_e is to the electron temperature in K and T_g is the gas temperature in K. The rate coefficients are expressed in $cm^3\ s^{-1}$ or $cm^6\ s^{-1}$ for binary or ternary reactions, respectively.

Reaction	Rate coefficient	Ref.	Note
$e^- + N_2^+ \rightarrow N + N(g, E_x)$	$R \times 1.8 \times 10^{-7} \times \left(\frac{300}{T_e}\right)^{0.39}$	299	a
$e^- + N_3^+ \rightarrow N_2 + N$	$2 \times 10^{-7} \times \left(\frac{300}{T_e}\right)^{0.5}$	314	
$e^- + N_3^+ \rightarrow N_2(E_x) + N$	$6.91 \times 10^{-8} \times \left(\frac{T_e}{11604.5}\right)^{-0.5}$	314	c
$e^- + N_4^+ \rightarrow N_2 + N_2$	$2.3 \times 10^{-6} \times \left(\frac{300}{T_e}\right)^{0.53}$	299	
$e^- + N_4^+ \rightarrow N_2 + N + N$	$3.13 \times 10^{-7} \times \left(\frac{T_e}{11604.5}\right)^{-0.41}$	314	
$e^- + N^+ + e^- \rightarrow e^- + N$	$7 \times 10^{-20} \times \left(\frac{300}{T_e}\right)^{4.5}$	314	
$e^- + N^+ + M \rightarrow N + M$	$6 \times 10^{-27} \times \left(\frac{300}{T_e}\right)^{1.5}$	211	b
$e^- + N_2^+ + e^- \rightarrow e^- + N_2$	$1 \times 10^{-19} \times \left(\frac{T_e}{300}\right)^{-4.5}$	314	
$e^- + N_2^+ + M \rightarrow N_2 + M$	$2.49 \times 10^{-29} \times \left(\frac{T_e}{11604.5}\right)^{-1.5}$	314	b
$e^- + O^+ + O_2 \rightarrow O + O_2$	$6 \times 10^{-27} \times \left(\frac{300}{T_e}\right)^{1.5}$	211	
$e^- + O^+ + e^- \rightarrow e^- + O$	$7 \cdot 10^{-20} \cdot \left(\frac{300}{T_e}\right)^{4.5}$	299	
$e^- + O_2^+ + M \rightarrow O_2 + M$	1×10^{-26}	294	b
$e^- + O_2^+ + e^- \rightarrow e^- + O_2$	$1 \times 10^{-19} \times \left(\frac{T_e}{300}\right)^{-4.5}$	211	
$e^- + O_2^+ \rightarrow O + O$	$6.46 \times 10^{-5} \times T_e^{-0.5} \times T_g^{-0.5}$	315	
$e^- + O_2^+ \rightarrow O + O(1D)$	$1.08 \times 10^{-7} \left(\frac{T_e}{300}\right)^{-0.7}$	299	
$e^- + O_2^+ \rightarrow O + O(1S)$	$0.14 \times 10^{-7} \left(\frac{T_e}{300}\right)^{-0.7}$	299	
$e^- + O_4^+ \rightarrow O_2 + O_2$	$1.4 \times 10^{-6} \times \left(\frac{300}{T_e}\right)^{0.5}$	299	

$e^- + NO^+ + e^- \rightarrow e^- + NO$	$1.0 \times 10^{-19} \left(\frac{T_e}{300}\right)^{-4.5}$	211	
$e^- + NO^+ + M \rightarrow NO + M$	$2.49 \times 10^{-29} \times \left(\frac{T_e}{11604.5}\right)^{-1.5}$	314	b
$e^- + NO^+ \rightarrow O + N(g, E_x)$	$R \times 4.2 \times 10^{-7} \times \left(\frac{300}{T_e}\right)^{0.85}$	299	d
$e^- + N_2O^+ \rightarrow N_2 + O$	$2.0 \times 10^{-7} \times \left(\frac{300}{T_e}\right)^{0.5}$	299	
$e^- + NO_2^+ \rightarrow NO + O$	$2.0 \times 10^{-7} \times \left(\frac{300}{T_e}\right)^{0.5}$	299	
$e^- + O_2^+N_2 \rightarrow O_2 + N_2$	$1.3 \times 10^{-6} \times \left(\frac{300}{T_e}\right)^{0.5}$	299	

[a] In $N(g, E_x)$, g stands for the ground state of atomic N and E_x represents two of its electronically excited states: $N(2D)$ and $N(2P)$; R is equal to 0.5, 0.45 and 0.05 for N, $N(2D)$ and $N(2P)$, respectively.

[b] M represents any neutral molecule.

[c] $N_2(E_x)$ represents $N_2(A^3\Sigma_u^+)$ and $N_2(B^3\Pi_g)$.

[d] In $N(g, E_x)$, g stands for the ground state of atomic N and E_x represents the electronic excited state $N(2D)$; R is equal to 0.2 and 0.8 for N and $N(2D)$, respectively.

Appendix Table 6 Ion-neutral reactions included in the model and the corresponding rate coefficient expressions. T_g is the gas temperature in K. For certain reactions, T_{ion} is the effective temperature of the reacting ion in K. The calculations for T_{ion} can be found in [230]. The rate coefficients are expressed in $cm^3\ s^{-1}$ or $cm^6\ s^{-1}$ for binary or ternary reactions, respectively.

Reaction	Rate coefficient	Ref.	Note
$N_2^+ + N \rightarrow N^+ + N_2$	$7.2 \times 10^{-13} \times \left(\frac{T_{ion}}{300}\right)$	[299]	
$N_2^+ + N + N_2 \rightarrow N_3^+ + N_2$	$9.0 \times 10^{-30} \times \left(\frac{400}{T_{ion}}\right)$	[299]	
$N_4^+ + N_2 \rightarrow N_2^+ + N_2 + N_2$	$2.1 \times 10^{-16} \times \left(\frac{Tion}{121}\right)$	[299]	
$N^+ + N_2 + N_2 \rightarrow N_3^+ + N_2$	$1.7 \times 10^{-29} \times \left(\frac{300}{Tion}\right)^{2.1}$	[299]	
$N_2^+ + N_2 + N_2 \rightarrow N_4^+ + N_2$	$5.2 \times 10^{-29} \times \left(\frac{300}{T_{ion}}\right)^{2.2}$	[299]	
$N^+ + N + N_2 \rightarrow N_2^+ + N_2$	1.0×10^{-29}	[299]	
$N^+ + N \rightarrow N_2^+$	1.0×10^{-29}	[316]	
$N_3^+ + N \rightarrow N_2^+ + N_2$	6.6×10^{-11}	[299]	
$N_4^+ + N \rightarrow N^+ + N_2 + N_2$	1.0×10^{-11}	[299]	
$N_2^+ + N_2(A^3\Sigma_u^+) \rightarrow N_3^+ + N$	3.0×10^{-10}	[298]	
$O^- + M \rightarrow O + M + e^-$	4.0×10^{-12}	[298]	a
$O^- + O \rightarrow O_2 + e^-$	2.3×10^{-10}	[317]	
$O^- + O_2(g, v) + M \rightarrow O_3^- + M$	$1.1 \times 10^{-30} \times \exp\left(\frac{300}{T_g}\right)$	[317]	a, b
$O^- + O_2(g, v) \rightarrow O_3 + e^-$	5.0×10^{-15}	[299]	b
$O^- + O_3 \rightarrow O_2 + O_2 + e^-$	3.0×10^{-10}	[318]	
$O^- + O_3 \rightarrow O_3^- + O$	5.3×10^{-10}	[319]	
$O^+ + O + M \rightarrow O_2^+ + M$	1.0×10^{-29}	[211]	a
$O^+ + O_2(g, v) \rightarrow O + O_2^+$	$1.9 \times 10^{-11} \times \left(\frac{T_g}{300}\right)^{-0.5}$	[320]	b
$O^+ + O_3 \rightarrow O_2^+ + O_2$	1.0×10^{-10}	[211]	

$O_2^- + M \rightarrow O_2 + M + e^-$	$2.7 \times 10^{-10} \times \left(\frac{T_g}{300}\right)^{0.5} \times \exp\left(-\frac{5590}{T_g}\right)$	320	a
$O_2^- + O \rightarrow O_2 + O^-$	3.31×10^{-10}	317	
$O_2^- + O_2(g,v) + M \rightarrow O_4^- + M$	$3.5 \times 10^{-31} \times \left(\frac{T_g}{300}\right)^{-1.0}$	211,317,319	a, b
$O_2^- + O_2 \rightarrow O_2 + O_2 + e^-$	2.18×10^{-18}	321	
$O_2^- + O_3 \rightarrow O_3^- + O_2$	4.0×10^{-10}	317	
$O_2^+ + O_2(g,v) + M \rightarrow O_4^+ + M$	$2.4 \times 10^{-30} \times \left(\frac{T_g}{300}\right)^{-3.2}$	211	a, b
$O_3^- + M \rightarrow O_3 + M + e^-$	2.3×10^{-11}	320	a
$O_3^- + O \rightarrow O_2 + O_2 + e^-$	1.0×10^{-13}	319	
$O_3^- + O \rightarrow O_2^- + O_2$	2.5×10^{-10}	293	
$O_3^- + O \rightarrow O_3 + O^-$	1.0×10^{-13}	317	
$O_3^- + O_3 \rightarrow O_2 + O_2 + O_2 + e^-$	3.0×10^{-10}	319	
$O_4^- + O \rightarrow O^- + O_2 + O_2$	3.0×10^{-10}	211	
$O_4^- + O \rightarrow O_3^- + O_2$	4.0×10^{-10}	211	
$O_4^- + O_2 \rightarrow O_2^- + O_2 + O_2$	$1.0 \times 10^{-10} \times \exp\left(-\frac{1044}{T_g}\right)$	299	
$O_4^+ + O \rightarrow O_2^+ + O_3$	3.0×10^{-10}	211	
$O_4^+ + O_2 \rightarrow O_2^+ + O_2 + O_2$	$3.3 \times 10^{-6} \times \left(\frac{300}{T_g}\right)^{4.0} \times \exp\left(-\frac{5030}{T_g}\right)$	211	
$O^- + O_2(a^1\Delta) \rightarrow O_3 + e^-$	3.0×10^{-10}	299	
$O_2^- + O_2(a^1\Delta) \rightarrow O_2 + O_2 + e^-$	2.0×10^{-10}	299	
$O_2^- + O_2(b^1\Sigma^+) \rightarrow O_2 + O_2 + e^-$	3.6×10^{-10}	299	
$O_2^+ + O_2(E_x) + M \rightarrow O_4^+ + M$	$2.4 \times 10^{-30} \times \left(\frac{T_g}{300}\right)^{-3.2}$	299	a, c, d
$O_4^+ + O_2(a^1\Delta) \rightarrow O_2^+ + O_2 + O_2$	1.0×10^{-10}	299	

$O_4^- + O_2(E_x) \rightarrow O_2^- + O_2 + O_2$	1.0×10^{-10}	299	c
$O^- + O_2(a^1\Delta) \rightarrow O_2^- + O$	1.0×10^{-10}	299	
$O^- + O_2(E_x) + M \rightarrow O_3^- + M$	$1.1 \times 10^{-30} \times \exp\left(\frac{300}{T_g}\right)$	299	a, c, e
$O_2^- + O_2(E_x) + M \rightarrow O_4^- + M$	$3.5 \times 10^{-31} \times \exp\left(\frac{T_g}{300}\right)^{-1.0}$	211	a, c, f
$N^+ + N + O_2 \rightarrow N_2^+ + O_2$	1.0×10^{-29}	299	
$N^+ + N_2O \rightarrow NO^+ + N_2$	5.5×10^{-10}	299	
$N^+ + NO \rightarrow N_2^+ + O$	3.0×10^{-12}	299	
$N^+ + NO \rightarrow NO^+ + N$	8.0×10^{-10}	299	
$N^+ + NO \rightarrow O^+ + N_2$	1.0×10^{-12}	299	
$N^+ + O + M \rightarrow NO^+ + M$	1.0×10^{-29}	299	a
$N^+ + O \rightarrow N + O^+$	1.0×10^{-12}	299	
$N^+ + O_2 \rightarrow NO^+ + O$	2.5×10^{-10}	299	
$N^+ + O_2 \rightarrow O^+ + NO$	2.8×10^{-11}	299	
$N^+ + O_2 \rightarrow O_2^+ + N$	2.8×10^{-10}	299	
$N^+ + O_3 \rightarrow NO^+ + O_2$	5.0×10^{-10}	299	
$N_2^+ + N_2O \rightarrow N_2O^+ + N_2$	5.0×10^{-10}	299	
$N_2^+ + N_2O \rightarrow NO^+ + N + N_2$	4.0×10^{-10}	299	
$N_2^+ + NO \rightarrow NO^+ + N_2$	3.3×10^{-10}	299	
$N_2^+ + O \rightarrow NO^+ + N$	$1.3 \times 10^{-10} \times \left(\frac{300}{T_{ion}}\right)^{0.5}$	299	
$N_2^+ + O_2 \rightarrow O_2^+ + N_2$	$6.0 \times 10^{-11} \times \left(\frac{300}{T_{ion}}\right)^{0.5}$	299	
$N_2^+ + O_3 \rightarrow O_2^+ + O + N_2$	1.0×10^{-10}	299	
$N_2O^- + N \rightarrow NO + N_2 + e^-$	5.0×10^{-10}	298	
$N_2O^- + O \rightarrow NO + NO + e^-$	1.5×10^{-10}	298	
$N_2O^+ + NO \rightarrow NO^+ + N_2O$	2.9×10^{-10}	299	
$N_3^+ + NO \rightarrow N_2O^+ + N_2$	7.0×10^{-11}	299	
$N_3^+ + NO \rightarrow NO^+ + N + N_2$	7.0×10^{-11}	299	

$N_3^+ + O_2 \rightarrow NO_2^+ + N_2$	4.4×10^{-11}	299	
$N_3^+ + O_2 \rightarrow O_2^+ + N + N_2$	2.3×10^{-11}	299	
$N_4^+ + NO \rightarrow NO^+ + N_2 + N_2$	4.0×10^{-10}	299	
$N_4^+ + O \rightarrow O^+ + N_2 + N_2$	2.5×10^{-10}	299	
$N_4^+ + O_2 \rightarrow O_2^+ + N_2 + N_2$	2.5×10^{-10}	299	
$NO^- + N_2O \rightarrow NO + N_2O + e^-$	$4.26 \times 10^{-10} \times \exp\left(-\frac{107.2}{T_g}\right)$	322	
$NO^- + NO \rightarrow NO + NO + e^-$	$3.28 \times 10^{-10} \times \exp\left(-\frac{105.1}{T_g}\right)$	323	
$NO^- + N \rightarrow N_2O + e^-$	5.0×10^{-10}	299	
$NO^- + N_2O \rightarrow NO_2^- + N_2$	2.8×10^{-14}	299	
$NO^- + NO_2 \rightarrow NO_2^- + NO$	7.4×10^{-10}	299	
$NO^- + O \rightarrow NO_2 + e^-$	1.5×10^{-10}	298	
$NO^- + O_2 \rightarrow O_2^- + NO$	5.0×10^{-10}	299	
$NO_2^- + N \rightarrow NO + NO + e^-$	5.0×10^{-10}	298	
$NO_2^- + N_2O_5 \rightarrow NO_3^- + NO_2 + NO_2$	7.0×10^{-10}	299	
$NO_2^- + NO_2 \rightarrow NO_3^- + NO$	4.0×10^{-12}	299	
$NO_2^- + NO_3 \rightarrow NO_3^- + NO_2$	5.0×10^{-10}	299	
$NO_2^- + O_3 \rightarrow NO_3^- + O_2$	1.8×10^{-11}	299	
$NO_2^+ + NO \rightarrow NO^+ + NO_2$	2.9×10^{-10}	299	
$NO_3^- + N \rightarrow NO + NO_2 + e^-$	5.0×10^{-10}	298	
$NO_3^- + NO \rightarrow NO_2^- + NO_2$	3.0×10^{-15}	299	
$NO_3^- + O \rightarrow NO + O_3 + e^-$	1.5×10^{-10}	298	
$O^- + N \rightarrow NO + e^-$	2.6×10^{-10}	299	
$O^- + N_2(g, v) \rightarrow N_2O + e^-$	0.5×10^{-13}	299	b
$O^- + N_2(A^3\Sigma_u^+) \rightarrow O + N_2 + e^-$	2.2×10^{-9}	299	
$O^- + N_2(B^3\Pi_g) \rightarrow O + N_2 + e^-$	1.9×10^{-9}	299	

$O^- + N_2O \rightarrow N_2O^- + O$	2.0×10^{-12}	[299]	
$O^- + N_2O \rightarrow NO^- + NO$	2.0×10^{-10}	[299]	
$O^- + NO + M \rightarrow NO_2^- + M$	1.0×10^{-29}	[299]	a
$O^- + NO \rightarrow NO_2 + e^-$	2.6×10^{-10}	[299]	
$O^- + NO_2 \rightarrow NO_2^- + O$	1.2×10^{-9}	[299]	
$O^+ + N + M \rightarrow NO^+ + M$	1.0×10^{-29}	[299]	a
$O^+ + N \rightarrow N^+ + O$	1.3×10^{-10}	[299]	
$O^+ + N_2(g, v) + M \rightarrow NO^+ + N + M$	$6.0 \times 10^{-29} \times \left(\frac{300}{T_{ion}}\right)^2$	[299]	a, b
$O^+ + N_2(g, v) \rightarrow NO^+ + N$	$(1.5 - 2.0 \times 10^{-3} \times T_{ion} + 9.6 \times 10^{-7} \times T_{ion}^2) \times 1.0 \times 10^{-12}$	[299]	b
$O^+ + N_2O \rightarrow N_2O^+ + O$	2.2×10^{-10}	[299]	
$O^+ + N_2O \rightarrow NO^+ + NO$	2.3×10^{-10}	[299]	
$O^+ + N_2O \rightarrow O_2^+ + N_2$	2.0×10^{-11}	[299]	
$O^+ + NO \rightarrow NO^+ + O$	2.4×10^{-11}	[299]	
$O^+ + NO \rightarrow O_2^+ + N$	3.0×10^{-12}	[299]	
$O^+ + NO_2 \rightarrow NO_2^+ + O$	1.6×10^{-9}	[299]	
$O_2^- + N \rightarrow NO_2 + e^-$	5.0×10^{-10}	[299]	
$O_2^- + N_2(B^3\Pi_g) \rightarrow O_2 + N_2 + e^-$	2.5×10^{-9}	[299]	
$O_2^- + N_2(A^3\Sigma_u^+) \rightarrow O_2 + N_2 + e^-$	2.1×10^{-9}	[299]	
$O_3^- + N_2(B^3\Pi_g) \rightarrow O_3 + N_2 + e^-$	2.5×10^{-9}	[298]	
$O_3^- + N_2(A^3\Sigma_u^+) \rightarrow O_3 + N_2 + e^-$	2.1×10^{-9}	[298]	
$NO^- + N_2(B^3\Pi_g) \rightarrow NO + N_2 + e^-$	2.5×10^{-9}	[298]	

$NO^- + N_2(A^3\Sigma_u^+) \rightarrow NO + N_2 + e^-$	2.1×10^{-9}	298	
$N_2O^- + N_2(B^3\Pi_g) \rightarrow N_2O + N_2 + e^-$	2.5×10^{-9}	298	
$N_2O^- + N_2(A^3\Sigma_u^+) \rightarrow N_2O + N_2 + e^-$	2.1×10^{-9}	298	
$NO_2^- + N_2(B^3\Pi_g) \rightarrow NO_2 + N_2 + e^-$	2.5×10^{-9}	298	
$NO_2^- + N_2(A^3\Sigma_u^+) \rightarrow NO_2 + N_2 + e^-$	2.1×10^{-9}	298	
$NO_3^- + N_2(B^3\Pi_g) \rightarrow NO_3 + N_2 + e^-$	2.5×10^{-9}	298	
$NO_3^- + N_2(A^3\Sigma_u^+) \rightarrow NO_3 + N_2 + e^-$	2.1×10^{-9}	298	
$O_2^- + NO_2 \rightarrow NO_2^- + O_2$	7.0×10^{-10}	299	
$O_2^- + NO_3 \rightarrow NO_3^- + O_2$	5.0×10^{-10}	299	
$O_2^+ + N \rightarrow NO^+ + O$	1.2×10^{-10}	299	
$O_2^+ + N_2(g, v) + N_2 \rightarrow O_2^+N_2 + N_2$	$9.0 \times 10^{-31} \times \left(\frac{300}{T_{ion}}\right)^2$	299	b
$O_2^+ + N_2(g, v) \rightarrow NO^+ + NO$	1.0×10^{-17}	299	b
$O_2^+ + NO \rightarrow NO^+ + O_2$	6.3×10^{-10}	299	
$O_2^+ + NO_2 \rightarrow NO^+ + O_3$	1.0×10^{-11}	299	
$O_2^+ + NO_2 \rightarrow NO_2^+ + O_2$	6.6×10^{-10}	299	
$O_2^+N_2 + N_2 \rightarrow O_2^+ + N_2 + N_2$	$1.1 \times 10^{-6} \times \left(\frac{300}{T_{ion}}\right)^{5.3} \times \exp\left(-\frac{2360}{T_{ion}}\right)$	299	
$O_2^+N_2 + O_2 \rightarrow O_4^+ + N_2$	1.0×10^{-9}	299	

$O_3^- + N \rightarrow NO + O_2 + e^-$	5.0×10^{-10}	298	
$O_3^- + NO \rightarrow NO_2^- + O_2$	2.6×10^{-12}	299	
$O_3^- + NO \rightarrow NO_3^- + O$	1.0×10^{-11}	299	
$O_3^- + NO_2 \rightarrow NO_2^- + O_3$	7.0×10^{-11}	299	
$O_3^- + NO_2 \rightarrow NO_3^- + O_2$	2.0×10^{-11}	299	
$O_3^- + NO_3 \rightarrow NO_3^- + O_3$	5.0×10^{-10}	299	
$O_4^- + N_2 \rightarrow O_2^- + O_2 + N_2$	$1 \times 10^{-10} \times \exp\left(-\frac{1044}{T_g}\right)$	299	
$O_4^- + NO \rightarrow NO_3^- + O_2$	2.5×10^{-10}	299	
$O_4^+ + N_2(g, v) \rightarrow O_2^+N_2 + O_2$	$4.6 \times 10^{-12} \times \left(\frac{T_{ion}}{300}\right)^{2.5} \times \exp\left(-\frac{2650}{T_{ion}}\right)$	299	b
$O_4^+ + NO \rightarrow NO^+ + O_2 + O_2$	1.0×10^{-10}	299	

[a] M represents any neutral molecule.
[b] For any species indicated with (g, v), g and v stand for its ground and vibrationally excited state, respectively.
[c] $O_2(E_x)$ represents the electronically excited states: $O_2(a^1\Delta)$ and $O_2(b^1\Sigma^+)$.
[d] The rate coefficient is assumed to be equal to that of $O_2^+ + O_2 + M \rightarrow O_4^+ + M$.
[e] The rate coefficient is assumed to be equal to that of $O^- + O_2 + M \rightarrow O_3^- + M$.
[f] The rate coefficient is assumed to be equal to that of $O_2^- + O_2 + M \rightarrow O_4^- + M$.

Appendix Table 7 Ion-ion reactions included in the model, the corresponding rate coefficient expressions and the references. T_g is the gas temperature in K. The rate coefficients are expressed in $cm^3\ s^{-1} or\ cm^6\ s^{-1}$ for binary or ternary reactions, respectively.

Reaction	Rate coefficient	Ref.	Note
$O^- + O^+ + M \rightarrow O_2 + M$	$1.0 \times 10^{-25} \times \left(\frac{300}{T_g}\right)^{2.5}$	320	a
$O^- + O_2^+ + M \rightarrow O_3 + M$	$1.0 \times 10^{-25} \times \left(\frac{300}{T_g}\right)^{2.5}$	320	a
$O_2^- + O^+ + M \rightarrow O_3 + M$	$1.0 \times 10^{-25} \times \left(\frac{300}{T_g}\right)^{2.5}$	320	a
$O_2^- + O_2^+ + M \rightarrow O_2 + O_2 + M$	$1.0 \times 10^{-25} \times \left(\frac{300}{T_g}\right)^{2.5}$	320	a
$O_3^- + O^+ + M \rightarrow O_3 + O + M$	$2.0 \times 10^{-25} \times \left(\frac{300}{T_g}\right)^{2.5}$	298	a
$O_3^- + O_2^+ + M \rightarrow O_3 + O_2 + M$	$2.0 \times 10^{-25} \times \left(\frac{300}{T_g}\right)^{2.5}$	298	a
$O^- + O_2^+ \rightarrow O + O + O$	$2.60 \times 10^{-8} \times \left(\frac{300}{T_g}\right)^{0.44}$	317	a
$O_3^- + O_2^+ \rightarrow O + O + O_3$	$1.0 \times 10^{-7} \times \left(\frac{300}{T_g}\right)^{0.5}$	317	a
$O^- + O^+ \rightarrow O + O$	$4.0 \times 10^{-8} \times \left(\frac{300}{T_g}\right)^{0.43}$	317	
$O^- + O_2^+ \rightarrow O_2 + O$	$2.6 \times 10^{-8} \times \left(\frac{300}{T_g}\right)^{0.44}$	317	
$O_2^- + O^+ \rightarrow O + O_2$	$2.7 \times 10^{-7} \times \left(\frac{300}{T_g}\right)^{0.5}$	317	
$O_2^- + O_2^+ \rightarrow O_2 + O_2$	$2.01 \times 10^{-7} \times \left(\frac{300}{T_g}\right)^{0.5}$	317	
$O_2^- + O_2^+ \rightarrow O_2 + O + O$	$1.01 \times 10^{-13} \times \left(\frac{300}{T_g}\right)^{0.5}$	317	
$O_3^- + O^+ \rightarrow O_3 + O$	$1.0 \times 10^{-7} \times \left(\frac{300}{T_g}\right)^{0.5}$	321	

$O_3^- + O_2^+ \rightarrow O_2 + O_3$	$2.0 \times 10^{-7} \times \left(\frac{300}{T_g}\right)^{0.5}$	317	
$NO^- + A^+ + M \rightarrow NO + A + M$	$2.0 \times 10^{-25} \times \left(\frac{300}{T_g}\right)^{2.5}$	298	a, b
$NO_2^- + A^+ + M \rightarrow NO_2 + A + M$	$2.0 \times 10^{-25} \times \left(\frac{300}{T_g}\right)^{2.5}$	298	a, b
$N_2O^- + A^+ + M \rightarrow N_2O + A + M$	$2.0 \times 10^{-25} \times \left(\frac{300}{T_g}\right)^{2.5}$	298	a, b
$NO_3^- + A^+ + M \rightarrow NO_3 + A + M$	$2.0 \times 10^{-25} \times \left(\frac{300}{T_g}\right)^{2.5}$	298	a, b
$O_3^- + B^+ + M \rightarrow O_3 + B + M$	$2.0 \times 10^{-25} \times \left(\frac{300}{T_g}\right)^{2.5}$	298	a, c

[a] M represents any neutral molecule.
[b] A represents N, O, N_2, O_2, NO, NO_2 and N_2O species.
[c] B represents N, N_2, NO, NO_2 and N_2O species.

Appendix Table 8 Optical transitions of N_2 and O_2 molecules. The Einstein transition probabilities are expressed in s^{-1}.

Reaction	Rate coefficient	Ref.	Note
$N_2(A^3\Sigma_u^+) \rightarrow N_2$	0.5	299	
$N_2(B^3\Pi_g) \rightarrow N_2(A^3\Sigma_u^+)$	1.35×10^5	299	
$N_2(a'^1\Sigma_u^-) \rightarrow N_2$	1.0×10^2	299	
$N_2(C^3\Pi_u) \rightarrow N_2(B^3\Pi_g)$	2.45×10^7	299	
$O_2(a^1\Delta) \rightarrow O_2$	2.6×10^{-4}	299	
$O_2(b^1\Sigma^+) \rightarrow O_2$	8.5×10^{-2}	299	
$O_2(b^1\Sigma^+) \rightarrow O_2(a^1\Delta)$	1.5×10^{-3}	299	
$O_2(A^3\Sigma^+, C^3\Delta, c^1\Sigma^-) \rightarrow O_2$	11	299	a

[a] $O_2(A^3\Sigma^+, C^3\Delta, c^1\Sigma^-)$ is a combination of three electronic excited states at a threshold energy of 4.5 eV.

X. REFERENCES

(1) Smil, V. Global Population and the Nitrogen Cycle. *Sci Am* **1997**, No. July, 76–81.

(2) Canfield, D. E.; Glazer, A. N.; Falkowski, P. G. The Evolution and Future of Earth's Nitrogen Cycle. *Science (1979)* **2010**, *330* (6001), 192–196. https://doi.org/10.1126/science.1186120.

(3) Chanway, C. P.; Anand, R.; Yang, H. *Nitrogen Fixation Outside and inside Plant Tissues*; 2014. https://doi.org/10.5772/57532.

(4) Bergman, B.; Sandh, G.; Lin, S.; Larsson, J.; Carpenter, E. J. Trichodesmium - a Widespread Marine Cyanobacterium with Unusual Nitrogen Fixation Properties. *FEMS Microbiol Rev* **2013**, *37* (3), 286–302. https://doi.org/10.1111/j.1574-6976.2012.00352.x.

(5) Kuypers, M. M. M.; Marchant, H. K.; Kartal, B. The Microbial Nitrogen-Cycling Network. *Nat Rev Microbiol* **2018**, *16*, 263–276. https://doi.org/10.1038/nrmicro.2018.9.

(6) Smil, A. Nitrogen and Food Production : Proteins for Human Diets Nitrogen and Food Production : Proteins for Human Diets. **2021**, *31* (2), 126–131.

(7) Smil, V. Nitrogen and Food Production: Proteins for Human Diets. *Ambio* **2002**, *31* (2), 126–131. https://doi.org/10.1579/0044-7447-31.2.126.

(8) *Gapminder Population Data*.

(9) *United Nations - Population Division*.

(10) Erisman, J. W.; Sutton, M. a; Galloway, J.; Klimont, Z.; Winiwarter, W. How a Century of Ammonia Synthesis Changed the World. *Nat. GeoSci.* **2008**, *1* (October 2008), 636–639. https://doi.org/10.1038/ngeo325.

(11) Stewart, W. M.; Dibb, D. W.; Johnston, A. E.; Smyth, T. J. The Contribution of Commercial Fertilizer Nutrients to Food Production. *Agron J* **2005**, *97* (1), 1–6. https://doi.org/10.2134/AGRONJ2005.0001.

(12) Bodirsky, B. L.; Popp, A.; Lotze-campen, H.; Dietrich, J. P.; Rolinski, S.; Biewald, A.; Bonsch, M.; Humpeno, F.; Weindl, I.; Schmitz, C.; Mu, C.; Stevanovic, M. 2050 and Potential to Mitigate Nitrogen Pollution. *Nat Commun* **2014**, *5* (May), 3858. https://doi.org/10.1038/ncomms4858.

(13) Herridge, D. F.; Peoples, M. B.; Boddey, R. M. Global Inputs of Biological Nitrogen Fixation in Agricultural Systems. *Plant Soil* **2008**, *311*, 1–18. https://doi.org/10.1007/s11104-008-9668-3.

(14) Appl, M. Ammonia, 2. Production Processes. In *Ullmann's Encyclopedia of Industrial Chemistry*; Wiley-VCH Verlag GmbH & Co. KGaA, 2011. https://doi.org/10.1002/14356007.o02_o11.

(15) Cherkasov, N.; Ibhadon, A. O.; Fitzpatrick, P. A Review of the Existing and Alternative Methods for Greener Nitrogen Fixation. *Chem. Eng. Process.* **2015**, *90*, 24–33. https://doi.org/10.1016/j.cep.2015.02.004.

(16) Nayak-luke, R. M.; Banares-Alcantare, R. Techno-Economic Viability of Islanded Green Ammonia as a Carbon-Free Energy Vector and as a Substitute for Conventional Production. *Energy Environ. Sci.* **2020**, *13*, 2957–2966. https://doi.org/10.1039/D0EE01707H.

(17) Bicer, Y.; Dincer, I.; Zamfirescu, C.; Vezina, G.; Raso, F. Comparative Life Cycle Assessment of Various Ammonia Production Methods. *J. Clean. Prod.* **2016**, *135*, 1379–1395. https://doi.org/10.1016/J.JCLEPRO.2016.07.023.

(18) Patil, B. S.; Wang, Q.; Hessel, V.; Lang, J. Plasma N 2 -Fixation : 1900 – 2014. *Catal* **2015**, *256*, 49–66. https://doi.org/10.1016/j.cattod.2015.05.005.

(19) Baltrusaitis, J. Sustainable Ammonia Production. *ACS Sustain Chem Eng* **2017**, *5* (11), 9527. https://doi.org/10.1021/acssuschemeng.7b03719.

(20) Perez Sanchez, D. *Chemicals*; 2022.

(21) Smith, C.; Hill, A. K.; Torrente-Murciano, L. Current and Future Role of Haber-Bosch Ammonia in a Carbon-Free Energy Landscape †. *Energy Environ. Sci* **2020**, *13*, 331. https://doi.org/10.1039/c9ee02873k.

(22) Hochman, G.; Goldman, A. S.; Felder, F. A.; Mayer, J. M.; Miller, A. J. M.; Holland, P. L.; Goldman, L. A.; Manocha, P.; Song, Z.; Aleti, S. Potential Economic Feasibility of Direct Electrochemical Nitrogen Reduction as a Route to Ammonia. *ACS Sust. Chem. Eng.* **2020**, *8* (24), 8938–8948. https://doi.org/10.1021/acssuschemeng.0c01206.

(23) Winter, L. R.; Chen, J. G. N2 Fixation by Plasma-Activated Processes. *Joule* **2021**, *5* (2), 300–315. https://doi.org/10.1016/J.JOULE.2020.11.009.

(24) Kamphus, M. Emission Monitoring in Nitric Acid Plants. *Nitrogen+Syngas* **2014**, *328* (2), 48–53.

(25) Hessel, V.; Cravotto, G.; Fitzpatrick, P.; Patil, B. S.; Lang, J.; Bonrath, W. Industrial Applications of Plasma, Microwave and Ultrasound Techniques: Nitrogen-Fixation and Hydrogenation Reactions. *Chemical Engineering and Processing: Process Intensification* **2013**, *71*, 19–30. https://doi.org/10.1016/j.cep.2013.02.002.

(26) Barboun, P. M.; Hicks, J. C. Unconventional Catalytic Approaches to Ammonia Synthesis. **2020**. https://doi.org/10.1146/annurev-chembioeng.

(27) Guo, J.; Chen, P. Catalyst: NH3 as an Energy Carrier. *Chem* **2017**, *3* (5), 709–712. https://doi.org/10.1016/J.CHEMPR.2017.10.004.

(28) Howarth, R. W.; Jacobson, M. Z. How Green Is Blue Hydrogen? *Energy Sci Eng* **2021**, *9* (10), 1676–1687. https://doi.org/10.1002/ESE3.956.

(29) Briggs, W. M.; Hanekamp, J. C. Nitrogen Critical Loads: Critical Reflections on Past Experiments, Ecological Endpoints, and Uncertainties. *Dose-Response* **2022**, *20* (1), 1–10. https://doi.org/10.1177/15593258221075513/FORMAT/EPUB.

(30) Nieder, R.; Benbi, D. K. Reactive Nitrogen Compounds and Their Influence on Human Health: An Overview. *Reviews on Environmental Health*. De Gruyter Open Ltd June 1, 2022, pp 229–246. https://doi.org/10.1515/reveh-2021-0021.

(31) Matassa, S.; Boeckx, P.; Boere, J.; Erisman, J. W.; Guo, M.; Manzo, R.; Meerburg, F.; Papirio, S.; Pikaar, I.; Rabaey, K.; Rousseau, D.; Schnoor, J.;

Smith, P.; Smolders, E.; Wuertz, S.; Verstraete, W. How Can We Possibly Resolve the Planet's Nitrogen Dilemma? *Microbial Biotechnology*. John Wiley and Sons Ltd January 1, 2023, pp 15–27. https://doi.org/10.1111/1751-7915.14159.

(32) Aryal, B.; Gurung, R.; Camargo, A. F.; Fongaro, G.; Treichel, H.; Mainali, B.; Angove, M. J.; Ngo, H. H.; Guo, W.; Puadel, S. R. Nitrous Oxide Emission in Altered Nitrogen Cycle and Implications for Climate Change. *Environmental Pollution* **2022**, *314*. https://doi.org/10.1016/J.ENVPOL.2022.120272.

(33) Hanekamp, J. C.; Briggs, W. M. Nitrogen Critical Loads: Critical Reflections on Past Experiments, Ecological Endpoints and Uncertainties. *Dose-Response* **2022**, *20* (1). https://doi.org/10.1177/15593258221075512/FORMAT/EPUB.

(34) Huang, S.; Lv, W.; Bloszies, S.; Shi, Q.; Pan, X.; Zeng, Y. Effects of Fertilizer Management Practices on Yield-Scaled Ammonia Emissions from Croplands in China: A Meta-Analysis. *Field Crops Res* **2016**, *192*, 118–125. https://doi.org/10.1016/j.fcr.2016.04.023.

(35) Brightling, J. Ammonia and the Fertiliser Industry: The Development of Ammonia at Billingham. *Johnson Matthey Technology Review* **2018**, *62* (1), 32–47. https://doi.org/10.1595/205651318X696341.

(36) Rouwenhorst, K. H. R.; Jardali, F.; Bogaerts, A.; Lefferts, L. From the Birkeland-Eyde Process towards Energy-Efficient Plasma- Based NOX Synthesis: A Techno- Economic Analysis. *Energy Environ. Sci.* **2021**, *14*, 2520–2534. https://doi.org/https://doi.org/10.1039/D0EE03763J.

(37) Patil, B. S.; Peeters, F. J. J.; van Rooij, G. J.; Medrano, J. A.; Gallucci, F.; Lang, J.; Wang, Q.; Hessel, V. Plasma Assisted Nitrogen Oxide Production from Air: Using Pulsed Powered Gliding Arc Reactor for a Containerized Plant. *AIChE Journal* **2018**, *64* (2), 526–537. https://doi.org/10.1002/aic.15922.

(38) Gambarotta, S.; Scott, J. Multimetallic Cooperative Activation of N2. *Angewandte Chemie - International Edition* **2004**, *43* (40), 5298–5308. https://doi.org/10.1002/anie.200301669.

(39) Chen, X.; Li, N.; Kong, Z.; Ong, W.-J.; Zhao, X. Photocatalytic Fixation of Nitrogen to Ammonia: State-of-the-Art Advancements and Future Prospects. *Mater. Horiz.* **2017**, *5* (1), 1–132. https://doi.org/10.1039/C7MH00557A.

(40) Wang, W.; Patil, B.; Heijkers, S.; Hessel, V.; Bogaerts, A. Nitrogen Fixation by Gliding Arc Plasma: Better Insight by Chemical Kinetics Modelling. *ChemSusChem* **2017**, *10* (10), 2110–2157. https://doi.org/10.1002/cssc.201700611.

(41) Birkeland, K. On the Oxidation of Atmospheric Nitrogen in Electric Arcs. *Trans. Faraday. Soc.* **1906**, *58*, 98–116. https://doi.org/10.1039/TF9060200098.

(42) Patil, B. S. Plasma (Catalyst) – Assisted Nitrogen Fixation : Reactor Development for Nitric Oxide and Ammonia Production, Eindhoven University of Technology, 2017.

(43) Bogaerts, A.; Neyts, E. C. Plasma Technology: An Emerging Technology for Energy Storage. *ACS Energy Lett* **2018**, *3* (4), 1013–1027. https://doi.org/10.1021/acsenergylett.8b00184.

(44) Chen, J. G.; Crooks, R. M.; Seefeldt, L. C.; Bren, K. L.; Morris Bullock, R.; Darensbourg, M. Y.; Holland, P. L.; Hoffman, B.; Janik, M. J.; Jones, A. K.; Kanatzidis, M. G.; King, P.; Lancaster, K. M.; Lymar, S. v.; Pfromm, P.; Schneider, W. F.; Schrock, R. R. Beyond Fossil Fuel–Driven Nitrogen Transformations. *Science (1979)* **2018**, *360* (873), 1–7. https://doi.org/10.1126/science.aar6611.

(45) Hollevoet, L.; Jardali, F.; Gorbanev, Y.; Creel, J.; Bogaerts, A.; Martens, J. A. Towards Green Ammonia Synthesis through Plasma-Driven Nitrogen Oxidation and Catalytic Reduction. *Angewandte Chemie - International Edition* **2020**, *59* (52), 23825–23829. https://doi.org/10.1002/anie.202011676.

(46) Rouwenhorst, K. H. R.; Engelmann, Y.; van 'T Veer, K.; Postma, R. S.; Bogaerts, A.; Lefferts, L. Plasma-Driven Catalysis: Green Ammonia Synthesis with Intermittent Electricity. *Green Chem.* **2020**, *22* (19), 6258–6287. https://doi.org/10.1039/d0gc02058c.

(47) Armor, J. N. A History of Industrial Catalysis. *Catal Today* **2011**, *163* (1), 3–9. https://doi.org/10.1016/J.CATTOD.2009.11.019.

(48) Gorbanev, Y.; Engelmann, Y.; Van'T Veer, K.; Vlasov, E.; Ndayirinde, C.; Yi, Y.; Bals, S.; Bogaerts, A. Al2 O3-Supported Transition Metals for Plasma-Catalytic Nh3 Synthesis in a Dbd Plasma: Metal Activity and Insights into Mechanisms. *Catalysts* **2021**, *11* (10). https://doi.org/10.3390/catal11101230.

(49) *Ammonia: Zero-Carbon Fertiliser, Fuel and Energy Store*; 2020. https://royalsociety.org/-/media/policy/projects/green-ammonia/green-ammonia-policy-briefing.pdf (accessed 2023-02-22).

(50) Noussan, M.; Raimondi, P. P.; Scita, R.; Hafner, M. The Role of Green and Blue Hydrogen in the Energy Transition—a Technological and Geopolitical Perspective. *Sustainability (Switzerland)*. MDPI AG January 1, 2021, pp 1–26. https://doi.org/10.3390/su13010298.

(51) Ozan Gezerman, A. A Critical Assessment of Green Ammonia Production and Ammonia Production Technologies. https://doi.org/10.15255/KUI.2021.013.

(52) Rouwenhorst, K. H. R.; Krzywda, P. M.; Benes, N. E.; Mul, G.; Lefferts, L. Ammonia, 4. Green Ammonia Production. In *Ullmann's Encyclopedia of Industrial Chemistry*; Wiley, 2020; pp 1–20. https://doi.org/10.1002/14356007.w02_w02.

(53) Fridman, A. *Plasma Chemistry*; Intergovernmental Panel on Climate Change, Ed.; Cambridge University Press: Cambridge, 2005. https://doi.org/10.1017/CBO9781107415324.004.

(54) Rusanov, V. D.; Fridman, A. A.; Sholin, G. V. The Physics of a Chemically Active Plasma with Nonequilibrium Vibrational Excitation of Molecules. *Uspekhi Fizicheskih Nauk* **1981**, *134*, 449–472. https://doi.org/10.3367/UFNr.0134.198106a.0185.

(55) Petitpas, G. Rollier, J. Darmon, A. Gonzalez-aguilar, J. Metkemeijer, R. Fulcheri, L. Comparative Study of Non-Thermal Plasma Assisted Reforming Technologies. *Int J Hydrogen Energy* **2007**, *32*, 2848–2867.

(56) Bruggeman, P. J.; Iza, F.; Brandenburg, R. Plasma Sources Science and Technology Foundations of Atmospheric Pressure Non-Equilibrium Plasmas Topical Review Foundations of Atmospheric Pressure Non-Equilibrium Plasmas. *Plasma Sources Sci. Technol* **2017**, *26*, 123002. https://doi.org/10.1088/1361-6595/aa97af.

(57) van Alphen, S.; Vermeiren, V.; Butterworth, T.; van den Bekerom, D. C. M.; van Rooij, G. J.; Bogaerts, A. Power Pulsing to Maximize Vibrational Excitation Efficiency in N2 Microwave Plasma: A Combined Experimental and Computational Study. *Journal of Physical Chemistry C* **2020**, *124* (3), 1765–1779. https://doi.org/10.1021/acs.jpcc.9b06053.

(58) Vervloessem, E.; Aghaei, M.; Jardali, F.; Hafezkhiabani, N.; Bogaerts, A. Plasma-Based N2 Fixation into NOx: Insights from Modeling toward Optimum Yields and Energy Costs in a Gliding Arc Plasmatron. *ACS Sust. Chem. Eng.* **2020**, *8* (26), 9711–9720. https://doi.org/10.1021/acssuschemeng.0c01815.

(59) Mehta, P.; Barboun, P.; Go, D. B.; Hicks, J. C.; Schneider, W. F. Catalysis Enabled by Plasma Activation of Strong Chemical Bonds: A Review. *ACS Energy Lett.* **2019**, *4*, 1115–1133. https://doi.org/10.1021/acsenergylett.9b00263.

(60) Adamovich, I.; Agarwal, S.; Ahedo, E.; Alves, L. L.; Baalrud, S.; Babaeva, N.; Bogaerts, A.; Bourdon, A.; Bruggeman, P. J.; Canal, C.; Choi, E. H.; Coulombe, S.; Donkó, Z. The 2022 Plasma Roadmap: Low Temperature Plasma Science and Technology. *Journal of Physics D: Applied Physics J. Phys. D: Appl. Phys* **2022**, *55*. https://doi.org/10.1088/1361-6463/ac5e1c.

(61) Jardali, F.; Van Alphen, S.; Creel, J.; Ahmadi Eshtehardi, H.; Axelsson, M.; Ingels, R.; Snyders, R.; Bogaerts, A. NO x Production in a Rotating Gliding Arc Plasma: Potential Avenue for Sustainable Nitrogen Fixation . *Green Chemistry* **2021**, No. x, 1748–1757. https://doi.org/10.1039/d0gc03521a.

(62) von Woedtke, T.; Reuter, S.; Masur, K.; Weltmann, K. D. Plasmas for Medicine. *Phys Rep* **2013**, *530*, 291–320. https://doi.org/10.1016/j.physrep.2013.05.005.

(63) Eyde, S. Oxidation of Atmospheric Nitrogen and Development of Resulting Industries in Norway. *The Journal of Industrial and Engineering Chemistry* **1912**, *4*, 771–774.

(64) Rehbein, N.; Cooray, V. NOx Production in Spark and Corona Discharges. *J. Electrostat.* **2001**, *51–52*, 333–339.

(65) Hensel, K.; Machala, Z.; Janda, M.; Martis, V. Generation of Antimicrobial NO x by Atmospheric Air Transient Spark Discharge. *Plasma Chemistry and Plasma Processing* **2016**, *36*, 767–781. https://doi.org/10.1007/s11090-016-9694-5.

(66) Pavlovich, M. J.; Oni, T.; Galieher, C.; Curtis, B.; Clark, D. S.; Machala, Z.; Graves, D. B. Air Spark-like Plasma Source for Antimicrobial NO x Generation. *J. Phys. D.: Appl. Phys.* **2014**, *47*, 1–10. https://doi.org/10.1088/0022-3727/47/50/505202.

(67) Rahman, M.; Cooray, V. NOx Generation in Laser-Produced Plasma in Air as a Function Ofdissipated Energy. *Opt. Laser Technol.* **2003**, *35*, 543–546. https://doi.org/0.1016/S0030-3992(03)00077-X.

(68) Bian, W.; Song, X.; Shi, J.; Yin, X. Nitrogen Fixed into HNO 3 by Pulsed High Voltage Discharge. *J Electrostat* **2012**, *70* (2), 317–326. https://doi.org/10.1016/j.elstat.2012.03.010.

(69) Pei, X.; Gidon, D.; Yang, Y. J.; Xiong, Z.; Graves, D. B. Reducing Energy Cost of NO x Production in Air Plasmas. *Chemical Engineering Journal* **2019**, *362* (x), 217–228. https://doi.org/10.1016/j.cej.2019.01.011.

(70) Pei, X.; Gidon, D.; Graves, D. B. Specific Energy Cost for Nitrogen Fixation as NOxusing DC Glow Discharge in Air. *J Phys D Appl Phys* **2020**, *53* (4), 044002 (11pp). https://doi.org/10.1088/1361-6463/ab5095.

(71) Patil, B. S.; Cherkasov, N.; Lang, J.; Ibhadon, A. O.; Hessel, V.; Wang, Q. Low Temperature Plasma-Catalytic NOx Synthesis in a Packed DBD Reactor: Effect of Support Materials and Supported Active Metal Oxides. *Appl Catal B* **2016**, *194* (x), 123–133. https://doi.org/10.1016/j.apcatb.2016.04.055.

(72) Kim, T.; Song, S.; Kim, J.; Iwasaki, R. Formation of NOx from Air and N2/O2 Mixtures Using a Nonthermal Microwave Plasma System. *Jpn J Appl Phys* **2010**, *49* (12), 126201. https://doi.org/10.1143/JJAP.49.126201.

(73) Mutel, B.; Dessaux, O.; Goudmand, P. Energy Cost Improvement Ofthe Nitrogen Oxides Synthesis in a Low Pressure Plasma. *Rev. Phys. Appl.* **1984**, *19*, 461–464. https://doi.org/10.1051/rphysap:01984001906046100.

(74) Polak, L. S.; Ovsiannikov, A. A.; Slovetsky, D. I.; Vurzel, F. B. *Theoretical and Applied Plasma Chemistry*; Nauka (Science): Moscow, 1975.

(75) Asisov, R. I.; Givotov, V. K.; Rusanov, V. D.; Fridman, A. No Title. *Sov. Phys. High Energy Chem. (Khimia Vysokikh Energij)* **1980**, *14*, 366.

(76) Kelly, S.; Bogaerts, A. Nitrogen Fixation in an Electrode-Free Microwave Plasma. *Joule* **2021**, *5*. https://doi.org/10.1016/j.joule.2021.09.009.

(77) Patil, B. S.; Rovira Palau, J.; Hessel, V.; Lang, J.; Wang, Q. Plasma Nitrogen Oxides Synthesis in a Milli-Scale Gliding Arc Reactor: Investigating the Electrical and Process Parameters. *Plasma Chemistry and Plasma Processing* **2016**, *36* (1), 241–257. https://doi.org/10.1007/s11090-015-9671-4.

(78) Vervloessem, E.; Aghaei, M.; Jardali, F.; Hafezkhiabani, N.; Bogaerts, A. Plasma-Based N2Fixation into NOx: Insights from Modeling toward Optimum Yields and Energy Costs in a Gliding Arc Plasmatron. *ACS Sustain Chem Eng* **2020**, *8* (26), 9711–9720. https://doi.org/10.1021/acssuschemeng.0c01815.

(79) Van Alphen, S.; Jardali, F.; Creel, J.; Trenchev, G.; Snyders, R.; Bogaerts, A. Sustainable Gas Conversion by Gliding Arc Plasmas: A New Modelling Approach for Reactor Design Improvement. *Sustain Energy Fuels* **2021**, *5* (6), 1786–1800. https://doi.org/10.1039/d0se01782e.

(80) Krop, J.; Krop, E.; Pollo, I. Calculated Amounts of Nitric Oxide in a Nitrogen-Oxygen Plasma Jet. *Chemia Plasmy* **1979**, 242–249.

(81) van Alphen, S.; Ahmadi Eshtehardi, H.; O'Modhrain, C.; Bogaerts, J.; van Poyer, H.; Creel, J.; Delplancke, M. P.; Snyders, R.; Bogaerts, A. Effusion Nozzle for Energy-Efficient NOx Production in a Rotating Gliding Arc Plasma

Reactor. *Chem. Eng. J.* **2022**, *443*, 136529–136541. https://doi.org/10.1016/J.CEJ.2022.136529.

(82) Tsonev, I.; O'Modhrain, C.; Bogaerts, A.; Gorbanev, Y. Nitrogen Fixation by an Arc Plasma at Elevated Pressure to Increase the Energy Efficiency and Production Rate of NO x . *ACS Sustain Chem Eng* **2023**. https://doi.org/10.1021/ACSSUSCHEMENG.2C06357/SUPPL_FILE/SC2C06357_SI_001.PDF.

(83) Krop, J.; Pollo, I. J. Krop,. *Chemia* **1981**, *678*, 51–59.

(84) Namihira, T.; Katsuki, S.; Hackam, R.; Akiyama, H.; Okamoto, K. Production of Nitric Oxide Using a Pulsed Arc Discharge. *IEEE Trans. Plasma Sci.* **2002**, *30*, 1993–1998.

(85) Mutel, B.; Dessaux, O.; Goudmand, P. Energy Cost Improvement of the Nitrogen Oxides Synthesis in a Low Pressure Plasma. *Revue de Physique Appliquée* **1984**, *19* (6), 461–464. https://doi.org/10.1051/rphysap:01984001906046100.

(86) Vervloessem, E.; Gorbanev, Y.; Nikiforov, A.; de Geyter, N.; Bogaerts, A. Sustainable NOx Production from Air in Pulsed Plasma: Elucidating the Chemistry behind the Low Energy Consumption †. *Green Chem.* **2022**, *24*, 916–929. https://doi.org/10.1039/d1gc02762j.

(87) Britun, N.; Gamaleev, V.; Hori, M. Evidence of Near-the-Limit Energy Cost NO Formation in Atmospheric Spark Discharge. *Plasma Sources Sci Technol* **2021**, *30* (8). https://doi.org/10.1088/1361-6595/ac12bf.

(88) Zhou, D.; Zhou, R.; Zhou, R.; Liu, B.; Zhang, T.; Xian, Y.; Cullen, P. J.; Lu, X.; Ostrikov, K. (Ken). Sustainable Ammonia Production by Non-Thermal Plasmas: Status, Mechanisms, and Opportunities. *Chem. Eng. J.* **2021**, *421*, 129544–129557. https://doi.org/10.1016/J.CEJ.2021.129544.

(89) Bai, M.; Zhang, Z.; Bai, M.; Bai, X.; Gao, H. Synthesis of Ammonia Using CH4/N2 Plasmas Based on Micro-Gap Discharge under Environmentally Friendly Condition. *Plasma Chemistry and Plasma Processing* **2008**, *28* (4), 405–414. https://doi.org/10.1007/s11090-008-9132-4.

(90) Bai, M. Zhang, Z. Bai, X. Ning, W. Plasma Synthsis of Ammonia with a Microgap Dielectric Barrier Discharge at Ambient Pressure. *IEEE Trans. Plasma Sci.* **2003**, *31*, 1285–1291.

(91) Mizushima, T.; Matsumoto, K.; Sugoh, J. I.; Ohkita, H.; Kakuta, N. Tubular Membrane-like Catalyst for Reactor with Dielectric-Barrier- Discharge Plasma and Its Performance in Ammonia Synthesis. *Appl Catal A Gen* **2004**, *265* (1), 53–59. https://doi.org/10.1016/j.apcata.2004.01.002.

(92) Nakajima, J.; Sekiguchi, H. Synthesis of Ammonia Using Microwave Discharge at Atmospheric Pressure. *Thin Solid Films* **2008**, *516* (13), 4446–4451. https://doi.org/10.1016/j.tsf.2007.10.053.

(93) Gómez-Ramŕez, A.; Cotrino, J.; Lambert, R. M.; González-Elipe, A. R. Efficient Synthesis of Ammonia from N2 and H2 Alone in a Ferroelectric Packed-Bed DBD Reactor. *Plasma Sources Sci Technol* **2015**, *24* (6). https://doi.org/10.1088/0963-0252/24/6/065011.

(94) Gómez-Ramírez, A.; Montoro-Damas, A. M.; Cotrino, J.; Lambert, R. M.; González-Elipe, A. R. About the Enhancement of Chemical Yield during the Atmospheric Plasma Synthesis of Ammonia in a Ferroelectric Packed Bed Reactor. *Plasma Processes and Polymers* **2016**, *14* (6). https://doi.org/10.1002/PPAP.201600081.

(95) Peng, P.; Li, Y.; Cheng, Y.; Deng, S. Atmospheric Pressure Ammonia Synthesis Using Non-Thermal Plasma Assisted Catalysis. *Plasma Chemistry and Plasma Processing* **2016**, *36* (5), 1201–1210. https://doi.org/10.1007/s11090-016-9713-6.

(96) Peng, P.; Cheng, Y.; Hatzenbeller, R.; Addy, M. M.; Zhou, N.; Schiappacasse, C.; Chen, D.; Zhang, Y.; Anderson, E.; Liu, Y.; Chen, P. L.; Ruan, R. R. Ru-Based Multifunctional Mesoporous Catalyst 5for Low-Pressure and Non-Thermal Plasma Synthesis of Ammonia. *Int J Hydrogen Energy* **2017**, *42* (30), 19056–19066. https://doi.org/10.1016/j.ijhydene.2017.06.118.

(97) Aihara, K.; Akiyama, M.; Deguchi, T.; Tanaka, M.; Hagiwara, R.; Iwamoto, M. Remarkable Catalysis of a Wool-like Copper Electrode for NH3synthesis from

N2 and H2 in Non-Thermal Atmospheric Plasma. *Chem. Commun.* **2016**, *52*, 13560–13563. https://doi.org/https://doi.org/10.1039/C6CC06752B.

(98) Hong, J. Prawer, S. Murphy, A. B. Production of Ammonia by Heterogeneous Catalysis in a Pached-Bed Dielectric-Barrier Discharge: Influence of Argon Addition an Voltage. *IEEE Trans. Plasma Sci.* **2014**, *42*, 2338–2339.

(99) Bai, M.; Zhang, Z.; Bai, M.; Bai, X.; Gao, H. Conversion of Methane to Liquid Products, Hydrogen, and Ammonia with Environmentally Friendly Condition-Based Microgap Discharge. *J Air Waste Manage Assoc* **2008**, *58* (12), 1616–1621. https://doi.org/10.3155/1047-3289.58.12.1616.

(100) Kim, H. H.; Teramoto, Y.; Ogata, A.; Takagi, H.; Nanba, T. Atmospheric-Pressure Nonthermal Plasma Synthesis of Ammonia over Ruthenium Catalysts. *Plasma Processes and Polymers* **2017**, *14* (6), 1–9. https://doi.org/10.1002/PPAP.201600157.

(101) Hollevoet, L.; Vervloessem, E.; Gorbanev, Y.; Nikiforov, A.; De Geyter, N.; Bogaerts, A.; Martens, J. A. Energy-Efficient Small-Scale Ammonia Synthesis Process with Plasma-Enabled Nitrogen Oxidation and Catalytic Reduction of Adsorbed NOx. *ChemSusChem* **2022**, *15* (10), e202102526. https://doi.org/10.1002/cssc.202102526.

(102) Carreon, M. L. Plasma Catalytic Ammonia Synthesis : State of the Art and Future Directions. *J. Phys. D: Appl. Phys.* **2019**, *52*, 483001–483025. https://doi.org/10.1088/1361-6463/ab3b2c.

(103) Mingdong, B.; Xiyao, B.; Zhitao, Z.; Mindi, B. *Synthesis of Ammonia in a Strong Electric Field Discharge at Ambient Pressure*; 2000; Vol. 20.

(104) Peng, P.; Chen, P.; Addy, M.; Cheng, Y.; Zhang, Y.; Anderson, E.; Zhou, N.; Schiappacasse, C.; Hatzenbeller, R. In Situ Plasma-Assisted Atmospheric Nitrogen Fixation Using Water and Spray-Type Jet Plasma†. *Chem. Commun.* **2018**, *54*, 2886–2889. https://doi.org/10.1039/C8CC00697K.

(105) Iwamoto, M. Akiyama, M. Aihara, K. Deguchi, T. Ammmonia Synthesis on Wool-like Au, Pt, Pd, Ag or Cu Electrode Catalysts in Nonthermal Atmospheric-Pressure Plasma of N2 and H2. *ACS Catal.* **2017**, *7*, 6924–6929.

(106) Li, S.; Medrano, J. A.; Hessel, V.; Gallucci, F. Recent Progress of Plasma-Assisted Nitrogen Fixation Research: A Review. *Processes* **2018**, *6* (12). https://doi.org/10.3390/pr6120248.

(107) Peng, P.; Chen, P.; Schiappacasse, C.; Zhou, N.; Anderson, E.; Chen, D.; Liu, J.; Cheng, Y.; Hatzenbeller, R.; Addy, M.; Zhang, Y.; Liu, Y.; Ruan, R. A Review on the Non-Thermal Plasma-Assisted Ammonia Synthesis Technologies. *J Clean Prod* **2018**, *177*, 597–609. https://doi.org/10.1016/j.jclepro.2017.12.229.

(108) Uyama, H.; Matsumoto, U. Synthesis of Ammonia in High-Frequency Discharges ~. *Plasma Chem. Plasma Process.* **1989**, *9* (1), 13–24.

(109) Whitehead, J. C. Plasma–Catalysis: The Known Knowns, the Known Unknowns and the Unknown Unknowns. *Journal of Physics D: Applied Physics To* **2016**, *49*, 243001–243025. https://doi.org/10.1088/0022-3727/49/24/243001.

(110) Akay, G. Zhang, K. Process Intensification in Ammonia Synthesis Using Novel Coassenbled Supported Microporous Catalysts Promoted by Nonthermal. *Ind. Eng. Chem. Res.* **2017**, *56*, 457–468.

(111) Veer, K. Van; Engelmann, Y.; Reniers, F.; Bogaerts, A. Plasma-Catalytic Ammonia Synthesis in a DBD Plasma : Role of Microdischarges and Their Afterglows. **2020**.

(112) Gómez-Ramírez, A.; Montoro-Damas, A. M.; Cotrino, J.; Lambert, R. M.; González-Elipe, A. R. About the Enhancement of Chemical Yield during the Atmospheric Plasma Synthesis of Ammonia in a Ferroelectric Packed Bed Reactor. *Plasma Processes and Polymers* **2017**, *14* (6). https://doi.org/10.1002/ppap.201600081.

(113) Zhu, Y.; Xiong, Z.; Li, M.; Chen, X.; Lu, C. Investigation of NH 4 NO 3 Formation by Air Plasma and Wasted Ammonia. *Plasma Process Polym.* **2021**, *18* (8), 1–7. https://doi.org/10.1002/ppap.202000223.

(114) Hong, J.; Pancheshnyi, S.; Tam, E.; Lowke, J. J.; Prawer, S.; Murphy, A. B. Kinetic Modelling of NH3 Production in N2-H2 Non-Equilibrium Atmospheric-

Pressure Plasma Catalysis. *J Phys D Appl Phys* **2017**, *50* (15), 154005–154038. https://doi.org/10.1088/1361-6463/aa6229.

(115) Rouwenhorst, K. H. R.; Kim, H.-H.; Lefferts, L. Vibrationally Excited Activation of N 2 in Plasma-Enhanced Catalytic Ammonia Synthesis: A Kinetic Analysis. **2019**. https://doi.org/10.1021/acssuschemeng.9b04997.

(116) Mehta, P.; Barboun, P.; Herrera, F. A.; Kim, J.; Rumbach, P.; Go, D. B.; Hicks, J. C.; Schneider, W. F. Overcoming Ammonia Synthesis Scaling Relations with Plasma-Enabled Catalysis. *Nat Catal* **2018**, *1* (4), 269–275. https://doi.org/10.1038/s41929-018-0045-1.

(117) Uyama, H.; Nakamura, T.; Tanaka, S.; Matsumoto, O. Catalytic Effect of Iron Wires on the Syntheses of Ammonia and Hydrazine in a Radio-Frequency Discharge. *Plasma Chemistry and Plasma Processing* **1993**, *13* (1), 117–131.

(118) Uyama, H.; Uchikura, T.; Niijima, H.; Matsumoto, O. Synthesis of Ammonia with RF Discharge. Adsorption of Products on Zeolite. *Chem Lett* **1987**, *16* (4), 555–558. https://doi.org/10.1246/CL.1987.555.

(119) Sugiyama, K.; Akazawa, K.; Oshima, M.; Miura, H.; Matsuda, T.; Nomura, O. *Ammonia Synthesis by Means of Plasma over MgO Catalyst*; 1986; Vol. 6. https://doi.org/doi:10.1007/bf00571275.

(120) Hu, X.; Zhang, Y.; Wu, R. A.; Liao, X.; Liu, D.; Cullen, P. J.; Zhou, R. W.; Ding, T. Diagnostic Analysis of Reactive Species in Plasma-Activated Water (PAW): Current Advances and Outlooks. *Journal of Physics D: Applied Physics*. IOP Publishing Ltd January 13, 2022. https://doi.org/10.1088/1361-6463/ac286a.

(121) Janda, M.; Hensel, K.; Tóth, P.; Hassan, M. E.; Machala, Z.; Nastuta, V. The Role of HNO 2 in the Generation of Plasma-Activated Water by Air Transient Spark Discharge. *Appl. Sci.* **2021**, *11* (15), 7053–7073. https://doi.org/10.3390/app11157053.

(122) Shaw, P.; Kumar, N.; Kwak, H. S.; Park, J. H.; Uhm, H. S.; Bogaerts, A.; Choi, E. H.; Attri, P. Bacterial Inactivation by Plasma Treated Water Enhanced by Reactive Nitrogen Species. *Sci Rep* **2018**, *8*, 11268. https://doi.org/10.1038/s41598-018-29549-6.

(123) Chen, X.; Li, N.; Kong, Z.; Ong, W.-J.; Zhao, X. Photocatalytic Fixation of Nitrogen to Ammonia: State-of-the-Art Advancements and Future Prospects. *Mater. Horiz.* **2018**, *5*, 27. https://doi.org/10.1039/c7mh00557a.

(124) Bradu, C.; Kutasi, K.; Magureanu, M.; Puac, N.; Zivkovic, S. Reactive Nitrogen Species in Plasma-Activated Water: Generation, Chemistry and Application in Agriculture. *Journal of Physics D: Applied Physics J. Phys. D: Appl. Phys* **2020**, *53*, 223001–223022. https://doi.org/10.1088/1361-6463/ab795a.

(125) Abdelaziz, A. A.; Kim, H. H. Temperature-Dependent Behavior of Nitrogen Fixation in Nanopulsed Dielectric Barrier Discharge Operated at Different Humidity Levels and Oxygen Contents. *J Phys D Appl Phys* **2020**, *53* (11). https://doi.org/10.1088/1361-6463/ab5c78.

(126) Liu, Z.; Tian, Y.; Niu, G.; Wang, X.; Duan, Y. Direct Oxidative Nitrogen Fixation from Air and H2O by a Water Falling Film Dielectric Barrier Discharge Reactor at Ambient Pressure and Temperature. *ChemSusChem* **2021**, *14* (6), 1507–1511. https://doi.org/10.1002/CSSC.202002794.

(127) Gorbanev, Y.; O'Connell, D.; Chechik, V. Non-Thermal Plasma in Contact with Water: The Origin of Species. *Chem. Eur. J.* **2016**, *22* (10), 3496–3505. https://doi.org/10.1002/chem.201503771.

(128) Dinh, D. K.; Muzammil, I.; Kang, W. S.; Kim, D.; Lee, D. H. Reducing Energy Cost of in Situ Nitrogen Fixation in Water Using an Arc-DBD Combination. *Plasma Scources Sci. Technol.* **2021**, *30*, 055020–055029. https://doi.org/10.1088/1361-6595/abff72.

(129) Sakakura, T.; Takatsuji, Y.; Morimoto, M.; Haruyama, T. Nitrogen Fixation through the Plasma/Liquid Interfacial Reaction with Controlled Conditions of Each Phase as the Reaction Locus. *Electrochemistry* **2020**, *88* (3), 190–194. https://doi.org/10.5796/electrochemistry.19-00080.

(130) Sakakura, T.; Murakami, N.; Takatsuji, Y.; Haruyama, T. Nitrogen Fixation in a Plasma/Liquid Interfacial Reaction and Its Switching between Reduction and Oxidation. *J. Phys. Chem. C* **2020**, *124* (17), 9401–9408. https://doi.org/10.1021/acs.jpcc.0c02392.

(131) KUBOTA, Y.; KOGA, K.; OHNO, M.; HARA, T. Synthesis of Ammonia through Direct Chemical Reactions between an Atmospheric Nitrogen Plasma Jet and a Liquid. *Plasma and Fusion Research* **2010**, *5*, 042–042. https://doi.org/10.1585/PFR.5.042.

(132) Tsuchida, Y.; Murakami, N.; Sakakura, T.; Takatsuji, Y.; Haruyama, T. Drastically Increase in Atomic Nitrogen Production Depending on the Dielectric Constant of Beads Filled in the Discharge Space. *ACS Omega* **2021**, *6*, 48. https://doi.org/10.1021/acsomega.1c04201.

(133) Haruyama, T.; Namise, T.; Shimoshimizu, N.; Uemura, S.; Takatsuji, Y.; Hino, M.; Yamasaki, R.; Kamachi, T.; Kohno, M. Non-Catalyzed One-Step Synthesis of Ammonia from Atmospheric Air and Water. *Green Chem.* **2016**, *18* (16), 4536–4541. https://doi.org/10.1039/c6gc01560c.

(134) Sakakura, T.; Murakami, N.; Takatsuji, Y.; Morimoto, M.; Haruyama, T. Contribution of Discharge Excited Atomic N, N2*, and N2+ to a Plasma/Liquid Interfacial Reaction as Suggested by Quantitative Analysis. *ChemPhysChem* **2019**, *20* (11), 1467–1474. https://doi.org/10.1002/cphc.201900212.

(135) Sakakura, T.; Uemura, S.; Hino, M.; Kiyomatsu, S.; Takatsuji, Y.; Yamasaki, R.; Morimoto, M.; Haruyama, T. Excitation of H2O at the Plasma/Water Interface by UV Irradiation for the Elevation of Ammonia Production. *Green Chem.* **2018**, *20* (3), 627–633. https://doi.org/10.1039/c7gc03007j.

(136) Toth, J. R.; Abuyazid, N. H.; Lacks, D. J.; Renner, J. N.; Sankaran, R. M. A Plasma-Water Droplet Reactor for Process-Intensified, Continuous Nitrogen Fixation at Atmospheric Pressure. *ACS Sust. Chem. Eng.* **2020**, *8* (39), 14845–14854. https://doi.org/10.1021/acssuschemeng.0c04432.

(137) Peng, P.; Schiappacasse, C.; Zhou, N.; Addy, M.; Cheng, Y.; Zhang, Y.; Anderson, E.; Chen, D.; Wang, Y.; Liu, Y.; Chen, P.; Ruan, R. Plasma in Situ Gas-Liquid Nitrogen Fixation Using Concentrated High-Intensity Electric Field. *J. Phys. D: Appl. Phys.* **2019**, *52* (49), 494001–494009. https://doi.org/10.1088/1361-6463/ab3ea6.

(138) Gromov, M.; Kamarinopoulou, N.; De Geyter, N.; Morent, R.; Snyders, R.; Vlachos, D.; Dimitrakellis, P.; Nikiforov, A. Plasma-Assisted Nitrogen Fixation: The Effect of Water Presence. *Green Chemistry* **2022**, *24* (24), 9677–9689. https://doi.org/10.1039/d2gc03063b.

(139) Gorbanev, Y.; Vervloessem, E.; Nikiforov, A.; Bogaerts, A. Nitrogen Fixation with Water Vapor by Nonequilibrium Plasma: Toward Sustainable Ammonia Production. *ACS Sust. Chem. Eng.* **2020**, *8* (7), 2996–3004. https://doi.org/10.1021/acssuschemeng.9b07849.

(140) Hawtof, R.; Ghosh, S.; Guarr, E.; Xu, C.; Sankaran, R. M.; Renner, J. N. Catalyst-Free, Highly Selective Synthesis of Ammonia from Nitrogen and Water by a Plasma Electrolytic System. *Sci. Adv.* **2019**, *5* (1), eaat5778-9. https://doi.org/10.1126/sciadv.aat5778.

(141) Sun, J.; Alam, D.; Daiyan, R.; Masood, H.; Zhang, T.; Zhou, R.; Cullen, P. J.; Lovell, E. C.; Jalili, A. (Rouhollah); Amal, R. A Hybrid Plasma Electrocatalytic Process for Sustainable Ammonia Production. *Energy Environ. Sci.* **2021**, *14*, 865–872. https://doi.org/10.1039/d0ee03769a.

(142) Patel, H.; Sharma, R. K.; Kyriakou, V.; Pandiyan, A.; Welzel, S.; van de Sanden, M. C. M.; Tsampas, M. N. Plasma-Activated Electrolysis for Cogeneration of Nitric Oxide and Hydrogen from Water and Nitrogen. *ACS Energy Lett* **2019**, *4*, 2091–2095. https://doi.org/10.1021/acsenergylett.9b01517.

(143) Komuro, A.; Ando, A. Simulation of Spatio-Temporal Variation of OH Radical Density in Atmospheric-Pressure Streamer Discharge. *Plasma Sources Sci Technol* **2017**, *26* (6). https://doi.org/10.1088/1361-6595/aa638d.

(144) Gromov, M.; Leonova, K.; De Geyter, N.; Morent, R.; Snyders, R.; Britun, N.; Nikiforov, A. N2oxidation Kinetics in a Ns-Pulsed Discharge above a Liquid Electrode. *Plasma Sources Sc. Technol.* **2021**, *30* (6), 65024–65038. https://doi.org/10.1088/1361-6595/abff71.

(145) Machala, Z.; Tarabová, B.; Sersenová, D.; Janda, M.; Hensel, K. Chemical and Antibacterial Effects of Plasma Activated Water: Correlation with

Gaseous and Aqueous Reactive Oxygen and Nitrogen Species, Plasma Sources and Air Flow Conditions. *J. Phys. D: Appl. Phys* **2019**, *52*, 034002–034019. https://doi.org/10.1088/1361-6463/aae807.

(146) Sander, R. Henry's Law Constants. In *NIST Chemistry WebBook, NIST Standart Reference Database Number 69*; Eds. P.J. Linstrom and W.G. Mallard, National Institute of Standards and Technology: Gaithersburg MD, 20899.

(147) Xie, D.; Sun, Y.; Zhu, T.; Fan, X.; Hong, X.; Yang, W. Ammonia Synthesis and By-Product Formation from H2O, H2 and N2 by Dielectric Barrier Discharge Combined with an Ru/Al2O3 Catalyst. *RSC Adv* **2016**, *6* (107), 105338–105346. https://doi.org/10.1039/c6ra21351k.

(148) Montoya, J. H.; Tsai, C.; Vojvodic, A.; Nørskov, J. K. The Challenge of Electrochemical Ammonia Synthesis: A New Perspective on the Role of Nitrogen Scaling Relations. *ChemSusChem* **2015**, *8* (13), 2180–2186. https://doi.org/10.1002/CSSC.201500322.

(149) Pattyn, C.; Maira, N.; Buddhadasa, M.; Vervloessem, E.; Iseni, S.; Roy, N. C.; Remy, A.; Delplancke, M. P.; De Geyter, N.; Reniers, F. Disproportionation of Nitrogen Induced by DC Plasma-Driven Electrolysis in a Nitrogen Atmosphere. *Green Chemistry* **2022**, *24* (18), 7100–7112. https://doi.org/10.1039/d2gc01013e.

(150) Liu, Y.; Liu, D.; Zhang, J. Fluid Model of Plasma-Liquid Interaction: The Effect of Interfacial Boundary Conditions and Henry's Law Constants. *AIP Adv* **2021**, *11*, 055019. https://doi.org/10.1063/5.0042945.

(151) Tian, W.; Tachibana, K.; Kushner, M. J. Plasmas Sustained in Bubbles in Water: Optical Emission and Excitation Mechanisms. *J. Phys. D.: Appl. Phys.* **2014**, *47*, 055202–055215. https://doi.org/10.1088/0022-3727/47/5/055202.

(152) Liu, D. X.; Liu, Z. C.; Chen, C.; Yang, A. J.; Li, D.; Rong, M. Z.; Chen, H. L.; Kong, M. G. Aqueous Reactive Species Induced by a Surface Air Discharge: Heterogeneous Mass Transfer and Liquid Chemistry Pathways. *Sci Rep* **2016**, *6*, 23737–23748. https://doi.org/10.1038/srep23737.

(153) Heirman, P.; Van Boxem, W.; Bogaerts, A. Reactivity and Stability of Plasma-Generated Oxygen and Nitrogen Species in Buffered Water Solution: A Computational Study. *Physical Chemistry Chemical Physics* **2019**, *21* (24), 12881–12894. https://doi.org/10.1039/c9cp00647h.

(154) Bruggeman, P.; Leys, C. Non-Thermal Plasmas in and in Contact with Liquids. *J. Phys. D.: Appl. Phys.* **2009**, *42*, 05001. https://doi.org/10.1088/0022-3727/42/5/053001.

(155) Kovacevic, V.; Sretenovic, G. B.; Obrabovic, B. M.; Kuraica, M. M. Low-Temperature Plasmas in Contact with Liquids-a Review of Recent Progress and Challenges. *J. Phys D: Appl. Phys.* **2022**, *55*, 473002–473043. https://doi.org/10.1088/1361-6463/ac8a56.

(156) Spiller, M.; Moretti, M.; De Paepe, J.; Vlaeminck, S. E. Environmental and Economic Sustainability of the Nitrogen Recovery Paradigm: Evidence from a Structured Literature Review. *Resour Conserv Recycl* **2022**, *184*. https://doi.org/10.1016/J.RESCONREC.2022.106406.

(157) Morral, E.; Gabriel, D.; Dorado, A. D.; Gamisans, X. A Review of Biotechnologies for the Abatement of Ammonia Emissions. *Chemosphere* **2021**, *273*. https://doi.org/10.1016/J.CHEMOSPHERE.2020.128606.

(158) Muys, M.; Coppens, J.; Boon, N.; Vlaeminck, S. E. Photosynthetic Oxygenation for Urine Nitrification. **2018**. https://doi.org/10.2166/wst.2018.200.

(159) Iriawan, H.; Andersen, S. Z.; Zhang, X.; Comer, B. M.; Barrio, J.; Chen, P.; Medford, A. J.; Stephens, I. E. L.; Chorkendorff, I.; Shao-Horn, Y. Methods for Nitrogen Activation by Reduction and Oxidation. *Nature Reviews Methods Primers*. Springer Nature December 1, 2021. https://doi.org/10.1038/s43586-021-00053-y.

(160) Merakeb, L.; Robert, M. Advances in Molecular Electrochemical Activation of Dinitrogen. *Curr Opin Electrochem* **2021**, *29*. https://doi.org/10.1016/J.COELEC.2021.100834.

(161) Rutledge, H. L.; Tezcan, F. A. Electron Transfer in Nitrogenase. *Chem Rev* **2020**, *120* (12), 5158–5193. https://doi.org/10.1021/ACS.CHEMREV.9B00663.

(162) Oldroyd, G. E. D.; Dixon, R. Biotechnological Solutions to the Nitrogen Problem. *Curr Opin Biotechnol* **2014**, *26*, 19–24. https://doi.org/10.1016/J.COPBIO.2013.08.006.

(163) Boujenna, A.; Garcia Del Moral, L. F. Biotechnological Approaches to Develop Nitrogen-Fixing Cereals: A Review. *Spanish Journal of Agricultural Research* **2021**, *19* (4), 2171–9292. https://doi.org/10.5424/sjar/2021194-18346.

(164) Sakarika, M.; Spanoghe, J.; Sui, Y.; Wambacq, E.; Grunert, O.; Haesaert, G.; Spiller, M.; Vlaeminck, S. E. Purple Non-Sulphur Bacteria and Plant Production: Benefits for Fertilization, Stress Resistance and the Environment. *Microbial Biotechnology*. John Wiley and Sons Ltd September 1, 2020, pp 1336–1365. https://doi.org/10.1111/1751-7915.13474.

(165) Deng, J.; Iñiguez, J. A.; Liu, C. Electrocatalytic Nitrogen Reduction at Low Temperature. *Joule* **2018**, *2* (5), 846–856. https://doi.org/10.1016/J.JOULE.2018.04.014.

(166) Zheng, J.; Jiang, L.; Lyu, Y.; Jiang, S. P.; Wang, S. Green Synthesis of Nitrogen-to-Ammonia Fixation: Past, Present, and Future. *Energy and Environmental Materials*. John Wiley and Sons Inc April 1, 2022, pp 452–457. https://doi.org/10.1002/eem2.12192.

(167) Soloveichik, G. Electrochemical Synthesis of Ammonia as a Potential Alternative to the Haber–Bosch Process. *Nature Catalysis*. Nature Publishing Group May 1, 2019, pp 377–380. https://doi.org/10.1038/s41929-019-0280-0.

(168) Medford, A. J.; Hatzell, M. C. Photon-Driven Nitrogen Fixation: Current Progress, Thermodynamic Considerations, and Future Outlook. *ACS Catal* **2017**, *7* (4), 2624–2643. https://doi.org/10.1021/ACSCATAL.7B00439/ASSET/IMAGES/LARGE/CS-2017-00439R_0011.JPEG.

(169) Xue, X.; Chen, R.; Yan, C.; Zhao, P.; Hu, Y.; Zhang, W.; Yang, S.; Jin, Z. Review on Photocatalytic and Electrocatalytic Artificial Nitrogen Fixation for Ammonia Synthesis at Mild Conditions: Advances, Challenges and Perspectives. *Nano Research*. Tsinghua University Press June 1, 2019, pp 1229–1249. https://doi.org/10.1007/s12274-018-2268-5.

(170) Singh, A. R.; Rohr, B. A.; Schwalbe, J. A.; Cargnello, M.; Chan, K.; Jaramillo, T. F.; Chorkendorff, I.; Nørskov, J. K. Electrochemical Ammonia Synthesis - The Selectivity Challenge. *ACS Catal* **2017**, *7*, 706–709. https://doi.org/10.1021/acscatal.6b03035.

(171) Sremački, I.; Gromov, M.; Leys, C.; Morent, R.; Snyders, R.; Nikiforov, A. An Atmospheric Pressure Non-Self-Sustained Glow Discharge in between Metal/Metal and Metal/Liquid Electrodes. *Plasma Processes and Polymers* **2020**, *17* (6), 1–12. https://doi.org/10.1002/ppap.201900191.

(172) Engeln, R.; Klarenaar, B.; Guaitella, O. Foundations of Optical Diagnostics in Low-Temperature Plasmas. *Plasma Sources Sci. Technol.* Institute of Physics Publishing June 1, 2020, pp 063001–063015. https://doi.org/10.1088/1361-6595/ab6880.

(173) Fantz, U. Basics of Plasma Spectroscopy. *Plasma Sources Sci. Technol.* **2006**, *15* (4), S137–S147. https://doi.org/10.1088/0963-0252/15/4/S01.

(174) Pearse, R. W. B.; Gaydon, A. G. *Identification of Molecular Spectra*; Chapman & Hall LTD: London, 1950; Vol. Second Edition.

(175) Linstrom, P. J.; Mallard, W. G. *NIST Standard Reference Database Number 69*; 2005.

(176) J. Luque; D.R. Crosley. LIFBASE: Database and Spectral Simulation Program . SRI International 1999.

(177) Lieberman, M. A.; Lichtenberg, A. J. *Principles of Plasma Discharges and Plasma Materials Processing*, second.; John Wiley & Sons: New Jersey, 2005; Vol. Second Edition.

(178) van Duc Long, N.; Al-Bared, M.; Lin, L.; Davey, K.; Tran, N. N.; Pourali, N.; Ken Ostrikov, K.; Rebrov, E.; Hessel, V. Understanding Plasma-Assisted

Ammonia Synthesis via Crossing Discipline Borders of Literature: A Critical Review. *Chem. Eng. Sci.* **2022**, *263*, 118097–118110. https://doi.org/10.1016/J.CES.2022.118097.

(179) Itikawa, Y. Cross Sections for Electron Collisions with Ammonia. *J. Phys. Chem. Ref. Data* **2017**, *46* (4), 043103–043111. https://doi.org/10.1063/1.5001918.

(180) Itikawa, Y. Cross Sections for Electron Collisions with Nitric Oxide. *J. Phys. Chem. Ref. Data* **2016**, *45* (3), 033106–033115. https://doi.org/10.1063/1.4961372.

(181) Buckley, S. G.; Damm, C. J.; Vitovec, W. M.; Anne Sgro, L.; Sawyer, R. F.; Koshland, C. P.; Lucas, D. Ammonia Detection and monitoring with Photofragmentation Fluorescence. *Appl. Opt.* **1998**, *37*, 8382–8391. https://doi.org/https://doi.org/10.1364/AO.37.008382.

(182) Hartinger, K. T.; Nord, S.; Monkhouse, P. B. Quenching of Fluorescence from Na(3 2 P) and K(4 2 P) Atoms Following Photodissociation of NaCl and KCl at 193 Nm. *Appl. Phys. B* **1997**, *64*, 363–367.

(183) Zhou, M.; Zhu, Z. Properties of Transitions between X3Σ–, A3Π, A1Δ, B1Σ+, and C1Π States of NH Radicals. *Comput. Theor. Chem.* **2021**, *1204*, 113458–113468. https://doi.org/10.1016/J.COMPTC.2021.113358.

(184) Luque, J.; Crosley, D. R. Transition Probabilities and Electronic Transition Moments of the A2Σ+ - X2Π and D2Σ+ - X2Π Systems of Nitric Oxide. *J. Chem. Phys.* **1999**, *111* (16), 7405–7415. https://doi.org/10.1063/1.480064.

(185) Hofzumahaus, A.; Stuhl, F. Electronic Quenching, Rotational Relaxation, and Radiative Lifetime of NH(A3Π,V′=0,N′). *J. Chem. Phys.* **1984**, *82* (7), 3152–3159. https://doi.org/10.1063/1.448213.

(186) Tamura, M.; Berg, P. A.; Harrington, J. E.; Luque, J.; Jeffries, J. B.; Smith, G. P.; Crosley, D. R. Collisional Quenching of CH(A), OH(A), and NO(A) in Low Pressure Hydrocarbon Flames. *Combust Flame* **1998**, *114* (3–4), 502–514. https://doi.org/10.1016/S0010-2180(97)00324-6.

(187) Greenblatt, G. D.; Ravishankara, A. R. Collisional Quenching of NO(A, v' =0) by Various Gases. *Chem. Phys. Lett.* **1987**, *136* (6), 501–505. https://doi.org/10.1016/0009-2614(87)80506-7.

(188) Paul, P. H.; Gray, J. A.; Durant, J. L.; Thoman, J. W. Collisional Electronic Quenching Rates for NO (A2sigma+ v' = 0). *Chem. Phys. Lett.* **1996**, *259*, 508–514. https://doi.org/https://doi.org/10.1016/0009-2614(96)00763-4.

(189) Mo, Y.; Ottinger, C.; Shen, G. Collision-Induced Intersystem Crossing from NH(A1Δ, b 1∑+) to NH(A3∏): Gateway-Mediated and Direct Mechanisms. *J. Chem. Phys.* **1999**, *111* (10), 4598–4612. https://doi.org/10.1063/1.479221.

(190) Griffiths, P. R.; Haseth, J. A. de. *OICENTENNIAL. 1 807 A WILEY ll 2 2007. ; › r Fourier Transform Infrared Spectrometry Second Edition*.

(191) Gordon, I. E.; Rothman, L. S.; Hargreaves, R. J.; Hashemi, R.; Karlovets, E. v.; Skinner, F. M.; Conway, E. K.; Hill, C.; Kochanov, R. v.; Tan, Y.; Wcisło, P.; Finenko, A. A.; Nelson, K.; Bernath, P. F.; Birk, M.; Boudon, V.; Campargue, A.; Chance, K. v.; Coustenis, A.; Drouin, B. J.; Flaud, J. M.; Gamache, R. R.; Hodges, J. T.; Jacquemart, D.; Mlawer, E. J.; Nikitin, A. v.; Perevalov, V. I.; Rotger, M.; Tennyson, J.; Toon, G. C.; Tran, H.; Tyuterev, V. G.; Adkins, E. M.; Baker, A.; Barbe, A.; Canè, E.; Császár, A. G.; Dudaryonok, A.; Egorov, O.; Fleisher, A. J.; Fleurbaey, H.; Foltynowicz, A.; Furtenbacher, T.; Harrison, J. J.; Hartmann, J. M.; Horneman, V. M.; Huang, X.; Karman, T.; Karns, J.; Kassi, S.; Kleiner, I.; Kofman, V.; Kwabia-Tchana, F.; Lavrentieva, N. N.; Lee, T. J.; Long, D. A.; Lukashevskaya, A. A.; Lyulin, O. M.; Makhnev, V. Y.; Matt, W.; Massie, S. T.; Melosso, M.; Mikhailenko, S. N.; Mondelain, D.; Müller, H. S. P.; Naumenko, O. v.; Perrin, A.; Polyansky, O. L.; Raddaoui, E.; Raston, P. L.; Reed, Z. D.; Rey, M.; Richard, C.; Tóbiás, R.; Sadiek, I.; Schwenke, D. W.; Starikova, E.; Sung, K.; Tamassia, F.; Tashkun, S. A.; vander Auwera, J.; Vasilenko, I. A.; Vigasin, A. A.; Villanueva, G. L.; Vispoel, B.; Wagner, G.; Yachmenev, A.; Yurchenko, S. N. The HITRAN2020 Molecular Spectroscopic Database. *J. Quant. Spectrosc. Radiat. Transf.* **2022**, *277*, 107949. https://doi.org/10.1016/J.JQSRT.2021.107949.

(192) Barney, W. S.; Wingen, L. M.; Lakin, M. J.; Brauers, T.; Stutz, J.; Finlayson-Pitts, B. J. Infrared Absorption Cross-Section Measurements for Nitrous Acid (HONO) at Room Temperature. *Journal of Physical Chemistry A* **2000**, *104* (8), 1692–1699. https://doi.org/10.1021/jp9930503.

(193) Engeln, R.; Klarenaar, B.; Guaitella, O. Foundations of Optical Diagnostics in Low-Temperature Plasmas. *Plasma Sources Sci Technol* **2020**, *29* (6). https://doi.org/10.1088/1361-6595/ab6880.

(194) Pipa, A. v.; Ropcke, J. Analysis of the Mid-Infrared Spectrum of the Exhaust Gas from an Atmospheric Pressure Plasma Jet (APPJ) Working with an Argon-Air Mixture. *IEEE Trans. Plasma Sci.* **2009**, *37* (6), 1000–1003. https://doi.org/10.1109/TPS.2009.2013865.

(195) Cantrell, C. A.; Davidson, J. A.; McDaniel, A. H.; Shetter, R. E.; Calvert, J. G. Infrared Absorption Cross Sections for N2O5. *Chem. Phys. Lett.* **1988**, *148* (4), 358–363. https://doi.org/10.1016/0009-2614(88)87288-9.

(196) Maki, A. G.; Sams, R. L. Diode Laser Spectra of Cis-HONO near 850 Cm-1 and Trans-HONO near 1700 Cm-1. *J. Mol. Struct.* **1983**, *100*, 215–221. https://doi.org/10.1016/0022-2860(83)90093-5.

(197) Privat-Maldonado, A.; Gorbanev, Y.; Dewilde, S.; Smits, E.; Bogaerts, A. Reduction of Human Glioblastoma Spheroids Using Cold Atmospheric Plasma: The Combined Effect of Short- and Long-Lived Reactive Species. **2018**. https://doi.org/10.3390/cancers10110394.

(198) Gorbanev, Y.; Verlackt, C. C. W.; Tinck, S.; Tuenter, E.; Foubert, K.; Cos, P.; Bogaerts, A. Combining Experimental and Modelling Approaches to Study the Sources of Reactive Species Induced in Water by the COST RF Plasma Jet. *Phys. Chem. Chem. Phys.* **2018**, *20* (4), 2797–2808. https://doi.org/10.1039/c7cp07616a.

(199) Boxem, W. van; Paal, J. van der; Gorbanev, Y.; Vanuytsel, S.; Dewilde, S.; Bogaerts, A. Anti-Cancer Capacity of Plasma-Treated PBS : Effect of Chemical Composition on Cancer Cell Cytotoxicity Supplementary Information Calibration Curves Chemical Kinetics Model. 1–9.

(200) Bolleter W. T.; Bushman C. J.; Tiddwell P. W. Spectrophotometric Determination of Ammonia as Indophenol. *Anal. Chem.* **1961**, *33* (4), 592–594. https://doi.org/https://doi.org/10.1021/ac60172a034.

(201) Hu, B.; Tian, • X L; Shi, • W N; Zhao, • J Q; Wu, • P; Mei, • S T. Spectrophotometric Determination of Hydroxylamine in Biological Wastewater Treatment Processes. *Int. J. Environ. Sci. Technol.* **2018**, *15*, 323–332. https://doi.org/10.1007/s13762-017-1387-y.

(202) Bengtsson, G.; Fronæus, S.; Bengtsson-Kloo, L. The Kinetics and Mechanism of Oxidation of Hydroxylamine by Iron(III). *Journal of the Chemical Society, Dalton Transactions* **2002**, No. 12, 2548–2552. https://doi.org/10.1039/B201602H.

(203) Watt, G. W.; Chrisp, J. D. A Spectrophotometric Method for the Determination of Hydrazine. *Anal. Chem.* **1952**, *24* (12), 2006–2008. https://doi.org/https://doi.org/10.1021/ac60072a044.

(204) Blgeleisen, J.; Mayer, M. G. Calculation of Equilibrium Constants for Isotopic Exchange Reactions. *J Chem Phys* **1947**, *15* (5), 261–267. https://doi.org/10.1063/1.1746492.

(205) Hagelaar, G. J. M.; Pitchford, L. C. Solving the Boltzmann Equation to Obtain Electron Transport Coefficients and Rate Coefficients for Fluid Models. *Plasma Sources Sci Technol* **2005**, *14*, 722–733. https://doi.org/10.1088/0963-0252/14/4/011.

(206) Atkinson, R.; Baulch, D. L.; Cox, R. A.; Hampson, R. F.; Kerr, J. A.; Troe, J. Evaluated Kinetic and Photochemical Data for Atmospheric Chemistry: Supplement III. *Int J Chem Kinet* **1989**, *21* (2), 115–150. https://doi.org/10.1002/kin.550210205.

(207) Atkinson, R.; Baulch, D. L.; Cox, R. A.; Crowley, J. N.; Hampson, R. F.; Hynes, R. G.; Jenkin, M. E.; Rossi, M. J.; Troe, J. Evaluated Kinetic and Photochemical Data for Atmospheric Chemistry: Volume II - Gas Phase Reactions of Organic Species. *Atmos Chem Phys* **2004**, *6* (11), 3625–4055. https://doi.org/10.5194/acp-6-3625-2006.

(208) Atkinson, R.; Baulch, D. L.; Cox, R. A.; Crowley, J. N.; Hampson, R. F.; Hynes, R. G.; Jenkin, M. E.; Rossi, M. J.; Troe, J.; Wallington, T. J. Evaluated Kinetic and Photochemical Data for Atmospheric Chemistry: Volume IV - Gas Phase Reactions of Organic\newline Halogen Species. *Atmos Chem Phys* **2004**, *8* (15), 4141–4496. https://doi.org/10.5194/acp-8-4141-2008.

(209) Atkinson, R.; Baulch, D. L.; Cox, R. A.; Crowley, J. N.; Hampson, R. F.; Hynes, R. G.; Jenkin, M. E.; Rossi, M. J.; Troe, J.; Center, P. R.; Science, L. H.; Centre, T.; Park, S. Evaluated Kinetic and Photochemical Data for Atmospheric Chemistry: Volume I – Gas Phase Reactions of Ox, HOx, NOx and SOx Species. *J. Phys. Chem. Ref. Data* **2004**, *I*, 1461–1738. https://doi.org/10.5194/acp-4-1461-2004.

(210) Kossyi, I. A.; Kostinsky, A. Y.; Matveyev, A. A.; Silakov, V. P. Kinetic Scheme of the Non-Equilibrium Discharge in Nitrogen-Oxygen Mixtures. *Plasma Sources Sci Technol* **1992**, *1* (3), 207–220. https://doi.org/10.1088/0963-0252/1/3/011.

(211) Tsang, W.; Hampson, R. F. Chemical Kinetic Data Base for Combustion Chemistry. Part I. Methane and Related Compounds. *J Phys Chem Ref Data* **1986**, *15* (3), 1087–1279. https://doi.org/10.1063/1.555759.

(212) Tsang, W.; Herron, J. T. Chemical Kinetic Data Base for Propellant Combustion I. Reactions Involving NO, NO2, HNO, HNO2, HCN and N2O. *J Phys Chem Ref Data* **1991**, *20* (906), 609–663. https://doi.org/10.1063/1.555890.

(213) Alves, L. L. “The IST-Lisbon Database on LXCat.” *J. phys. Conf. Series* **2014**, *565* (1).

(214) *Phys4entry database, CNR IMIP Bari and SER&Practices, retrieved in february 2019*.

(215) Vervloessem, E.; Aghaei, M.; Jardali, F.; Hafezkhiabani, N.; Bogaerts, A. Plasma-Based N2Fixation into NOx: Insights from Modeling toward Optimum Yields and Energy Costs in a Gliding Arc Plasmatron. *ACS Sust. Chem. Eng.* **2020**, *8* (26), 9711–9720. https://doi.org/10.1021/acssuschemeng.0c01815.

(216) Adamovich, I. v.; MacHeret, S. O.; Rich, J. W.; Treanor, C. E. Vibrational Energy Transfer Rates Using a Forced Harmonic Oscillator Model. *J Thermophys Heat Trans* **2008**, *12* (1), 57–65. https://doi.org/10.2514/2.6302.

(217) Esposito, F.; Armenise, I.; Capitelli, M. N-N2 State to State Vibrational-Relaxation and Dissociation Rates Based on Quasiclassical Calculations. *Chem Phys* **2006**, *331* (1), 1–8. https://doi.org/10.1016/j.chemphys.2006.09.035.

(218) Esposito, F.; Armenise, I.; Capitta, G.; Capitelli, M. O-O2 State-to-State Vibrational Relaxation and Dissociation Rates Based on Quasiclassical Calculations. *Chem Phys* **2008**, *351* (1–3), 91–98. https://doi.org/10.1016/j.chemphys.2008.04.004.

(219) Bengt Andersson; Ronnie Andersson; Love Haokansson; Mikael Mortensen; Rahman Sudiyo; Berend van Wachem. *Computational Fluid Dynamics for Engineers* ; Cambridge Universtiy Press: Cambridge, 2012.

(220) Kaushik, N.; Uddin, N.; Sim, G. B.; Hong, Y. J.; Baik, K. Y.; Kim, C. H.; Lee, S. J.; Kaushik, N. K.; Choi, E. H. Responses of Solid Tumor Cells in DMEM to Reactive Oxygen Species Generated by Non-Thermal Plasma and Chemically Induced ROS Systems. *Sci Rep* **2015**, *5*, 1–11. https://doi.org/10.1038/srep08587.

(221) Ananth, A.; Dharaneedharan, S.; Seo, H. J.; Heo, M. S.; Boo, J. H. Soft Jet Plasma-Assisted Synthesis of Zinc Oxide Nanomaterials: Morphology Controls and Antibacterial Activity of ZnO. *Chemical Engineering Journal* **2017**, *322*, 742–751. https://doi.org/10.1016/j.cej.2017.03.100.

(222) Akishev, Y. S.; Aponin, G. I.; Grushin, M. E.; Karal'nik, V. B.; Monich, A. E.; Pan'kin, M. V.; Trushkin, N. I. Development of a Spark Sustained by Charging the Stray Capacitance of the External Circuit in Atmospheric-Pressure Nitrogen. *Plasma Physics Reports* **2007**, *33* (7), 584–601. https://doi.org/10.1134/S1063780X07070082.

(223) Pipa, A. V.; Brandenburg, R. The Equivalent Circuit Approach for the Electrical Diagnostics of Dielectric Barrier Discharges : The Classical Theory and

Recent Developments. *Atoms* **2019**, *7* (14), 2–18. https://doi.org/10.3390/atoms7010014.

(224) Zhao, B.; He, L.; Du, H.; Zhang, H. Electrical Characteristics of an Alternating Current Plasma Igniter in Airflow. *Plasma Science and Technology* **2014**, *16* (4), 370–373. https://doi.org/10.1088/1009-0630/16/4/12.

(225) Attri, P.; Park, J.; Backer, J. De; Kim, M.; Yun, J.; Heo, Y.; Dewilde, S.; Shiratani, M.; Ha, E.; Lee, W.; Bogaerts, A. Structural Modification of NADPH Oxidase Activator (Noxa 1) by Oxidative Stress : An Experimental and Computational Study. *Int J Biol Macromol* **2020**, *163*, 2405–2414. https://doi.org/10.1016/j.ijbiomac.2020.09.120.

(226) Pintassilgo, C. D.; Guaitella, O.; Rousseau, A. Heavy Species Kinetics in Low-Pressure Dc Pulsed Discharges in Air. *Plasma Sources Sci Technol* **2009**, *18* (2), 025005 (12pp). https://doi.org/10.1088/0963-0252/18/2/025005.

(227) Lo, A.; Cessou, A.; Boubert, P.; Vervisch, P. Space and Time Analysis of the Nanosecond Scale Discharges in Atmospheric Pressure Air: I. Gas Temperature and Vibrational Distribution Function of N 2 and O2. *J Phys D Appl Phys* **2014**, *47* (11), 115201. https://doi.org/10.1088/0022-3727/47/11/115201.

(228) Rusanov, V. D.; Fridman, A. A. The Physics of a Chemically Active Plasma with Nonequilibrium Vibrational Excitation of Molecules. *Sov. Phys. Usp.* **1981**, *24*, 447–474.

(229) Pancheshnyi, S.; Eismann, B.; Hagelaar, G. J. M.; Pitchford, L. C. *Computer code ZDPlaskin*. University of Toulouse, LAPLACE, CNRS-UPS-INP, Toulouse, France. http://www.zdplaskin.laplace.univ-tlse.fr.

(230) Bruggeman, P. J.; Sadeghi, N.; Schram, D. C.; Linss, V. Gas Temperature Determination from Rotational Lines in Non-Equilibrium Plasmas: A Review. *Plasma Sources Sci Technol* **2014**, *23* (2). https://doi.org/10.1088/0963-0252/23/2/023001.

(231) Wandell, R. J.; Wang, H.; Bulusu, R. K. M.; Gallan, R. O.; Locke, B. R. Formation of Nitrogen Oxides by Nanosecond Pulsed Plasma Discharges in

Gas–Liquid Reactors. *Plasma Chemistry and Plasma Processing* **2019**, 643–666. https://doi.org/10.1007/s11090-019-09981-w.

(232) Stark, R. H.; Ernst, U.; El-Bandrawy, M.; Schoenbach, K. H. Microhollow Cathode Discharges in Atmospheric Air. In *IEEE Conference Record - Abstracts. 1999 IEEE International Conference on Plasma Science. 26th IEEE International Conference (Cat. No.99CH36297),*; 1999; p 117. https://doi.org/10.1109/PLASMA.1999.829328.

(233) Namihira, T.; Katsuki, S.; Hackam, R.; Akiyama, H.; Okamoto, K. Production of Nitric Oxide Using a Pulsed Arc Discharge. *IEEE Trans. Plasma Sci.* **2002**, *30*, 1993–1998.

(234) Uddi, M.; Jiang, N.; Adamovich, I. V.; Lempert, W. R. Nitric Oxide Density Measurements in Air and Air/Fuel Nanosecond Pulse Discharges by Laser Induced Fluorescence. *J Phys D Appl Phys* **2009**, *42* (7), 075205. https://doi.org/10.1088/0022-3727/42/7/075205.

(235) Ono, R.; Oda, T. Measurement of Vibrationally Excited O2(v = 6) in the Afterglow of Pulsed Positive Corona Discharge. *Plasma Sources Sci Technol* **2009**, *18* (3), 035006. https://doi.org/10.1088/0963-0252/18/3/035006.

(236) Lo, A.; Cessou, A.; Vervisch, P. Space and Time Analysis of the Nanosecond Scale Discharges in Atmospheric Pressure Air : II . Energy Transfers during the Post-Discharge. *J Phys D Appl Phys* **2014**, *47*, 115202–115211. https://doi.org/10.1088/0022-3727/47/11/115202.

(237) Šimek, M.; Bonaventura, Z. Non-Equilibrium Kinetics of the Ground and Excited States in N2-O2 under Nanosecond Discharge Conditions: Extended Scheme and Comparison with Available Experimental Observations. *J Phys D Appl Phys* **2018**, *51* (50), 504004. https://doi.org/10.1088/1361-6463/aadcd1.

(238) Popov, N. A. Pulsed Nanosecond Discharge in Air at High Specific Deposited Energy: Fast Gas Heating and Active Particle Production. *Plasma Sources Sci Technol* **2016**, *25* (4), 044003 (17pp). https://doi.org/10.1088/0963-0252/25/4/044003.

(239) Anastasopoulou, A.; Butala, S.; Lang, J.; Hessel, V.; Wang, Q. Life Cycle Assessment of the Nitrogen Fixation Process Assisted by Plasma Technology and Incorporating Renewable Energy. *Ind. Eng. Chem. Res.* **2016**, *55*, 8141−8153. https://doi.org/10.1021/acs.iecr.6b00145.

(240) Gorbanev, Y.; O'Connell, D.; Chechik, V. Non-Thermal Plasma in Contact with Water: The Origin of Species. *Chemistry - A European Journal* **2016**, *22* (10), 3496–3505. https://doi.org/10.1002/CHEM.201503771.

(241) Lide, D. R. *CRC Handbook of Chemistry and Physics*; CRC Press: Boca Raton: Florida, USA, 1992.

(242) Gorbanev, Y.; Soriano, R.; O'connell, D.; Chechik, V. An Atmospheric Pressure Plasma Setup to Investigate the Reactive Species Formation. *J. Vis. Exp* **2016**, *117*, 54765. https://doi.org/10.3791/54765.

(243) Fridman, A. *Plasma Chemistry*; 2008. https://doi.org/10.1017/CBO9780511546075.

(244) *Fuel Cell Technologies Office Multi-Year Research, Development, and Demonstration Plan, Section 3.1 Hydrogen Production (U.S. Department of Energy).* https://www.energy.gov/sites/prod/files/2015/06/f23/fcto_myrdd_production.pdf (accessed 2023-03-27).

(245) Service, R. F. The Hydrogen Backlash. *Science (1979)* **2004**, *305* (5686), 958–961. https://doi.org/10.1126/SCIENCE.305.5686.958.

(246) Chen, J. G.; Crooks, R. M.; Seefeldt, L. C.; Bren, K. L.; Morris Bullock, R.; Darensbourg, M. Y.; Holland, P. L.; Hoffman, B.; Janik, M. J.; Jones, A. K.; Kanatzidis, M. G.; King, P.; Lancaster, K. M.; Lymar, S. V; Pfromm, P.; Schneider, W. F.; Schrock, R. R. Beyond Fossil Fuel-Driven Nitrogen Transformations. *Science (1979)* **2018**, *360*, eaar6611. https://doi.org/10.1126/science.aar6611.

(247) Uhm, H. S. Generation of Various Radicals in Nitrogen Plasma and Their Behavior in Media. *Phys Plasmas* **2015**, *22* (12), 123506–123513. https://doi.org/10.1063/1.4936796.

(248) Padarauskas, A.; Ol~auskaite, V.; Paliulionyte, V.; Pranailyte, B. Simultaneous Separation of Nitrate, Nitrite and Ammonium by Capillary Electrophoresis. *Chromatographia* **2000**, *52*, 133–137.

(249) Chen, C.; Lu, Y.; Banares-Alcantara, R. Direct and Indirect Electrification of Chemical Industry Using Methanol Production as a Case Study. *Appl Energy* **2019**, *243*, 71–90. https://doi.org/10.1016/j.apenergy.2019.03.184.

(250) Bruggeman, P. J.; Kushner, M. J.; Locke, B. R.; Gardeniers, J. G. E.; Graham, W. G.; Graves, D. B.; Hofman-Caris, R. C. H. M.; Maric, D.; Reid, J. P.; Ceriani, E.; Fernandez Rivas, D.; Foster, J. E.; Garrick, S. C.; Gorbanev, Y.; Hamaguchi, S.; Iza, F.; Jablonowski, H.; Klimova, E.; Kolb, J.; Krcma, F.; Lukes, P.; MacHala, Z.; Marinov, I.; Mariotti, D.; Mededovic Thagard, S.; Minakata, D.; Neyts, E. C.; Pawlat, J.; Petrovic, Z. L.; Pflieger, R.; Reuter, S.; Schram, D. C.; Schröter, S.; Shiraiwa, M.; Tarabová, B.; Tsai, P. A.; Verlet, J. R. R.; Von Woedtke, T.; Wilson, K. R.; Yasui, K.; Zvereva, G. Plasma-Liquid Interactions: A Review and Roadmap. *Plasma Sources Science and Technology*. Institute of Physics Publishing September 30, 2016, pp 053002–053118. https://doi.org/10.1088/0963-0252/25/5/053002.

(251) Gorbanev, Y.; Leifert, D.; Studer, A.; O'connell, D.; Chechik, V.; Li, R.; Chemcomm, /. Initiating Radical Reactions with Non-Thermal Plasmas. *Chem. Commun* **2017**, *53*, 3685–36488. https://doi.org/10.1039/c7cc01157a.

(252) Kelly, S.; Turner, M. M. Atomic Oxygen Patterning from a Biomedical Needle-Plasma Source. *J Appl Phys* **2013**, *114* (12), 123301–123309. https://doi.org/10.1063/1.4821241.

(253) Blgeleisen, J.; Mayer, M. G. Calculation of Equilibrium Constants for Isotopic Exchange Reactions. *J Chem Phys* **1947**, *15* (5), 261–267. https://doi.org/10.1063/1.1746492.

(254) Zhang, T.; Zhou, R.; Zhang, S.; Zhou, R.; Ding, J.; Li, F.; Hong, J.; Dou, L.; Shao, T.; Murphy, A. B.; Ostrikov, K.; Cullen, P. J. Sustainable Ammonia Synthesis from Nitrogen and Water by One-Step Plasma Catalysis. *Energy Environ. Mater.* **2022**. https://doi.org/10.1002/eem2.12344.

(255) Gordon, I.E., Rothman, L.S., Hargreaves, R.J., Hashemi, R., Karlovets, E.V., Skinner, F.M., Conway, E.K., Hill, C., Kochanov, R.V., Tan, Y., Wcisło, P., Finenko, A.A., Nelson, K., Bernath, P.F., Birk, M., Boudon, V., Campargue, A., Chance, K.V., Coustenis, S. N. The HITRAN2020 Molecular Spectroscopic Database. *J. Quant. Spectrosc. Radiat. Transf.* **2022**, *277*, 107949.

(256) Baulch, D. L.; Cobos, C. J.; Cox, R. A.; Frank, P.; Hayman, G.; Just, Th.; Kerr, J. A.; Murrells, T.; Pilling, M. J.; Troe, J.; Walker, R. W.; Warnatz, J. Evaluated Kinetic Data for Combusion Modelling. Supplement I. *J. Phys. Chem. Ref. Data* **1994**, *23*, 847–1033. https://doi.org/10.1063/1.555953.

(257) Bruggeman, P.; Brandenburg, R. Atmospheric Pressure Discharge Filaments and Microplasmas: Physics, Chemistry and Diagnostics. *J. Phys. D: Appl. Phys.* **2013**, *46* (46), 464001–464029. https://doi.org/10.1088/0022-3727/46/46/464001.

(258) Liu, Y.; Tan, Z.; Chen, X.; Li, X.; Wang, X. A Numerical Investigation on the Effects of Water Vapor on Electron Energy and Oh Production in Atmospheric-Pressure He/H2o and Ar/H2o Plasma Jets. *IEEE Trans Plasma Sci.* **2019**, *47* (3), 1593–1604. https://doi.org/10.1109/TPS.2019.2896060.

(259) Jiang, B.; Zhao, S.; Wang, Y.; Wenren, Y.; Zhu, Z.; Harding, J.; Zhang, X.; Tu, X.; Zhang, X. Plasma-Enhanced Low Temperature NH3-SCR of NOx over a Cu-Mn/SAPO-34 Catalyst under Oxygen-Rich Conditions. *Appl. Catal. B* **2021**, *286*, 119886–119897. https://doi.org/10.1016/j.apcatb.2021.119886.

(260) Grossale, A.; Nova, I.; Tronconi, E.; Chatterjee, D.; Weibel, M. The Chemistry of the NO/NO2-NH3 “Fast” SCR Reaction over Fe-ZSM5 Investigated by Transient Reaction Analysis. *J. Catal.* **2008**, *256* (2), 312–322. https://doi.org/10.1016/j.jcat.2008.03.027.

(261) Kubota, H.; Liu, C.; Toyao, T.; Maeno, Z.; Ogura, M.; Nakazawa, N.; Inagaki, S.; Kubota, Y.; Shimizu, K.-I. Formation and Reactions of NH4NO3 during Transient and Steady-State NH3-SCR of NOx over H-AFX Zeolites: Spectroscopic and Theoretical Studies. *ACS Catal.* **2020**, *10* (3), 2334–2344. https://doi.org/https://doi.org/10.1021/acscatal.9b05151.

(262) Mebel, A. M.; Lh, M. C.; Morokuma, K.; Melius, C. F. Theoretical Study of the Gas-Phase Structure, Thermochemistry, and Decomposition Mechanisms of NH4NO2 and NH4(NO2)2. *J. Phys. Chem.* **1995**, *99* (18), 6842–6848. https://doi.org/https://doi.org/10.1021/j100018a015.

(263) Sun, Q.; Gao, Z.-X.; Wen, B.; Sachtler, W. M. H. Spectroscopic Evidence for a Nitrite Intermediate in the Catalytic Reduction of NOx with Ammonia on Fe/MFI. *Catal. Letters* **2002**, *78*, 1–5. https://doi.org/https://doi.org/10.1023/A:1014981206924.

(264) Savara, A.; Li, M. J.; Sachtler, W. M. H.; Weitz, E. Catalytic Reduction of NH4NO3 by NO: Effects of Solid Acids and Implications for Low Temperature DeNOx Processes. *Appl. Catal. B* **2008**, *81* (3–4), 251–257. https://doi.org/10.1016/j.apcatb.2007.12.008.

(265) Zhang, X.; Zhang, Y.; Lu, H.; Zhu, Z.; Han, J. Characteristics of Ammonia Oxidation in a Dielectric Barrier Discharge Reactor. *IEEE Trans. Plasma Sci.* **2020**, *48* (10), 3616–3620. https://doi.org/10.1109/TPS.2020.3025092.

(266) Kim, D.-J.; Choi, Y.; Kim, K.-S. Effects of Process Variables on NOx Conversion by Pulsed Corona Discharge Process. *Plasma Chem. Plasma Process.* **2001**, *21* (4), 625–650. https://doi.org/https://doi.org/10.1023/A:1012007319848.

(267) Hippler, H.; Krasteva, N.; Nasterlack, S.; Striebel, F. Reaction of OH + NO2: High Pressure Experiments and Falloff Analysis †. *J. Phys. Chem. A* **2006**, *110*, 6781–6788. https://doi.org/10.1021/jp0562734.

(268) Pagsberg, P.; Ratajczak ', E.; Sillesen, A.; Latajka, Z. Kinetics and Thermochemistry of the Reversible Gas Phase Reaction HONO + NH3 = H3N-HONO Studied by Infrared Diode Laser Spectroscopy. *Chem. Phys. Lett.* **1994**, *227*, 6–12. https://doi.org/https://doi.org/10.1016/0009-2614(94)00787-X.

(269) Mozurkewich, M. The Dissociation Constant of Ammonium Nitrate and Its Dependence on Temperature, Relative Humidity and Particle Size. *Atmos Environ* **1993**, *27* (2), 261–270.

(270) Vyazovkin, S.; Clawson, J. S.; Wight, C. A. Thermal Dissociation Kinetics of Solid and Liquid Ammonium Nitrate. *Chem. Mater.* **2001**, *13* (3), 960–966. https://doi.org/10.1021/cm000708c.

(271) Shan, Y.; Shi, X.; He, G.; Liu, K.; Yan, Z.; Yu, Y.; He, H. Effects of NO2 Addition on the NH3-SCR over Small-Pore Cu−SSZ-13 Zeolites with Varying Cu Loadings. *J. Phys. Chem. C* **2018**, *122* (45), 25948–25953. https://doi.org/10.1021/acs.jpcc.8b05930.

(272) Feick, G.; Hainer, R. M. On the Thermal Decomposition of Ammonium Nitrate. Steady-State Reaction Temperatures and Reaction Rate. *J. Am. Chem. Soc.* **1954**, *76*, 5860–5863. https://doi.org/https://doi.org/10.1021/ja01651a096.

(273) Li, M.; Henao, J.; Yeom, Y.; Weitz, E.; Sachtler, W. M. H. Low Activation Energy Pathway for the Catalyzed Reduction of Nitrogen Oxides to N 2 by Ammonia. *Catal. Letters* **2004**, *98*, 5–9. https://doi.org/https://doi.org/10.1007/s10562-004-6441-y.

(274) Hu, X.; Zhang, Y.; Antonio Wu, R.; Liao, X.; Liu, D.; Cullen, P. J.; Zhou, R.-W.; Ding, T. Diagnostic Analysis of Reactive Species in Plasma-Activated Water (PAW): Current Advances and Outlooks. *J. Phys. D: Appl. Phys.* **2022**, *55*, 023002–023018. https://doi.org/10.1088/1361-6463/ac286a.

(275) Ito, S.; Takaoka, T.; Kishi, S.; Okuda, H.; Fujii, S. Studies of the Clinical Application of Serum Leucine Aminopeptidase (LAP) Activity Determined with Leucinamide as Substrate. *Gastroenterologia Japanica* **1975**, *10* (1), 20–28.

(276) Jirásek, V.; Lukeš, P. Formation of Reactive Chlorine Species in Saline Solution Treated by Non-Equilibrium Atmospheric Pressure He/O2 Plasma Jet. *Plasma Sources Sci Technol* **2019**, *28* (3), 035015–035039. https://doi.org/10.1088/1361-6595/ab0930.

(277) Bothner-By, A.; Friedman, L. The Reaction of Nitrous Acid with Hydroxylamine. *J Chem Phys* **1952**, *20* (3), 459–462. https://doi.org/10.1063/1.1700442.

(278) P.T. Nunally. T. P. Nunnally, PhD Thesis, Drexel University, 2011., Drexel University, 2011.

(279) www.comsol.com. COMSOL Multiphysics v. 5.4. *COMSOL Multiphysics v. 5.4 Comsol AB*.

(280) Wagman, D. D.; Evans, W. H.; Parker, V. B.; Schumm, R. H.; Halow, I.; Bailey, S. M.; Churney Kenneth L.; Nuttall, R. L. The NBS Tables of Chemical Thermodynamic Properties: Selected Values for Inorganic and C1 and C2 Organic Substances in SI Units. *J. Phys. Chem. Ref. Data.* **1982**, *11*, 1–392.

(281) Laporta, V.; Little, D. A.; Celiberto, R.; Tennyson, J. Electron-Impact Resonant Vibrational Excitation and Dissociation Processes Involving Vibrationally Excited N2molecules. *Plasma Sources Sci Technol* **2014**, *23*, 065002. https://doi.org/10.1088/0963-0252/23/6/065002.

(282) Laporta, V.; Little, D. A.; Celiberto, R.; Tennyson, J. Electron-Impact Resonant Vibrational Excitation and Dissociation Processes Involving Vibrationally Excited N2molecules. *Plasma Sources Sci Technol* **2014**, *23*, 065002. https://doi.org/10.1088/0963-0252/23/6/065002.

(283) Alves, L. L. "The IST-Lisbon Database on LXCat." *J. phys. Conf. Series* **2014**, *565* (1).

(284) *Morgan database, www.lxcat.net, retrieved in february 2018.* retrieved february 2018.

(285) *Itikawa database, www.lxcat.net, retrieved in february 2018.* retrieved february 2018.

(286) Laporta, V.; Celliberto, R.; Tennyson, J. Resonant Vibrational-Excitation Cross Sections and Rate Constants for Low-Energy Electron Scattering by Molecular Oxygen. *plasma sources sci. Technol.* **2013**, *22*, 025001. https://doi.org/10.1088/0963-0252/22/2/025001.

(287) Itikawa, Y. Cross Sections for Electron Collisions with Oxygen Molecules. *J Phys Chem Ref Data* **2009**, *38* (1), 1–20. https://doi.org/10.1063/1.3025886.

(288) Itikawa, Y. Cross Sections for Electron Collisions with Oxygen Molecules. *J Phys Chem Ref Data* **2009**, *38* (1), 1–20. https://doi.org/10.1063/1.3025886.

(289) Eliasson, B.; Kogelschatz, U. *Basic Data for Modelling of Electrical Discharges in Gases: Oxygen*; Baden: ABB Asea Brown Boveri, 1986.

(290) Alves, L. L. “The IST-Lisbon Database on LXCat.” *J. phys. Conf. Series* **2014**, *565* (1).

(291) Lawton, S. A.; Phelps, A. V. Excitation of the B^1 Sigma_g^+ State of O_2 by Low Energy Electrons. *J. chem. Phys.* **1978**, *69* (3), 1055–1068. https://doi.org/10.1063/1.436700.

(292) Khvorostovskaya, L. E.; Yankovsky, V. A. Negative Ions, Ozone, and Metastable Components in Dc Oxygen Glow Discharge. *Contributions to Plasma Physics* **1991**, *31* (1), 71–88. https://doi.org/10.1002/ctpp.2150310109.

(293) Hokazono, H.; Obara, M.; Midorikawa, K.; Tashiro, H. Theoretical Operational Life Study of the Closed-Cycle Transversely Excited Atmospheric CO2laser. *J Appl Phys* **1991**, *69* (10), 6850–6868. https://doi.org/10.1063/1.347675.

(294) *Quantemol database, www.lxcat.net, retrieved in february 2018.* retrieved february 2018.

(295) *Hayashi database, www.lxcat.net, retrieved in february 2018.* retrieved february 2018.

(296) Gordillo-V’azquez, F. J. Air Plasma Kinetics under the Influence of Sprites. *J. Phys. D.: Appl. Phys.* **2008**, *41*, 234016–234049. https://doi.org/10.1088/0022-3727/41/23/234016.

(297) Wang, W.; Snoeckx, R.; Zhang, X.; Cha, M. S.; Bogaerts, A. Modeling Plasma-Based CO2 and CH4 Conversion in Mixtures with N2, O2, and H2O: The Bigger Plasma Chemistry Picture. *Journal of Physical Chemistry C* **2018**, *122* (16), 8704–8723. https://doi.org/10.1021/acs.jpcc.7b10619.

(298) Capitelli. *Plasma Kinetics in Atmospheric Gases*; Springer, 2000.

(299) Kewley, D. J.; Hornung, H. G. Free-Piston Shock-Tube Study of Nitrogen Dissociation. *Chem Phys Lett* **1974**, *25* (4), 531–536. https://doi.org/10.1016/0009-2614(74)85360-1.

(300) Clyne, M. A. A.; Stedman, D. H. Rate of Recombination of Nitrogen Atoms. *J Phys Chem* **1967**, *71* (9), 3071–3073. https://doi.org/10.1021/j100868a056.

(301) Van Gaens, W.; Bogaerts, A. Erratum: Kinetic Modelling for an Atmospheric Pressure Argon Plasma Jet in Humid Air (J. Phys. D: Appl. Phys. 46 (2013) 275201)). *J Phys D Appl Phys* **2014**, *47* (7), 079502 (3pp). https://doi.org/10.1088/0022-3727/47/7/079502.

(302) Tsang, W.; Hampson, R. F. Chemical Kinetic Data Base for Combustion Chemistry. Part I. Methane and Related Compounds. *J Phys Chem Ref Data* **1986**, *15* (3), 1087–1279. https://doi.org/10.1063/1.555759.

(303) Atkinson, R.; Baulch, D. L.; Cox, R. A.; Hampson, R. F.; Kerr Chairman, J. A.; Troe, J. Evaluated Kinetic and Photochemical Data for Atmospheric Chemistry: Supplement III. IUPAC Subcommittee on Gas Kinetic Data Evaluation for Atmospheric Chemistry. *J Phys Chem Ref Data* **1997**, *18* (2), 881–1097. https://doi.org/10.1063/1.555832.

(304) Hippler, H.; Rahn, R.; Troe, J. Temperature and Pressure Dependence of Ozone Formation Rates in the Range 1-1000 Bar and 90-370 K. *J Chem Phys* **1990**, *93* (9), 6560–6569. https://doi.org/10.1063/1.458972.

(305) Heimerl, J. M.; Coffee, T. P. The Unimolecular Ozone Decomposition Reaction. *Combust Flame* **1979**, *35* (C), 117–123. https://doi.org/10.1016/0010-2180(79)90015-4.

(306) Suzzi Valli, G.; Orrú, R.; Clementi, E.; Laganà, A.; Crocchianti, S. Rate Coefficients for the N+O2reaction Computed on an Ab Initio Potential Energy Surface. *J Chem Phys* **1995**, *102* (7), 2825–2832. https://doi.org/10.1063/1.468660.

(307) Hjorth, J.; Notholt, J.; Restelli, G. No Title. *Int. J. Chem. Kinet.* **1992**, *24*, 51–65. https://doi.org/10.1002/kin.550240107.

(308) Herron, J. T. Rate of the Reaction NO+N. *J Chem Phys* **1961**, *35* (3), 1138–1139. https://doi.org/10.1063/1.1701202.

(309) Bemand, P. P.; Clyne, M. A. A.; Watson, R. T. Atomic Resonance Fluorescence and Mass Spectrometry for Measurements of the Rate

Constants for Elementary Reactions: O 3PJ + NO 2 → NO + O2 and NO + O3 → NO 2 + O2. *Journal of the Chemical Society, Faraday Transactions 2: Molecular and Chemical Physics* **1974**, *70* (02), 564–576. https://doi.org/10.1039/F29747000564.

(310) Graham, R. A.; Johnston, H. S. The Photochemistry of the Nitrate Radical and the Kinetics of the Nitrogen Pentoxide-Ozone System. *J. Phys. Chem.* **1978**, *82* (3), 254–268. https://doi.org/10.1021/j100492a002.

(311) Ashmore, P. G.; Burnett, M. G. Concurrent Molecular and Free Radical Mechanisms in the Thermal Decomposition of Nitrogen Dioxide. *J. Chem. Soc. Faraday Trans. 2* **1962**, 253–261. https://doi.org/10.1039/TF9625800253.

(312) Campbell, I. M.; Thrush, B. A. Behaviour of Carbon Dioxide and Nitrous Oxide in Active Nitrogen. *Transactions of the Faraday Society* **1966**, *62*, 3366–3374. https://doi.org/10.1039/tf9666203366.

(313) Nighan, W. L. Electron Energy Distributions and Collision Rates in Electrically Excited N2, CO, and CO2. *Phys. Rev.* **1970**, *2* (5), 1989–2000. https://doi.org/10.1103/PhysRevA.2.1989.

(314) Beverly, R. E. Ion Aging Effects on the Dissociative-Attachment Instability in CO2 Lasers. *Opt Quantum Electron* **1982**, *14* (6), 501–513. https://doi.org/10.1007/BF00610306.

(315) Whitaker, M.; Biondi, M. A.; Johnsen, R. Electron-Temperature Dependence of Dissociative Recombination of Electrons with N2^+. *Phys Rev A (Coll Park)* **1981**, *24*, 743–745. https://doi.org/10.1103/PhysRevA.24.743.

(316) Gudmundsson, J. T.; Thorsteinsson, E. G. Oxygen Discharges Diluted with Argon: Dissociation Processes. *Plasma Sources Sci Technol* **2007**, *16* (2), 399–412. https://doi.org/10.1088/0963-0252/16/2/025.

(317) Ionin, A. A.; Kochetov, I. V.; Napartovich, A. P.; Yuryshev, N. N. Physics and Engineering of Singlet Delta Oxygen Production in Low-Temperature Plasma. *J Phys D Appl Phys* **2007**, *40* (2), R25–R36. https://doi.org/10.1088/0022-3727/40/2/R01.

(318) Cenian, A.; Chernukho, A.; Borodin, V. Modeling of Plasma-Chemical Reactions in Gas Mixture of CO2 Lasers. II. Theoretical Model and Its Verification. *Contributions to Plasma Physics* **1995**, *35* (3), 273–296. https://doi.org/10.1002/ctpp.2150350309.

(319) Beuthe, T. G.; Chang, J.-S. Related Content Chemical Kinetic Modelling of Non-Equilibrium Ar- CO 2 Thermal Plasmas. *Jpn J Appl Phys* **1997**, *36* (4997), 4997–5002. https://doi.org/10.1143/JJAP.36.4997.

(320) Eliasson, B.; Hirth, M.; Kogelschatz, U. Ozone Synthesis from Oxygen in Dielectric Barrier Discharges. *J Phys D Appl Phys* **1987**, *20* (11), 1421–1437. https://doi.org/10.1088/0022-3727/20/11/010.

(321) Mcfarland, M.; Dunkin, D. B.; Fehsenfeld, F. C.; Schmeltekopf, A. L.; Ferguson, E. E. Collisional Detachment Studies of NO-. *J Chem Phys* **1972**, *56* (5), 2358–2364. https://doi.org/10.1063/1.1677542.

(322) Mcfarland, M.; Dunkin, D. B.; Fehsenfeld, F. C.; Schmeltekopf, A. L.; Ferguson, E. E. Collisional Detachment Studies of NO-. *J Chem Phys* **1972**, *56* (5), 2358–2364. https://doi.org/10.1063/1.1677542.

XI. LIST OF ABREVIATIONS

Abbreviations	Meaning
k_{iq}	Quenching coefficient
λ_0	Emission line
σ_I	Cross-section
A	Einstein transition coefficient
BNF	Biological nitrogen fixation
c	Speed of light
CCS	Carbon Capture and Storage
CFD	Computational fluid dynamics
DBD	Dielectric barrier discharge
DNA	Deoxy ibonucleic acid
EC	Energy consumption
EC	Energy consumption
EEDF	Electron energy distribution function
E_p/E_k	Foton energy
e-V	Electron vibrational
E_x	Electronically excited state
FHO	Forced harmonic oscillator
FTIR	Fourier-transform infra-red
g	Ground state
h	Planck’s constant
HB	Haber-Bosch
I	Current
I	Signal intensity
ICCD	Intensified charged coupled device
IR	Infra-red

K_b	Boltzmann constant
L	Path length
LCA	Life cycle assessment
LNT	Lean NO_x trap
m_e	Mass of and electron
MFC	Mass flow controller
m_H	Mass of a hydrogen atom
MW	Microwave
N	Nitrogen
Nd	Not defined
n_e	Electron density
NF	Nitrogen Fixation
OES	Optical emission spectroscopy
P	Power
P	Probability of electron impact excitation
P	Power
PAW	Plasma activated water
PNOCRA	Plasma nitrogen oxidation with catalytic reduction to ammonia
PR	Production rate
PTW	Plasma treated water
Q	Effective quenching rates
q	Fraction of signal that is visible after quenching
RF	Radio frequency
RNA	Ribonucleic acid
RNS	Reactive nitrogen species

RONS	Reactive oxygen and nitrogen species
ROS	Reactive oxygen species
RSS	Rayleigh scattering spectroscopy
T_D	Discharge period
T_e	Electron temperature
TEA	Techno-economical analysis
T_g	Gas temperature
T_{rot}	Rotational temperature
tt	Treatment time
T_v	Vibrational temperature
UAN	Urea Ammonium Nitrate
UV-VIS	Ultra-violet – visible (light)
V	Voltage
VDF	Vibrational distribution function
VOC	Volatile organic compounds
v_r	Relative velocity
VT	Vibrational-translational
VV	Vibrational-vibrational
V_x	Vibrationally excited state

XII. LIST OF PUBLICATIONS

As first author

1. **Vervloessem, E.**, Gromov, M., De Geyter, N., Bogaerts, A., Gorbanev, Y., & Nikiforov, A. (2023). NH_3 and HNO_x formation and loss in nitrogen fixation from air with water vapor by non-equilibrium plasma. *ACS Sust. Chem. Eng.*, 11, 4289-4298. DOI:10.1021/acssuschemeng.3c00208

2. **Vervloessem, E.**, Gorbanev, Y., Nikiforov, A., De Geyter, N., & Bogaerts, A. (2022). Sustainable NO_x production from air in pulsed plasma: elucidating the chemistry behind the low energy consumption. *Green Chem.*, *24*, 916–929. DOI:10.1039/d1gc02762j

3. **Vervloessem, E**., Aghaei, M., Jardali, F., Hafezkhiabani, N., & Bogaerts, A. (2020). Plasma-based N_2 fixation into NO_x: Insights from modeling toward optimum yields and energy costs in a gliding arc plasmatron. *ACS Sust. Chem. Eng.*, *8*(26), 9711–9720. DOI:10.1021/acssuschemeng.0c01815

As co-author

4. Gorbanev, Y., **Vervloessem, E.**, Nikiforov, A., & Bogaerts, A. (2020). Nitrogen fixation with water vapor by non-equilibrium plasma: toward sustainable ammonia production. *ACS Sust. Chem. Eng.*, *8*, 2996–3004. DOI:10.1021/acssuschemeng.9b07849

5. Hollevoet, L; **Vervloessem E.**; Gorbanev, Y.; Nikiforov, A.; De Geyter, N.; Bogaerts, A.; Martens, J. (2022). Energy-Efficient Small-Scale Ammonia Synthesis Process with Plasma-Enabled Nitrogen Oxidation and Catalytic Reduction of Adsorbed NOx. *ChemSusChem*., *15,* e202102526.
DOI: 10.1002/cssc.202102526

6. Pattyn, C.; Maira, N.; Buddhadasa, M.; **Vervloessem, E.**; Iseni, S.; Roy, N.; Remy, A.; Delplancke, M.; De Geyter, N.; Reniers, F. (2022). Disproportionation of nitrogen induced by CD plasma-driven electrolysis in a nitrogen atmosphere. *Green Chemistry., 24, 7100 – 7112.*
DOI: 10.1039/d2gc01013e

XIII. CONFERENCE CONTRIBUTIONS

1. Poster presentation at the Conference on Cold Plasma Sources and Applications (COPSA 2018), Ypres, Belgium (November 2018), presenting “Plasma-based N_2 fixation into NO_x: Insights from modeling toward optimum yields and energy costs in a gliding arc plasmatron”
2. Oral presentation at the International Symposium of Plasma Chemistry (ISPC 2019), Naples, Italy (June 2019), presenting “Modelling the chemistry of a N_2/O_2 plasma in a gliding arc plasmatron”
3. Oral presentation at the Chemistry Conference for Young Scientists (ChemCYS 2020), Blankenberge, Belgium (February 2020), presenting “Plasma-based N_2 fixation into NO_x: Insights from modeling toward optimum yields and energy costs in a gliding arc plasmatron”
4. Poster presentation at the Solvay Workshop on Plasma Technology and Other Green Methods for Nitrogen Fixation, Brussels, Belgium (November 2021), presenting “Sustainable NO_x Production from Air in Pulsed Plasma: Elucidating the chemistry behind the low energy consumption”
5. Oral presentation at the 9^{th} Central European Symposium for Plasma Chemistry (Cesp 2022), Vysoke Tatry, Slovakia (September 2022), presenting “Nitrogen fixation with water vapor by nonequilibrium plasma”

OTHER ACHIEVEMENTS

Thesis supervision

1. Supervisor Dante De Koning (Master's thesis, 2020, PLASMANT)
2. Co-supervisor Wouter Kruijsse (Bachelor's thesis 2022, PLASMANT)

Organizing activities

1. Co-organizing "Proefkot" – Promoting STEM to children between 9 and 13 years old (November 2019, June 2020 (video), October 2020 and February 2021).
2. Co-organizing video "Chemie in de Keuken" for "Dag van de Wetenschap" – A day filled with science activities for all ages throughout Flanders (November 2020).
3. Part of the organizing committee of ChemCYS 2020 (Chemistry Conference for Young Scientists).
4. Part of the organizing committee of CRF-ChemCYS 2022 (Chemical Research Flanders and Chemistry Conference for Young Scientists).
5. Co-organizing "Wetenschapsquiz" – science quiz (November 2021, November 2022, November 2023).
6. Helping hand at evening lectures (Kékulé, UA, 2019 & 2021; KVCV lectures 2018 – 2023).

Geef elke dag de kans om de mooiste dag van je leven te worden..

- Bomma (Mark Twain)

Pride is not the opposite of shame, but its source.
True humility is the antidote to shame.
- Uncle Iroh